Modelling and Investigation of NMDAR-Mediated Calcium Signalling at Hippocampal Dendritic Spine in Alzheimer's Disease

by

Jingyi Liang

A thesis submitted in partial fulfilment

of the requirements for the Degree of

Doctor of Philosophy

in Computational Systems Biology

at

Lincoln University

New Zealand

2016

Abstract of a thesis submitted in partial fulfilment of the
requirements for the Doctor of Philosophy.

Abstract

Modelling and Investigation of NMDAR-Mediated Calcium Signalling at Hippocampal Dendritic Spine in Alzheimer's Disease

by

Jingyi Liang

Alzheimer's disease (AD) is a devastating, incurable neurodegenerative disease affecting millions of people worldwide. Dysregulation of intracellular Ca^{2+} signalling has been observed as an early event prior to the presence of clinical symptoms of AD and is believed to be a crucial factor contributing to its pathogenesis.

Mathematical modelling and computational analysis offer great opportunities to overcome the experimental limitation and investigate alterations in AD to advance our understanding of the Ca^{2+} dysregulations of AD and their contributions to disease pathology. In this study, we develop a mathematical model of a CA1 pyramidal dendritic spine, integrating essential components and reactions related to NMDAR-mediated Ca^{2+} response in the dendritic spine. We conduct computational experiments using this model to mimic alterations under AD conditions to investigate how they are involved in the Ca^{2+} dysregulation in the dendritic spine. The alterations in glutamate availability, as well as NMDAR availability and activity, are studied individually and globally. The simulation results suggest that alterations in glutamate availability mostly affect synaptic response and have limited effects on extrasynaptic receptors. Overactivation of extrasynaptic NMDARs in AD is unlikely induced by presynaptic stimulation, but by upregulation of resting level of glutamate, possibly resulted from these alterations. Furthermore, internalisation of synaptic NR2A-NMDAR shows great damage to postsynaptic Ca^{2+} response in comparison with the internalisation of NR2B-NMDARs, thus, the suggested neuroprotective role of the latter one is very limited during synaptic transmission in AD.

We also simulate alterations of the internal Ca^{2+} store, ER, under AD conditions by including ER-related components to the model and investigate how these alterations affect the roles of ER in NMDAR-mediated Ca^{2+} response in the spine head. Simulation results suggest that the

proposed neuroprotective function of up-regulation in RyR expression may make the cell more vulnerable by amplifying the cytosolic Ca^{2+} level. The simulation results also suggest alterations in ER may have more impacts in basal synaptic transmission than high frequency-induced transmissions in AD. In addition, the simulation results predict that inhibition of SERCA pumps may be beneficial to rescue the spine head from Ca^{2+} dysregulation by ER Ca^{2+} overload in AD.

To further study the effects of alterations of NMDARs in their roles in downstream events, we add a CaMKII state transition model to the downstream of our Ca^{2+} model to study how alterations of NMDAR affect CaMKII state transition, an important event in the early phase of LTP. Simulation results suggest a cooperation between NR2A- and NR2B-NMDAR is required for LTP induction. Under AD conditions, internalisation of membrane NMDARs may be the cause of loss of synapse number by disrupting CaMKII-NMDAR formation.

Keywords**:** Alzhemer's disease, Amyloid-β, Ca^{2+} dysregulation, glutamate transimission, AMPAR, NMDAR, ER, CaMKII-NMDAR formation, mathmatical modelling, parameter esitimation, ordinary differential equations

Acknowledgements

First of all, I would like to express my deepest gratitude to my supervisor, Professor Don Kulasiri, for his constant encouragement and guidance. Without his supervision, this thesis would not have been possible. I would also express my appreciation to my associate supervisor, Professor Sandhya Samarasinghe, for her insightful ideas and comments on my study. I am truly grateful for all the support they have provided me, which helped me to become an independent researcher.

I would like to thank all members of C-fACS (Centre for Advanced Computational Solutions) team. It is very enjoyable to work with this team and I have a wonderful time. In particular, I would like to thank Dr. Yao He and Dr. Thusangi Wannige for their discussions, suggestions and sharing of ideas. I would also like to thank Dr. Zhongkun Zhou, Dr. Pramuditha Waidyarathne and Fatima Jamal for their friendship and support during my doctoral study.

I would like to express my appreciation to Lincoln University for providing the Lincoln University Doctoral Scholarship during my study.

I would like to thank my friends and flatmates for their companionship, making my life in New Zealand very delightful. I would also like to acknowledge Dr. Mark Wilson and Robyn Wilson for their warm care and generous support.

Finally, I want to thank my parents, Hongde Liang and Jihong Zhu, my sisters, Jiayu Liang and Mingyu Liang, and my grandma, Yunling Ji, for their unconditional love and supports.

Table of Contents

List of Tables

List of Figures

Abbreviations

Terminology

AD	Alzheimer's disease
AMPAR	α-amino-3-hydroxy-5-methyl-4-isoxazolepropionic acid receptor
AP	action potential
APP	amyloid precursor protein
Aβ	amyloid-β
bAP	backpropagation of action potentials
Ca^{2+}	calcium
Ca_4CaM	fully-bound Ca^{2+}-CaM complex
CaD	calbindin
CaM	calmodulin
CaMKII	Ca^{2+}-Calmodulin-dependent Kinase-II
CICR	Ca^{2+}-induced Ca^{2+} release
CPA	cyclopiazonic acid
EAAT	excitatory amino acid transporter
eNMDAR	Extrasynaptic NMDA receptor
EPSP	excitatory postsynaptic potential
ER	endoplasmic reticulum
GluR	glutamate receptors
HFS	high-frequency stimulation at 100 Hz
iGluR	ionotropic glutamate receptor
IP3	inositol 1,4,5-trisphosphate
IP3R	inositol 1,4,5-trisphosphate receptor
LHS	low-frequency stimulation at 10 Hz
LTP	long-term potentiation
MAPE	mean absolute percentage error
MCMC	Markov Chain Monte Carlo
mGluR	metabotropic glutamate receptor
NCX	sodium-calcium exchanger
NMDAR	N-methyl-D-aspartate receptor
NMDAR-LTP	NMDAR-dependent LTP
ODE	ordinary differential equation
PMCA	plasma membrane Ca^{2+} ATPase

PS	presenilins
PSD	postsynaptic density
Q10	temperature Coefficient
ROS	reactive oxygen species
RyR	ryanodine receptor
SERCA	sarcoplasmic reticulum Ca^{2+} ATPase
sNMDAR	synaptic NMDAR
ST	state transition
TBS	theta burst stimulation
Thr286	threonine 286
VDCC	voltage-dependent calcium channel
APP	amyloid precursor protein

Key testing factors and outputs

$[\mathbf{Ca^{2+}}]_{\mathbf{cyto}}$	cytosolic Ca^{2+} concentration
$[\mathbf{Ca^{2+}}]_{\mathbf{cyto0}}$	basal Ca^{2+} concentration of cytosol
$[\mathbf{Ca^{2+}}]_{\mathbf{ER0}}$	basal Ca^{2+} concentration of ER
$[\mathbf{Ca^{2+}}]_{\mathbf{RyR}}$: $[\mathbf{Ca^{2+}}]_{\mathbf{NMDAR}}$ ratio	the ratio of total Ca^{2+} ions enters via RyR to those via the NMDAR
$[\mathbf{Ca^{2+}}]_{\mathbf{spine}}$	Ca^{2+} concentration in the spine head
CaMKII-NMDAR*	CaMKII with NMDAR bound to T site of any active subunit
$\mathbf{J_{ER}}$	net Ca^{2+} flux from the ER to the cytosol
$\mathbf{J_{leakER}}$	ER membrane leakage
$\mathbf{J_{RyR}}$	Ca^{2+} flux via RyRs
$\mathbf{J_{SERCA}}$	Ca^{2+} flux via SERCA pumps
$\mathbf{Po_{RyR}}$	the fraction of RyRs opened by cytosolic Ca^{2+}
$\mathbf{V_{RyR}}$	RyR Ca^{2+} release rate
$\mathbf{v_{SERCA}}$	maximum rate of SERCA
4 TBS	4 trains of paring TBS

Chapter 1
Introduction

1.1 Alzheimer's disease and Ca^{2+} dysregulation

Alzheimer's disease (AD) is the leading cause of dementia and, unfortunately, is still incurable. About 47 million people worldwide are affected by AD or other dementia (Prince, Comas-Herrera et al. 2016). AD is characterized by progressive and irreversible loss of memory and cognitive function, while the exact pathophysiology and pathogenesis of the disease are still unknown. Various hypotheses have been proposed and attempted to explain the causes of AD, such as the amyloid deposition hypothesis (Hardy and Higgins 1992, Hardy and Selkoe 2002, Karran, Mercken et al. 2011), the tau hypothesis (Braak and Braak 1991, Iqbal, del C. Alonso et al. 2005, Wischik, Wischik et al. 2010) and the cholinergic hypothesis (Bartus, Dean et al. 1982, Francis, Palmer et al. 1999, Craig, Hong et al. 2011). Although much progress has been made with these hypotheses, they cannot explain all the physiological changes that occur during the development of this disease.

Calcium (Ca^{2+}) dysregulation has been observed in the brains of AD patients before the presence of overt clinical symptoms or the development of the classic biological hallmarks of amyloid plaques and neurofibrillary tangles (Gouras, Tsai et al. 2000, Oddo, Caccamo et al. 2006). Genetic studies have also revealed altered levels of the genes and proteins that are related to intracellular Ca^{2+} signalling pathways in AD cells (Kelliher, Fastbom et al. 1999, Emilsson, Saetre et al. 2006). Under healthy conditions in the nervous system, Ca^{2+} signalling accounts for diverse functions in brain physiology; for example, neurotransmitter release, neuronal excitability, neuronal development, synaptic plasticity, gene expression and neuronal survival and death (Verkhratsky 2005).

Because of the ubiquitous role Ca^{2+} plays in the nervous system, its dysregulation could induce numerous alterations and cause dysfunctions. Ca^{2+} hypothesis of AD, which was first proposed by Khachaturian, and many subsequent experimental research suggest that the sustained disturbance of intracellular Ca^{2+} signalling may contribute to the major symptoms of AD and may be the predominant cause of neurodegeneration in AD (Khachaturian 1994, Thibault, Gant et al. 2007, Berridge 2010). Intracellular Ca^{2+} dynamics is intimately associated with cognitive and memory-related neuronal functions such as neural rhythm and synaptic plasticity.

In pyramidal neurons of the hippocampus, N-methyl-D-aspartate receptor (NMDAR) and α-amino-3-hydroxy-5-methyl-4-isoxazolepropionic acid receptor (AMPAR) at membrane play crucial roles in mediating the Ca^{2+} response of postsynaptic neuron and synaptic plasticity formation (Regehr and Tank 1990). Dysregulations of these membrane receptors have been exclusively studied and are believed to contribute to pathological changes in AD (Danysz and Parsons 2012). Inside the neuron, Endoplasmic reticulums (ERs) as the largest intracellular Ca^{2+} stores are widely distributed within neurons and participate in Ca^{2+} signalling. ER Ca^{2+} dysregulation in neurons has been shown to further affect downstream events, such as triggering membrane hyperpolarization, reducing electrical excitability and mitochondrial dysfunction (Stutzmann, Caccamo et al. 2004, Schon and Area-Gomez 2013). It is believed that alteration of ER Ca^{2+} signalling is a key upstream event in AD pathophysiology that initiates and accelerates other severe events such as amyloid plaque deposition and neuronal apoptosis (Cheung, Shineman et al. 2008). Ca^{2+} dysregulation in ER contributes to the persistent rise in cytosolic basal Ca^{2+} level, which in turns affects sleep/wake cycle (Berridge 2014). In AD, increase in wakefulness significantly disrupts the processes of memory consolidation and erasure during sleep, and contributes to the loss of memory. Upregulation in basal Ca^{2+} level observed in AD transgenic mice is suggested to interrupt mechanisms related to learning and memory (Kuchibhotla, Goldman et al. 2008). Increase in intracellular Ca^{2+} level shows to enhance long-term depression (LTD), a form of synaptic plasticity which weakens synapses, and may result in memory deficits (Li, Hong et al. 2009). Other key features of AD, such as inflammation and oxidative stress, are also related to intracellular Ca^{2+} dysregulation. Chronic neuroinflammation is one of early features of AD, which is critically linked to the disease pathogenesis (Ferreira, Clarke et al. 2014). Inflammation can be induced by amyloid-β (Aβ) directly or by increasing oxidative stress during aging in the brain (Floyd and Hensley 2002, Berridge 2014). Inflammatory responses of astrocytes and microglia lead to local aberrant Ca^{2+} signalling as well as promote Ca^{2+} signalling in neurons, contributing to memory loss and apoptosis in AD (Berridge 2014). Beside inflammation, increased generation of reactive oxygen species (ROS) during aging or stimulated by Aβ can affect Ca^{2+} signalling pathway directly (Christen 2000). This leads to elevated intracellular Ca^{2+} level and causes excitotoxic effects and neuronal death (Ermak and Davies 2002, Uttara, Singh et al. 2009). Meanwhile, the increased intracellular Ca^{2+} level stimulates mitochondria and induce excessive mitochondria ROS formation, leading to aggravated neuronal oxidative stress (Müller, Cheung et al. 2011).

In addition to important roles in enormous intracellular responses, intracellular Ca^{2+} dynamics

regulates intercellular communication between neurons and between neurons and other cells (Pasti, Volterra et al. 1997, Augustine 2001). Abnormal intracellular Ca^{2+} in presynaptic terminal impairs the release of neurotransmitters (Palop and Mucke 2010). This will disturb synaptic transmission and ultimately result in aberrant network activity. Moreover, appropriate spino-dendritic compartmentalization provides a foundation for proper neuronal signalling and intercellular communication. In AD transgenic mice, intracellular Ca^{2+} dysregulation is related to the loss of Ca^{2+} compartmentalization and alteration of neuronal morphology, which affect dendritic signal integration and interneuronal communication (Kuchibhotla, Goldman et al. 2008). Besides, exosome is one of important factors for interneuronal communication, by which lipids, proteins and RNAs can be transferred to target neurons. Its secretion is strongly promoted by increased intracellular Ca^{2+} (Chivet, Hemming et al. 2012). In AD, release of pathogenic proteins, such as Aβ, amyloid precursor protein (APP), Tau and cystatin C in AD, is also associated with exosome secretion. This might explain the spreading of the pathology of AD in the nervous system in the brain (Rajendran, Honsho et al. 2006, Ghidoni, Paterlini et al. 2011, Chivet, Hemming et al. 2012). Furthermore, reduced local connectivity and disturbed global functional organization have been observed in brains of AD patients (Supekar, Menon et al. 2008). It is suggested that these dysregulation on local interneuronal communication may underlie the mechanisms of disturbances on brain synchrony and functional connectivity among distinct brain regions (Arendt 2009, Sanz-Arigita, Schoonheim et al. 2010).

1.2 Motivation and main research questions

Ca^{2+} dysregulation in the dendritic spine has been reported in response to different alterations in AD conditions (see Chapter 2). Under experimental conditions, the resulting effects of these alterations are being studied in transgenic animal models or by injecting certain factors, such as Aβ, into healthy animals or cells. It is expensive and challenging to study these complex behaviours because of the limitations of the current available technology. Controversial results from different research groups may be due to different experiment materials or methods they used. Systems biology provides great opportunities to study this kind of problem, using mathematical modelling and computational methods. Therefore, insights can be obtained by properly interpreting the simulation results from thoughtfully-designed computational experiments. In this thesis, we aim to answer the following questions on the Ca^{2+} dysregulation in AD using mathematical modelling:

(1) How would alterations in glutamate transmission and NMDARs reported in AD affect the Ca^{2+} response in the dendritic spine? Which type of alteration is the most vulnerable one?

To answer this question, we need to select key alterations that have previously been suggested to link to Ca^{2+} dysregulation of the spine head in AD. A mathematical Ca^{2+} model then needs to be developed to represent a CA1 pyramidal dendritic spine, according to published experimental observations or data. The model should also able to test the selected alterations after including the relevant mechanisms. The simulation results should be able to bring new insights about dysregulation in NMDAR-mediated postsynaptic Ca^{2+} responses by different alterations in AD.

(2) As the major internal Ca^{2+} source, how would ER affect the Ca^{2+} response in the postsynaptic spine head under AD conditions? How may these effects contribute to synapse dysfunction?

To answer these questions, we need to take the ER Ca^{2+} signalling into consideration. The Ca^{2+} model should be modified by putting ER components into suitable locations in the spine head model, and certain parameters should be calibrated or estimated in the presence of ER. Then, this model is used to test key alterations in ER in AD. The simulation results should provide predictions on the impacts in the postsynaptic Ca^{2+} response by different alterations in ER.

(3) How would alterations in synaptic NMDARs affect their roles in Ca^{2+} signalling and in the downstream form of the CaMKII-NMDAR complex, a critical factor in long-term potentiation (LTP) induction? Which alteration would predominantly suppress NMDAR-mediated LTP induction? What pathological consequences in AD may these effects link to?

To answer these questions we add components related to the CaMKII-NMDAR complex formation into the Ca^{2+} model. Then, with this model, we investigate the effects of different alterations of NMDARs on Ca^{2+} signalling as well as downstream key events leading to CaMKII-NMDAR complex formation. The simulation results should provide new insights into contributions by subunit-specific alterations of synaptic NMDARs in postsynaptic responses.

1.3 Objectives for this study

This study invesitgat key alterations related to Ca^{2+} signalling in spine head in AD using mathmatical models of CA1 pyramidal dendritic spine. There are three major objectives in this study.

(1) To investigate the effects of Aβ-dependent disturbances in NMDAR-mediated Ca^{2+} dynamics in the dendritic spine

We develop a mathematical model based on the characteristics of the CA1 pyramidal dendritic spine. This model integrates the major events of the NMDAR-mediated Ca^{2+} response to presynaptic stimulation the dendritic spine. We use this model to mimic Aβ-dependent alterations in the availability of glutamate and NMDAR, as reported under the AD condition. By manipulating the key parameters related to these alterations, we explore their effects on the postsynaptic Ca^{2+} responses, both individually and globally.

(2) To investigate the effects of disturbances of ER in the NMDAR-mediated Ca^{2+} dynamics in the dendritic spine

We extend the model developed for Objective (1) by including the ER components in the model. We focus on major alterations relating to Ca^{2+} handling by ER under the AD condition, and analyse the effects of them on the Ca^{2+} response in the spine head.

(3) To study the effects of Ca^{2+} dysregulation in a chosen downstream event, CaMKII-NMDAR complex formation

We add a model of the state transitions of CaMKII downstream to our Ca^{2+} model to understand the contributions of NMDAR to the NMDAR-dependent LTP. We use this model

to investigate the roles of NMDARs with different subunit compositions - as a Ca^{2+} channel and as a binding partner of CaMKII in the PSD. We also investigate the effects of disturbances on the availability of different NMDARs under AD conditions on the Ca^{2+} signalling and downstream CaMKII activation.

1.4 Thesis structure

This thesis consists of six chapters. Figure 1.1 illustrates the organization of chapters and the main research questions to be answered in Chapters 3 to 5, respectively, are also included.

In the current chapter, Chapter 1, we introduce AD and Ca^{2+} dysregulations in AD and discuss the motivations and objectives of the thesis. Chapter 2 reviews the experimental findings of Ca^{2+} dysregulation in AD, including the latest publications. We also discuss existing computational modelling approaches in Ca^{2+} signalling studies and their potential to understand the underlying causes of AD. In Chapter 3, we develop a mathematical model of a CA1 pyramidal dendritic spine. We use this model to explore proposed disturbances of Aβ under the AD condition and their contribution to glutamatergic signalling and NMDAR-mediated Ca^{2+} signalling in the dendritic spine. Chapter 4 extends the Ca^{2+} model in Chapter 3 with intracellular ER components to investigate the major alterations of ER reported in AD, and their roles in Ca^{2+} signalling in the dendritic spine on AD pathology. Chapter 5 links our Ca^{2+} model to a CaMKII state transition model. We use the integrated model to extend our understanding of the effects of disturbances on NMDAR availability under AD conditions on downstream CaMKII activation in the early phase LTP. In the final chapter, Chapter 6, we summarise the work and the contribution of this thesis and suggest future directions that could be taken to broaden our understanding about Ca^{2+} dysregulation in AD.

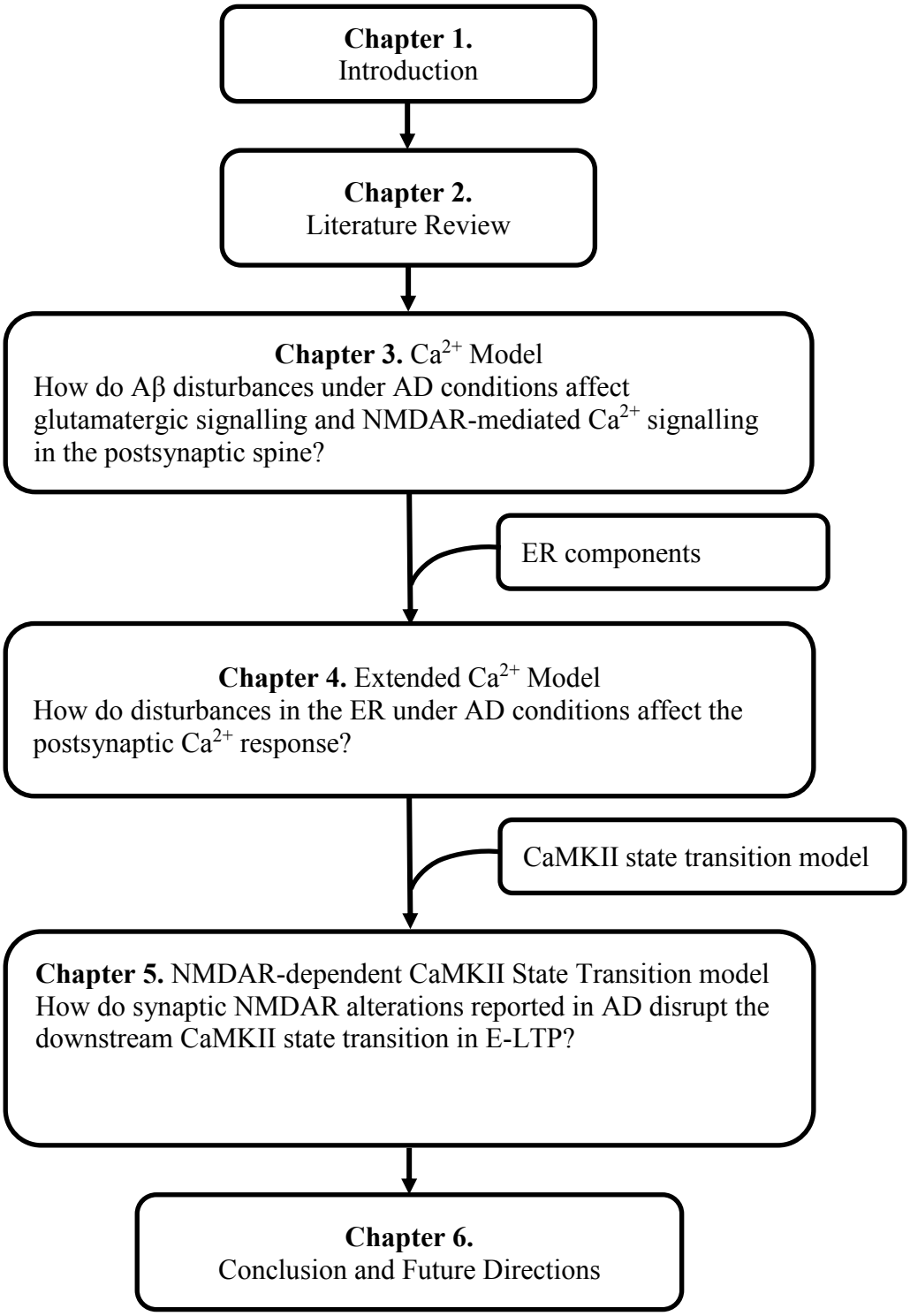

Figure 1.1. Chapter organization of the thesis.

Chapter 2
Background and Literature Review

Ca^{2+} is the most universal second messenger in a variety of cells. The ubiquitous nature of Ca^{2+} accounts for its diverse functions in cell regulation (Toescu and Verkhratsky 2007). In the nervous system, Ca^{2+} signalling plays essential roles in brain physiology, including neuronal development, synaptic plasticity and neuron survival/death. Therefore, maintaining Ca^{2+} homeostasis is crucial for normal brain activity in the healthy state (Zundorf and Reiser 2011). Dysregulation of intracellular Ca^{2+} signalling has been observed as an early event prior to the presence of clinical symptoms of AD and is believed to be a crucial factor contributing to its pathogenesis (Gouras, Tsai et al. 2000, Oddo, Caccamo et al. 2006). In Section 2.1 of this chapter, we first introduce the mechanisms of NMDAR-mediated Ca^{2+} signalling in the dendritic spine under healthy conditions. Then, in Section 2.2, we review the experimental findings and conflicting interpretations about Ca^{2+} dysregulation in AD, including the latest publications, with an emphasis on its effect on the factors involved in NMDAR-mediated Ca^{2+} signalling. We also discuss computational modelling approaches in Ca^{2+} signalling studies in Section 2.3, and the existing models and their potential to understand the underlying causes of AD in Section 2.4.

2.1 NMDAR-mediated Ca^{2+} transients in the dendritic spine

In the nervous system, a chemical synapse is a junction that comprises a presynaptic terminal, a postsynaptic component and a synaptic cleft between them (Figure 2.1). Through a synapse, the electrical signal from a presynaptic cell is converted into a chemical signal (neurotransmitter release), which can be transferred to the postsynaptic cell. At the distal dendritic spine, a region called the postsynaptic density (PSD) attached to the postsynaptic site of the spine head is enriched with large numbers of proteins, including neurotransmitter receptors, cytoskeleton proteins, ion channels and other signalling proteins. These proteins function collaboratively to translate the chemical signal from the presynaptic terminal into a postsynaptic response (Ghosh and Greenberg 1995).

The NMDAR-mediated Ca^{2+} transient in the dendritic spine is initialled by the presynaptic neurotransmitter release induced by the action potential (AP) at the presynaptic terminal. The neurotransmitter released activates postsynaptic receptors, such as NMDAR and AMPAR. The Ca^{2+} influx through NMDAR into the cytosol determines various neuronal activities, such

as synaptic remodelling, synaptic plasticity and cognitive functions (Sabatini, Maravall et al. 2001).

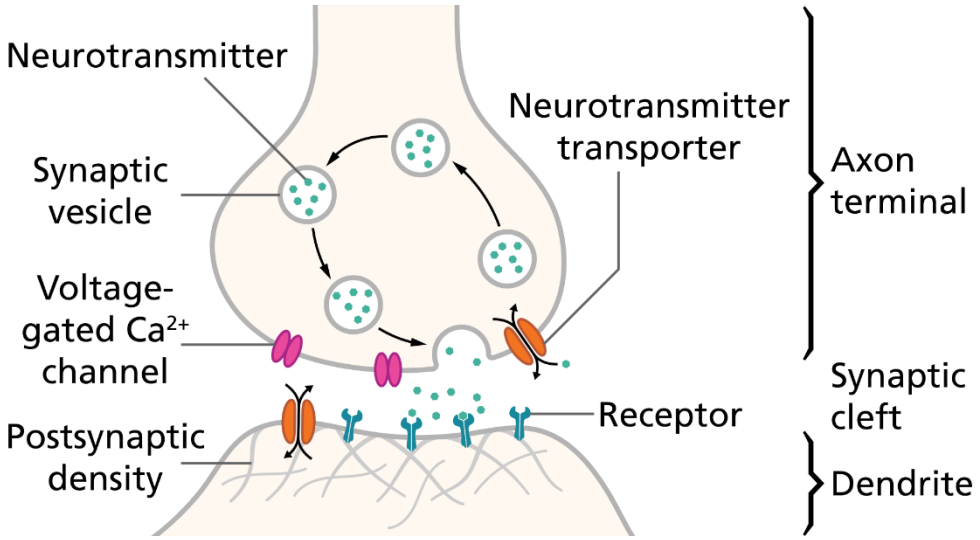

Figure 2.1. Structure of a typical chemical synapse (by Thomas Splettstoesser - Own work, CC BY-SA 4.0, https://commons.wikimedia.org/w/index.php?curid=41349083)

2.1.1 Glutamate

When the action potential reaches the presynaptic terminal it will promote the release of neurotransmitter vesicles into the synaptic cleft (Pinheiro and Mulle 2008). Glutamate is the major excitatory neurotransmitter in the central nervous system and each vesicle contains thousands of glutamate molecules (Nakanishi 1992). The glutamate molecules released diffuse across the synaptic cleft and into the extrasynaptic space. In addition, glutamate can also be released from the glial cells induced by their intracellular Ca^{2+} oscillations, which initiates the neuronal synchrony by activating extrasynaptic NMDARs (Fellin, Pascual et al. 2004).

The clearance of glutamate is achieved by high affinity glutamate transporters (i.e. sodium and potassium coupled glutamate transporters or excitatory amino acid transporters (EAATs)) on surrounding glial cells. To date, five subtypes of these have been identified at different locations (for reviews see (Danbolt 2001) and (Vandenberg and Ryan 2013)). The glutamate transporters play a role in maintaining the extrasynaptic glutamate levels to avoid the pathologic accumulation of extrasynaptic glutamate, which may cause excessive activation of the glutamate receptors and, ultimately, neuronal death (Sheldon and Robinson 2007).

2.1.2 Glutamate receptors

Once released, glutamate can activate both metabotropic glutamate receptors (mGluRs) and ionotropic glutamate receptors (iGluRs) (Michaelis 1998, Dingledine, Borges et al. 1999). The mGluRs themselves do not function as ion channels, instead, they trigger other signalling pathways, indirectly leading to cellular events, such as the opening of ion channels. The opening of intracellular Ca^{2+} channels initiated by the activation of mGluRs is discussed in Section 2.1.3. The iGluRs are located at chemical synapses, both pre- and postsynaptically, and mediate vesicle fusion and postsynaptic response, respectively (Engelman and MacDermott 2004). iGluRs have also been found in the extrasynaptic space, where they can be activated by glutamate spillover from the synaptic cleft or by the ectopic release of glutamate, such as release from the adjacent glia (Fellin, Pascual et al. 2004, Petralia, Wang et al. 2010). In the mammalian central nervous system, there are three major types of iGluRs: AMPAR, NMDAR and the kainate receptor. The kainate receptor is less well studied than the other two and is not the focus of this research. AMPAR and NMDAR are mobile and their trafficking from their synthesis sites and between the synaptic and extrasynaptic zones is crucial to their synaptic transmission and the formation of different forms of synaptic plasticity (Collingridge, Isaac et al. 2004).

2.1.2.1 NMDAR

NMDAR is the major type of Ca^{2+} channel contributing to the postsynaptic Ca^{2+} response in pyramidal neurons of the hippocampus (Bloodgood and Sabatini 2007). Morover, it has also been found at extrasynaptic locations, such as the dendritic spine neck, the dendritic shaft, and in neuron bodies. It is a heterotetramer, mostly comprising two NR1 and two NR2 subunits (Furukawa, Singh et al. 2005). There are eight and four splice variants of NR1 and NR2 subunits, respectively. Those subunits share similar membrane topologies in that they contain an extracellular N-terminal domain with three transmembrane regions (M1, M3 and M4), a pore lining region (M2), an extracellular N-terminus and an intracellular C-terminus (Cull-Candy 2001). The agonists bind to the their extracellular binding domains; in NR1 subunits it is the glycine-binding site, whereas in NR2, it is the glutamate-binding sites. To activate NMDAR, all binding sites at the four subunits need to be occupied. Therefore, it requires the binding of two molecules of glutamate to the NR2 subunits and two molecules of agonist to the NR1 subunits. Recent research has found that NMDARs at different locations are gated by different co-agonists: D-serine for the synaptic NMDARs and glycine for the extrasynaptic NMDARs (Papouin, Ladépêche et al. 2012). The affinity for glutamate by NMDAR depends on their NR2 subunit composition. The NMDAR subunit compositions at different locations

change during postnatal development (Petralia 2012). The ratio of NR2A to NR2B increases at the synaptic site and decreases at the extrasynaptic site during postnatal development. In mature synapses, NR2A-NMDARs are predominant at the synaptic sites, which take about 60% of the total synaptic NMDARs (Cheng, Hoogenraad et al. 2006). In contrast, NMDARs located outside the synaptic region are mainly NR1/NR2B-NMDARs. They are proposed to play opposite physiological roles in mediating intracellular signalling and death pathways: activation of synaptic NMDARs shows neuroprotective effects, whereas stimulation of extrasynaptic NMDARs contributes to cell death (Hardingham and Bading 2010).

In addition to the binding of glutamates and their co-agonists, Ca^{2+} entry through NMDAR requires the relief of Mg^{2+} blocks (Mayer, Westbrook et al. 1984). The Ca^{2+} permeation of NMDAR is mainly mediated by the M2 and M4 regions. The receptor is voltage-dependent and blocked by physiological concentrations of Mg^{2+} at resting membrane potential. During stimulation, the Mg^{2+} block is relieved by membrane depolarization, which can be produced by the opening of AMPARs. NMDARs are often found to be co-localized with AMPARs at the central synapses (Dingledine, Borges et al. 1999).

2.1.2.2 AMPAR

AMPAR is not permeable or less permeable to Ca^{2+} in comparison to NMDAR (Michaelis 1998). The activation of AMPAR by glutamate is fast and leads to a brief depolarization that only lasts for a few milliseconds. When the so-called excitatory postsynaptic potentials (EPSPs) generated by AMPAR are large enough, they will generate an action potential at the postsynaptic neuron. Therefore, the number of AMPAR in PSD is crucial for synaptic transmission and different types of synaptic plasticity formation. Their numbers in PSD are not fixed but are precisely mediated by the trafficking mechanisms (Collingridge, Isaac et al. 2004).

2.1.3 ER

Intraneuronally, NMDAR-dependent Ca^{2+} influx is augmented via Ca^{2+}-induced Ca^{2+} release (CICR) from intracellular Ca^{2+} stores. In the ER, Ca^{2+} homeostasis and signalling are precisely mediated by release and sequestration mechanisms, via Ca^{2+} channels and pumps, to accomplish the regulation of numerous downstream activities (Berridge, Bootman et al. 2003, Verkhratsky 2005). The mechanisms of intracellular Ca^{2+} signalling is briefly illustrated in Figure 2.2. ER Ca^{2+} handling involves Ca^{2+} release from the ER through two types of Ca^{2+} channels, inositol 1,4,5-trisphosphate receptors (IP_3Rs) and ryanodine receptors (RyRs), and

Ca^{2+} uptake via the Ca^{2+} pumps, the sarcoendoplasmic reticulum Ca^{2+} transport ATPase (SERCA) pumps. Two separate mechanisms involved in the process of Ca^{2+} release from the ER via IP_3Rs and RyRs are inositol 1,4,5-trisphosphate (IP_3)-induced Ca^{2+} release and Ca^{2+}-induced Ca^{2+} release (CICR), respectively.

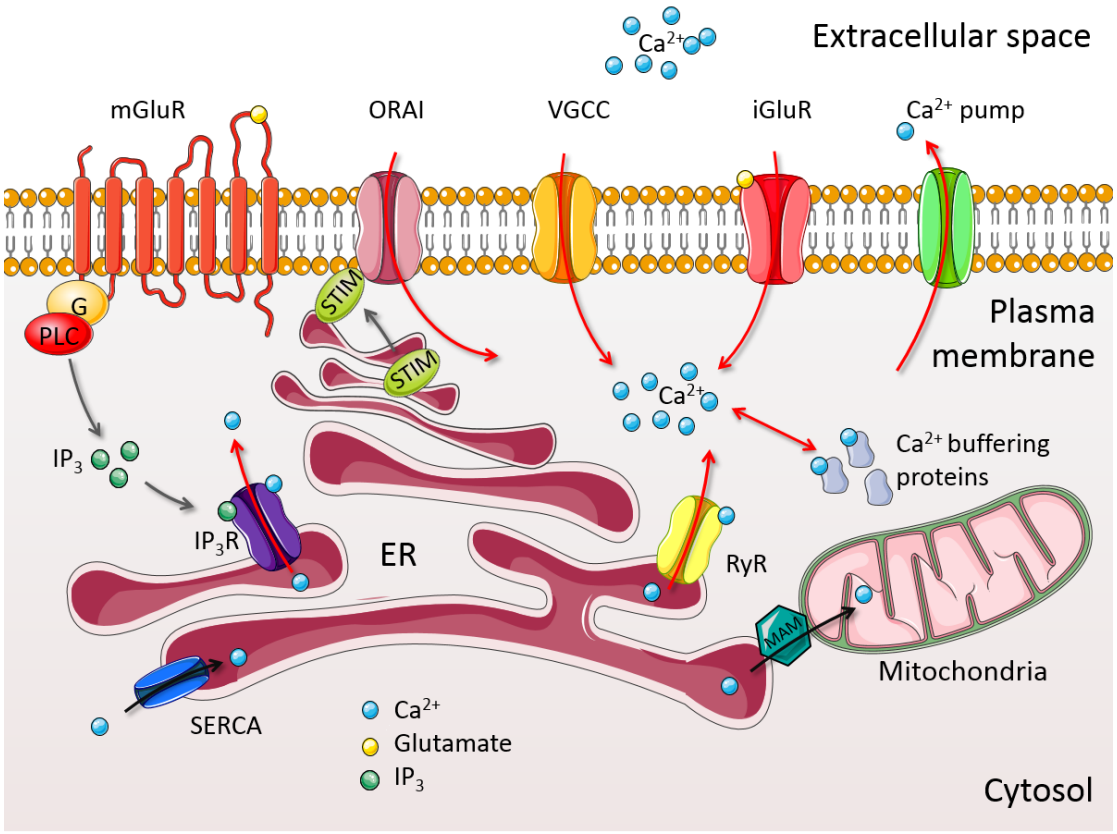

Figure 2.2. Neuronal ER Ca^{2+} signalling. Intracellular Ca^{2+} concentration is regulated by ion channels (e.g., voltage-gated Ca^{2+} channels (VGCCs) and ionotropic glutamate receptors (iGluRs)) and transporters in the plasma membrane. Intracellularly, the regulation of Ca^{2+} homeostasis involves Ca^{2+} ions bind to Ca^{2+} buffer proteins and release from organelles, especially ER. Ca^{2+} ions release from ER via IP_3Rs and RyRs and uptake by ER via SERCA. Activation of IP_3Rs requires IP_3, which is generated by stimulation of metabotropic glutamate receptors (mGluRs) in the plasma membrane. Depletion in ER Ca^{2+} level promotes Ca^{2+} influx via membrane store-operated Ca^{2+} channels, such as ORAI, by translocation of the stromal interaction molecules (STIMs) into the ER–plasma membrane junctions. Besides, Ca^{2+} ions in ER can be transported into mitochondria via mitochondria-associated ER membrane (MAM) to stimulate mitochondrial metabolism. This figure is produced using Servier Medical Art (http://www.servier.com/Powerpoint-image-bank).

IP_3R is a ligand-gated Ca^{2+} channel embedded in the ER membrane and is activated by the intracellular second messenger, IP_3 (Bezprozvanny 2005). IP_3-mediated Ca^{2+} release is initiated by the agonist stimulation of G protein-coupled plasma membrane receptors, such as mGluRs. Subsequently, mGluRs catalyze the activation of G-proteins, which, in turn, activate

phospholipase C (PLC). PLC catalyzes a membrane phospholipid, phosphatidyl inositol-bisphosphate (PIP_2), to release IP_3 and diacyl glycerol (DAG) (Mattson, LaFerla et al. 2000). In addition, IP_3Rs are also regulated by cytosolic Ca^{2+} after activation, in a rapidly stimulated and slowly inhibited, fashion (Foskett, White et al. 2007, Taufiq Ur, Skupin et al. 2009). They can interact locally with nearby channels to coordinate Ca^{2+}release in clusters through the CICR process (Berridge 1997). This will generate the hierarchical recruitment of elementary Ca^{2+} release events and lead to the propagation of regenerative Ca^{2+} waves through cells in response to strong extracellular stimulation (Foskett, White et al. 2007, Rahman and Taylor 2009).

The other Ca^{2+} channel, RyR, is the largest ion channel protein to date and exists in three isoforms, RyR1, RyR2 and RyR3, all of which can be found in the brain (Galeotti, Vivoli et al. 2008). These RyR subtypes seem to have different involvement in memory processing, synaptic plasticity and other events in the brain (Galeotti, Vivoli et al. 2008, Adasme, Haeger et al. 2011). Ca^{2+} release through RyRs is stimulated by cytosolic Ca^{2+} ions via the process of CICR. Although IP_3Rs can also be activated by Ca^{2+} ions, as mentioned above, CICR is more usually related to RyR-mediated Ca^{2+} release. As an inherent, positive feedback mechanism, CICR can greatly amplify the initial Ca^{2+} signals and contribute to subsequent neuronal events, such as neurotransmitter release and Ca^{2+}-dependent gene expression (Hidalgo, Bull et al. 2004).

The SERCA pump of the ER has the highest affinity for Ca^{2+} and plays an opposite role to the Ca^{2+} channels: it refills the ER by pumping Ca^{2+} ions back from the cytosol (Green, Demuro et al. 2008). SERCAs, together with Ca^{2+}-buffering proteins, Ca^{2+} pumps and transporters on other organelles or plasma membrane, form a Ca^{2+} buffering system which contributes to buffer cytosolic Ca^{2+} transients and restores the cytosolic Ca^{2+} concentration back to resting levels (Wuytack, Raeymaekers et al. 2002). SERCA pumps are suggested to play an interdependent role to refilling ER Ca^{2+} stores and maintaining the CICR process (Buchholz, Pottorf et al. 2012). Furthermore, SERCA pumps are one of the key factors in store-operated Ca^{2+} entry (SOCE), a process involving extracellular Ca^{2+} influx via the plasma membrane Ca^{2+} channels in response to the depletion of intracellular Ca^{2+} stores (Stutzmann and Mattson 2011). The tight coupling between the ER refilling and SOCE is managed by SERCA pumps (Manjarres, Rodriguez-Garcia et al. 2010).

The ER is physically in contact with other cytoplasmic organelles and the plasma membrane. Through these contact sites, ER Ca^{2+} release is closely coupled with other cellular events via

communication with other cytoplasmic organelles, especially mitochondria, and with Ca^{2+} channels in the plasma membrane (Elbaz and Schuldiner 2011). Depletion in the ER Ca^{2+} level will cause SOCE and Ca^{2+} refilling via store-operated Ca^{2+} channels (SOCs) located in the plasma membrane. In the ER, a family of Ca^{2+} sensor proteins, the stromal interaction molecules (STIMs), will be activated by the decreased ER Ca^{2+} level and translocate into the ER–plasma membrane junctions. STIMs can then activate SOCs, such as the ORAI channels, and induce the Ca^{2+} influx via them (reviewed in (Soboloff, Rothberg et al. 2012)). The ER is physically connected to the mitochondria by a lipid, raft-like structure, called mitochondria-associated ER membrane (MAM) (Rowland and Voeltz 2012). The MAM plays important roles in multiple cellular functions, including maintaining intracellular Ca^{2+} homeostasis. It allows selective transmission of Ca^{2+} ions from the ER to the mitochondria and, thereby, regulates the functions of the mitochondria and cell survival. This process is regulated by a set of proteins localized in the MAMs (reviewed in (Hayashi, Rizzuto et al. 2009)).

2.2 Overview on AD and Ca^{2+} dysregulation

AD was first described by Alois Alzheimer in 1906 (Goedert and Spillantini 2006). It is the most common form of all neurodegenerative diseases, and it is the leading cause of dementia, resulting in progressive loss of memory, cognitive function and, ultimately, death. Aging is the most important risk factor for developing AD. Based on the age of onset, AD is often divided into two categories: early-onset and late-onset. Less than 5 percent of all AD cases are early-onset AD, which affects people younger than 65. About 13% of early-onset AD cases is familial AD (FAD), because of inherited genetic mutations. In contrast, the rest AD cases, including the late-onset ones which have an age of onset of over 65, are called sporadic AD (SAD) and they are not inherited and caused by unestablished factors (Thies and Bleiler 2013). Noticeably, although FAD and SAD have different onset times and development speeds, they present similar neurodegenerative processes, such as a loss of memory and neuronal cell death (Stutzmann and Mattson 2011).

AD is characterised by the the abnormal accumulation of harmful proteins, Aβ protein plaques and neurofibrillary tangles in the nervous system (Mattson 2004). It is widely believed that these hallmarks are in connection with a massive loss of neurons and synapses in the patients' brains. AD has been identified for more than 100 years, however, to date, the cause of AD is still not fully understood. Scientists believe that AD is a result of multiple factors and to explain

the underlying mechanisms of AD pathophysiology, various hypotheses have been proposed, such as amyloid hypothesis, tau hyperphosphorylation hypothesis, oxidative stress hypothesis cholesterol hypothesis and vascular hypothesis (Selkoe 1991, Hardy and Higgins 1992, Francis, Palmer et al. 1999, Spires-Jones, Stoothoff et al. 2009). Amyloid hypothesis is the dominant hypothesis and many other hypotheses are variants of it (Hardy and Selkoe 2002, Selkoe and Hardy 2016).

2.2.1 Amyloid hypothesis

The amyloid hypothesis was first proposed in the early 1990s (Selkoe 1991, Hardy and Higgins 1992). It suggests that AD is initiated by Aβ oligomers and Aβ plaques in brain tissue. Aβ deposition may directly injure brain neurons and contribute to neuronal toxicity, neuronal death and the subsequent degeneration and cognitive deficiencies in AD patients. During the past 20 years, Aβ deposition has been widely accepted to be the leading cause of AD by the majority of researchers and a large number of experimental research projects are being carried out based on the amyloid hypothesis.

Aβ is produced from a sequence beginning with the cleavage of its precursor, called the amyloid precursor protein (APP), by certain secretase enzymes (Patterson, Feightner et al. 2008, Duyckaerts, Delatour et al. 2009). The process of APP cleavage is illustrated in Figure 2.3. APP is a transmembrane protein with a long extracellular N-terminal domain, a transmembrane domain, and a short intracellular C-terminal domain (Turner, O'Connor et al. 2003). APP can be cleaved by two different kinds of enzymes, α-secretase and β-secretase, at different sites to produce two different peptides. The α-secretase cleaves APP within the critical Aβ region that lies in part of the extracellular N-terminal and transmembrane domains. The cleavage releases a large soluble amino-terminal fragment, sAPPα, and a smaller C-terminal fragment, which will be further cleaved by γ-secretase. Cleavage by α-secretase prevents the generation and release of the Aβ peptide and, thereby, it is called the non-amyloidogenic pathway in APP processing. In the alternative amyloidogenic pathway, APP is cleaved by β-secretase outside the critical Aβ region, releasing sAPPβ and a smaller C-terminal fragment. The γ-secretase further cleaves the C-terminal fragment releasing the Aβ. The majority of Aβ peptides are 40 residues in length ($A\beta_{40}$), while a small proportion (≈10%) are 42 residues in length ($A\beta_{42}$) (LaFerla, Green et al. 2007). Compared with $A\beta_{40}$, $A\beta_{42}$ is more hydrophobic and readily forms amyloid plaques, which are considered to play a causal role in the progression of AD (Patterson, Feightner et al. 2008). Therefore, $A\beta_{42}$ is believed to be the most neurotoxic form of the Aβ peptides.

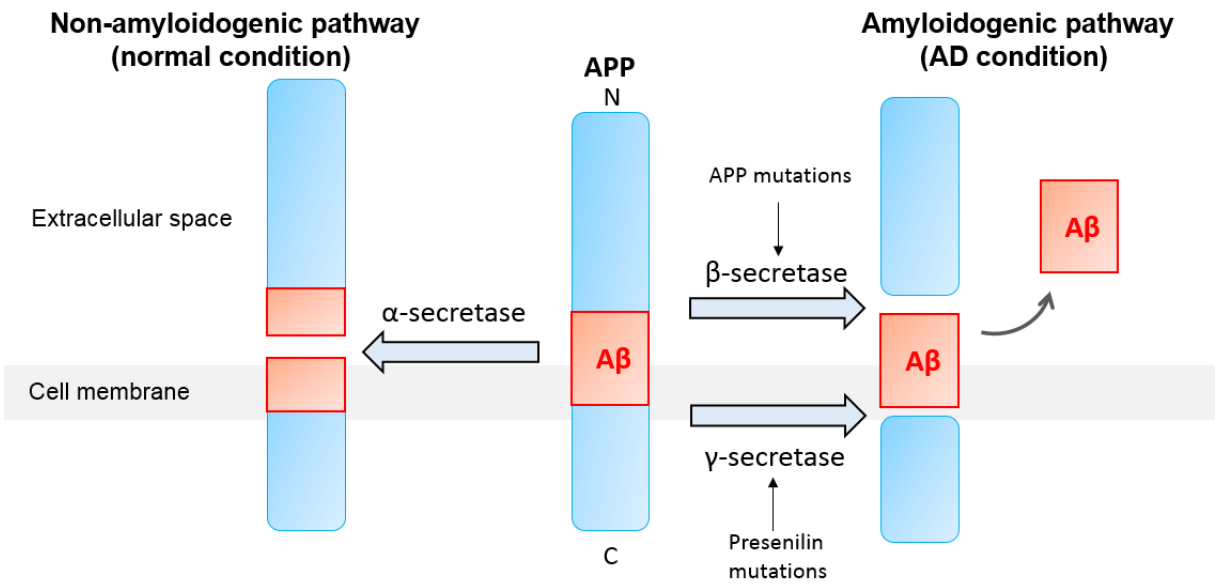

Figure 2.3. The process of APP cleavage. The transmembrane protein APP can undergo a series of proteolytic cleavage by different secretase enzymes. When it is cleaved by α-secretase in the middle of the Aβ domain, it is not amyloidogenic. However, when APP is cleaved by β- and γ-secretase enzymes, neurotoxic Aβ peptides are released, which can accumulate into oligomer aggregates. Mutations in the APP gene tend to inhibit cleavage by α-secretase and, consequently, enable preferential cleavage by β-secretase. Mutations in the presenilin-1 and presenilin-2 genes, which are components of the γ-secretase complex, increase cleavage by γ-secretase at this site. In both situations, the result is excess Aβ peptide production.

Under normal physiological conditions, Aβ peptides can be removed from brains quickly by its clearance mechanisms. For example, Aβ peptides can be degraded proteolytically by multiple enzymes, especially neprilysin (NEP) and insulin degrading enzyme (IDE) (Jiang, Lee et al. 2008). The balance between production and clearance of Aβ determines steady levels of Aβ. An imbalance will result in the deposition of Aβ and formation of amyloid plaques. In FAD, mutations of APP, presenilins 1 and 2 genes will lead into increasing production of Aβ and the ratio of $A\beta_{42}/A\beta_{40}$ increases the cleavage activity of β-secretase and γ-secretase (LaFerla, Green et al. 2007, Duyckaerts, Delatour et al. 2009). In SAD, rather than an overproduction of Aβ, the formation of amyloid plaques is more likely attributed to the failure of Aβ clearance. The initial cause of this failure is still unclear.

Aβ has the ability to self-associate and exists in many different assembly forms, ranging from oligomers to fibrils and amyloid plaques. Initially, fibrillar Aβ that constitutes amyloid plaque was assumed to be toxic. However, recent research suggests that Aβ oligomers are the most toxic form, and may result in nerve damage (Shankar and Walsh 2009, Crews and Masliah

2010). Aβ oligomers at pathophysiological levels are considered to contribute to the activation of inflammatory neuronal cascades, oxidative stress, mitochondrial disturbances, Ca^{2+} metabolism deregulation, tau protein phosphorylation and neuronal apoptosis (Golde 2003, Sanz-Blasco, Valero et al. 2008, Berridge 2010, Jin, Shepardson et al. 2011, Mucke and Selkoe 2012). Moreover, Aβ oligomers can inhibit hippocampal long-term potentiation (LTP) and facilitate hippocampal long-term depression (LTD) and, thus, cause impairments in synaptic plasticity, learning, and memory (Malchiodi-Albedi, Paradisi et al. 2011).

2.2.2 Ca^{2+} hypothesis

Aβ is proposed to cause neuronal toxicity via a variety of pathways, and several hypotheses extending from the amyloid hypothesis attempt to further elucidate the alterations resulting from amyloid pathology. The most important, and feasible, pathway is through the Ca^{2+} signalling systems by triggering deregulation of Ca^{2+} homeostasis. The Ca^{2+} hypothesis that links altered Ca^{2+} signalling to Aβ-induced neuronal dysfunction is becoming more popular, and is supported by accumulating experimental evidence (Van Dam and De Deyn 2006). The deregulation of Ca^{2+} homeostasis is suggested to account for the decline in cognitive function in the early stages of AD, and neuronal loss in the late stage of AD. Therefore, the focus of this research is mainly on the amyloid and Ca^{2+} hypotheses.

Aβ oligomers may interact with neuronal membranes and result in a significant elevation of intracellular Ca^{2+} levels in AD. High levels of Ca^{2+} are toxic and will induce neural apoptosis, the most common form of programmed cell death, leading to neuronal dysfunction and neurodegeneration in both SAD and FAD (Berridge 2010). Meanwhile, alteration of Ca^{2+} signalling may accelerate Aβ formation, thus, a degenerative feed-forward cycle of Aβ formation and dysregulation of Ca^{2+} signalling is formed.

Since 1987, when Khachaturian (1987) first proposed the Ca2+ hypothesis, a growing body of evidence reveals that dysregulation of Ca^{2+} signalling plays a crucial role in the initiation and development of AD (LaFerla 2002, Berridge 2010, Berridge 2013). A rise in the resting level of cytosolic Ca^{2+} in neurons has been reported in both transgenic AD animal models and autopsies of brains from patients who have died from AD, which suggests it is a causal factor in neuronal excitotoxicity, synaptic loss and cell death during the development of AD (Lopez, Lyckman et al. 2008).

2.2.3 Dysregulation of glutamatergic transmission by Aβ in AD

The extracellular Aβ oligomers have been shown to impair intracellular Ca^{2+} homeostasis by promoting an influx of extracellular Ca^{2+} through the plasma membrane (Demuro, Mina et al. 2005, Kawahara, Ohtsuka et al. 2011). This can disrupt the plasma membrane Ca^{2+} permeability, particularly by forming Ca^{2+}-permeable pores that affect certain Ca^{2+}-permeable channels and/or interact with membrane lipids and affect their integrity. In this section, we review dysregulation related to the NMDAR-mediated Ca^{2+} response in the dendritic spine as observed under AD conditions.

2.2.3.1 Glutamate excitotoxicity in AD

An excessive extracellular glutamate concentration will cause a mild, chronic activation of glutamate receptors, especially NMDARs, and lead to neurodegeneration, which is also called excitotoxicity (Danysz and Parsons 2012). Several studies have shown that a dysfunctional glutamatergic system in AD could be a critical upstream event, which leads to the overactivation of NMDARs and pathological NMDAR-mediated Ca^{2+} influx into the neuron that, subsequently, triggers apoptotic pathways (Li, Hong et al. 2009, Hardingham and Bading 2010). An elevated resting level of extracellular glutamate has been found in AD patients (Talantova, Sanz-Blasco et al. 2013). Researchers have linked Aβ to upregulation in glutamate availability and excitotoxicity in AD, suggesting that Aβ is the culprit behind enhanced excitotoxicity, either by increasing glutamate release or by reducing glutamate uptake by transporters (Butterfield and Pocernich 2003, Ondrejcak, Klyubin et al. 2010, Danysz and Parsons 2012).

Aβ is suggested to promote glutamate release from presynaptic terminal (Bobich, Zheng et al. 2004, Chin, Ma et al. 2007, Kabogo, Rauw et al. 2010). Aβ may participate and act as a positive regulator in the glutamate release under healthy conditions (Abramov, Dolev et al. 2009). In aged neurons, $A\beta_{23-25}$ has been found to augment glutamate release (Arias, Arrieta et al. 1995). Puzzo, Privitera et al. (2008) reported that a picomolar level of $A\beta_{42}$ could enhance LTP by increasing neurotransmitter release, whereas low nanomolar levels of $A\beta_{42}$ lead to synaptic depression. Palop and Mucke (2010) proposed a bell-shaped relationship between extracellular Aβ and the synaptic transmission that low and high levels of Aβ depress the postsynaptic transmission while intermediate levels facilitate the presynaptic vesicle release.

In addition, Aβ is suggested to potentiate the release of glutamate from glia cells (Noda, Nakanishi et al. 1999, Orellana, Shoji et al. 2011). Aβ induces excitotoxic levels of glutamate release from astrocytes, which can lead to the activation of extrasynaptic NMDARs and

synaptic loss (Barger and Basile 2001, Talantova, Sanz-Blasco et al. 2013). This may be a result of the abnormal Ca^{2+} signalling in the glia cells observed in AD (Kuchibhotla, Lattarulo et al. 2009).

In contrast, Aβ oligomers may disturb glutamate clearance mechanisms by affecting the glutamate transporters (Harris, Carney et al. 1995, Harris, Wang et al. 1996, Parpura-Gill, Beitz et al. 1997, Fernández-Tomé, Brera et al. 2004, Matos, Augusto et al. 2008). A number of studies have revealed reduced levels of vesicular glutamate transporters (VGLUT) and excitatory amino acid transporters (EAAT) in AD (Masliah, Hansen et al. 1996, Masliah, Alford et al. 2000, Kirvell, Esiri et al. 2006). Moroever, the decreased glutamate transporter activity found in AD is suggested to be associated with this excitotoxicity and neurodegeneration (Masliah, Hansen et al. 1996). The lack of transporters and/or reduced activity of these transporters contributes to the increase in glutamate availability in the synaptic cleft and extrasynaptic space (Danysz and Parsons 2012). Persistent activation of postsynaptic NMDAR may lead to receptor desensitisation and affect synaptic functions, such as synaptic plasticity (Li, Hong et al. 2009), whereas prolonged extrasynaptic NMDAR promotes neuronal Aβ production (Bordji, Becerril-Ortega et al. 2010, Bordji, Becerril-Ortega et al. 2011).

2.2.3.2 Dysregulation on NMDAR in AD

Several research studies have shown the colocalisation of Aβ oligomers with NMDARs, suggesting that they may directly interact with NMDARs (Dewachter, Filipkowski et al. 2009, Alberdi, Sanchez-Gomez et al. 2010, Texidó, Martín-Satué et al. 2011). Aβ oligomers are reported to directly interact with NMDARs (De Felice, Velasco et al. 2007) and activate NR2B-NMDAR, leading to an increase in cytosolic Ca^{2+} levels (Ferreira, Bajouco et al. 2012). The precise underlying mechanisms are yet to be uncovered. Besides, Aβ may also cause a slowed desensitisation by disturbing the cellular prion protein-mediated NMDAR activity (You, Tsutsui et al. 2012). Furthermore, the increase of NMDAR activity may inhibit the α-cleavage of APP and promotes the amyloidogenic processing of APP (Kamenetz, Tomita et al. 2003, Lesné, Ali et al. 2005, Hoe, Fu et al. 2009).

Aβ oligomers may also disturb the distribution of NMDARs (Snyder, Nong et al. 2005). Interestingly, the full-length APP is found to increase surface NR2B containing NMDAR (but not NR2A-containing one) and decrease its internalisation in primary hippocampal neurons (Hoe, Fu et al. 2009). However, following exposure of $A\beta_{25–35}$ and full-length $A\beta_{1–40}$ deposits, a decrease in the number of NMDARs positive cells is observed in the immediate surrounding

of $A\beta_{25–35}$ and full-length $A\beta_{1–40}$ deposits in mature hippocampal slice cultures (Johansson, Radesäter et al. 2006). Pretreatment of cultured hippocampal neurons with $A\beta_{1–42}$ significantly reduces surface expression of NR1, without affecting the total NR1 expression (Goto, Niidome et al. 2006). Treatment of mature hippocampal cells with Aβ oligomers rapidly decreases the expression of surface NMDARs (Lacor, Buniel et al. 2007). In cultured cortical neurons, $A\beta_{1–42}$ has been shown to reduce the surface expression of NR1 and NR2B subunits of the whole cell as well as at the synaptic site, without any changes in the total level of synaptic NMDARs (including both internal and surface receptors) (Snyder, Nong et al. 2005). Similarly, a decrease in the surface expression of synaptic NR2B containing NMDAR is observed in primary hippocampal neurons pre-incubated with Aβ oligomers and in APP transgenic mice (Dewachter, Filipkowski et al. 2009). In contrast, extrasynaptic NMDARs are not affected by the presence of Aβ oligomers (Snyder, Nong et al. 2005).

In addition, Aβ-induced surface expression of NMDAR can be restored by the γ-secretases inhibitor (Snyder, Nong et al. 2005). Taken all together, it is suggested that Aβ may play a role in mediating the trafficking of NMDARs, especially by promoting synaptic NR2B-NMDAR endocytosis. Aβ can bind to 7α-nicotinic acetylcholine receptors (nAchRs) with high affinity (Wang, Lee et al. 2000). Snyder, Nong et al. (2005) hypothesised that the Aβ-dependent endocytosis of NMDARs is initiated by Aβ binding to the nAchRs, which leads to activation of protein phosphatase 2B and dephosphorylation and activation of tyrosine phosphatase STEP. The activation of STEP may promote dephosphorylation of the phosphotyrosine residue Tyr1472 of NMDAR, which locates in a region which regulates NMDAR endocytosis and interaction with synaptic scaffolding proteins. Kessels, Nabavi et al. (2013) showed that Aβ oligomers promote the switch in subunit composition from NR2B- to NR2A-NMDAR, which normally occurs during development.

The loss of synaptic NMDARs may also contribute to the depression of glutamatergic transmission and reductions in memory formation. Aβ is reported to decrease NMDAR-mediated synaptic responses and inhibit NMDAR-dependent LTP (Chen, Wei et al. 2002, Li, Jin et al. 2011). However, to some extent, the internalisation of synaptic NMDARs may be a neuroprotective mechanism against the glutamate-induced neurotoxicity and excessive Ca^{2+} influx (Chuang, Gao et al. 1992, Goto, Niidome et al. 2006).

2.2.4 Dysregulation of ER Ca^{2+} handling in AD

The ER, as the major Ca^{2+} storage compartment, has been studied with the focus on its effects in Ca^{2+} signalling in AD (Popugaeva and Bezprozvanny 2013, Liang, Kulasiri et al. 2015).

Research carried on stabilizing ER Ca^{2+} signalling in AD cells or animal models have offered new strategies for the prevention of disease progression (Ito, Oka et al. 1994, Lee, Hwang et al. 2006, Thibault, Gant et al. 2007, Chakroborty, Briggs et al. 2012). The mechanism causing these alterations in ER Ca^{2+} signalling is not fully understood, while current research is mainly on the disturbing effects from mutations in presenillin or/and deposition of Aβ oligomers.

2.2.4.1 Disruption of ER Ca^{2+} homeostasis by the Aβ peptide

Aβ can affect the ER Ca^{2+} signalling by promoting an influx of extracellular Ca^{2+} through the plasma membrane (Demuro, Mina et al. 2005, Kawahara, Ohtsuka et al. 2011). For example, there is growing evidence that links overactivation of NMDARs to ER Ca^{2+} dysregulation (Kelly and Ferreira 2006, Costa, Lacor et al. 2012). Aβ oligomers can induce ER stress through interaction with NMDARs, resulting in a massive Ca^{2+} influx (Costa, Lacor et al. 2012). This will subsequently activate downstream NADPH oxidase (NOX)-mediated superoxide production and, consequently, impair ER Ca^{2+} homeostasis and even trigger ER stress-mediated apoptotic pathway (Ferreiro, Resende et al. 2006). Costa et al., have demonstrated that Aβ-induced ER stress can be effectively inhibited by ifenprodil, an antagonist of NR2B subunits, which could be a potential therapeutic strategy for AD (Costa, Lacor et al. 2012).

Intracellular Aβ oligomers are also shown to directly disrupt Ca^{2+} handling of intracellular Ca^{2+} stores, especially ERs (Figure 2.4) (Demuro and Parker 2013). They are believed to be produced from APP residing on the ER and in other intracellular compartments, as well as by uptake from the extracellular space (Mohamed and Posse de Chaves 2011). The accumulation of intracellular Aβ oligomers has been observed prior to the presence of extracellular Aβ deposition in the cerebral cortex and hippocampus in AD brains, suggesting that intracellular $Aβ_{42}$-induced Ca^{2+} dysregulation may play a crucial role in early AD pathogenesis (Gouras, Tsai et al. 2000, Oddo, Caccamo et al. 2006).

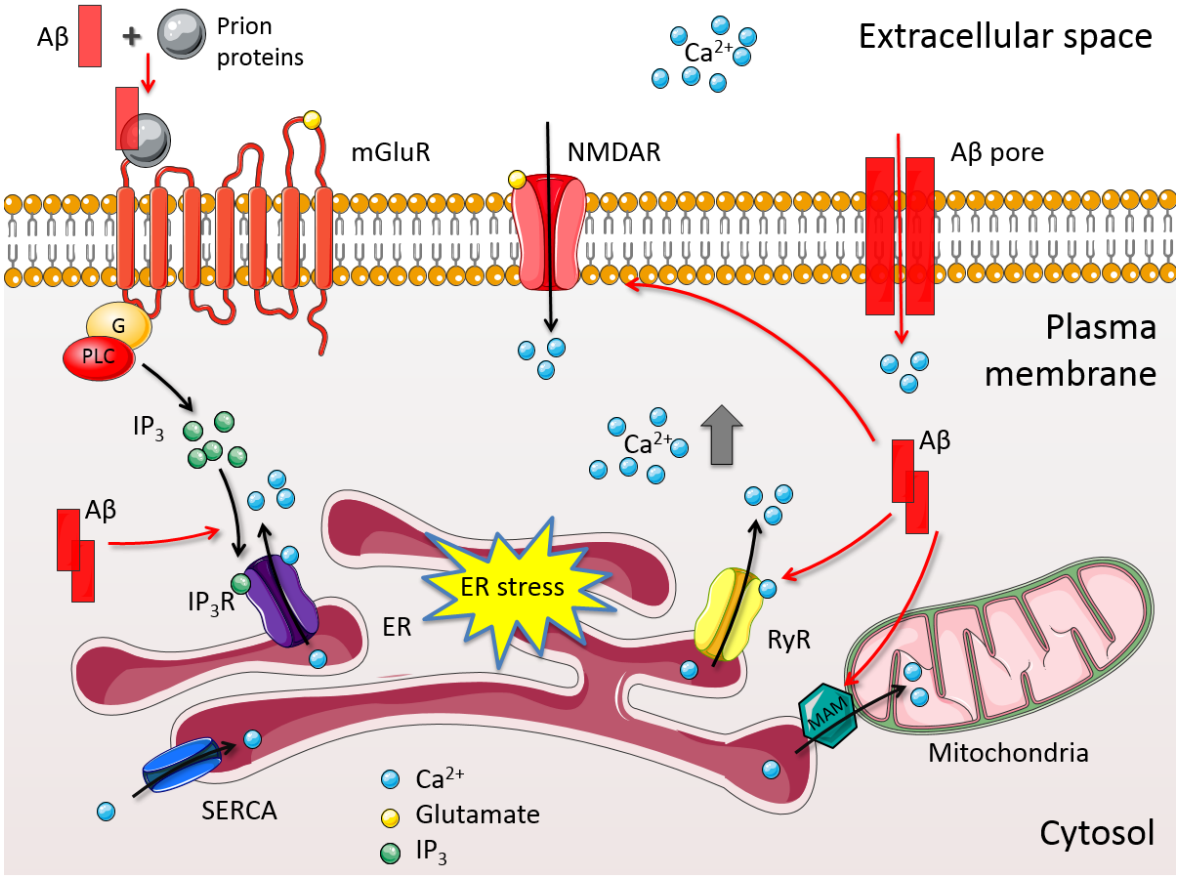

Figure 2.4. Mechanisms that might contribute intracellular Ca^{2+} dysregulation in AD. Evidences show that Aβ oligomers may disturb intracellular Ca^{2+} homeostasis and result in ER stress, by disturbing membrane conductance, forming Ca^{2+}-permeable pores as well as perturbing ER Ca^{2+} handling. Aβ oligomers may directly modulate activity of IP_3Rs and RyRs. Aβ oligomers are also suggested to accelerate the production of IP_3, therefore, induce IP_3Rs opening and Ca^{2+} release from ER. Besides, Aβ oligomers may promote ER Ca^{2+} transmission to mitochondria via MAM and lead to mitochondrial dysfunction. Furthermore, alteration of intracellular Ca2+ homeostasis may in turn promote the production of Aβ peptides. This figure is produced using Servier Medical Art (http://www.servier.com/Powerpoint-image-bank).

$Aβ_{42}$ oligomer pores can also be formed in the membranes of intracellular organelles and result in Ca^{2+} leakage into the cytosol; the disruption is comparatively mild (Demuro, Mina et al. 2005, Demuro and Parker 2013). Most research has demonstrated that Aβ oligomers enhance Ca^{2+} liberation from the ER, mainly by altering Ca^{2+} release via IP3Rs and RyRs (Kelliher, Fastbom et al. 1999, Ferreiro, Oliveira et al. 2004, Stutzmann, Smith et al. 2006, Schapansky, Olson et al. 2007). Pereira's group suggested an ER-specific apoptotic pathway trigged by Aβ-induced perturbation of ER Ca^{2+} homeostasis (Ferreiro, Resende et al. 2006). Their research showed that continuous production could induce ER stress, perturb ER Ca^{2+} homeostasis and lead to increased levels of cytosolic Ca^{2+}. Together with other Aβ-induced alterations, such as increased activity of caspase-3, it would further affect mitochondrial

function and, ultimately, trigger the apoptotic pathway and lead to neuronal death.

Aβ exposure has been shown to disturb IP_3R-regulated Ca^{2+} handling by promoting IP_3-mediated Ca^{2+} release from the ER in neurons (Schapansky, Olson et al. 2007). Similarly, Lopez et al. observed that the accumulation of intracellular Aβ in a 3xTg-AD mouse model enhanced Ca^{2+} release via IP_3R on the ER as well as increased Ca^{2+} influx on the plasma membrane, which potentially can lead to a large elevation of resting cytosolic free Ca^{2+} level (Lopez, Lyckman et al. 2008). In addition, the Aβ has also been reported to affect Ca^{2+} flux via IP_3Rs indirectly by modulating upstream events. For example, Aβ directly interacts with IP_3 and promotes binding of IP_3 ligands to their receptors in rats (Cowburn, Wiehager et al. 1995). Increased levels of both astrocytic mGlu5 receptor mRNA and protein have been observed in Aβ40 treatment *in vitro* (Casley, Lakics et al. 2009). Likewise, Renner et al. reported that Aβ oligomers altered the lateral diffusion of mGluR5 within the plasma membrane and stimulated their signalling activity which, therefore, affected downstream IP_3 production (Renner, Lacor et al. 2010). Aβ oligomers can bind to cellular prion proteins and active mGluR5, which may also lead to increased production of IP_3 (Um, Kaufman et al. 2013). In addition, recent research has reported that intracellular $Aβ_{42}$ oligomers induce Ca^{2+} liberation from the ER via IP_3Rs by stimulating PLC-mediated IP3 production in *Xenopus* oocytes (Demuro and Parker 2013). Another study demonstrated that $Aβ_{42}$-induced Ca^{2+} release from ER may mostly depend on activating PLC and, subsequent, IP3 generation rather than by direct interaction with IP_3Rs (Allan, Bultynck et al. 2013).

Similarly, intracellular $Aβ_{42}$ oligomers also disrupt RyR-regulated Ca^{2+} signals. $Aβ_{42}$ oligomers appear to increase the channel open probability of RyRs and change their gating kinetics, leading to enhanced Ca^{2+} liberation from the ER. Shtifman et al. demonstrated that Aβ can directly modify and activate RyR type1 by reconstituting RyR in a planar lipid bilayer to study inclusion body myositis, a skeletal muscle disorder, which may share a similar pathogenesis with AD (Shtifman, Ward et al. 2010). This is consistent with their earlier study on the inclusion body myositis showing that Aβ overexpression increases RyRs' sensitivity to the agonist caffeine and susceptibility to CICR (Christensen, Shtifman et al. 2004). In addition, the elevation of RyR expression has also been reported to result in the accumulation of intracellular Aβ oligomers. For example, Supnet et al. reported increased levels of RyR type3 in non-TgCRND8 neurons after treatment with $Aβ_{42}$ oligomers, suggesting that $Aβ_{42}$ may potentiate Ca^{2+} release from the ER and disturb intracellular Ca^{2+} homeostasis by directly increasing RyR expression (Supnet, Grant et al. 2006, Supnet, Noonan et al. 2010).

Moreover, Aβ oligomers also upregulate the MAM function in post-mortem AD brains and APPSwe/Lon mice (Hedskog, Pinho et al. 2013). Increased expression of MAM-associated proteins and a number of contact sites have been observed in primary hippocampal neurons. This may, consequently, promote Ca^{2+} transmission from the ER to mitochondria and may lead to mitochondrial dysfunction and AD pathology.

Interestingly, the APP intracellular domain (AICD), which is generated together with Aβ by γ-secretases cleavage, may also be associated with ER signalling. AICD has been suggested to be involved in regulating IP_3-mediated Ca^{2+} signalling, although the precise mechanism is unknown (Smith, Green et al. 2005). AICD may promote the expression of IP_3R based on its transcriptional activity (Kasri, Kocks et al. 2006). Alternatively, in another study, AICD was shown to activate glycogen synthase kinase-3β (GSK3β), a modulator of the IP3R expression, which may be a potential mechanism by which AICD mediated ER Ca^{2+} signalling (Ryan and Pimplikar 2005). In addition, Oule's et al. observed disrupted ER Ca^{2+} homeostasis contributed to the increased expression of RyR levels in APP-overexpressing transgenic mice, suggesting AICD may also mediate RyR expression (Oule`s, Del Prete et al. 2012).

2.2.4.2 Presenilin mutation and its roles in ER Ca^{2+} homeostasis

Presenilins (PSs), a family of highly conserved membrane proteins with multi-transmembrane domains, are primarily located in the ER membrane and can be found in the cell body and in the dendrites of neurons (Brunkan and Goate 2005). Missense mutations in the genes encoding presenilin-1 (*PSEN1*) and presenilin-2 (*PSEN1*) account for the majority of the inherited forms of AD, FAD (Shen and Kelleher 2007, Supnet and Bezprozvanny 2011). *PSEN1* mutations are the most common genetic cause and, to date, 185 *PSEN1* mutations have been identified in patients with FAD, listed on the Alzheimer Disease & Frontotemporal Dementia Mutation Database (Cruts, Theuns et al. 2012). In contrast, the *PSEN2* mutation is a relatively rare cause of FAD, with only 13 mutations have been identified (Cruts, Theuns et al. 2012). Mutations in PS genes are suggested to play a causal role in the cognitive impairment and pathogenesis of FAD (Saura, Choi et al. 2004). Much research has reported that both mutations in both *PSEN1* and *PSEN2* are associated with the dysregulation of Ca^{2+} signalling, disturbance of Aβ production and neuronal death, although the underlying mechanisms are still under investigation. Proposed effects of PS mutation are summarizes in Figure 2.5.

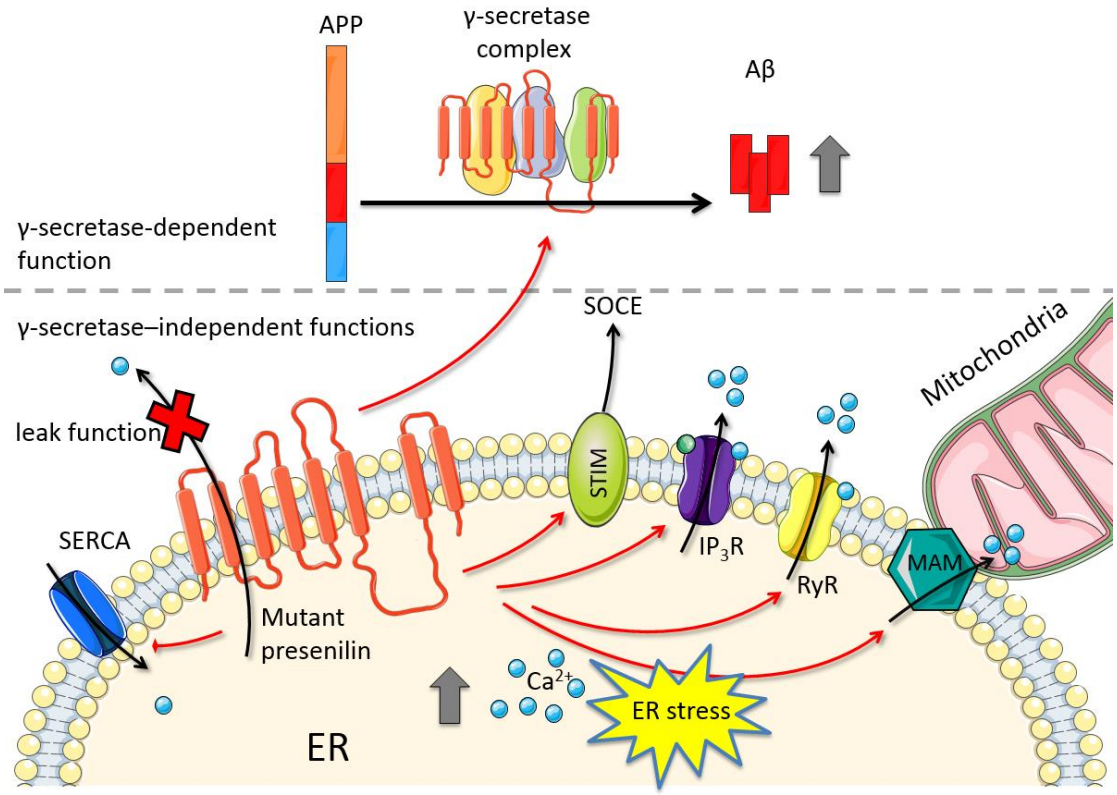

Figure 2.5. Proposed effects of PS mutation. PS mutation affects both its γ-secretase-dependent function and γ-secretase-independent function. Mutant PS disturbs the proteolytic cleavage of the APP and promotes Aβ production. Inside of the neuron, mutant PS may physically associate with ER membrane receptors and SERCA pumps to disturb their functions. Furthermore, PS is proposed to function as an ER Ca^{2+} leak channel. Mutations on it may diminish this function and lead to ER Ca^{2+} dysregulation. This figure is produced using Servier Medical Art (http://www.servier.com/Powerpoint-image-bank).

However, unlike FAD, causes of SAD are much more complex, involving both genetic and environmental risk factors. Therefore, it remains a great challenge to study the key factors in SAD (Young and Goldstein 2012). Research on microRNA (miRNA) may be helpful to explain the pathogenesis of SAD as well as FAD. miRNAs are small noncoding RNAs, which negatively regulate gene expression at the posttranscriptional level (He and Hannon 2004). Dysregulation of several miRNAs have been observed in AD brains and are suggested to relate to AD pathology (Van den Hove, Kompotis et al. 2014). Increase in hallmark genes such as *APP* and *PSEN1* observed in SAD brains may be a result of dysregulation in miRNAs which target these genes (reviewed in (Maes, Chertkow et al. 2009)). Thus, abnormal level of miRNAs may indirectly affect Ca^{2+} signalling and Aβ production in AD. Therefore, Identify specific miRNAs for AD, especially SAD, will be useful for modelling SAD in the laboratory, which remains underdeveloped. Besides miRNAs may serve as potential biomarkers in AD, which may contribute to the early diagnosis and therapeutic research

(Young and Goldstein 2012).

2.2.4.2.1 Role of PS as a subunit of γ-secretases

The PS protein is synthesized in the ER and can be transported to the plasma membrane or endosomal structure compartments to form a catalytic subunit of γ-secretases, together with nicastrin, APH-1 and PEN-2 (Nelson, Supnet et al. 2011). γ-secretases mediate the proteolytic cleavage of the APP via the amyloidogenic pathway to release Aβ peptide fragments. PS mutations are suggested to promote the amyloidogenic processing of APP and can result in the increasing formation of $A\beta_{42}$ relative to $A\beta_{40}$, which has been found both in the fibroblasts of AD patients and animal models (De Strooper, Iwatsubo et al. 2012). Compared with $A\beta_{40}$, $A\beta_{42}$ is less soluble and is considered to be the most toxic, pathogenic form of Aβ, which contributes to synaptic dysfunction, neuronal toxicity and the formation of senile plaques (Hardy and Selkoe 2002). Likewise, Shen and Kelleher proposed in the presenilin hypothesis that the loss of γ-secretase cleavage function in PS mutations in AD may lead to increased production of $A\beta_{42}$ relative to $A\beta_{40}$ (Shen and Kelleher 2007). The effects of Aβ on ER Ca^{2+} regulation are discussed in later sections.

2.2.4.2.2 Roles of PS mutations in ER Ca^{2+} signalling

At it is independent of the γ-secretase activity, PS is also suggested to play other physiological roles，including mediation of neurotransmitter release and regulation of intracellular Ca^{2+} homeostasis (Nelson, Supnet et al. 2011, De Strooper, Iwatsubo et al. 2012). This review will focus on its role relating to ER Ca^{2+} signalling.

Early research on fibroblasts from asymptomatic members of AD families linked the PS mutation to enhanced Ca^{2+} release from the ER (Ito, Oka et al. 1994). Alterations in ER Ca^{2+} signalling have been consistently observed in later research on cells expressing mutant PS (Leissring, Paul et al. 1999) or tissues from animal models expressing mutant PS genes (Leissring, Akbari et al. 2000, Stutzmann, Caccamo et al. 2004). Mutations in PS are also reported to directly attenuate SOCE. Normal presenillins may negtively regulate SOCE, which could explain the attenuated SOCE found in cells with FAD PS mutations (Leissring, Akbari et al. 2000, Herms, Schneider et al. 2003, Bojarski, Herms et al. 2008). Furthermore, Bojarski et al. have demonstrated that FAD mutations in PS affect the cellular levels of STIM1 and STIM2 differently and result in the attenuation of SOCE (Bojarski, Pomorski et al. 2009). They suggest that SOCE in the neurons of FAD patients may be affected by the disturbed expression of STIM genes or proteins. A recent study in mutant presenilin mice showed that downregulation of STIM2 protein impaired the SOCE in mature spines (Sun,

Zhang et al. 2014).

Inhibited SOCE, together with the reduced ER Ca^{2+} content by PS mutations, would ultimately result in disruption of intracellular Ca^{2+} homeostasis (Giacomello, Barbiero et al. 2005). Increased vulnerability of neurons to excitotoxicity, to mitochondrial impairment and to apoptosis have been observed in PS1 mutant knock-in mice, which are suggested to be associated with enhanced Ca^{2+} release from the ER (Guo, Fu et al. 1999). Presenilins have also been observed to be highly enriched in MAM (Area-Gomez, de Groof et al. 2009). This suggests a potential role for PS in ER–mitochondria Ca^{2+} cross-talk and possible links between FAD mutations in PS to mitochondrial dysfunctions, which could be another key deficit in AD (Zampese, Fasolato et al. 2011, Area-Gomez, Del Carmen Lara Castillo et al. 2012). FAD mutations in PS have shown to upregulate MAM function and ER-mitochondria communication, which may play central role in AD pathogenesis (reviewed in (Schon and Area-Gomez 2013)).

The mechanisms by which PS mutations disturb intracellular Ca^{2+} signalling remain controversial. Current research focused on the influence of PS mutations on Ca^{2+} uptake or leak functions by the ER, suggests that the dysregulation is caused by an enhanced expression of ER Ca^{2+} release channels or alterations in the properties of Ca^{2+} channels and pumps by FAD mutants in PS1 or PS2 (Cheung, Shineman et al. 2008, Rybalchenko, Hwang et al. 2008, Cheung, Mei et al. 2010). Enhanced IP_3-evoked Ca^{2+} responses related to PS mutation have been observed in several cell lines and brain slices from AD animal models (Guo, Sopher et al. 1997, Leissring, Paul et al. 1999, Chan, Mayne et al. 2000, Cheung, Mei et al. 2010). Increased proportions of neurons responding to the IP_3 have also been observed in cortical neurons of mutant PS1 knock-in mice (Stutzmann, Caccamo et al. 2004). Rather than changing the level of IP_3Rs, both of FAD mutants, PS1 and PS2, have been observed to strongly enhance the gating activity for Ca^{2+} release of IP_3Rs, which might be a potential mechanism for how PS mutations alters ER Ca^{2+} signalling. PSs have been shown to influence the activity of IP_3Rs by physically interacting with them directly to enhance IP_3R-evoked Ca^{2+} signalling (Cheung, Shineman et al. 2008). Kevin Foskett and collaborators found the sensitivity of IP_3R to a low level of cytosolic IP_3 increased in cells from FAD patients and PS1-AD mice (Cheung, Shineman et al. 2008, Cheung, Mei et al. 2010). They suggested that the mutations in PS activate IP_3R gating and shift it toward a high open-probability burst mode by affecting the gating kinetics through IP_3R-PS interaction. Mattson's group observed that PS1 mutations in rat neural cells perturbed ER Ca^{2+} regulation by activating IP_3Rs and this may further sensitize neurons to apoptosis and increase neuronal vulnerability to

excitotoxic and ischemic injury (Guo, Sopher et al. 1997, Mattson, Zhu et al. 2000). A recent study in PS FAD mouse models demonstrated that reduction of IP_3R1 expression can rescue neuron from exaggerated Ca^{2+} release and attenuate Aβ and tau accumulation (Shilling, Müller et al. 2014).

Similar to IP_3R, PS1 has been reported to physically interact with RyRs and may regulate intracellular Ca^{2+} signalling through modulation of the RyR ion channel gating by protein-protein interactions (Rybalchenko, Hwang et al. 2008). Goussakov et al. suggested that the reduced CICR threshold for RyR-mediated Ca^{2+} signalling in mutant PS neurons could be responsible for the enhanced RyR-evoked Ca^{2+} response and increased basal Ca^{2+} level (Goussakov, Miller et al. 2010). In addition to the alteration of RyRs activity, many researchers have demonstrated the upregulation of RyR expression levels in cells expressing PS mutations (Chan, Mayne et al. 2000, Stutzmann, Smith et al. 2007, Rybalchenko, Hwang et al. 2008, Zhang, Sun et al. 2010). For example, enhanced expression of RyR type 3 with an increased amplitude of caffeine-induced Ca^{2+} release has been observed in rat neural cells with the PS1 mutation and primary hippocampal neurons from PS1 mutant knock-in mice (Chan, Mayne et al. 2000). Likewise, increased Ca^{2+} release through RyRs has been observed with increased RyR expression across all ages in FAD-PS1 knock-in mice, which may be responsible for the dysregulation of cytosolic Ca^{2+} homeostasis (Stutzmann, Smith et al. 2006, Stutzmann, Smith et al. 2007). Lee et al. reported increased RyR expression in mutant PS2 transgenic mice and demonstrated that PS2 mutations sensitized neurons by enhancing Ca^{2+} release through RyRs and, ultimately, activating the caspase-3-dependent apoptotic pathway (Lee, Hwang et al. 2006). Surprisingly, recent research has found reduced levels of RyR proteins with an unaffected mRNA expression level in hippocampal slices from PS conditional double (PS1 and PS2) knock-out mice (Wu, Yamaguchi et al. 2013). They concluded that PS mediates intracellular Ca^{2+} homeostasis via regulation of RyR expression and function, while the underlying mechanism is undetermined. They suggested that PS regulates RyR expression but not at the mRNA transcription level.

PS also has been reported to physically associate with the SERCA pump and may act as a positive modulator for the normal functioning of this Ca^{2+} pump (Green, Demuro et al. 2008). La Ferla's group reported that overexpression of wild-type PSs (PS1 and PS2) and FAD PS1 mutations could stimulate SERCA activity and lead to Ca^{2+} overfilling in the ER, and the absence of both types of presenilins would affect SERCA function (Green, Demuro et al. 2008). The opposite results by another group showed that both wild-type and mutant PS2 could reduce SERCA activity (Brunello, Zampese et al. 2009). They suggest PS2 is stronger

in inhibiting SERCA activity compared with PS1. These different conclusions may be because of the different cell types they used or other unknown mechanisms involved.

2.2.4.2.3 PS as a Ca^{2+} leaking channel of the ER

Besides interaction with ER Ca^{2+} channels and pumps, it has been proposed by Bezprozvanny's group that PSs themselves may act as Ca^{2+}-leak channels on the ER membrane (Tu, Nelson et al. 2006). FAD mutations in PS may diminish this function and lead to ER Ca^{2+} dysregulation. They observed Ca^{2+} permeable channel formation in planar lipid bilayers by wild-type PS1 and PS2 (but not FAD mutants). They suggested PSs might act as low-conductance, passive Ca^{2+} leak channels at the ER membrane in hippocampal neurons, whereas FAD PS mutations might disrupt this function and lead to overfilling of ER Ca^{2+} stores (Tu, Nelson et al. 2006, Zhang, Sun et al. 2010). They also observed that the cysteine point mutations in selected transmembrane (TM) of PS1 in mouse models led to a loss of its ER Ca^{2+} leak function, suggesting that the hydrophilic water-filled catalytic cavity (between TM6 and TM7) of PS may play a role in forming a low conductance Ca^{2+}-permeable pore (Nelson, Supnet et al. 2011). In Bezprozvanny's latest review (Bezprozvanny 2013), he points out that this hypothesis can be explained and supported by two other recent independent research papers on the crystal structure of an archaeal presenilin homolog PSH1 (Li, Dang et al. 2013) and a quantitative model of cellular Ca^{2+} signal combines with siRNA perturbations to identify key proteins in Ca^{2+} homeostasis regulation (Bandara, Malmersjo et al. 2013).

Increased expression in RyRs has been observed to partially compensate for the loss of the ER Ca^{2+} leak function in PS, suggesting a protective role for RyRs in AD (Tu, Nelson et al. 2006, Zhang, Sun et al. 2010). This is consistent with a previous study carried by the Supnet group, which suggests that the observed upregulation of RyR type3 in neurons of TgCRND8 AD mice may protect neurons against the increased excitotoxicity in AD (Supnet, Grant et al. 2006). The results from their subsequent study have revealed that up-regulation of RyR type3 does not affect neuronal health or global Ca^{2+} homeostasis, while knockdown of RyR type3 promotes neuronal death of TgCRND8-cultured cortical neurons, but not in non-transgenic neurons, further supporting the hypothesis of the compensation and neuroprotective roles of RyRs in AD (Supnet, Noonan et al. 2010). This hypothesis could be an explanation for how neurons maintain Ca^{2+} homeostasis and neuronal function against the effects from mutations in the early stages of AD (Supnet and Bezprozvanny 2010).

However, the hypothesis of PS is an ER Ca^{2+} leaking channel has been challenged by several recent studies. Cheung et al. argue that PS may not participate in the Ca^{2+} permeability of ER

membranes and, instead of a Ca^{2+} overload, FAD mutant PS reduced or had no effect on the Ca^{2+} levels in the ER (Cheung, Shineman et al. 2008). Likewise, Shilling et al. investigated ER Ca^{2+} filling rates, basal ER Ca^{2+} fill levels and ER Ca^{2+} leak rates from three different cell systems using different indicators, and concluded that the FAD mutant PS2 may not induce ER Ca^{2+} overfilling and PS may not function as an ER Ca^{2+} leak channel (Shilling, Mak et al. 2012). A reduced ER Ca^{2+} load has also been reported for both PS1 and PS2 mutations in other research (Brunello, Zampese et al. 2009). Furthermore, a recent study carried by Wu et al. showed that in the hippocampus of PS conditional double knock-out mice, the ER Ca^{2+} level stayed at a normal level while the levels of RyR proteins were reduced with impaired RyR function for regulating Ca^{2+} release (Wu, Yamaguchi et al. 2013).

2.2.5 ER alteration may influence Aβ production

Alteration of intracellular Ca^{2+} homeostasis shows conflicting effects on the production of Aβ peptides. Sustained elevation in the cytosolic Ca^{2+} level has been reported to accelerate Aβ formation, which suggests that reduction of Ca^{2+} release from the ER could be a potential neuroprotective strategy against Aβ peptide neurotoxicity (Querfurth and Selkoe 1994, Ferreiro, Oliveira et al. 2004, Isaacs, Senn et al. 2006). Increased expression and activity of RyRs have been found in the brains of patients in the early stages of AD and also in mice models, and this may contribute to the progression of AD pathogenesis (Kelliher, Fastbom et al. 1999, Bruno, Huang et al. 2012, Chakroborty, Kim et al. 2012). Early research showed that the elevation of intracellular Ca^{2+} levels after treatment with Ca^{2+} ionophore led to increased Aβ generation in human cell lines (Querfurth and Selkoe 1994). Later, the same group reported that RyR activation by caffeine resulted in an elevation of intracellular Ca^{2+} level, which further enhanced the release of Aβ from APP in HEK293 cells (Querfurth, Jiang et al. 1997). Likewise, a study of tissues from post mortem AD brains has shown the loss of RyRs is correlated with amyloid deposition (Kelliher, Fastbom et al. 1999). Recent research on Tg2576 mouse models has revealed that reduced RyR-mediated Ca^{2+} release after treatment with dantrolene, a RyR inhibitor, could reduce both intracellular and extracellular Aβ loads and slow down the loss of memory and cognitive function. This possibly resulted from the decreasing Thr-668-dependent APP phosphorylation and β- and γ-secretases activities by interaction with Ca^{2+} (Oule`s, Del Prete et al. 2012). However, there are conflicting results from other groups who reported that knock-out of RyR type3 neurons or ones after long-term exposure to RyR inhibitor, dantrolene, presented with an increased amyloid pathologic condition, suggesting a potential neuroprotective role for RyR (Supnet, Noonan et al. 2010, Zhang, Sun et al. 2010).

Likewise, IP_3R and its regulation of cytosolic Ca^{2+} signalling may also affect the generation of Aβ. Cheung et al. reported reduced Aβ production in IP_3R-deficient cells, which suggested that amyloidogenic processing of APP might be closely related to IP_3R-mediated Ca^{2+} release (Cheung, Shineman et al. 2008). Pierrot et al. suggested increased Ca^{2+} liberation from the ER alone may not be enough to trigger intraneuronal Aβ production, which requires influx of extracellular Ca^{2+} and a sustained increase in cytosolic Ca^{2+} concentration (Pierrot, Ghisdal et al. 2004). This is consistent with results from a recent study, which investigated the interactions between genes of different Ca^{2+} channels in the AD pathway from a genetic perspective using an online database (Koran, Hohman et al. 2014) . In their study, Gene *RYR3* and *CACNA1C* have shown to interact significantly with each other, suggesting this interaction may result in Ca^{2+} dysregulation, leading to enhanced Aβ production and deposition.

However, there are studies which shows increase in the cytosolic Ca^{2+} level reduces Aβ production. The role of IP_3R in Aβ generation is controversial. Severely reduced levels of both IP_3 and IP_3Rs have been observed in AD brains, and the loss of IP_3Rs is suggested to be important for amyloid production and deposition by altering Ca^{2+} homeostasis (Kurumatani, Fastbom et al. 1998). Other studies have demonstrated that the elevation of intracellular Ca^{2+} can decrease amyloid production and promote the anti-amyloidogenic processing of APP (Buxbaum, Ruefli et al. 1994, Dreses-Werringloer, Lambert et al. 2008). For example, an increased level of cytosolic Ca^{2+} followed treatment with high levels of thapsigargin, an inhibitor of SERCA, leading to decreased Aβ formation (Buxbaum, Ruefli et al. 1994). This is consistent with results from a recent study, which suggests increase Ca^{2+} influx via SOCE significantly by overexpression of STIM1 can actually inhibit Aβ secretion (Zeiger, Vetrivel et al. 2013). These contradicting observations may result from different experimental conditions, such as cell lines chosen, or different detection methods (Kurumatani, Fastbom et al. 1998).

In addition, Dreses-Werringloer et al. identified a gene called Ca^{2+} homeostasis modulator 1 (*CALHM1*), which was mostly expressed in the hippocampus and was located in AD linkage regions (Dreses-Werringloer, Lambert et al. 2008). It encodes a multipass transmembrane glycoprotein, CALHM1, the majority of which is localized in the ER and plasma membrane. CALHM1 may function as a component of a cerebral Ca^{2+} channel, which controls cytosolic Ca^{2+} concentrations and APP processing (Dreses-Werringloer, Lambert et al. 2008, Gallego-Sandin, Alonso et al. 2011). A recent study showed *CALHM1* P86L polymorphism modulates Aβ levels in the cerebrospinal fluid of cognitively healthy individuals at risk of AD, which

further confirmed that CALHM1 is involved in AD pathogenesis (Koppel, Campagne et al. 2011). Dreses-Werringloer et al. also proposed that a P86L polymorphism in the *CALHM1* gene may interfere with CALHM1-mediated Ca^{2+} permeability to increase Aβ production, and may be associated with SAD (Dreses-Werringloer, Lambert et al. 2008). This notion is supported by subsequent research carried out in populations from countries such China (Cui, Zheng et al. 2010), Spain (Boada, Antunez et al. 2010) and Iran (Aqdam, Kamali et al. 2010). However, it has been challenged by studies carried out in Caucasian (Minster, Demirci et al. 2009) and Asian populations (Tan, Ho et al. 2011), which were unable to show an association between *CALHM1* polymorphism and the risk of AD. Lambert et al. suggested *CALHM1* P86L polymorphism may modulate the age of onset of AD by interacting with the ε4 allele of the apolipoprotein E gene, rather than be an independent risk genetic determinant of AD (Lambert, Sleegers et al. 2010).

2.3 Modelling Ca^{2+} dynamics in dendritic spines

A number of models for the Ca^{2+} dynamics in the dendritic spines have been proposed for different types of neurons. Some of them have been modified and extended to study Ca^{2+}-mediated downstream events, such as the induction of different types of synaptic plasticity (De Schutter and Smolen 1998). These Ca^{2+} models generally contain similar components, such as Ca^{2+} influxes from extracellular spces and/or release from an internal Ca^{2+} source, Ca^{2+} extrusion from the cytosol and interactions between Ca^{2+} and various intracellular proteins. In multi-compartment models, which take the geometry of the spine head and dendrite into consideration, and simulate the whole model as a series of compartments, among which Ca^{2+} ions diffuse. In this section, we review the exsiting models related to the NMDAR-mediated Ca^{2+} response in dendritic spines regarding these components.

2.3.1 Simulation of membrane Ca^{2+} influx from extracellular spaces

2.3.1.1 Simulation of glutamate release, uptake and diffusion

There are a number of models for presynaptic neurons that contain components related to glutamate vesicle release with different levels of detail (Senn, Markram et al. 2001, Nadkarni, Bartol et al. 2010) that are beyond the scope of this thesis. In contrast, most models of the postsynaptic Ca^{2+} response to the presynatpic stimualtion assume the release of glutamate from a vesicle is instantaneous and, thus, uses a constant glutamate concentration per release (Barbour and Häusser 1997). Other models use simple equations to represent glutamate release from a vesicle as a non-instantaneous process (Rusakov and Kullmann 1998).

The spatiotemporal profile of the glutamate concentration in the synaptic cleft and the extrasynaptic space following release are due to their diffusion and uptake. The transient of a single pulse of glutamate at certain locations can be simply modelled as a process with a fast rise time and a slow decay time or a square-wave pulse (Sterratt, Graham et al. 2011). Complex models make an approximation of the synaptic cleft and the extracellular space. They then simulate the gluamate concentration using diffusion equations, which are either partial differential equations or analytical solutions for them. The synaptic cleft can be approximated as a two-dimensional disc or a three-dimensional flat cylinder whereas the extrasynaptic space is a spherical, isotropic porous medium containing obstacles (Barbour and Häusser 1997, Rusakov and Kullmann 1998). The diffusion space is divided into different small diffusion compartments, such as concentric cylindrical or spherical shells (Rusakov 2001) and, in the diffusion compartments of the extrasynaptic space, the gluatmate concentration with time is simulated as a diffusion-reaction process, which accounts for the diffusion of glutamate as well as the uptake of glutamate by gluatmate transporters in the adjacent glia. The kinetics of binding glutamate to different glutamate transporters can be modelled as a chain reaction (Rusakov and Kullmann 1998); or follow the proposed schemes that contain more reaction details (Grewer, Gameiro et al. 2008).

2.3.1.2 Simulation of kinetics of glutamate receptors

The Ca^{2+} influx depends on the number of opened Ca^{2+} channels as well as the difference between the membrane potential and the reversal potential. Markov's kinetic models are mostly used to describe the state-transtion of AMPAR and NMDAR by glutamates. The receptor between the different states includes a closed state, a ligand-binding state (single-bound and double-bound, respectively), a desensitisation state and an open state, which are determined by various rate constants. The values of these rate constants are estimated by fitting the specific model schemes to the single-channel experimental data. For example, there are six-state (Patneau and Mayer 1991), seven-state (Jonas, Major et al. 1993) and twelve-state (Nielsen, DiGregorio et al. 2004) models for AMPAR, and a five-state model (Lester and Jahr 1992) for NMDAR. In these models, the fully bound receptors by two glutamate can directly transition to the open state. In contrast, there are a number of NMDAR models that take into consideration the conformational changes of the fully bound receptors by including two desensitised states before moving to the open state (Banke and Traynelis 2003, Popescu, Robert et al. 2004, Erreger, Dravid et al. 2005, Schorge, Elenes et al. 2005, Kussius and Popescu 2009). Most NMDAR models only consider the glutamate binding-steps and exclude the coagonist binding-steps by fitting the data obtained from experiments under the condition

of a saturated concentration of glycine (Ambert, Greget et al. 2010).

The relief of the Mg^{2+} blockage of NMDAR is generally treated as a instantaneous event and the model proposed by Jahr and Stevens (1990) is widely used for simulating it as a membrane voltage-dependent process. Morover, there are few models that simulate the relief of Mg^{2+} blockage as a slow component and include it into their kinetic models (Kampa, Clements et al. 2004, Vargas-Caballero and Robinson 2004).

2.3.2 Simulation of Ca^{2+} release from ER

ER as an important compartment appears in numerous synaptic and neuronal models, because of its crucial role of internal Ca^{2+} source and its ubiquitous distribution across the neuron. In synaptic level, models mostly include Ca^{2+} ions flux via proteins (such as NMDARs and sodium Ca^{2+} exchangers) on the post synaptic plasma membrane and Ca^{2+}-mediated membrane electrical activity as the aspect of contribution from Ca^{2+} dynamics (Holmes and Levy 1990, Holcman, Schuss et al. 2004, Rubin, Gerkin et al. 2005). In spite of this, several synaptic models include ER as an internal Ca^{2+} source to study its response to synaptic Ca^{2+} fluctuation during the signal transduction process in synapses (Schiegg, Gerstner et al. 1995, Volfovsky, Parnas et al. 1999, Doi, Kuroda et al. 2005). In contrast, ER as an internal compartment is generally includes in the most models to study its contribution on cytosolic events such as intracellular propagation of Ca^{2+} waves (Sneyd, Girard et al. 1993, Fink, Slepchenko et al. 2000).

In Ca^{2+} signalling models of the ER, the uptake mechanism is basically governed by modelling the gating behavior of its two Ca^{2+} channels, IP_3R and RyR. At molecular level, different kinetic schemas have been developed for these channels.

Models of the IP_3R-regulated Ca^{2+} release have been the focus of many research on account of their significance in Ca^{2+} oscillations and synaptic plasticity. Modelling of the IP_3R shows more complexity in its dynamics as a result of its activation and inhibition, and the involvement of a G protein-coupled receptor-induced IP_{3-} production process. The first model for IP_3-induced Ca^{2+} release was proposed by De Young and Keizer, which assumed that there were three equivalent and independent subunits of IP_3R involved and all of them have to be in particular conducting states to open the channel (De Young and Keizer 1992). Similar to De Young and Keizer's four-state model, there were other models that used Markov kinetic schemes to describe transitions between states. They are based on the assumption that each subunit of the IP_3R receptor has different multiple transitional states; for example, three (Gin,

Kirk et al. 2006) and seven transitional states (Doi, Kuroda et al. 2005). A well-known simplified two-state model based on De Young and Keizer's model was developed by Li and Rinzel, who used Hodgkin-Huxley style equations based on the assumption of instantaneous activation following slow inactivation of IP_3R by Ca^{2+} (Li and Rinzel 1994). Many follow-up models have been developed based on, or influenced by, the De Young–Keizer model or the Li-Rinzel simplified model. In addition, the models have been also developed based on other different assumptions such as sequential binding behavior (Bezprozvanny 1994), receptor conformation changes (Dawson, Lea et al. 2003), adaptation of IP_3R and saturable fashion of IP_3 (Dawson, Lea et al. 2003), or built to investigate different aspects, such as open probability of IP_3R on steady states (Kaftan, Ehrlich et al. 1997, Mak, McBride et al. 2001) and IP_3 metabolism (LeBeau, Yule et al. 1999). The development of IP_3R models has been reviewed in detail by Sneyd and Falcke (Sneyd and Falcke 2005).

RyR-regulated Ca^{2+} signalling has been ignored in some models of intracellular Ca^{2+} dynamics, since IP_3R itself is enough to be responsible for CICR as it is sensitive to both IP_3 and Ca^{2+} ions. However, it is important to include RyRs to simulate the Ca^{2+} signalling more realistically. For example, by using Chemesis, a neural simulation software, Blackwell and Kotaleski demonstrated that the involvement of RyR channels affects the model simulation behavior of Ca^{2+} wave propagation (Blackwell and Kotaleski 2003). The models, which included RyR-regulated Ca^{2+} signalling, have considered that both RyR and IP_3R contribute to Ca^{2+} release from the ER and the CICR is governed by RyR (De Schutter and Smolen 1998, Nakano, Yoshimoto et al. 2013). Similar strategies to IP_3R modelling have been applied in RyR models. For example, there are models of RyRs using Markov kinetic schemes which describe the transitions between activated and inactivated states or multi-states (Sachs, Qin et al. 1995, Keizer and Levine 1996, Saftenku, Williams et al. 2001).

2.3.3 Simulation of Ca^{2+} pumps and membrane leakage

Ca^{2+} pumps include plasma membrane Ca^{2+} pumps, which remove Ca^{2+} from the cytosol, and SERCA pumps, which are the only contributors to the elevation of ER Ca^{2+} levels. These pumps have been present in cytosolic Ca^{2+} signalling models and been shown to modify Ca^{2+} transient and oscillation. In most models, they have been modelled as unidirectional pumps that are activated by the increase in cytosolic Ca^{2+} and defined by a simple Hill equation or Michaelis-Menten kinetics with a Hill coefficient (Zador, Koch et al. 1990, Blaustein and Lederer 1999, Schuster, Marhl et al. 2002, Bondarenko, Szigeti et al. 2004). A few complex models have taken into consideration the multiple transition states of SERCA activation

(Matsuoka, Sarai et al. 2003, Yano, Petersen et al. 2004) or the effect of Ca^{2+}-buffering on SERCA (Higgins, Cannell et al. 2006). A leak influx of Ca^{2+} through the membrane into the cytosol is always used to balance the Ca^{2+} eflux through the pumps in the resting state. The membrane leakage is modelled as either a constant leak influx (Zador, Koch et al. 1990) or as a process with a constant rate and in proportion to the concentration gradient across the membrane (Shannon, Ginsburg et al. 2000).

2.3.4 Simulation of Ca^{2+} buffering and diffusion

Ca^{2+} ions also interact with a variety of buffer proteins, such as calmodulin and calbindin, and fluorescent dyes in both the cytosolic space and the ER lumina (Berridge, Bootman et al. 2003). In order to study the buffering effects on Ca^{2+} dynamics and make the simulation more reliable, various assumptions relating to buffering behavior have been made and added to the Ca^{2+} signalling model. It would obviously make the model more complex and larger to include details of binding events, such as the effects from different buffers. Therefore, simplified theories for Ca^{2+} buffering have been applied. For example, excess buffer approximation (EBA) and rapid buffer approximation (RBA) are two important simplifications, which assume the mobile buffers are exceeded and cannot be saturated, and binding of Ca^{2+} ions to buffers is much faster compared with the changes in cytosolic Ca^{2+} concentration, respectively (Sterratt, Graham et al. 2011). Besides, diffusion of Ca^{2+} ions has been included in some models which consider the effect of concentration gradients from geometry facts (Volfovsky, Parnas et al. 1999). The intracellular compartment is divided into multi-pool and movement of Ca^{2+} ions between two adjacent subcompartments is driven by Brownian motion (Sterratt, Graham et al. 2011). Radial and/or longitudinal diffusion will be considered based on model assumptions. Either deterministic or stochastic strategies can be applied to simulation of diffusion processing by using partial differential equations (Blackwell 2013).

2.3.5 Simulation software

There are a great deal of simulation tools available to date, and they can be generally classified into two categories: general purpose software and biological simulation software (reviewed in (Alves, Antunes et al. 2006, Brette, Rudolph et al. 2007, Blackwell 2013)) (Table A.1 in Appendix A). Tools that belong to the former category, such as MATLAB, XPPAUT, Mathematica and Python, require the user have some programming capability. The power of these tools provides the user great opportunities to analyze the model freely. Tools

that fall into the second category include common biological simulation tools such as CellDesigner, VCell, MCell and COPASI, as well as specific software packages for neuron simulation, such as GENESIS and NeuroRD. These tools have built-in capabilities for simulation on biological processes and are widely used by biologists. Most of these softeware have friendly graphical user interface (GUI) for model development, while others have Command-line interface (CLI) or require scripting languages (Figure A.1 in Appendix A).

2.4 Modelling intracellular signalling related to AD

Modelling intracellular signalling in computational neuroscience has been used to study complex temporal and spatial characteristics of nerve systems for decades. Well-established modelling methods of Ca^{2+} signalling provide good foundations for modelling studies of AD and Ca^{2+}-related disease. However, only a few models have been developed to simulate or partly simulated the dysregulation of Ca^{2+} signalling in neurons related to AD. There has been some progress in the mathematical modelling of Aβ-induced alterations as a function of ion channels in neuronal plasma membranes. For example, based on the observation that Aβ induced a voltage-dependent decrease in membrane conductance in rat hippocampal neurons, Good and Murphy developed a mathematical model of Aβ-mediated blockages of fast-inactivating K^+ channels (Good and Murphy 1996). The simulation results show good agreement with experiments in the aspect of stimulation responses and Ca^{2+} buffering capacity. Through simulation they hypothesized that blockages of a fast-inactivating K^+ current by Aβ as an early event plays a crucial role in the neurotoxicity of Aβ in AD and could lead to increased intracellular Ca^{2+} levels and membrane excitability resulting in neuronal neurotoxicity and, eventually, death. A recently published model based on Good and Murphy's model has been developed to further explore Aβ-induced blockages of fast-inactivating K+ channels as well as to study the Aβ-induced increase of membrane conductance during Aβ-neuron interaction in a short time-scale (Wilson, Gates et al. 2013). This model included the voltage-clamp and the membrane conductance mechanisms, which enabled it to simulate Aβ-neuron interactions under various experimental conditions, make comparisons with available data and generate predictions. Good's group also utilized mathematical kinetic analysis methods to study the potential mechanism underlying Aβ-induced G protein activation (Wang, Kazantzi et al. 2003). By using experimental rate data to examine the proposed underlying mechanisms, four possible different mechanisms have been tested to find the best fit of the rate expression with experimental data. Based on the results, they suggested that Aβ oligomers activate the G protein while excessive Aβ aggregation might inhibit further GTPase activity. In addition, models using simulation software packages

such as NEURON have been constructed to simulate the effects of Aβ on the neuronal membrane. For example, Kidd and Sattelle used NEURON to construct a model neuron to study the blockage effects by Aβ on A-type K^+ currents of Drosophila larval cholinergic neurons and made predictions on their firing properties related to the alteration of the steady-state properties of the A-type K+ current (Kidd and Sattelle 2006). Similarly, Morse et al. also used NEURON to analyze the hyper-excitability induced by Aβ via blocking A-type K^+ currents observed in proximal dendrites in AD animal models (Morse, Carnevale et al. 2010). Through simulation they hypothesized the disruption Aβ-induced blockage of A-type K^+ currents at oblique branches may be most vulnerable and may play an important role in the decline of cognitive function in the early stage of AD.

Although dysregulation of intracellular Ca^{2+} signalling has been widely studied experimentally, little work has been done on computational model development in this area. Tiveci et al. developed a model of brain energy metabolism by including Ca^{2+} dynamics to an existing hemodynamic model of the brain (Tiveci, Akin et al. 2005). This model is able to investigate the effects of the existence of Ca^{2+} dynamics on the blood oxygenation level dependent (BOLD) signal based on experimental observations. They also used this model to simulate AD cases and, based on the simulation results, they suggested the cerebral blood flow changes observed in AD cases might be the cause of negative BOLD effects and increased cytosolic Ca^{2+} level. As well as modelling Ca^{2+} dynamics in neurons, there are also several models of Ca^{2+} signalling in astrocytes, the predominant glial cells in the central nervous system. Toivari et al. developed a computational stochastic model of Ca^{2+} signalling in rat cortical astrocytes, (Toivari, Manninen et al. 2011). This model was used to study the effects of $A\beta_{25-35}$ and transmitters on intracellular Ca^{2+} signalling in astrocytes. The simulation results were consistent with their experimental findings on $A\beta_{25-35}$ and transmitters induced Ca^{2+} transient. Another example is a model constructed by Riera et al. This model was based on spontaneous Ca^{2+} oscillations in astrocytes and used it to simulate Ca^{2+} dynamics in wild-type (WT) and Tg2576 mice (Riera, Hatanaka et al. 2011). Through simulations, they suggested an increased Ca^{2+} influx from the extracellular space in APP transgenic mice might be activate astrocytes and play a crucial role in intracellular Ca^{2+} dysregulation. Furthermore, De Caluwé and Dupont recently developed a simple theoretical model to study the positive feedback loop between Aβ and cytosolic Ca^{2+} (De Caluwé and Dupont 2013). Despite this being a simplified model, which has excluded detailed molecular mechanisms, it was still able to reveal a bistable switch between 'healthy' and the 'pathological' states, depending on the concentration of Aβ and cytosolic Ca^{2+}. A model which concentrated more on the effects of

Aβ on Ca^{2+} signalling in a single neuron is yet to be developed.

Chapter 3
Computational modelling of disturbances of Aβ on glutamatergic transmission

Aβ oligomers interact with multiple key proteins in glutamatergic synaptic transmission (Figure 3.1). In this chapter, we investigate these proposed disturbances of Aβ: (1) Aβ reduces glutamate uptake by glutamate transporters; (2) Aβ promotes glutamate vesicle release from the presynaptic terminal and astrocytes; and (3) Aβ induces the internalisation of the surface experession of the glutamate receptors: AMPARs and the NMDARs. (1) and (2) may lead to an upregulation in glutamatergic signalling by increasing the glutamate availability to its receptors. This may be a reason for the Ca^{2+} overload observed in Alzheimer's disease (AD) through the overactivation of NMDARs located at extrasynaptic sites that, subsequently, trigger the death pathways (Li, Hong et al. 2009, Hardingham and Bading 2010). In contrast, (3) may contribute to the depression of synaptic activity and a reduction in memory formation (Mota, Ferreira et al. 2014). However, this reduction in the surface receptor numbers is suggested to be a neuroprotective mechanism, to some extent, in response to the glutamate-induced excitotoxicity and excessive Ca^{2+} influxes from the extrasynaptic receptors (Goto, Niidome et al. 2006). These experimental observations show paradoxical effects Aβ on the Ca^{2+} dynamics of the postsynaptic neurons. These effects lead to different interpretations of disturbances in the downstream events that are mediated by the cytosolic Ca^{2+} levels.

We develop a computational model of a CA1 pyramidal dendritic spine to explore these issues both individually and globally. This spine model is stimulated by presynaptic electrical stimulus inputs, which trigger a sequence of events that include glutamate release and transmission, glutamate receptor activation at the postsynaptic neuron at various sites, and the Ca^{2+} influx via the opened receptor channels. Therefore, we are able to use this model to study the above-mentioned disturbances and identify their contributions to the Ca^{2+} dynamic in the postsynaptic spine.

NMDAR is a key receptor that is involved in, or relates to, all events included in this model of the glutamate-mediated state transition behaviour of the NMDAR and the NMDAR-dependent Ca^{2+} influx. NMDAR is located at both the synaptic and extrasynaptic sites, and the current understanding is that it plays opposite physiological roles in mediating intracellular signalling and cell death pathways (see Hardingham and Bading (2010)). Aβ

shows differential disturbances on the activities of NMDARs with different subunit composition and at different locations (see Chapter 2.3.2). Therefore, we include location-specific and NR2 subunit-specific characteristics in this model to understand the Aβ–induced dysregulation of intracellular Ca^{2+} and its relationship with the balance between synaptic and extrasynaptic NMDARs (sNMDARs and eNMDARs) in the dendritic spine of the pyramidal neurons.

Under experimental conditions, Aβ is usually given at a much higher concentration than that in human brains with AD (Sebollela, Freitas-Correa et al. 2012). It is inappropriate to study the concentration dependence of Aβ disturbances based on the results of these experiments; therefore, we mimic the disturbances of Aβ by perturbing key related parameters and observing the alterations in model behaviour. The perturbation in the parameters represents the degree of Aβ disturbance at different stages of AD pathology.

The main contribution of this model is that it allows us to investigate different motifs of disturbance from Aβ on glutamatergic signalling and NMDAR-mediated postsynaptic Ca^{2+} dynamics. Specific numbers and subtypes of NMDAR at three locations are chosen, based on the literature, to demonstrate typical conditions in the CA1 pyramidal neurons. In this chapter, we develop the model in Section 3.1. In Section 3.2 we present the calibration and the estimation of unknown parameters with respect to the experimental findings based on the healthy condition. In Section 3.3, we discuss the model performance under healthy conditions. In Section 3.4 we use the model to mimic the Aβ-dependent disturbances in synaptic transmission and receptor distribution under AD conditions. In Section 3.4, we give a brief discussion and conclusions.

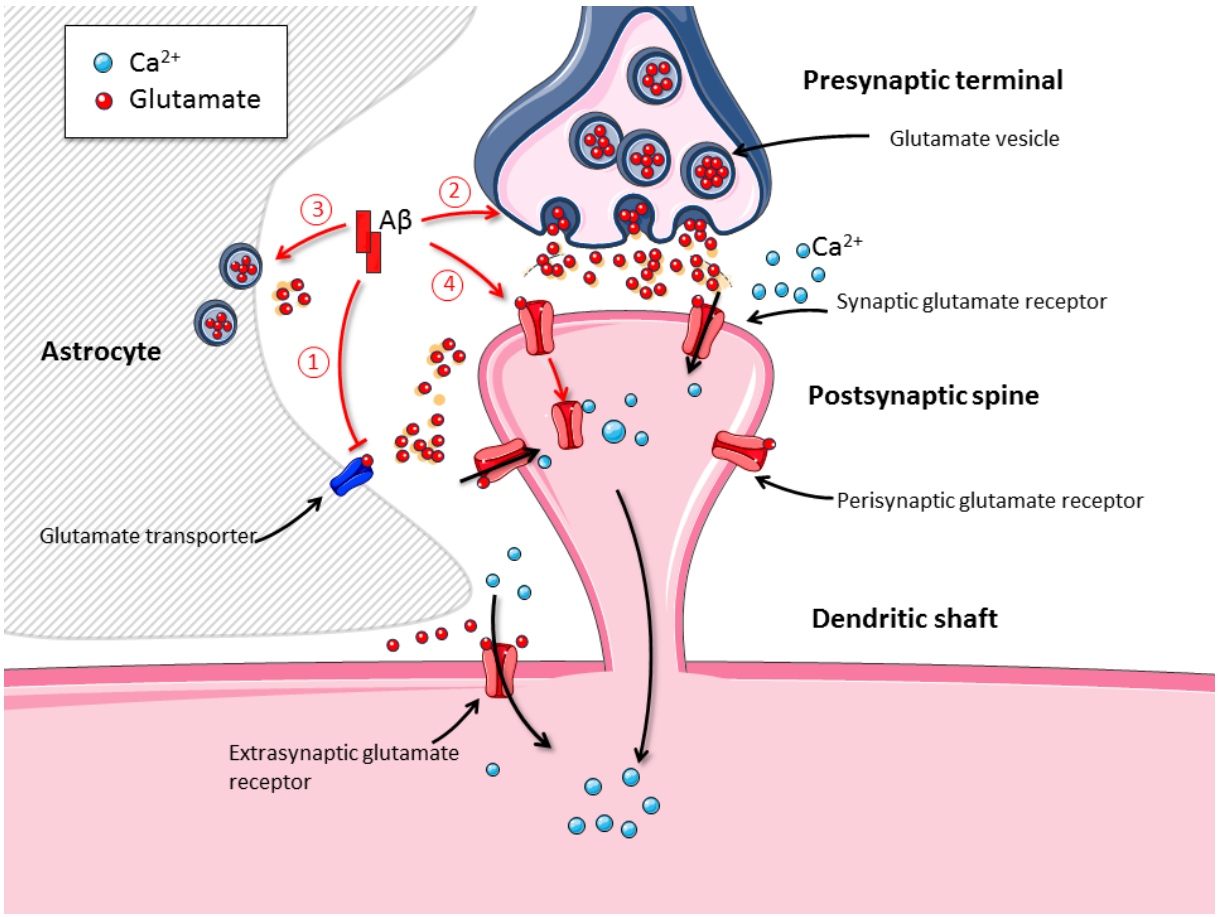

Figure 3.1. Disturbances in glutamatergic synaptic transmission by Aβ in AD. Referring to the arrow labels: ① Aβ inhibits glutamate clearance by the glutamate transporters; and ②and ③ Aß promotes glutamate vesicle release from the presynaptic terminal and ambient astrocytes, respectively; and ④Aβ also mediates the internalisation of surface receptors at the synaptic site. ①, ② and ③ result in an increase in extracellular glutamate concentration and, ultimately, may lead to the over activation of synaptic glutamate receptors or of receptors at distant locations from the release site. In contrast, ④leads to a decrease in functional synaptic receptors may depress synaptic activity. This figure is produced using Servier Medical Art (http://www.servier.com/Powerpoint-image-bank).

3.1 Model overview

To model NMDAR-mediated glutamate-induced Ca^{2+} dynamics in a single synaptic spine and the adjacent dendritic shaft of a CA1 pyramidal neuron, we construct a mathematical model consisting of three parts: (1) glutamate release, diffusion and uptake (Figure 3.2A); (2) glutamate receptor state transition (Figure 3.2B); and (3) Ca^{2+} dynamics (Figure 3.2C). In this section, we present the model development in detail.

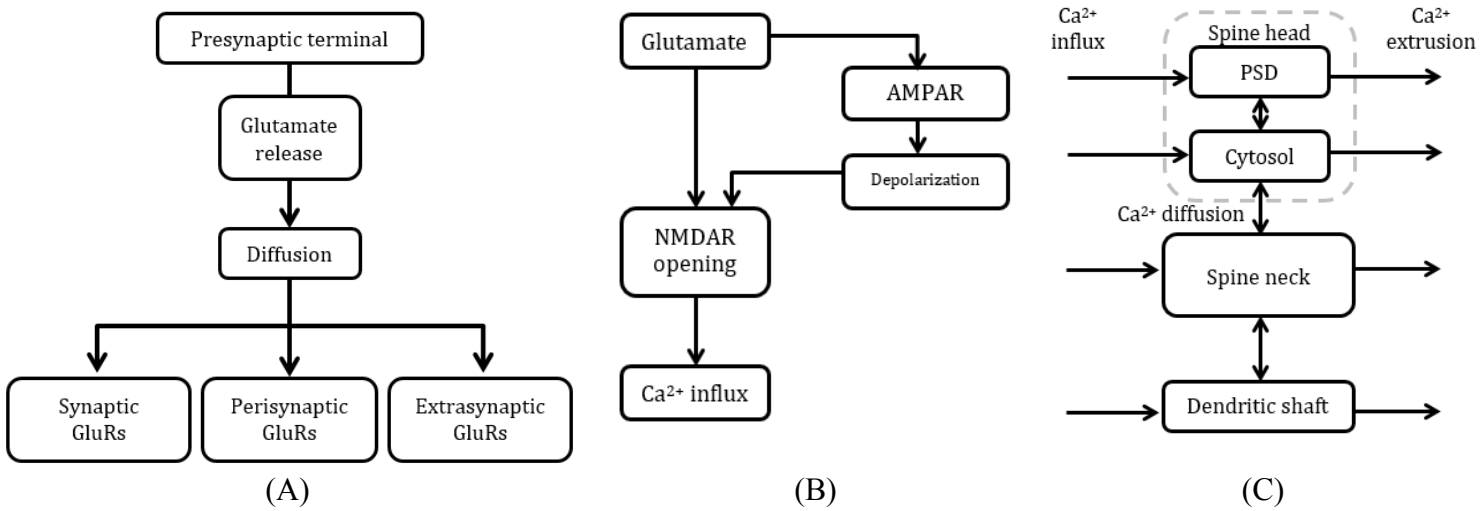

Figure 3.2. Conceptual framework of the three parts of the model. (A) After presynaptic stimulation, glutamate is released from the presynaptic terminal into the synaptic cleft. It is then diffused across the synaptic cleft and into the extrasynaptic space. Through diffusion, glutamate can bind to the glutamate receptors (GluRs) at different locations. (B) NMDAR and AMPAR are the most common ionotropic GluRs. NMDAR is the major Ca^{2+} channel; Ca^{2+} influx via NMDAR requires both the binding of glutamate to NMDAR and the removal of its Mg^{2+} blockage. The latter can be achieved by membrane depolarisation after the activation of AMPARs. (C) A four-compartment Ca^{2+} model of the dendritic spine and its adjacent dendritic shaft includes the mechansims for Ca^{2+} influx, extrusion and buffering in each compartment and diffusion between the two neighbouring compartments.

3.1.1 Glutamate release, diffusion and uptake

We simulate the glutamate release from the presynaptic terminal and diffusion inside the synaptic cleft, and in the extrasynaptic space, based on the model of Rusakov and Kullmann (1998). The schematic two-dimensional profile of the glutamate diffusion model is given in Figure 3.3. The spine head and the presynaptic terminal are modelled as two opposite hemispheres with the same radius and there is no glutamate diffusion within them. The synaptic cleft is a flat cylinder between these two hemispheres, with a height of 20 nm. We assume the volume of the spine head is 0.1 μm^3, which gives a radius of 363 nm for the synaptic cleft and the two opposite hemispheres. The extrasynaptic space is a spherically isotropic porous medium surrounded by the two hemispheric obstacles.

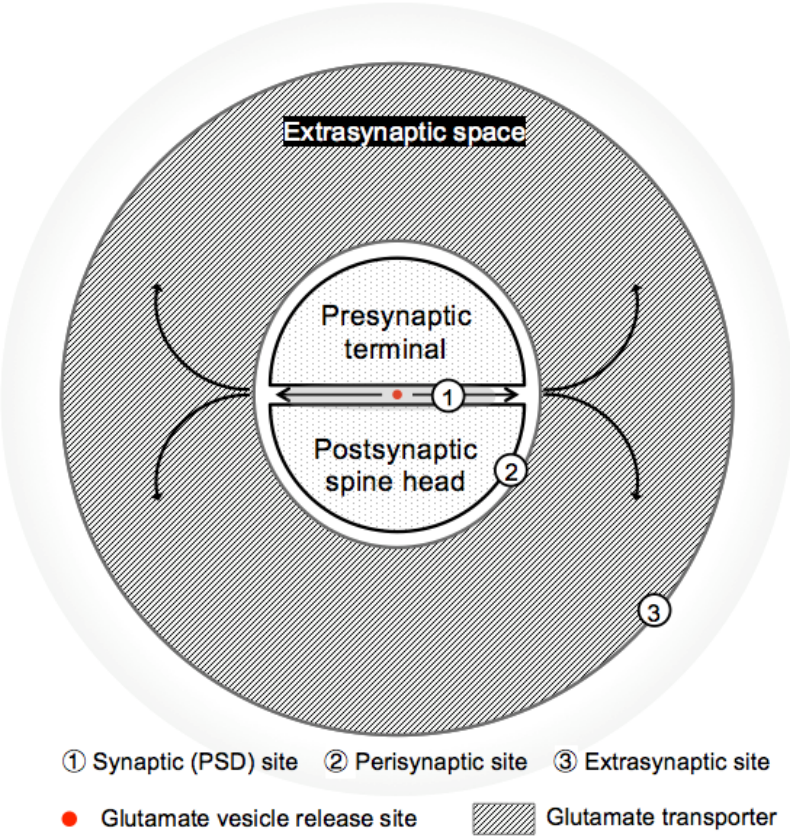

Figure 3.3. Schematic two-dimensional profile of the glutamate diffusion model. Glutamate is released at the centre of the synaptic cleft and diffused across the synaptic cleft and into the extrasynaptic space. The synaptic cleft is assumed to be a flat cylinder with 20 thin concentric shells. The extrasynaptic space is a porous medium with spherical concentric shells. The arrows denote the diffusion direction of the glutamate. Glutamate transporters are homogenously distributed in the extrasynaptic space. Three grey areas (marked with ①, ② and ③) represent the synaptic (PSD), perisynaptic and extrasynaptic sites. The glutamate concentration at each site is used for calculating local receptor activity in the NMDAR and AMPAR models.

The glutamate vesicle release site is assumed to be a point source and is placed in the centre of the presynaptic terminal surface. Each vesicle contains 100 mM glutamate, which is about 1500 glutamate molecules (Meldrum 2000). Single and multiple vesicular release events can be simulated by changing the total number of glutamate molecules released. The time course of a single glutamate vesicle release is modelled by the function

$$\phi(t) = \sigma^2 t\, exp(-\sigma t) \tag{3.1}$$

where $\phi(t)$ is the fraction of all glutamate molecules in a single that is released at time t and $\sigma = 39$ ms^{-1} is the release time constant (Rusakov and Kullmann 1998). Once released, glutamate molecules diffuse through the flat cylindrical cleft. After they escape from the cleft into the extrasynaptic space, the effective glutamate diffusion coefficient (D_{Glu}) is reduced by a tortuosity factor λ, from D_{Glu} to $D_{Glu}{}^{*} = \frac{D_{Glu}}{\lambda^2}$. Before moving to the extrasynaptic space, the glutamate concentration in the last cylinder shell of the cleft is scaled by $\frac{1}{\alpha}$, where α is the extracellular volume fraction (see Appendix B for the explanation). The spherical extrasynaptic space is modelled as 50 concentric shells with a thinness of 20 nm. The resting level of glutamate concentration in the extrasynaptic space is set to 0.25 μM (Herman and Jahr 2007, Talantova, Sanz-Blasco et al. 2013). The glutamate concentration in the last cylinder shell, which is 1.36 μm from the release site, is fixed at resting level (open boundary condition).

Uptake of glutamate is governed by glial glutamate transporters. We assume that there are no glutamate transporters inside the synaptic cleft. In the extrasynaptic space, glutamate transporters are distributed homogenously at a concentration (B_{total}) of 0.5 mM (Rusakov 2001). A gap between the glial sheath and spine head is considered and, thus, the distribution of glutamate transporters starts at 20 nm from the edge of the dendritic cleft. A simple kinetic scheme is applied to the glutamate binding and uptake by glial transporters

$$Glu + Tr \overset{k_{1f};\, k_{1b}}{\longleftrightarrow} Glu - Tr \overset{k_2}{\rightarrow} Tr,$$

where Glu is the glutamate, Tr is the unbound surface transporter and $Glu - Tr$ is the glutamate-transporter complex (Rusakov and Kullmann 1998). The reactions include a rapid reversible binding between Glu and Tr with rate constants k_{1f} and k_{1b} and a relatively slow translocation from the surface into the glial cell at rate constant, k_2. The values of the

parameters are listed in Table 3.1. The reaction is assumed to obey mass action kinetics (see Appendix C.1 for the explanation), and the model eqations for transporters are in Appendix D.1. To track the glutamate concentration after release at different locations, we define the PSD site, and perisynaptic and extrasynaptic sites as follows: the surface of the PSD region and the perisynaptic zone are set from 0 to 150 nm and 365 nm away from the centre of the postsynaptic surface, respectively (Newpher and Ehlers 2008) (Figure 3.3 ① and ②). The extrasynaptic space is set beyond the outside border of the perisynaptic zone and we assume that the extrasynaptic receptors are located at the dendritic shaft. Based on the model geometry data in Table 3.1, the extrasynaptic site is about 826 nm away from the release point (Figure 3.3 ③).

Table 3.1. Model geometry and glutamate transmission related parameters.

Description	Symbol	Value	Reference
Volume of spine head		0.1 μm^3	
Volume of PSD		0.01 μm^3	
Radius of PSD	r_{PSD}	150 nm	(Rusakov and Kullmann 1998, Sorra and Harris 2000)
Height of cleft	h_{cleft}	20 nm	
Radius of cleft	r_{cleft}	363 nm	
Length of dendritic neck	l_{neck}	750 nm	(Holmes and Levy 1990, Sorra and Harris 2000)
Radius of dendritic neck	r_{neck}	50 nm	
Length of dendritic shaft	l_{shaft}	1000 nm	(Holmes and Levy 1990, O'Donnell, Nolan et al. 2011)
Radius of dendritic shaft	r_{shaft}	500 nm	
Distance of the glial sheath from the synaptic cylinder surface		20 nm	(Rusakov 2001)
Thickness of cylinder shell (cleft)	dr_1	10 nm	
Thickness of sphere shell (extrasynaptic space)	dr_2	20 nm	
Glutamate vesicle content	Glu_0	1500 molecules	(Meldrum 2000)
Glutamate diffusion constant in the cleft	D_{Glu}	0.2 μm^2 ms^{-1}	(Rusakov and Kullmann 1998) (20-24 °C)
Tortuosity factor	λ	1.34	
Extracellular volume fraction	α	0.12	
Transporter concentration	B_{total}	0.5 mM	
Binding rate constant	k_{1f}	0.1 ms^{-1}	
Unbinding rate constant	k_{1b}	5 mM^{-1} ms^{-1}	
Translocation rate	k_2	0.1 ms^{-1}	
Resting glutamate concentration		0.25 μM	(Herman and Jahr 2007, Talantova, Sanz-Blasco et al. 2013)

3.1.2 Activation of the ionotropic glutamate receptors: NMDARs and AMPARs

Glutamate receptors are located at the synaptic, perisynaptic and extrasynaptic membrane surfaces and have various receptor numbers (Table 3.2). For each receptor, the local glutamate concentration it receives depends on its distance from the release site. Because the number of glutamates is much greater than the number of these receptors, we do not consider the glutamate uptake by these receptors in the glutamate diffusion model. After computing the local glutamate concentrations at the location of the different receptors from the glutamate diffusion model, we input these glutamate concentrations into the receptor state kinetic models to investigate the dynamics of these receptors. We assume each receptor is independent of each other. Therefore, to get the total number of receptors opened by ligand at each time point, we first calculate the fraction of a single receptor in the open state and multiply it by the total number of receptors at each particular location. The multi-state kinetic schemes of each type of receptor are described by groups of deterministic ordinary differential equations (ODEs) with reaction rate constants. Differential equations are numerically solved using *ode15s* in Matlab. The set of ODEs are in Appendix E.

3.1.2.1 Distribution of receptor numbers

Both AMPAR and NMDAR are not fixed on the plasma membrane. They undergo trafficking from the intracellular synthesis sites to function sites on the surface of the plasma membrane. They are inserted into the membrane by exocytosis; move between different sites via lateral diffusion on the membrane; and can be internalised by endocytosis (Li, Jin et al. 2011). Although the trafficking of receptors play important roles in mediating postsynaptic activity, we have not included it in this model because it is a relatively slower process compared to the reactions in this model. Therefore, we assume the numbers of all receptors at different locations are constant during each simulation.

The NMDAR number per synapse is relatively stable, about 20, among the different sizes of synapses (Newpher and Ehlers 2008, Chua, Kindler et al. 2010). A hippocampal slice study suggests that the ratio of eNMDARs to synaptic ones is around 1:2, with no exchange between them (Harris and Pettit 2007). Moreover, only about 25% of eNMDARs are located at the perisynaptic site (Hardingham and Bading 2010).

NMDAR consists of two NR1 subunits and two NR2 subunits. The subunit composition of NMDARs at different locations changes during postnatal development (reviewed in (Petralia 2012)). The ratio of NR2A to NR2B increases at the synaptic site and decreases at the

extrasynaptic site, respectively, during postnatal development. In mature synapses, NR2A-NMDARs are predominant at the synaptic sites, which takes about 60% of the total synaptic NMDARs (Cheng, Hoogenraad et al. 2006). In contrast, perisynaptic NMDARs and extrasynaptic NMDARs are mainly NR1/NR2B-NMDARs (pNR2B-NMDAR and eNR2B-NMDAR). Based on the experimental observations we select numbers for each type of NMDAR at different locations to represent NMDAR distribution in a mature synapse, as listed in Table 3.2.

Unlike NMDARs, the number of AMPARs depends on the spine geometry and is positively correlated with the PSD size (Takumi, Ramirez-Leon et al. 1999, Newpher and Ehlers 2008). The average density of AMPARs is suggested to be uniformly distributed at different synapses and will be of a much higher density in synaptic sites rather than in extrasynaptic sites (Tanaka, Matsuzaki et al. 2005). We assume that the functional AMPARs are homogenously located in the membrane of PSD and at the dendritic shaft with different densities, and there is no AMPAR in the rest of the membrane of the spine. The number of AMPARs per spine is critical for the generation of the temporary depolarisation of the postsynaptic membrane potential after stimulation, which is also called the excitatory postsynaptic potential (EPSP). We estimate the AMPAR numbers in PSD based on the established experimental data in Section 3.2.3. The number of AMPARs at the dendritic shaft is low and stable, and is calculated based on the membrane surface area. The receptor density in Table 3.2 is taken from (Tanaka, Matsuzaki et al. 2005).

3.1.2.2 Kinetic model of a single NMDAR

NMDARs are heteromeric tetramers and the activation of an NMDAR requires both the binding of glutamate molecules to the NR2 subunits and the binding of coagonists (d-serine or glycine) to the NR1 subunits (Papouin, Ladepeche et al. 2012). In this study, we simulate the state transition of NMDAR by using a subtype specific kinetic model (Erreger, Dravid et al. 2005) (Figure 3.4 A). We assume that the two NR1 subunits are always occupied by coagonists. Therefore, the activation of the receptor depends only on the glutamate concentration. In this model, NR1/NR2A-NMDAR and NR1/NR2B-NMDAR share the same activation schemes but with different reaction rate constants (Table 3.2), which allows us to investigate the effects of the different types of NMDAR. This eight-state kinetic scheme incorporates separate binding steps of two glutamate molecules, two desensitised states (D1 and D2) and two conformational change stages (RA2f and RA2s) before opening (O). Channel opening requires both faster and slower conformational changes in the NR1 and NR2

subunits, respectively. These two transition processes are independent and can happen in any order. The dynamics of this kinetic scheme is simulated by seven ODEs (see Appendix E.2). Therefore, by solving the ODEs, the open fraction of a single NMDAR, $Po_{NMDAR}(t)$, is calculated from the fraction of NMDARs at state O and at time t.

3.1.2.3 Kinetic model of AMPAR

The dynamics of a single AMPAR is simulated by a seven-state model (Figure 3.4 B) (Jonas, Major et al. 1993). This model contains binding states of one and two glutamate molecules (R_AG and R_AG_2), the open state (O_A), and their corresponding desensitised states (D_1, D_2, D_o). We apply the same simulation procedure as for the NMDAR dynamic simulation to obtain the open fraction of AMPAR, $Po_{AMPAR}(t)$, by solving six ODEs (see Appendix E.3).

3.1.2.4 Differential contribution of AMPAR and NMDAR in Ca^{2+} signalling

NMDAR is the major Ca^{2+} channel on the neuron membrane that contributes to the Ca^{2+} influx from the extracellular space during the synaptic activation in CA1 pyramidal neurons (Bloodgood and Sabatini 2007). The full opening of a NMDAR depends on both the ligand concentration and the membrane voltage. In this section we discuss the ligand concentration-dependent property of NMDARs. Modelling of the voltage-dependent property of NMDAR is presented in Section 3.1.4. Experimental evidence shows that AMPAR has a low Ca^{2+} ion permeability (Tempia, Kano et al. 1996), thus, we have not included AMPAR as a Ca^{2+} channel. However, AMPAR indirectly mediated the Ca^{2+} dynamics leading to membrane depolarisation after activation. This will remove the Mg^{2+} blockage of NMDARs, as well as activate the voltage-dependent Ca^{2+} channels (VDCCs) on the membrane, and allow extracellular Ca^{2+} ions to enter into the neuron.

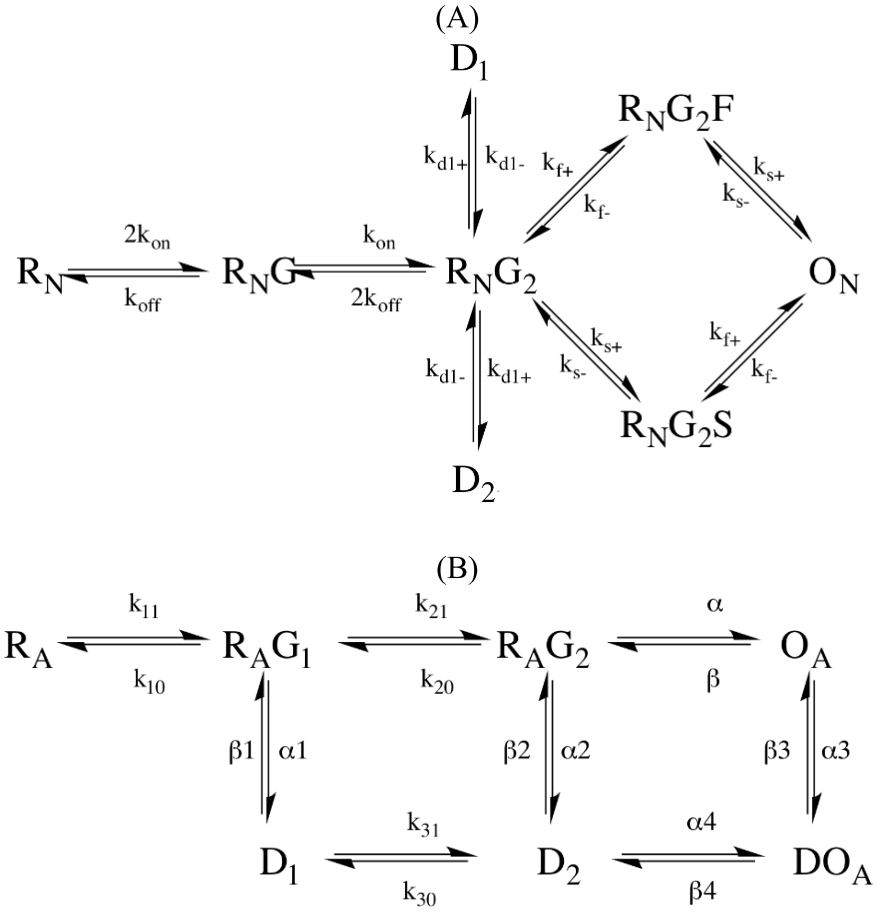

Figure 3.4. Markov kinetic scheme of (A) NMDAR and (B) AMPAR. The kinetic rate constants are listed in Table 3.2.

Table 3.2. NMDAR and AMPAR parameters

Receptor type	Location	Number	Reference
NR1/NR2A–NMDAR	PSD (sNR2A-NMDAR)	12	(Cheng, Hoogenraad et al. 2006, Harris and Pettit 2007, Chua, Kindler et al. 2010)
	Perisynaptic site	0	
	Extrasynaptic site	0	
NR1/NR2B-NMDAR	PSD (sNR2B-NMDAR)	8	
	Perisynaptic site (pNR2B-NMDAR)	3	
	Extrasynaptic site (pNR2b-NMDAR)	8	
AMPAR	PSD (sAMPAR)	85 receptors	
	Extrasynaptic site (eAMPAR)	20 receptors/μm^2	(Tanaka, Matsuzaki et al. 2005)
Receptor type	**Reaction rate constants**	**Value**	**Reference**
NR2A–NMDARs (20-24 °C)	k_{on}	0.0316 $\mu M^{-1} ms^{-1}$	(Erreger, Dravid et al. 2005)
	k_{off}	1.01 ms^{-1}	
	k_{d1+}	0.0851 ms^{-1}	
	k_{d1-}	0.0297 ms^{-1}	
	k_{d2+}	0.23 ms^{-1}	
	k_{d2-}	0.00101 ms^{-1}	
	k_{f+}	0.230 ms^{-1}	
	k_{f-}	0.178 ms^{-1}	
	k_{s+}	3.140 ms^{-1}	
	k_{s-}	0.174 ms^{-1}	
NR2B–NMDARs (20-24 °C)	k_{on}	0.00283 $\mu M^{-1} ms^{-1}$	
	k_{off}	0.0381 ms^{-1}	
	k_{d1+}	0.550 ms^{-1}	
	k_{d1-}	0.0814 ms^{-1}	
	k_{d2+}	0.112 ms^{-1}	
	k_{d2-}	0.00091ms^{-1}	
	k_{f+}	0.048 ms^{-1}	
	k_{f-}	0.23 ms^{-1}	
	k_{s+}	2.836 ms^{-1}	
	k_{s-}	0.175 ms^{-1}	
AMPAR (22 °C)	k_{11}	0.00459 $\mu M^{-1} ms^{-1}$	(Jonas, Major et al. 1993)
	k_{10}	4.26 ms^{-1}	
	k_{21}	0.0284 $\mu M^{-1} ms^{-1}$	
	k_{20}	3.26 ms^{-1}	
	k_{31}	0.00127 $\mu M^{-1} ms^{-1}$	
	k_{30}	0.0457 ms^{-1}	
	α	4.24 ms^{-1}	
	β	0.9 ms^{-1}	
	α_1	2.89 ms^{-1}	
	β_1	0.0392 ms^{-1}	
	α_2	0.172 ms^{-1}	
	β_2	0.000727 ms^{-1}	
	α_3	0.0177 ms^{-1}	
	β_3	0.004 ms^{-1}	
	α_4	0.0168 ms^{-1}	
	β_4	0.1904	

3.1.3 Membrane potential

The removal of the Mg^{2+} blockage of NMDARs and the activation of VDCC depends on the membrane depolarisation after stimulation. We build an electrical model (Figure 3.5) of a single spine and its adjacent dendritic shaft to capture the dynamics of the membrane potential. We construct the electrical model based on the morphological features, as described in Section 3.1.1.

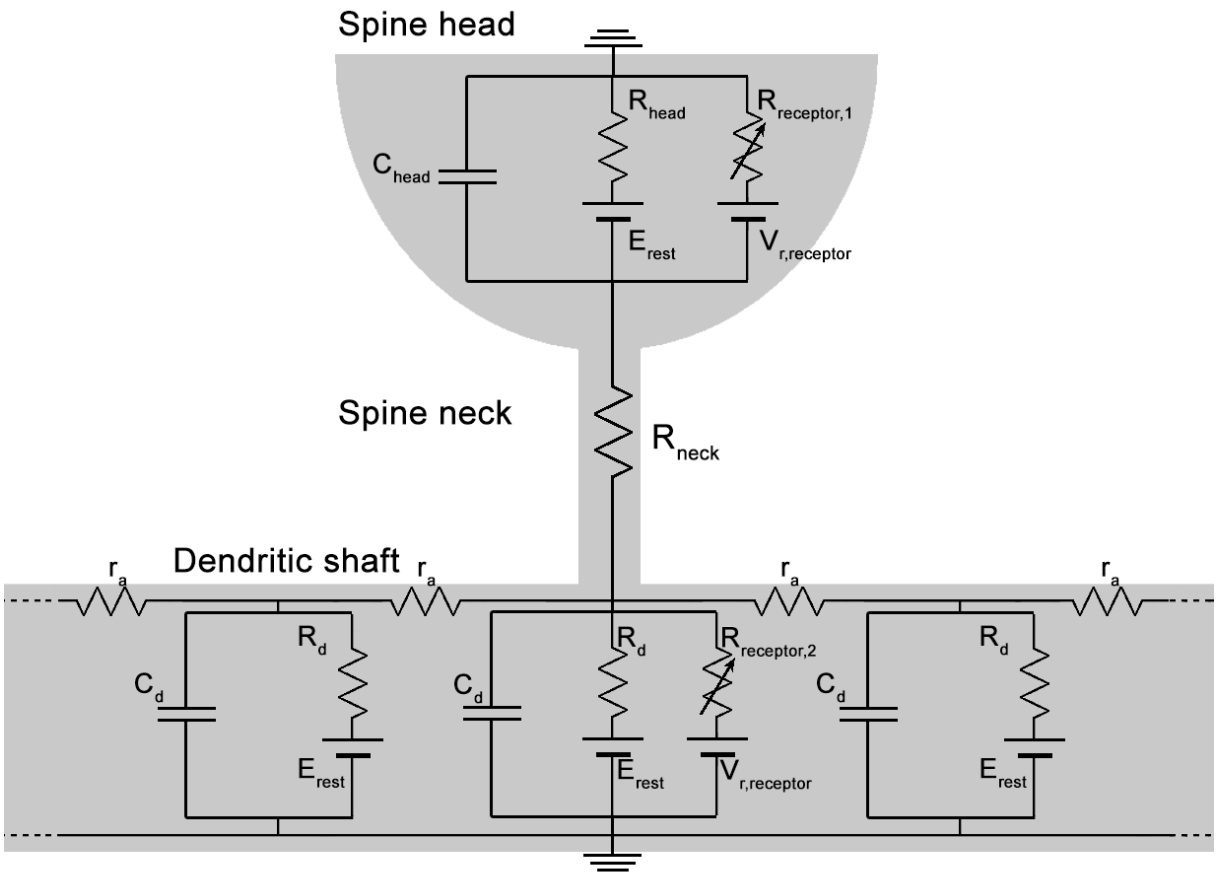

Figure 3.5. Passive electrical model of a dendritic spine and the adjacent dendritic shaft of a CA1 pyramidal neuron. The spine head and dendritic shaft are modelled as separate compartments, with membrane capacitances, C_{head} and C_d, and resistances, R_{head} and R_d, respectively. $R_{receptor,1}$ and $R_{receptor,2}$ are the resistance of receptors in the membrane of the spine head and the dendritic shaft, respectively. The spine head and dendritic compartments are connected by the spine neck, with neck resistance, R_{neck}.. The dendritic shaft is modelled as a series of identical cylindrical compartments. The resting potential, E_{rest}, is assumed to be the same in all compartments (E_{rest} =-70 mV).

3.1.3.1 Spine head and spine neck

The spine head is modelled as an isopotential hemispherical compartment. Its membrane capacitance and resistance can be calculated by its surface area (A_{head}), the specific membrane resistance (R_m) and the specific capacitance (C_m) (Koch 1998)

$$R_{head} = \frac{R_m}{A_{head}}, and$$

$$C_{head} = C_m A_{head}.$$

Therefore, the postsynaptic membrane potential is

$$C_{head}\frac{dV_{head}}{dx} = \frac{E_{rest} - V_0}{R_{head}} - I_{syn} + I_{receptor,1}, \quad (3.2)$$

where $I_{receptor,1}$ represents the current of receptors on the spine head and I_{syn} represents the current flow through the spine neck. Based on Ohm's law, I_{syn} can be calculated as the voltage drop from the spine head (V_{head}) to the dendrite shaft (V_d) across the spine neck resistance (R_{neck})

$$I_{syn} = \frac{V_{head} - V_d}{R_{neck}}.$$

3.1.3.2 Spine neck resistance

The spine neck is simulated as an electrical cylindrical resistor of length l_{neck} and radius r_{neck}, therefore, its resistance is

$$R_{neck} = R_i l_{neck} \pi r_{neck}^2$$

where R_i is the specific axial resistance (or specific cytoplasmic resistivity). In the CA1 pyramidal neuron, the values of neck length and width range from 0.157 μm to 1.8 μm and 0.059 μm to 0.292 μm, respectively (Sorra and Harris 2000). If we assume a specific axial resistance of R_i=200 Ω cm, the neck resistance ranges from 13.4 MΩ to 330 MΩ. The large resistance of the spine neck between the compartments of the spine head and dendritic shaft determines the decrement of the EPSP amplitude from the spine head to its parent dendritic shaft after stimulation. It is suggested that the R_{neck} is negatively correlated to the EPSP amplitude of the dendritic shaft membrane potential after stimulation (Araya, Jiang et al. 2006). Therefore, we calibrate the size of spine neck to generate realistic electrical results

according to the literature (see Section 3.2.2)

3.1.3.3 Dendritic shaft

The dendritic shaft is simulated as a long passive cylinder that is divided into several identical compartments (Sterratt, Graham et al. 2011). Each compartment has a length of λ and a diameter of d. The current can flow between neighbouring compartments, which is expressed as the voltage drop between neighbouring compartments across the axial resistance. Therefore, for compartment, j, its membrane potential ($V_{d,j}$) is

$$C_{d,j}\frac{dV_{d,j}}{dt} = \frac{E_{rest}-V_{d,j}}{R_{d,j}} + \frac{V_{d,j+1}-V_{d,j}}{r_a} - \frac{V_{d,j}-V_{d,j-1}}{r_a} + I_{syn,j} + I_{receptor,2}, \tag{3.3}$$

where $C_{d,j}$, and $R_{d,j}$ are the membrane capacitance and membrane resistance of the dendritic compartments and r_a is the axial resistance between the neighbouring dendritic compartments. They can be calculated from the specific resistances, R_m and R_a, and the size of the compartment. Thus, Eq. (3.3) can be written as

$$\pi d\lambda C_m\frac{dV_{d,j}}{dt} = \frac{E_{rest}-V_{d,j}}{\frac{R_m}{\pi d\lambda}} + \frac{V_{d,j+1}-V_{d,j}}{\frac{R_a}{\pi\left(\frac{d}{2}\right)^2}\lambda} - \frac{V_{d,j}-V_{d,j-1}}{\frac{R_a}{\pi\left(\frac{d}{2}\right)^2}\lambda} + I_{syn,j}I_{receptor,2}.$$

Multiply both sides by $R_m/\pi d\lambda$ and then

$$\tau_m\frac{dV_{d,j}}{dt} = E_{rest} - V_{d,j} + \frac{R_m d}{4R_a}\left(\frac{V_{d,j+1}-2V_{d,j}+V_{d,j}}{\lambda^2}\right) + \frac{R_m}{\pi d\lambda}\left(I_{syn,j}+I_{receptor,2}\right).$$

Let the compartment length $\lambda = \sqrt{\frac{R_m d}{4R_i}}$.

Then

$$\tau_m\frac{dV_{d,j}}{dt} = E_{rest} - V_{d,j} + \left(V_{d,j+1}-2V_{d,j}+V_{d,j}\right) + \sqrt{\frac{4R_m R_i}{\pi^2 d^3}}\left(I_{syn,j}+I_{receptor,2}\right).$$

In the last term, $I_{syn,j}$ is the total input current by the attached spine necks

$$I_{syn,j} = \sigma I_{syn}$$

where σ is the density of the attached spines per compartment. $I_{receptor,2}$ represents the current of the receptors on the dendritic shaft. We assume σ = 1 because we focus on the stimulation on a single dendritic spine rather than the co-activation between neighbouring spines.

In this study, the basal dendrite is represented as a series of cylindrical compartments with sealed ends on both sides. The sealed end boundary condition assumes that the resistance of the compartment is very high; therefore, the exit current flow via the end is negligible. We assume only one spine is attached to the middle point of the dendrite. Therefore, for N dendritic compartments, the change in voltages are

$$\tau_m \frac{dV_{d,1}}{dt} = E_{rest} - V_{d,1} + 2V_{d,2} - 2V_{d,1} + \sqrt{\frac{4\mathrm{R}_m\mathrm{R}_i}{\pi^2 d^3}}\left(I_{syn,j} + I_{receptor,2}\right), \tag{3.4}$$

$$\tau_m \frac{dV_{d,j}}{dt} = E_{rest} - V_{d,j} + \left(V_{d,j+1} - 2V_{d,j} + V_{d,j}\right), j = 2 \ldots N-1, and \tag{3.5}$$

$$\tau_m \frac{dV_{d,N}}{dt} = E_{rest} - V_{d,1} + 2V_{d,N-1} - 2V_{d,N}. \tag{3.6}$$

3.1.3.4 Receptor current

The total input current of the spine head and the shaft are a summation of the current of both local NMDARs and AMPARS:

$$I_{receptor,1} = I_{NMDAR,PSD} + I_{NMDAR,\text{perisynaptic}} + I_{AMPAR,PSD}, and$$

$$I_{receptor,2} = I_{NMDAR,d} + I_{AMPAR,d}.$$

The receptor current at a specific location i ($\mathrm{I_{NMDAR,i}}$ and $\mathrm{I_{AMPAR,i}}$) is

$$I_{NMDAR,i} = Po_{NMDAR,i} G_{NMDAR,i} B(V_i)\left(V_i - V_{r,NMDAR}\right), and \tag{3.7}$$

$$I_{AMPAR,i} = Po_{AMPAR,i} G_{AMPAR,i}\left(V_i - V_{r,AMPAR}\right), \tag{3.8}$$

where $\mathrm{V_{r,NMDAR}}$and $\mathrm{V_{r,AMPAR}}$ are the reversal potentials for NMDAR and AMPAR, respectively. $\mathrm{Po_{NMDAR,i}}$ and $\mathrm{Po_{AMPAR,i}}$ are the fractions of the NMDARs and AMPARs in the open states at site i, respectively. V_i is the membrane voltage of site i.

$\mathrm{G_{NMDAR,i}}$ and $\mathrm{G_{AMPAR,i}}$ are the maximum conductances for the corresponding type of receptor at site i. These are the conductances when all NMDARs and AMPARs are saturated

$$G_{NMDAR,i} = g_{NMDAR} * N_{NMDAR,i}, and \tag{3.9}$$

$$G_{AMPAR,i} = g_{AMPAR} * N_{AMPAR,i}, \tag{3.10}$$

where $\mathrm{g_{NMDAR}}$ and $\mathrm{g_{AMPAR}}$ are the single channel conductance of NMDARs and AMPARs,

respectively. $N_{NMDAR,i}$and $N_{AMPAR,i}$ are the total NMDAR and AMPAR numbers at site i.

Eq. (3.7), $B(V_i)$ describes the Mg^{2+} blockage of NMDARs under V_i at each time step (Jahr and Stevens 1990)

$$B(V_i) = \frac{1}{1 + \frac{[Mg]}{3.57}\exp(-0.062V_i)}, \tag{3.11}$$

where [Mg] is the extracellular magnesium concentration (1 mM). The values of the parameters in this section are listed in Table 3.3.

Table 3.3. Membrane potential related parameters

Description	Symbol	Value	Reference
Specific resistance	R_m	30 kΩ· cm^2	(Mainen, Carnevale et al. 1996)
Specific capacitance	C_m	1 μF/cm^2	
Specific cytoplasmic resistivity	R_i	100 kΩ· cm	
Membrane time constant	τ_E	$R_m \cdot C_m$	
Resting membrane potential	E_{rest}	-70 mV	(Schiegg, Gerstner et al. 1995)
Single channel conductance of NMDAR	g_{NMDAR}	45 pS (20-24 °C)	(Spruston, Jonas et al. 1995)
Single channel conductance of AMPAR	g_{AMPAR}	10 pS (20-24 °C)	(Spruston, Jonas et al. 1995)
Reversal potentials for NMDAR and AMPAR	$V_{r,NMDAR}$ $V_{r,AMPAR}$	0 mV	(Jahr and Stevens 1990)
Extracellular magnesium concentration	[Mg]	1 mM	(Jahr and Stevens 1990)

3.1.4 Compartmental model of Ca^{2+}dynamics

We construct a four-compartment model to represent a pyramidal neuron dendritic spine and its adjacent dendritic shaft. The four compartments are the PSD, cytosol, spine neck and dendritic shaft (Figure 3.6).The geometry of the spine is consistent with what is described in the diffusion model (Table 3.1). The spine head is assumed to be a hemisphere and is divided into PSD and cytosol compartments. The PSD compartment is a cylinder attached to the postsynaptic membrane and the rest of the spine head is in the cytosol compartment. We assume the volume of the spine head is 0.1 μm^3 (radius = 0.363 μm) and PSD takes 10% of the total volume of the spine head (Harris, Jensen et al. 1992, Ventura and Harris 1999). Therefore, the compartment volumes of PSD and cytosol are 0.01 and 0.09 μm^3, respectively. The radius of PSD is 150 μm and the height of its compartment is calculated from its volume, which is about 0.142 μm. The spine neck is represented as a long thin cylinder, which is coaxial with the spine head. The size of the spine neck is discussed in Section 3.2.2. The dendritic shaft is another cylinder that is attached to the bottom of the spine neck with a radius of 0.5 μm and a length of 1 μm.

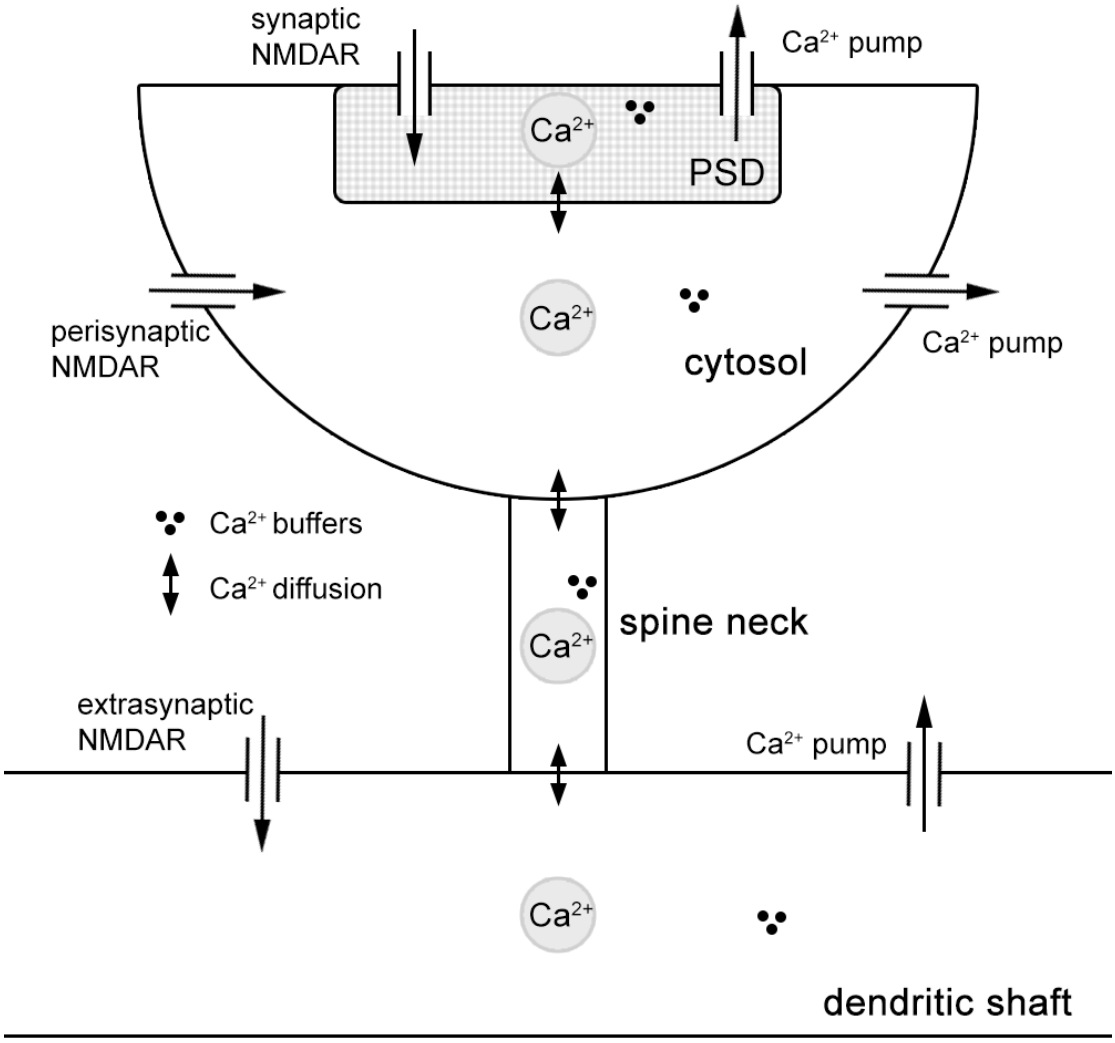

Figure 3.6. Schematic diagram of Ca^{2+} dynamics at the dendritic spine head and its adjacent dendritic shaft, for a CA1 pyramidal neuron. The spine head is divided into two compartments, PSD and cytosol. A thin long spine neck links the spine head to the dendritic shaft, which allows Ca^{2+} to diffuse from the spine head to the dendrite. Ca^{2+} enters the PSD, cytosol and the dendritic shaft via NMDARs and is extruded by Ca^{2+} pumps at all compartments. Ca^{2+} buffers are distributed homogenously within each compartment. Diffusion of Ca^{2+} between compartments is also considered. This schematic diagram does not represent the actual scale of the model.

Extracellular Ca^{2+}ions entering each compartment result from the local membrane Ca^{2+}current that is then buffered by various Ca^{2+} buffer proteins extruded via membrane Ca^{2+} pumps and diffused from the spine head to the dendrite. We assume the molecules are well-mixed in each compartment and only diffusion of Ca^{2+} between the compartments is considered. The Ca^{2+} dynamics in PSD, spine head, spine neck and dendritic shaft are governed by

$$\frac{d[Ca^{2+}]_j}{dt} = J_{I_{Ca},j} + J_{mem,j} + J_{diffusion,j} - J_{buffer,j}, \tag{3.12}$$

where j indicates the compartment index (j=1, PSD; 2, cytosol; 3, spine neck; 4, dendritic shaft). The values of the parameters are in Table 3.4.

3.1.4.1 Ca^{2+}influx by Ca^{2+}current

In Eq. (3.12), $J_{I_{Ca},j}$ is the Ca^{2+} influx by the Ca^{2+} current, mediated by the membrane ionotropic receptors (NMDAR in this study). The Ca^{2+}current at the spine head and dendritic shaft is assumed to be a fixed fraction of the total local input current. The fraction of the Ca^{2+} current in the total cation current through NMDARs is about 10% (Schiegg, Gerstner et al. 1995) whereas, through AMPARs, is about 0.6% (Garaschuk, Schneggenburger et al. 1996). Therefore, the Ca^{2+}influx into the spine head and dendritic shaft is mainly mediated by local NMDARs. We only consider the contribution of AMPARs to the depolarisation of the synaptic membrane and ignore the Ca^{2+} influx via AMPAR in this study. The Ca^{2+}influx via NMDAR is given by

$$J_{NMDAR,i} = -\frac{I_{NMDAR,i}}{Z_{Ca}\, F\, Vol_i}, \tag{3.13}$$

where $I_{NMDAR,i}$ is the NMDAR current calculated in Eq. (3.7), $f_{Ca} = 10\%$ is the fraction of Ca^{2+} current carried by NMDAR (Schiegg, Gerstner et al. 1995), F= 96485.3 C Mol^{-1} is Faraday's constant, $Z_{Ca} = 2$ is the valence of Ca^{2+} ions and Vol_j is the volume of compartment i. $J_{Ca,j}$ is not valid when $j = 3$.

3.1.4.2 VDCCs

VDCCs are located at both the spine head and the dendritic shaft. We calculate the Ca^{2+} current by VDCCs as

$$I_{VDCC,i} = G_{VDCC,i} mh\left(V_i - V_r^{Ca^{2+}}\right),$$

where $G_{VDCC,i}$ and V_i are the maximum conductance of VDCC and membrane potential at site I, respectively. $G_{VDCC,i}$ is estimated in Section 3.2.2. $V_r^{Ca^{2+}}$ is the membrane reversal potential of the Ca^{2+} ions

$$V_r^{Ca^{2+}} = \frac{RT}{Z_{ca}F} ln \frac{Ca_o}{Ca_i}, \tag{3.14}$$

where R is the ideal gas constant, T is the absolute temperature in Kelvin, $Z_{ca}$is the valence of Ca^{2+} and F is the Faraday constant. Ca_o represents the extracellular Ca^{2+} concentration (Ca_o =100 μM) and Ca_i represents the cytosolic Ca^{2+} concentration in compartment i, respectively. $m\ and\ h$ represent the activation and deactivation of VDCC, and they are calculated as

$$\frac{dm}{dt} = (1-m)\alpha_m - m\beta_m, and$$

$$\frac{dh}{dt} = (1-h)\alpha_h - h\beta_h,$$

where

$$\alpha_m = \frac{8.5}{1+\exp\left(-\frac{V_i-8}{12.5}\right)},$$

$$\beta_m = \frac{35}{1+\exp(\frac{V_i+74}{14.5})},$$

$$\alpha_h = \frac{0.0015}{1+\exp(\frac{V_i+29}{8})}, and$$

$$\beta_h = \frac{0.0055}{1+\exp(-\frac{V_m+23}{8})}.$$

3.1.4.3 Ca^{2+} pumps and leakage

We assume there is no ER in the dendritic spine, therefore, Ca^{2+} extrusion from the cytosol of CA1 pyramidal neurons is mainly mediated by two types of membrane pump: the plasma membrane Ca^{2+} ATPase (PMCA) and the sodium Ca^{2+} exchanger (NCX). PMCA has about a 10-fold higher affinity for Ca^{2+} but a lower turnover rate than the NCX. We follow the model

of Schiegg, Gerstner et al. (1995) to simulate Ca^{2+} extrusion using first–order Michaelis-Menten kinetics (see Appendix C.4 for the explanation). They are modelled as

$$J_{mem,j} = -\sum_{n} \frac{A_j}{V_j} Ps_n V_{max,n} \frac{[Ca^{2+}]_j}{[Ca^{2+}]_j + K_{d,n}} + \frac{A_j}{V_j} J_{leak,j}, \tag{3.15}$$

where the maximum pumping velocity of pump $n, (n = 1, PMCA; 2, NCX)$ at compartment, j is calculated by the multiplication of the maximum turnover rates of Ca^{2+} of pump n, $V_{max,n}$, by its surface density, Ps_n, and the ratio of surface area to volume of compartment j, $\frac{A_j}{V_j}$. $K_{d,n}$ is the dissociation constant for pump n. $J_{leak,j}$ is the Ca^{2+} leakage flux via the membrane, which balances the Ca^{2+}concentration at the resting level. The densities of pumps at different locations are difficult to be precisely estimated from experimental data; therefore, we estimate the values of them in Section 3.2.4 using a Markov chain Monte Carlo (MCMC) (see Appendix F.1) from the experimental data (Sabatini, Oertner et al. 2002).

3.1.4.4 Diffusion

We simulate the Ca^{2+} diffusion between compartments using Fick's first law (Sterratt, Graham et al. 2011). The concentration change of Ca^{2+} in compartment j due to diffusion is

$$\begin{aligned} J_{diffusion,j} = -\frac{D_{Ca}}{V_j}\Bigg[& \left(\frac{A}{\delta}\right)_{j,j-1} \left([Ca^{2+}]_j - [Ca^{2+}]_{j-1}\right) \\ & - \left(\frac{A}{\delta}\right)_{j+1,j} \left([Ca^{2+}]_{j+1} - [Ca^{2+}]_j\right)\Bigg], \end{aligned} \tag{3.16}$$

where D_{Ca} is the diffusion coefficient of Ca^{2+}, and V_j is the volume of compartment j.

$\left(\frac{A}{\delta}\right)_{p,q} = \frac{A_{pq}}{\Delta l_{pq}}$ describes the movement of Ca^{2+} ions from compartment p to q,

where A_{pq} is the cross-sectional area of the two compartments and Δl_{pq} is the distance between the midpoints of compartments p and q.

3.1.4.5 Buffering

In each compartment, we include a general form of an endogenous immobile Ca^{2+} buffer protein and two mobile buffer proteins: calbindin (CaD) and calmodulin (CaM).The buffers' capacity for Ca^{2+} decides the shape of the decay in the cytosolic Ca concentration after reaching a peak. The last part in Eq. (3.12) is Ca^{2+} buffering by all types of endogenous

buffers. The concentration of immobile buffer protein in each compartment is estimated in Section 3.2.2. The simulation details of immobile Ca^{2+} buffer, CaD and CaM are in Appendix D.2.

Table 3.4. Parameters for the spine compartment model

Description	Symbol	Value	Reference
Pump affinity (PMCA)	$K_{M,1}$	0.2 μM	(Sabatini, Oertner et al. 2002) (Carafoli 1992, Blaustein and Lederer 1999)
Turnover rate (PMCA)	$V_{max,1}$	100 ms^{-1}(37 °C)	
Pump affinity (NCX)	$K_{M,2}$	20 Mm	
Turnover rate (NCX)	$V_{max,2}$	1000 ms^{-1}(37 °C)	
Ca^{2+} diffusion coefficient	D_{Ca}	0.220 μm^2/ms (20-24 °C)	(Allbritton, Meyer et al. 1992)
Forward rate constant of mobile buffer	k_{bf}	0.176 μM^{-1} ms^{-1}	MCMC estimated
Backward rate constant of mobile buffer	k_{bb}	0.624 ms^{-1}	
Total buffer concentration in compartment *j*	$[B]_{total,j}$	108.78 μM (spine head) 116.97 μM (dendritic shaft)	

3.2 Parameter calibration and estimation

3.2.1 Temperature Coefficient (Q10) corrections

Since most reaction and diffusion rates are affected by the environmental temperature, it is necessary to correct the values of the rate constants in regard to their temperature sensitivity. The temperature coefficient (Q10) measures the degree of temperature dependence when increasing the temperature by 10°C. It is calculated according to

$$Q_{10} = \left(\frac{R_2}{R_1}\right)^{\frac{10}{T_2 - T_1}},$$

where $R_1$and R_2 are the rate constants at temperatures T_1 and T_2 ($T_1 < T_2$), respectively. Therefore, the corrected value, R_{sim}, of a parameter with original value, R_o, from the original temperature T_o to simulation temperature T_{sim} is

$$R_{sim} = \begin{cases} R_o \times Q_{10}^{\frac{T_{sim}-T_o}{10}}, T_{sim} > T_o \\ \frac{R_o}{Q_{10}^{\frac{T_o-T_{sim}}{10}}}, \quad T_{sim} < T_o \end{cases}.$$

The values of Q10 for each type of parameter are listed in Table 3.5. The simulation temperature used in this chapter is 34°C.

Table 3.5. Q10 values for biological processes

Biological processes	**Q10**
Diffusion	1.3
Glutamate transporter kinetics	3
AMPAR kinetics	2.4
AMPAR conductance	1.5
NMDAR kinetics	3
NMDAR conductance	1.6
Pump kinetics	3
Buffer kinetics	2.15
VDCC gating kinetics	3
VDCC conductance	1.5

3.2.2 Resistance

We explore the dependency of the spine neck size on the $EPSP_{spine}$ and the ratio of EPSP at the spine head to the dendrite shaft ($EPSP_{spine}/EPSP_{shaft}$). We vary the length and width of the spine neck in the physiological range (Sorra and Harris 2000) and investigate its effects on the $EPSP_{spine}$ and the $EPSP_{spine}/EPSP_{shaft}$ (Figure 3.7). The results are consistent with the experimental observation that as the increment in spine neck length, the $EPSE_{spine}$ decrement of the EPSP amplitude from the spine head to its parent dendritic shaft increases linearly. The longer spine neck results in a larger resistance and allows more EPSP to stay in the spine head with a higher $EPSP_{peak.}$ In contrast, the spine head EPSP decrement decreases exponentially with the enlargement in the spine width.

(A)

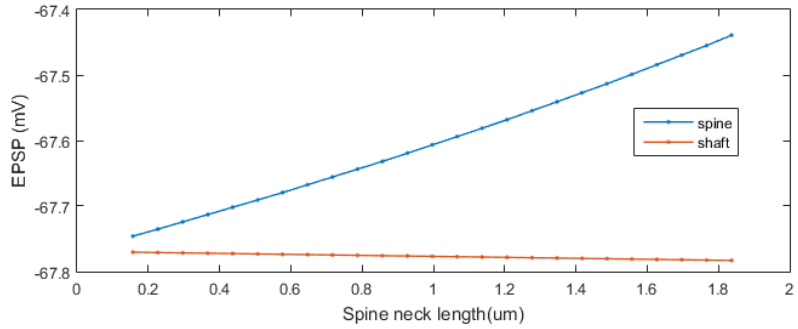

(B)

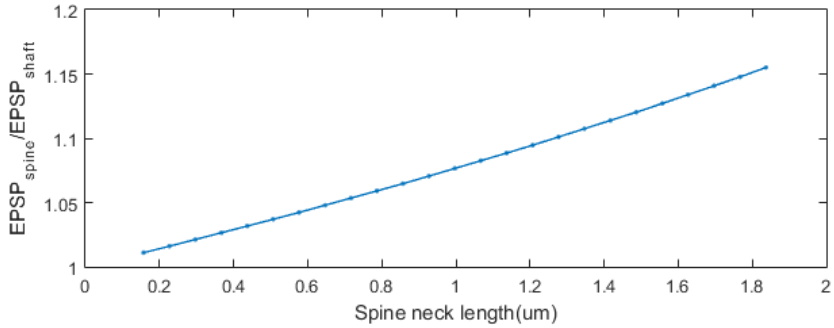

(C)

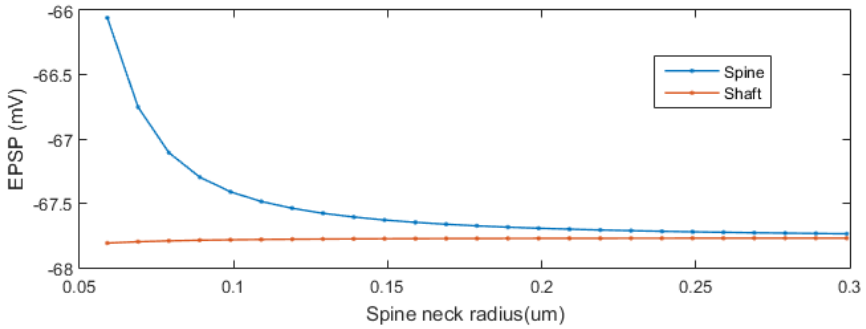

(D)

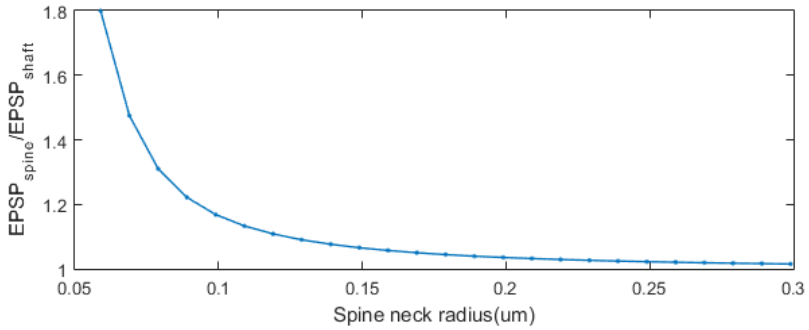

Figure 3.7. Effect of spine neck size on the EPSP amplitude in the spine head and the spine-shaft EPSP ratio. (A) and (B) are simulated by varying the spine neck length from 0.157 to 1.8 µm while fixing the radius to 0.086 µm. (C) and (D) are simulated by varying

the spine neck width from 0.059 to 0.292 µm while fixing the length to 0.689 µm. The model is simulated with a medium AMPAR density in PSD (AMPAR = 42)

3.2.3 Synaptic AMPAR number and spine

Based on experimental observation, we assume the EPSP amplitude at synaptic site is lower than 5 mV after a single synaptic stimulation (Kovalchuk, Eilers et al. 2000, Palmer and Stuart 2009). The EPSP is mainly AMPAR-dependent and partially NMDAR-dependent. Therefore, we adjust the number of AMPARs to generate the expected EPSP amplitude. The range of AMPAR numbers for testing is calculated based on the spine head size and the density of AMPAR (Tanaka, Matsuzaki et al. 2005). It has been reported that the AMPAR density in synaptic site ranges from 874 to 946 receptor per μm^2 in single synapses in the immature cerebellum. The density rage is much wider in the adult cerebellum, 48 to 1210 receptors per μm^2 (Masugi-Tokita, Tarusawa et al. 2007). The area of PSD in this model is 0.07 μm^2 (r = 0.15 µm), which gives a range of AMPAR from three to 86. Figure 3.8 shows the number of AMPARs in PSD versus the $EPSP_{peak}$ at the spine head. The EPSP amplitude increases linearly with the increasing AMPAR density. The simulation is based on R_{neck} =157 MΩ, representing the resistance of a medium sized spine neck of CA1 pyramidal neurons (Sorra and Harris 2000). Therefore, we choose a medium sized spine neck with a radius of 0.05 µm and a length of 0.75 and a large AMPAR density, which gives 85 AMPARs in PSD in this model. It causes an $EPSP_{spine}$ of 4.5 mV and an $EPSP_{shaft}$ of 1.7 mV.

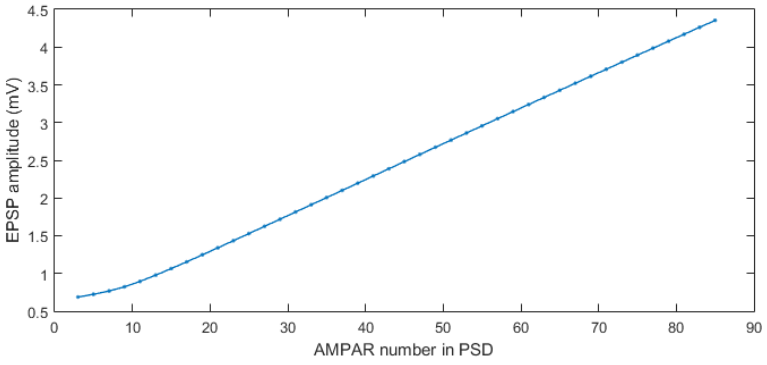

Figure 3.8. AMPAR numbers in PSD positively relate to the EPSP amplitude in the spine head.

3.2.4 VDCC, pump density and endogenous protein concentraintion

The pump densities for VDCC, PMCA and NCX and the concentration, forward/backward reaction rates of the endogenous immobile buffer and its concentration in the dendritic and

spine locations are estimated according to the experimental observations in Sabatini, Oertner et al. (2002). They estimate the Ca^{2+}dynamics at the dendritic spines of the CA1 pyramidal neurons and their parent dendrites by a single bAP in the condition of the absence of exogenous buffer (Ca^{2+} indicator) and the washout of mobile buffers. The results correspond to spines and small dendrites with surface-to-volume ratios of 4-20 μm^{-1} and 1-4 μm^{-1}, respectively. The geometry of our model lies well in these ranges (spine: μm^{-1}; dendrite: μm^{-1}). We choose four target data from the experiment by Sabatini, Oertner et al. (2002): the amplitudes of Ca^{2+} transient ($\Delta[Ca]_{bAP}$) in response to a single bAP in the spine and dendrite, and the corresponding decay time constant τ_{decay} (Table 3.6). All temperature-dependent rate constants are adjusted according to the temperature their experiments are conducted at 34°C (a near-physiological temperature).

The bAP is simulated by injecting potential into the spine head and dendrite compartment of the passive electrical model to generate amplitudes of bAPs 66.4 and 66.7 mV, respectively (Palmer and Stuart 2009). The simulation detail of bAP stimulation is in Appendix G.2. This leads to Ca^{2+} influx via VDCC at the spine head or the dendritic shaft. According to the experimental conditions in the experiment by Sabatini, Oertner et al. (2002), we set the glutamate concentration at the resting level (0.5 mM) to eliminate the NMDAR-dependent Ca^{2+} transient. Therefore, VDCCs provide the only Ca^{2+} source for the elevation of cytosolic Ca^{2+} level during bAP. Under this condition, the mobile buffers are significantly washed out. Therefore, we set the concentration of CaD and CaM in all compartments as zero.

The clearance of cytosolic Ca^{2+} is mediated by the endogenous protein and membrane pumps. The ability of the clearance can be evaluated by measuring the Ca^{2+} decay time constant τ_{decay}. We calculated the value of τ_{decay} according to the experiment of Sabatini, Oertner et al. (2002) by fitting a single exponential to the Ca^{2+} concentration after reaching the peak value and until t = 200 ms. The contribution of PMCA and NCX on Ca^{2+} extrusion in response to a single bAP in the dendritic spine is reported in Scheuss et al. (2006). We use the ratio of the fraction of Ca^{2+} removed by PMCA to NCX ($\frac{[Ca]_{PMCA}}{[Ca]_{NCX}}$) in the spine and dendrites from their research as an additional target data for parameter estimation (Table 3.6).

Table 3.6. Values of target experimental data, means of MCMC samples and with the parameter set with the lowest mean absolute percentage error (MAPE)

Target experimental data	Target value	Mean of MCMC samples	Set with the lowest MAPE
$\Delta[Ca]_{bAP}$ in spine(μM)	1.7 (±0.6)	1.200	1.668
$\Delta[Ca]_{bAP}$ in dendrite(μM)	1.5 (±0.5)	1.248	1.471
τ_{decay} in spine (ms)	12 (±4)	12.8772	11.8580
τ_{decay} in dendrite (ms)	15(±5)	16.4846	14.9430
$\frac{[Ca]_{PMCA}}{[Ca]_{NCX}}$ in spine	1.070	1.0716	0.9213
$\frac{[Ca]_{PMCA}}{[Ca]_{NCX}}$ in dendrite	0.825	0.8064	0.5409
MAPE		0.1097	0.0896

We estimate values of these parameters using the MCMC method (Haario, Laine et al. , Haario, Saksman et al. 2001) (see Appendix F.1). We use the summation of the mean absolute percentage error (MAPE) to measure the goodness of fit

$$M = \sum_{n=1}^{8} \left| \frac{x_n - x_n^t}{x_n} \right|$$

where $x_n$and x_n^t are the stimulated values and target values, respectively. Based on this equation, the MCMC converges to a set of parameter values with a minimum summation of the MAPE. The ranges of parameter (Table 3.7) are selected from the established experimental literature.

The range of VDCC density is calculated from the $\Delta[Ca]_{bAP}$ and τ_{decay} in Sabatini, Oertner et al. (2002), which gives the numbers of Ca^{2+} ions entered via VDCC at compartments the spine head and the dendritic shaft as about 1490-3116 and 13243-26486, respectively.

The means of MCMC samples and the parameter set with the lowest MAPE are listed in the last two columns in Table 3.7. In comparing the simulation results using the mean of MCMC samples and parameter set with the lowest MAPE, the latter shows that $\Delta[Ca]_{bAP}$ in spine and dendrite are closer to the mean of the experimental data and show differences in the amplitudes in Ca^{2+} transients between these two locations (Table 3.6). Therefore, we choose

the parameters with lowest MAPE for our model.

Table 3.7. Parameter ranges for MCMC and the estimated values by MCMC

Parameter	Range for MCMC	Mean of MCMC samples	Set with the lowest MAPE
VDCC density in spine head	2.23 - 4.66 μm^{-2}	3.577 μm^{-2}	3.498 μm^{-2}
VDCC density in shaft	7.29 – 14.57 μm^{-2}	11.106 μm^{-2}	9.855 μm^{-2}
PMCA density in spine head	200 - 2000 μm^{-2}	359.851 μm^{-2}	236.554 μm^{-2}
PMCA density in shaft	200 - 2000 μm^{-2}	577.689 μm^{-2}	296.785 μm^{-2}
NCX density in spine head	10 - 700 μm^{-2}	0.480 μm^{-2}	258.991 μm^{-2}
NCX density in shaft	100 -1000 μm^{-2}	733.058 μm^{-2}	551.426 μm^{-2}
Immobile buffer concentration in spine head	50 - 200 μM	138.069 μM	108.782 μM
Immobile buffer concentration in shaft	50 - 200 μM	142.134 μM	116.966 μM
Forward rate constant of immobile buffer	0.05 – 1 $\mu M^{-1}ms^{-1}$	0.205 $\mu M^{-1}ms^{-1}$	0.176 $\mu M^{-1}ms^{-1}$
Backward rate constant of immobile buffer	0.05 – 1 ms^{-1}	0.569 ms^{-1}	0.624 ms^{-1}

3.3 Model perfomance under healthy conditions

In this section, we simulate the healthy condition/control condition using the values of parameters estimated in Section 3.2. We investigate the model performance in response to presynaptic stimulation (EPSP stimuli; see Appendix G.1 for the detailed explanation) from different aspects: the glutamate profile, the open fraction of receptors at different locations and, consequently, the Ca^{2+} dynamics in the spine head and its parent dendritic shaft.

3.3.1 Glutamate profile and receptor activity

After release from the vesicle, the glutamates diffuse rapidly from the synaptic cleft. This gives a peak concentration of 0.7 mM and a sharp decrease to the resting level of less than 1 ms (Figure 3.9 A left panel). The maximum fractions of receptors opened are 0.37 (sNR2A-NMDAR), 0.044 (sNR2B-NMDAR) and 0.25 (sAMPAR), respectively (Figure 3.9 B top panel). A single EPSP stimulus is too weak to activate receptors at the presisynaptic and extrasynaptic sites (Figure 3.9 B bottom panel) because of the large extrasynaptic volume in comparison with the synaptic cleft, and the long distance between them and the release site. Even for the presynaptic NMDARs, the local glutamate concentration peak is 33 μM (Figure

3.9 A middle panel), which gives a maximum open fraction lower than 0.0025 (Figure 3.9 B bottom left panel).

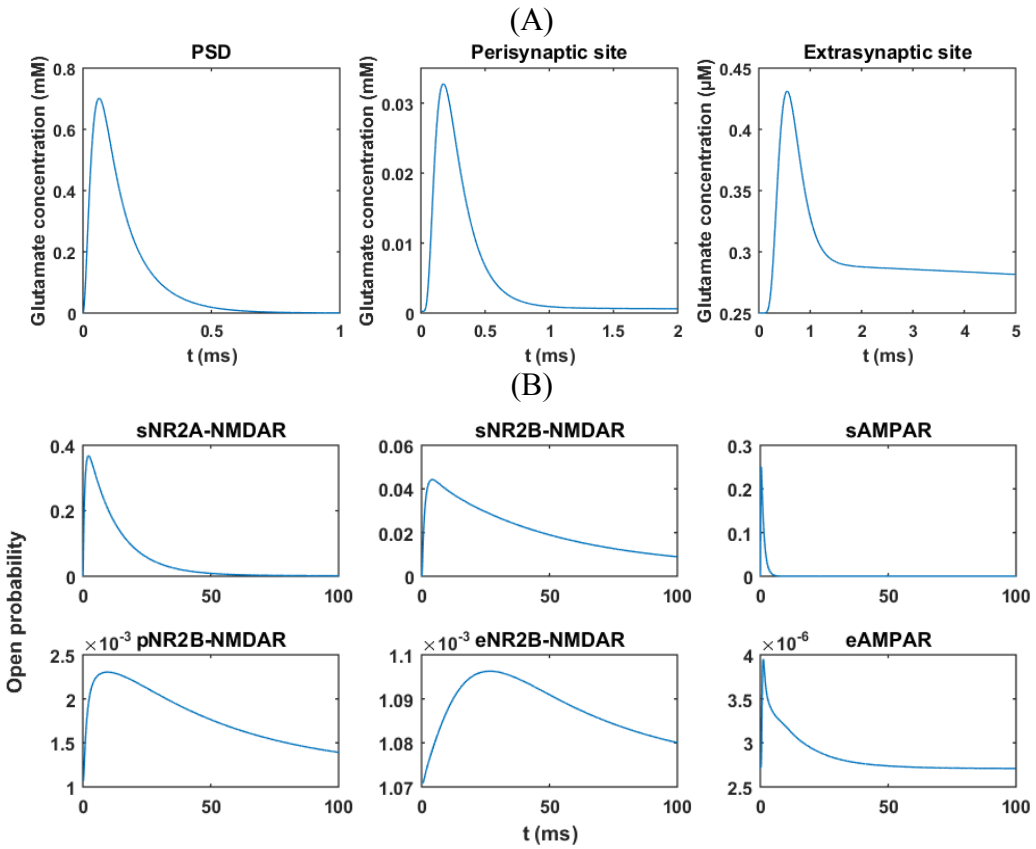

Figure 3.9. (A) Glutamate concentration and (B) receptor response at different locations in response to a single EPSP stimulus under the healthy condition.

3.3.2 Postsynaptic membrane depolarisation

A single EPSP stimulus leads to maximums of 4.5 mV and 1.7 mV depolarisation at the spine head and the dendritic shaft, respectively (Figure 3.10). The depolarisation levels are not strong enough to open more VDCCs than under the resting conditions. The Ca^{2+} influx depends mostly on the opening of NMDARs by depolarisation and the glutamates diffused from the release sites.

3.3.3 Mobile buffer proteins

In Section 3.2, we removed the mobile buffers, CaD and CaM, by setting their concentration

to zero to satisfy the experimental conditions for parameter estimation. Before starting further simulation, we need to return them back to their standard levels (Table 3.4). In response to a single vesicle release event from the presynaptic terminal (a single EPSP stimulus), the Ca^{2+} peak amplitude in the spine head is lower ($\Delta[Ca]_{EPSP} = 0.5\ \mu$M) with a slower decay time in the presence of CaD and CaM than in the absence ($\Delta[Ca]_{EPSP} = 1.8\ \mu$M) (Figure 3.11). A large fraction of free Ca^{2+} ions are removed by the mobile buffers. The value of $\Delta[Ca]_{EPSP}$ lies in the range estimated under experimental conditions (Sterratt, Graham et al. 2011). A single EPSP stimulus limits the effect on cytosolic Ca^{2+} to the spine head only. The change in Ca^{2+} levels in the dendritic shaft is negligible.

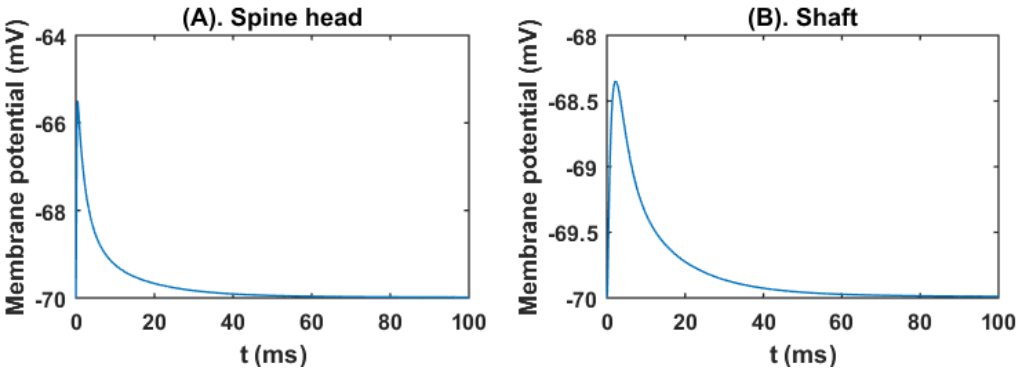

Figure 3.10. Membrane depolarisation by a single EPSP stimulus at (A) the spine head and (B) the dendritic shaft.

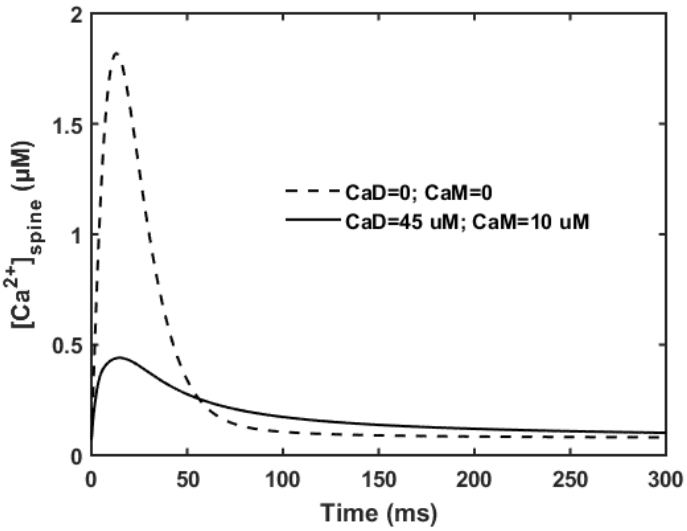

Figure 3.11. Ca^{2+} transient in the spine head in response to a single pulse presynaptic stimulation in the presence and absence of mobile buffers

3.3.4 Multipulse stimulation

We next simulate the model in response to different stimulation patterns: 1 s stimulation in LFS (10 Hz) and HFS (100 Hz) (see Appendix H for the detailed explanation). In both HFS and LFS conditions, glutamate transients at each stimulation pulse are well separated from each other because of the rapid diffusion. The peak concentrations induced by each stimulation are at the same level, with the only exception being at the extrasynaptic site. Under HFS, the peak glutamate concentration at the extrasynaptic site increases as more stimulation pulses arrive and approach a maximum concentration of around 0.47 µM in the HFS condition (Figure 3.12 B right panel).

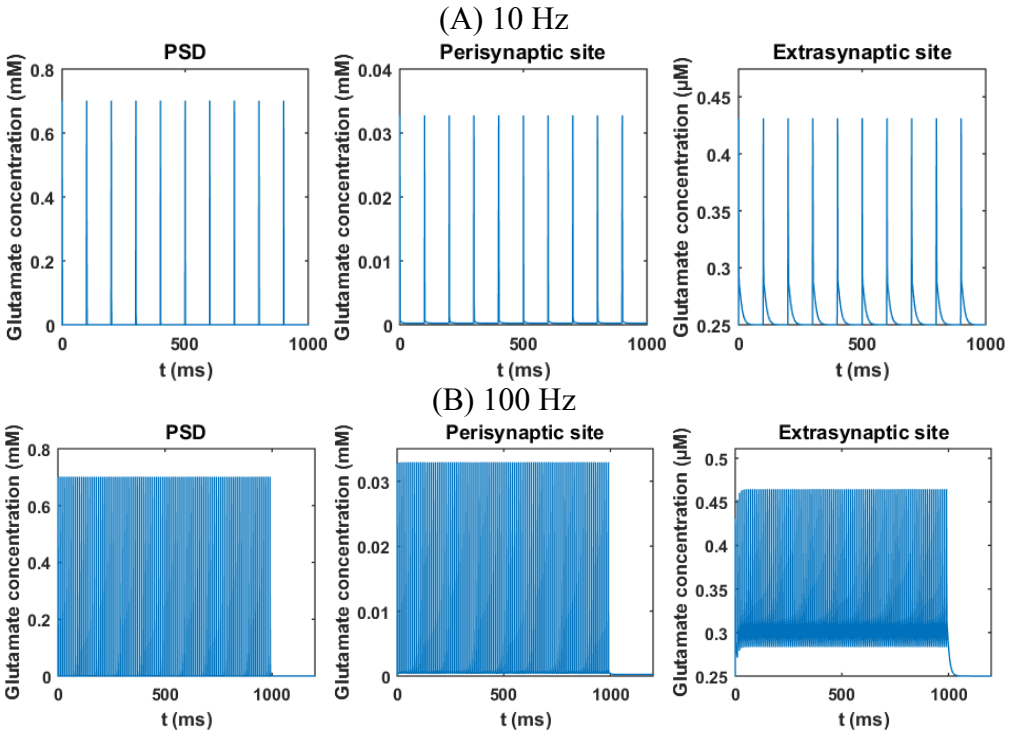

Figure 3.12. Glutamate concentration at different locations in response to (A) 1s of LFS (10 Hz) and (B) 1s of HFS (100 Hz).

The maximum fraction of NMDARs in PSD increases in response to the first few pulses and then decreases to a lower level under both LFS and HFS (Figure 3.13A andd B). The sNR2B-NMDAR shows a faster decrease in amplitude than under LFS and sNR2A-NMDAR. The decrease results in the fast desensitisation of NR2B-NMDAR.

In the perisynaptic and extrasynaptic sites, a higher fraction of NMDARs open as more pulses arrive at the synapse. The maximum fraction and the increase in the peak fraction are higher

in HFS than in LFS, indicating that the temporal summation of HFS allows more glutamate to accumulate after escaping from the synaptic cleft. This leads to a higher open fraction of glutamate receptors; however, it causes a significant increase in receptor desensitisation because of the prolonged exposure to higher levels of glutamate than in the resting level. Consequently, the Ca^{2+} transient in the spine head rises to a maximum of 3 µM after the first seven to eight pulses and decreases to around 1 µM before 400 ms after the start of the stimulation (Figure 3.13A and B).

(A)

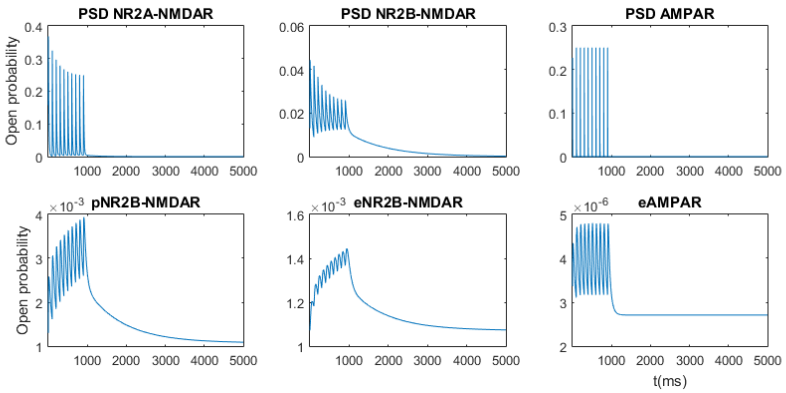

(B)

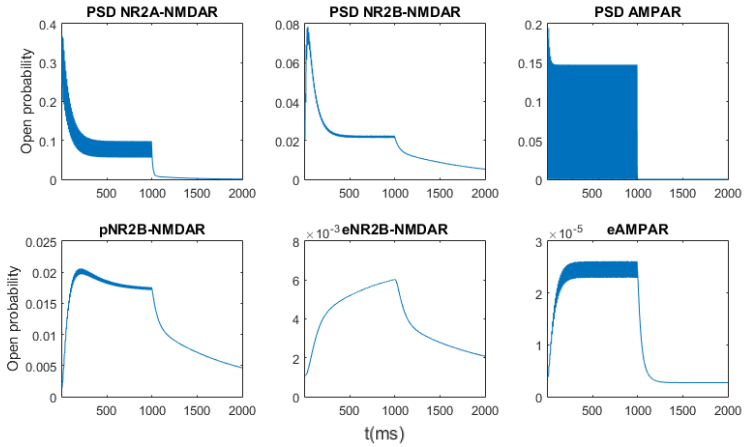

(C)

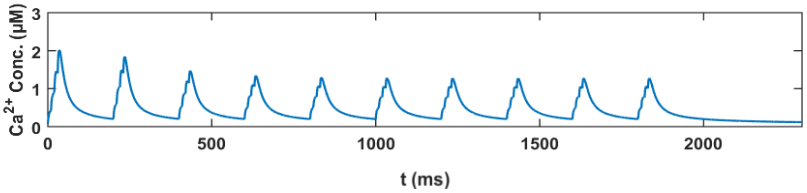

(D)

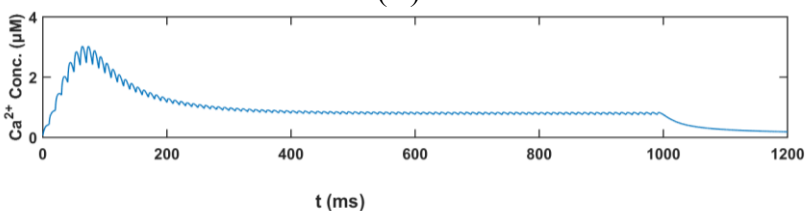

Figure 3.13. States transition of the receptors and Ca^{2+} transient in the spine head in response to 1s of LFS (10 Hz) and 1s of HFS (100 Hz). States transition of the receptors by type and location in response to LFS (A) and HFS (B). The Ca^{2+} ions transient in the spine head are induced by LFS (C) and HFS (D).

3.4 Computational experiments of Aβ-dependent disturbances

In this section, we investigate the Aβ-dependent disturbances on glutamatergic transmission through various computational experiments. We mimic the effects of Aβ on the following aspects individually: glutamate release and diffusion (Section 3.4.1), glutamate receptor distribution (Section 3.4.2). In Section 3.4.3, we investigate these disturbances on a global level to identify the different contributions made by the factors tested in Sections 3.4.1 and 3.4.2. The general procedure in the experiments is

Step 1. We first set a reasonable range for the factor to be tested and pick one value at a time while keeping the other parameters at the standard levels.

Step 2. We run the model for long enough without any stimulation input to reach a steady state, the values of which are used as the initial value for the experiment.

Step 3. For each set of parameters, three types of presynaptic stimulation patterns are used as inputs of the model: (1) a single EPSP stimulus (1 pulse), (2) low frequency stimulation (LHS) at 10 Hz, and (3) high frequency stimulation (HFS) at 100 Hz (see Appendix G.1 for the detailed explanation). All stimulation patterns last for 1 s , thus , there are 1, 10 and 100 pulses for each stimulation pattern, respectively. Simulation stops when the system returns back to the resting levels (initial state).

The major outputs we are collecting after simulation are as follows:

(1) Peak concentration of glutamate ($[Glu]_{peak}$) at the synaptic site, the perisynaptic site and the extrasynaptic site.

(2) The additional time for each receptor staying in the open/desensitised/bound states. We calculate the area under the curve of the fraction of receptors staying in a state against time and deduct the effects of the background fraction at resting level to get the total time in this state from the stimulation applied. The difference between this total time and the one produced from a standard value parameter set is the additional time of the receptor in this state after the change in testing factor.

(3) Additional Ca^{2+} ions entered by each type of NMDAR. The Ca^{2+} current from a NMDAR can be transferred to the Ca^{2+} ion influx by the following equation:

$$Ca^{2+}ion = -\frac{I_{ca^{2+}}(t)}{Z_{Ca}\ C},$$

where $I_{ca^{2+}}(t)$ is the Ca^{2+} current at time t, Z_{Ca}=2 is the valence of the Ca^{2+} ion and C = 6.24e18, where 1 C = 1 A ×1 s. We calculate the area under the curve of Ca^{2+} ion influx against time and deduct the effects of the background influx rate at resting level to get the total Ca^{2+} ions entered by the stimulation applied. Then, the difference between this total Ca^{2+} ions numbers and the one produced with a standard value parameter set is the additional number of Ca^{2+} ions entered through this type of receptor by the change in the factor tested.

(4) Peak amplitude of intracellular Ca^{2+} transient ($[Ca^{2+}]_{peak}$) and peak amplitude of membrane depolarisation (V_{peak}) in the spine head and dendritic shaft, respectively.

(5) Dynamics of the intracellular $Ca^{2+}$and membrane potential in the spine head and dendritic shaft, respectively.

3.4.1 Aβ-dependent disturbance on glutamate transmission

Experimental evidence suggests that the presence of Aβ may lead to an increase in the extrasynaptic glutamate levels by promoting the release of glutamate vesicles from the presynaptic terminal (Abramov, Dolev et al. 2009) inhibiting the glutamate uptake by glial glutamate transporters (Sheldon and Robinson 2007, Matos, Augusto et al. 2008), or inducing glutamate release from ambient astrocytes (Talantova, Sanz-Blasco et al. 2013). In this section, we investigate these disturbances one by one.

3.4.1.1 Increase in presynaptic release of glutamate

In this model, the number of vesicles per release is represented by the total number of glutamate molecules in the model. We vary the number of glutamates per release from 500 to 10000 and keep other parameters at the standard values. Because of the fast diffusion of glutamate in synaptic cleft and the extrasynaptic space, HFS shows no or minor (at extrasynatpic site) additive impacts on the $[Glu]_{peak}$. The $[Glu]_{peak}$ after a single pulse stimulation, LFS and HFS in three locations all linearly increase with the number of glutamate molecules released (Figure 3.14).

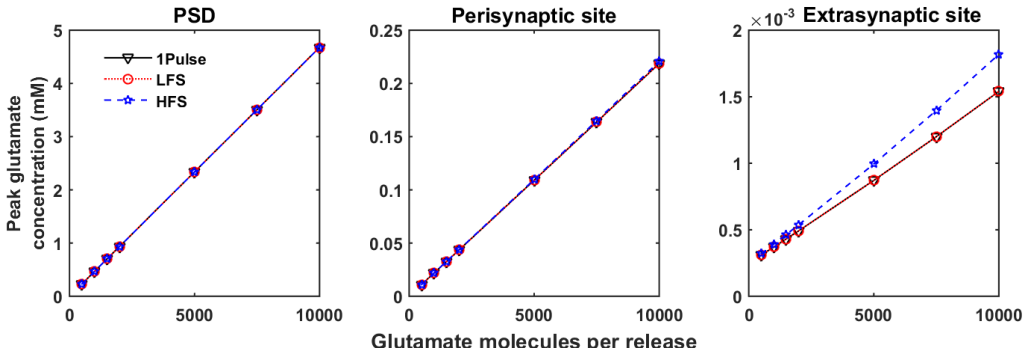

Figure 3.14. Maximum amplitudes of glutamate concentration at different locations with various amounts of glutamate released in response to three types of stimulation patterns.

Multiple vesicle releases have little effect on the transition states of sNR2A-NMDAR (Figure 3.15) and Ca^{2+} influx via it (Figure 3.16 A). For sNR2B-NMDAR, multiple vesicle releases lead to increases in its additional open time, additional desensitised time and additional bound time, however, these effects on its states transition are limited to conditions of a 1 pulse stimulation and LFS (Figure 3.15) and lead to more Ca^{2+} influx under these conditions (Figure 3.16 A). In contrast, the pNR2B-NMDAR shows an increase in additional open time, desensitised time, bound time and entered Ca^{2+} ions in response to all three tested stimulation protocols (Figure 3.15 and Figure 3.16 A). All these increases lead to a higher $[Ca^{2+}]_{peak}$ in the spine head with increasing numbers of glutamate releases (Figure 3.16 B). Especially under HFS, the Ca^{2+} level rises to a peak of about 4.8 μM in 55 ms (almost 3-fold higher than it is under the healthy condition), but then rapidly decreases to less than 1 μM after 35 pulses (350 ms), when increases the glutamate molecules per release to 10,000 (Figure 3.16 C). The decrease rate is positively correlated to the amount of glutamate per release, which is because of the desensitisation of NMDARs. Under multiple vesicle release conditions, each receptor stays longer in the desensitisation state and the increase in additional times of staying in the desensitisation state are more significant in comparison to the ones staying in the open state (Figure 3.15).

The eNR2B-NMDAR is minorly affected by the number of glutamate molecules released in response to the presynaptic stimulation (Figure 3.15 and Figure 3.16 A). This may because that a large fraction of the glutamate molecules released from the presynaptic neuron is uptaken by the glutamate transporters before diffusing to the extrasynaptic site or the long distance between the eNR2B-NMDAR location and the release site. In Figure 3.16 B and C, the elevation in the amplitude of Ca^{2+} transient when large numbers of glutamates are released

is largely a result of Ca^{2+} diffusion from the spine head.

When increasing the number of glutamate per release, sAMPAR but not eAMPAR stays in the open and desensitisation states for longer time under LHS and HFS. The V_{peak} of the spine head and dendritic shaft both increase with the release of the number of glutamate molecules (Figure 3.16 B).The large increase in membrane depolarisation in the dendritic shaft is mainly transferred from the spine head by the spine neck.

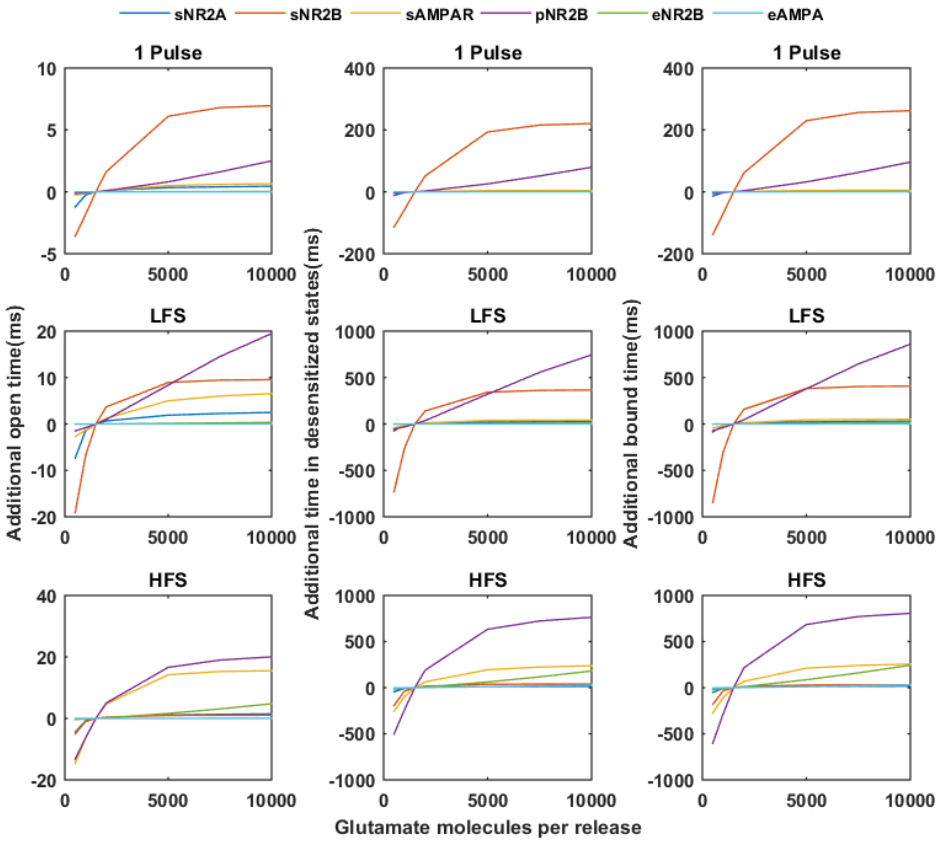

Figure 3.15. Additional times in the open and desensitisation states per receptor in response to various numbers of glutamate releases in comparison with the amount under control conditions (1500 molecules per release). sNR2A: synaptic NR2A-NMDAR; sNR2B: synatpic NR2A; sAMPAR: synaptic AMPAR; pNR2B: perisyantpic NR2B-NMDAR; eNR2B: extrasynaptic NR2B-NMDAR; eAMPAR: extrasynaptic AMPAR.

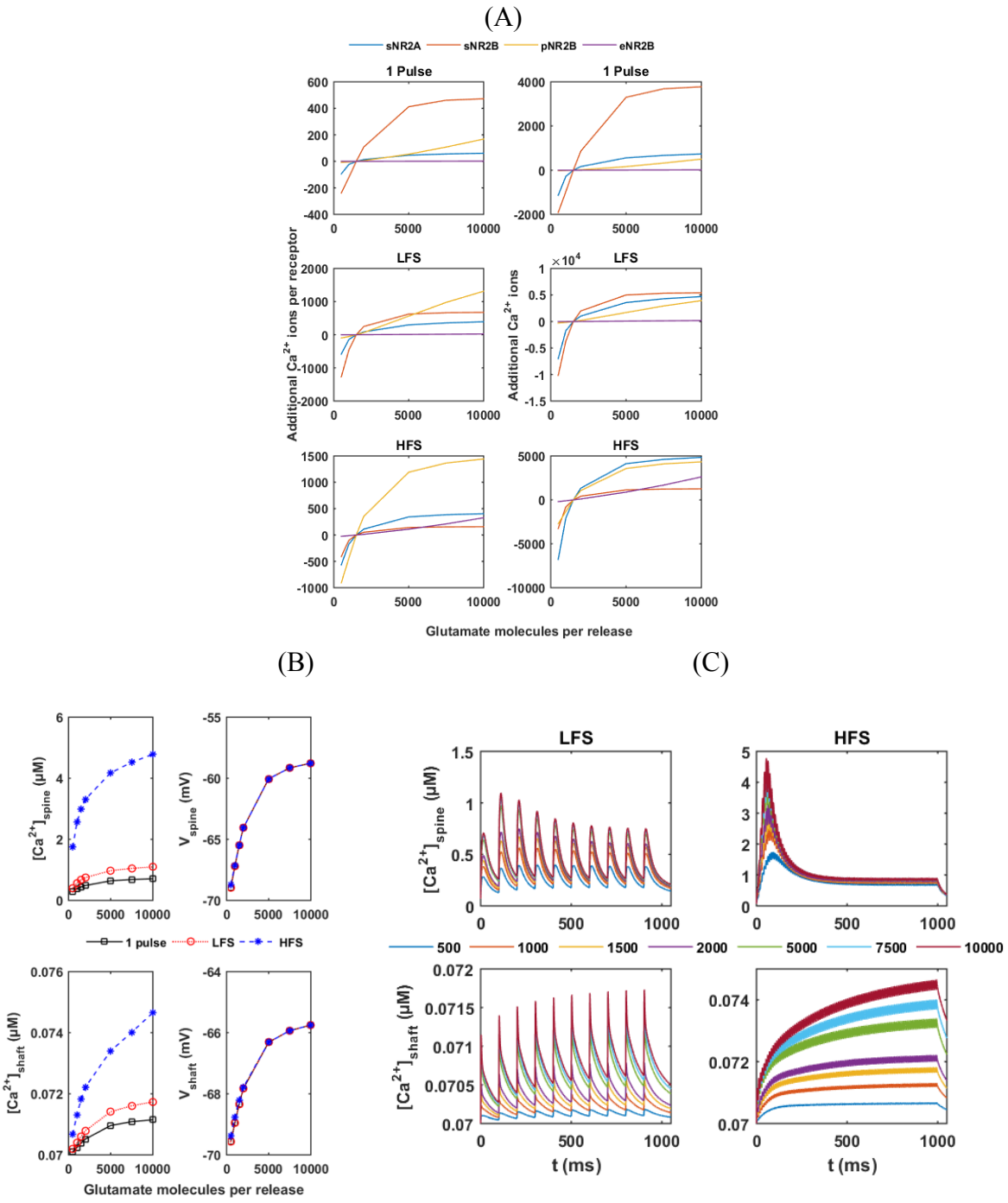

Figure 3.16. (A) Additional numbers of Ca^{2+} ions by NMDARs in response to various numbers of glutamate molecules released compared with the numbers under the standard condition (1500 molecules per release). (B and C) Ca^{2+} ions and the voltage responses in the spine head and dendritic shaft in response to a single pulse stimulation, LFS and HFS by various numbers of glutamate molecules released. sNR2A: synaptic NR2A-NMDAR; sNR2B: synatpic NR2A; pNR2B: perisyantpic NR2B-NMDAR; eNR2B: extrasynaptic NR2B-NMDAR.

3.4.1.2 Inhibition in uptaking extrasynaptic glutamate by the glutamate transporter

Experimental evidence suggests that Aβ may inhibit extrasynaptic glutamate uptake by reducing the number of glutamate transporters or their activities (Harris, Carney et al. 1995, Harris, Wang et al. 1996, Parpura-Gill, Beitz et al. 1997, Fernández-Tomé, Brera et al. 2004, Matos, Augusto et al. 2008. We examine if this down-regulation contributes to the abnormal opening of NMDARs by reducing the concentration of total glutamate transporter concentration (B_{total}) from the standard value of 0.5 mM (0% reduction) to 0 mM (100% reduction) and then running the model under different stimulation patterns.

The results show that there is no effect on the $[Glu]_{peak}$ at the postsynaptic site from reducing B_{total} whereas, when B_{total} = 0 mM (100% reduction), the $[Glu]_{peak}$ at the perisynaptic and extrasynaptic sites increases by about 3 μM and 1.5 μM (Figure 3.17 A), respectively, with slower decay to baseline (Figure 3.17 B). There are relatively minor effects on the transition state of the synaptic receptors in comparison with ones of pNR2B-NMDAR and eNR2B-NMDAR, especially under HFS (Figure 3.18 A). These changes result in no obvious effects on Ca^{2+} dynamics in the spine head but increases in the peaks of Ca^{2+} transient in the dendritic shaft (Figure 3.18 B).

We then increase the glutamate number per release from 1500 to 5000 to investigate if there are any significant changes in multi-vesicle release events by B_{total}. The results are consistent with the single-vesicle release experiment (Figure 3.19), suggesting that the down-regulation in glutamate uptake by glutamate transporters does not directly affect the postsynaptic spine in response to the presynaptic stimulations. Instead, it promotes Ca^{2+} influx via extrasynaptic receptors in the dendritic shaft, especially under HFS.

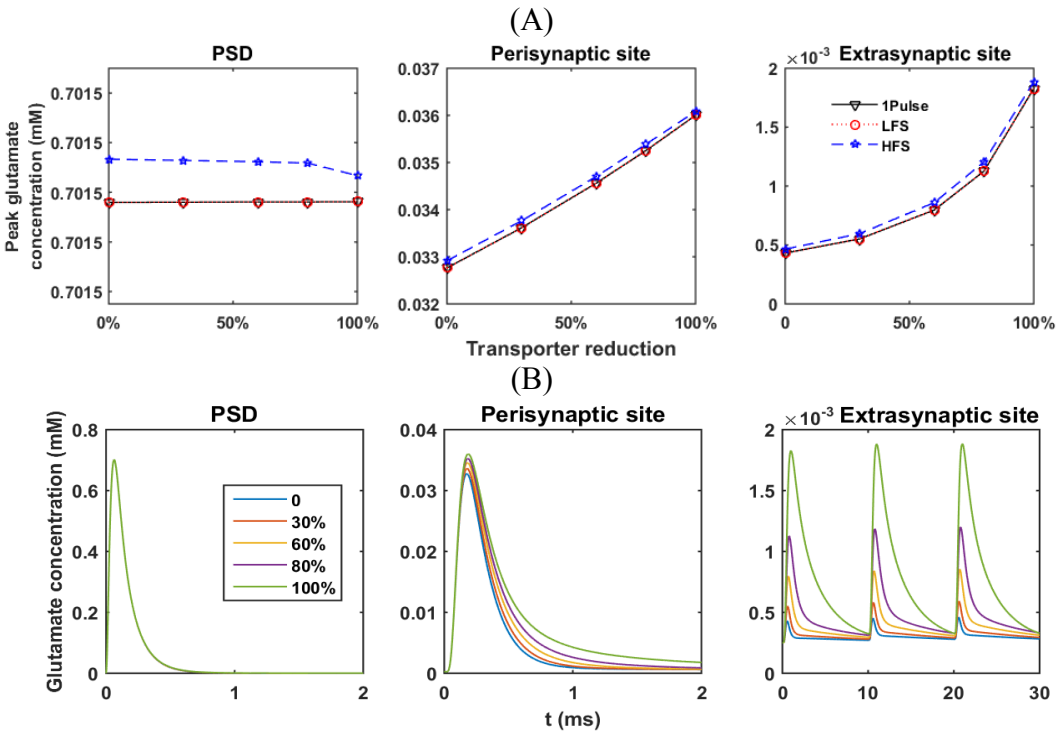

Figure 3.17. (A) Maximum amplitude and (B) time course of glutamate concentration at different locations with the reduction in transporter levels in response to three types of stimulation patterns. The x-axis denotes the degree of reduction in total glutamate transporter concentration (B_{total}) from the standard value, 0.5 mM (0: no reduction; 1: fully reduction and $B_{total} = 0$).

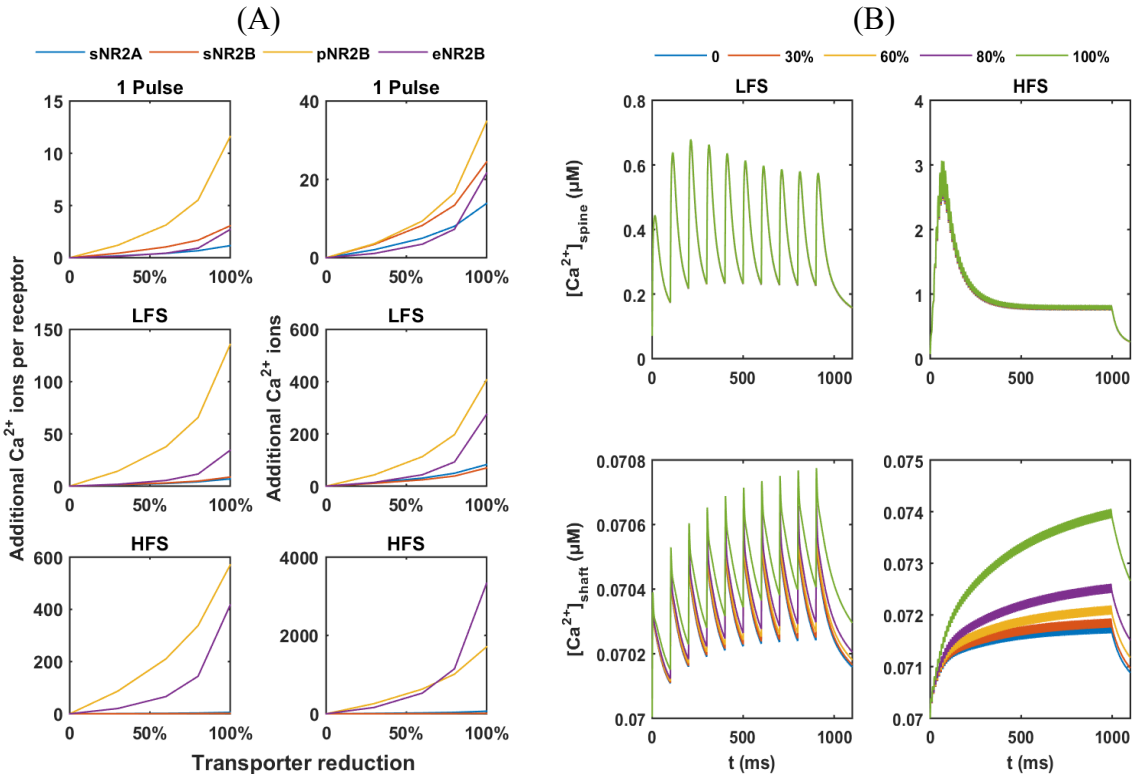

Figure 3.18. (A) Additional numbers of Ca^{2+} ions by NMDARs and (B) Ca^{2+} dynamics in the spine head and dendritic shaft with the reduction in transporter levels in response to three types of stimulation patterns. The glutamate number per release is 1500. sNR2A: synaptic NR2A-NMDAR; sNR2B: synatpic NR2A; pNR2B: perisyantpic NR2B-NMDAR; eNR2B: extrasynaptic NR2B-NMDAR.

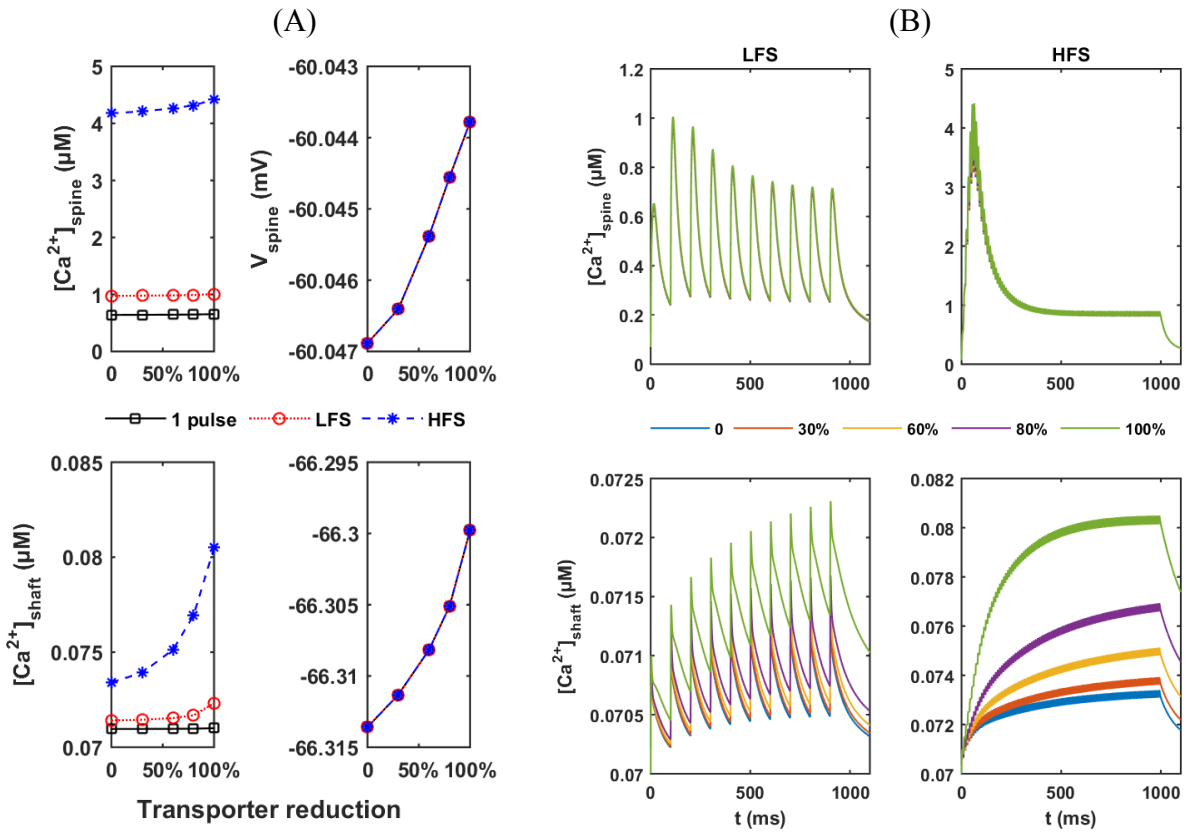

Figure 3.19. (A) Amplitudes of Ca^{2+} and voltage response and (B) Ca^{2+} dynamics in the spine head and dendritic shaft with the reduction in transporter levels in response to three types of stimulation patterns. The glutamate number per release is 5000.

3.4.1.3 Increase in the resting glutamate levels in the extrasynaptic space

Elevation in the resting level of extrasynaptic glutamate ($[Glu]_{rest}$) has been observed in the hippocampus of AD transgenic mice that overexpress human APP (Talantova, Sanz-Blasco et al. 2013). They reported that the resting level of 0.8 μM in 12-month-old mice is in contrast to 0.25 μM in the control ones, and with an even higher level of 3.3 μM in 22 to 24-month-old mice. To examine how the $[Glu]_{rest}$ affects the system, we vary the $[Glu]_{rest}$ from 0.01 μM to 100 μM and run the model for long enough to calculate the fraction of NR2A-NMDAR, NR2B-NMDAR and AMPAR in the open and desensitised bound states, respectively. Both NR2A- and NR2B-NMDAR reach the maximum open fractions (8% and 2%, respectively) when glutamate increases to about 2 μM (Figure 3.20 A). In contrast, the fraction of NR2A-NMDAR and NR2B-NMDAR in the desensitised state approaches a maximum of 81% at the same time (Figure 3.20 B). Only about 10% of receptors are not bound to glutamate (Figure 3.20 C). This may reduce the sensitivity of the postsynaptic neurons in response to stimulation.

The background opening of NR2B-NMDAR by $[Glu]_{rest}$ causes a persistent inward current and Ca^{2+} influx. When increasing the glutamate concentration to 10 μM, the background Ca^{2+} influx reaches the maximum of 580 (NR2A-NMDAR) and 160 (NR2B-NMDAR) Ca^{2+} ions per second, which is 5-10 Ca^{2+} ions per second under control conditions (Figure 3.20 D).

The open fraction of AMPAR is less affected by the elevation of glutamate concentration while its desensitisation fraction increases gradually and when the glutamate reaches a high level greater than 90 μM, it is almost fully desensitised (Figure 3.20 B).

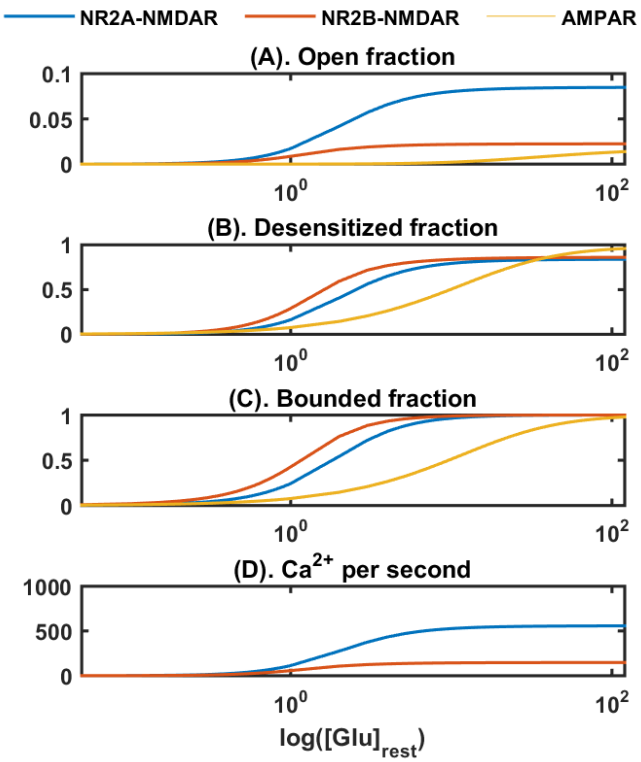

Figure 3.20. Effects of the resting level of extrasynaptic glutamate concentration $[Glu]_{rest}$ on the resting states of NR2A-NMDAR, NR2B-NMDAR and AMPAR. $[Glu]_{rest}$ increases from 0.01 µM to100 µM. Under control conditions $[Glu]_{rest}$ is 0.25 µM.

In the experiment of presynaptic stimulation, the elevation in resting extrasynaptic glutamate concentration increases the desensitisation time of all receptors to different extents while shows neglectable effects on their open time (Figure 3.21 A). In the spine head sNR2A-NMDAR, sNR2B-NMDAR and pNR2B-NMDAR are most affected, in terms of several milliseconds lower open time in comparison to the control conditions. Together with the increase in desensitisation time, especilly for pNR2B-NMDAR, this leads to fewer Ca^{2+} ions entering (Figure 3.21 B) and decreases in the $[Ca^{2+}]_{peak}$ in the spine head (Figure 3.21 C). For the eNR2B-NMDAR, it stays in the states for a longer time by the elevation in $[Glu]_{rest}$ (Figure 3.21 A). The open time of the eNR2B-NMDAR and the number of Ca^{2+} ions entering via it are not affected. In addition, the high level of $[Glu]_{rest}$ results in a high background open fraction of eNR2B-NMDAR and small increases in response to the presynaptic stimulations (Figure 3.22).

(A)

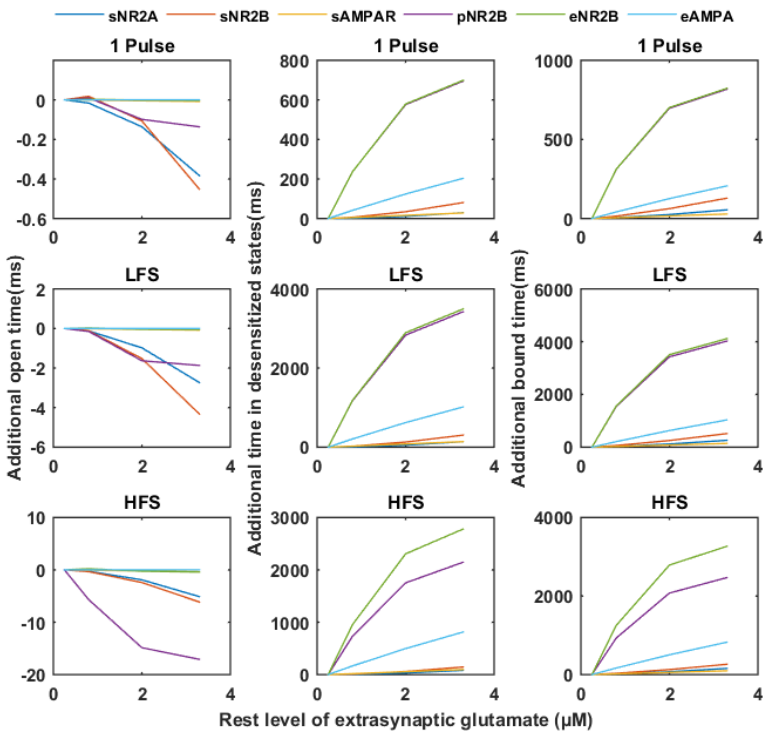

(B) (C)

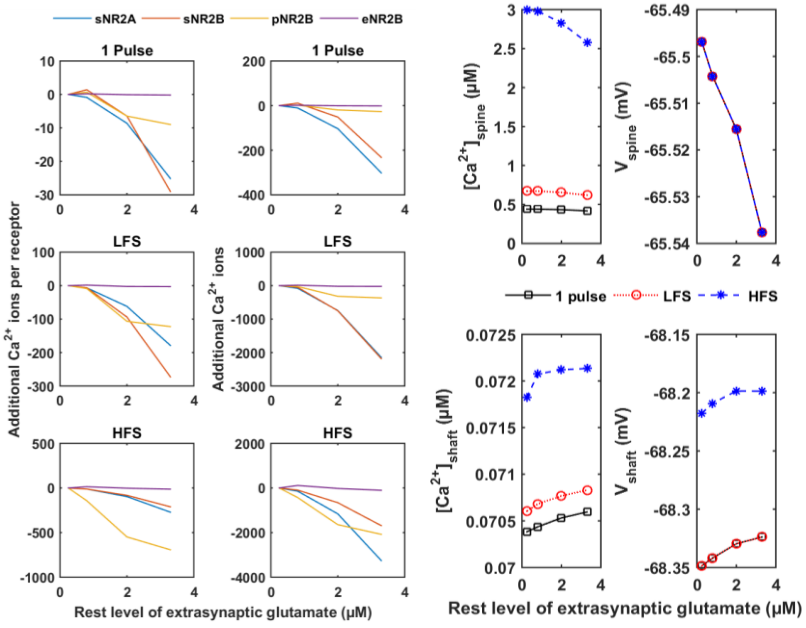

Figure 3.21. (A) Additional times in the open and desensitisation states per receptor and (B) additional numbers of Ca^{2+} ions by NMDARs in response to presynaptic stimulation (a single pulse stimulation, LFS and HFS) under the conditions of the increased resting level of the extrasynaptic glutamate concentration ($[Glu]_{rest}$) in comparison with the amount under standard conditions. (C) Amplitudes of Ca^{2+} and voltage response in the spine head and dendritic shaft at various $[Glu]_{rest}$. sNR2A: synaptic NR2A-NMDAR;

sNR2B: synatpic NR2A; sAMPAR: synaptic AMPAR; pNR2B: perisyantpic NR2B-NMDAR; eNR2B: extrasynaptic NR2B-NMDAR; eAMPAR: extrasynaptic AMPAR.

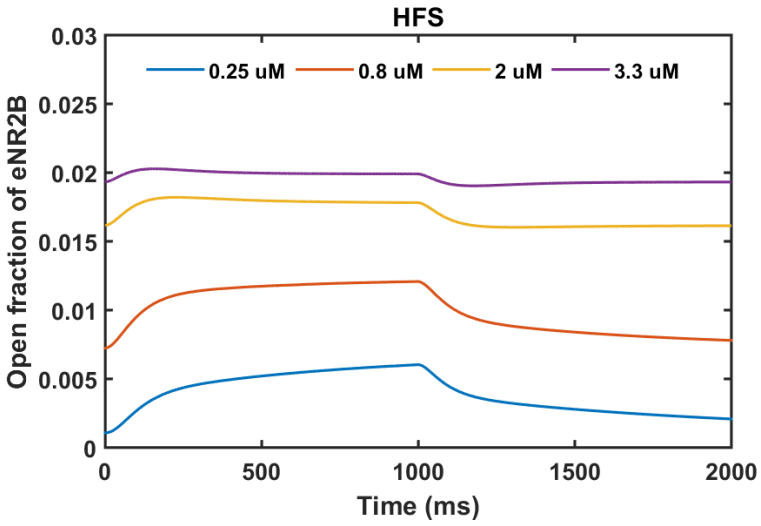

Figure 3.22. The fraction of eNR2B-NMDAR in the open state during simulation under HFS. The resting synaptic glutamate concentrations are 0.25 µM in the control condition (blue line) and 0.8 µM, 2 µM and 3.3 µM, representing the different stages of the disease.

3.4.1.4 Non-synaptic release of glutamate

Aβ has been found to induce glutamate release from astrocytes in AD transgenic mice (Talantova, Sanz-Blasco et al. 2013). The astrocyte stays close to the dendritic spine, which can potentially induce the extrasynaptic glutamate receptors. We simulate the astrocytic release of glutamate by applying a brief pulse of 1 mM glutamate to the extrasynaptic sites where eNR2B-NMDAR and eAMPAR are located. The lengths of the brief pulses are in the range of 1 ms to 20 ms. We assume the [Glu] in the synaptic cleft and presynaptic site will not be affected by this stimulation. The stimulation causes large amounts of Ca^{2+} to enter (Figure 3.23 B), which is increased with the length of the stimulation pulse. The Δ $[Ca^{2+}]$ in the dendritic shaft ranges from 13 to 17 nM and is not significantly increased by the longer stimulation (Figure 3.23 C). This is because the volume of the dendritic shaft is about 0.79 μm^3 in this model, about 8-fold the spine head volume, whereas the low number of eNR2B-NMDA is similar to the dendritic ones. The Ca^{2+} ions entered are largely diluted by the volume, therefore the $[Ca^{2+}]_{peak}$ is much less than in the spine head in response to the presynaptic stimulation. Moreover, the eAMPAR activated by the astrocytic glutamate release creates a 4 - 6 mV depolarisation (Figure 3.23 D). Because of the lower density of AMPAR in

the extrasynaptic site (20 receptor/μm^2) than in synaptic location (up to 1000 receptor/μm^2), even when increasing the stimulation time to 20 ms, it still fails to create a larger depolarisation to activate other voltage-dependent Ca^{2+} channels on the dendritic shaft membrane.

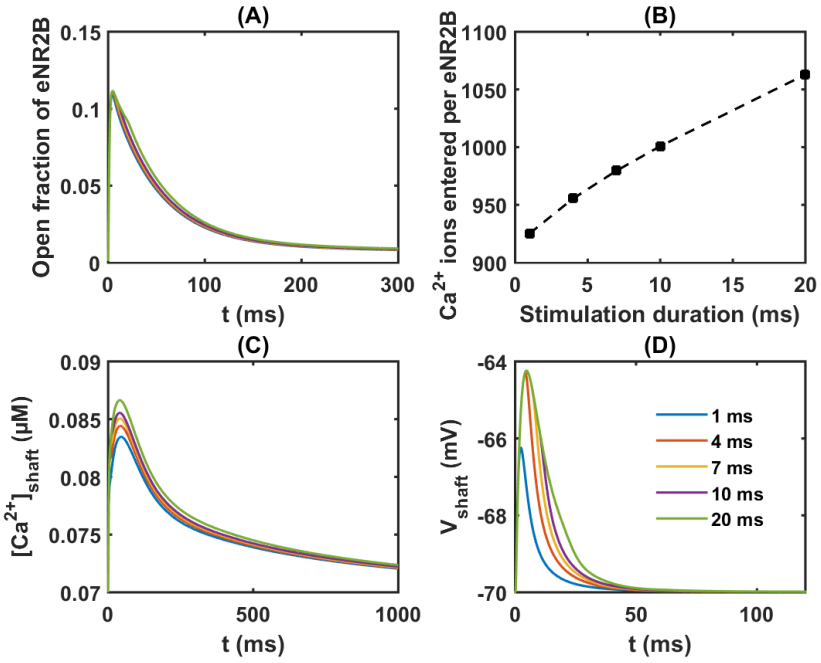

Figure 3.23 Effects of eNR2B-NMDAR activation by the astrocytic release of glutamate. In response a pulse of 1 mM glutamate with various time durations (1 ms, 4 ms, 7 ms, 10 ms and 20 ms). The fraction of eNR2B-NMDAR opens (A) and allows Ca^{2+} ions to enter the dendritic shaft (B). The corresponding Ca^{2+} transient and membrane depolarisations are shown in (C) and (D), respectively.

3.4.2 Receptors

3.4.2.1 Reduction in surface expression of NMDAR and AMPAR

To investigate the inhibition of Aβ on the membrane surface expression of different types of receptors, we decrease the number of each receptor from the standard value to zero to mimic the degree of reduction in their surface expression.

The reduction in sNR2A-NMDAR numbers shows negligible effects on the Ca^{2+} transient amplitude under a 1 pulse stimulus and LFS whereas, under HFS, the peak gradually decreases from 3 μM to nearly 0 μM with the increase in the reduction level (Figure 3.24*a*). It also shows minor effects on the depolarisation of the postsynaptic membrane (Figure 3.24*c*,

d). When setting the sNR2A-NMDAR number to zero, it causes about a 0.1 mV decrease in the depolarisation amplitude in comparison to the control conditions. The reduction in sNR2B-NMDAR number only affects the $[Ca^{2+}]_{peak}$ in the spine head under HFS. This is about a 1 µM reduction in the $[Ca^{2+}]_{peak}$ when sNR2B-NMDAR is fully removed (Figure 3.24*e*).

The reduction in sAMPAR number greatly affects the amplitude of the membrane depolarisation both in the spine head and the dendrite shaft. Completely removing the sAMPARs results in about a 5 mV and 2 mV lower V_{peak} in comparison with the control conditions in the spine head and dendritic shaft membrane, respectively (Figure 3.24*l*). In addition, the decrease in sAMPARs will not completely abolish the transient Ca^{2+} but will reduce the peak fractionally (Figure 3.24 *i, j*).

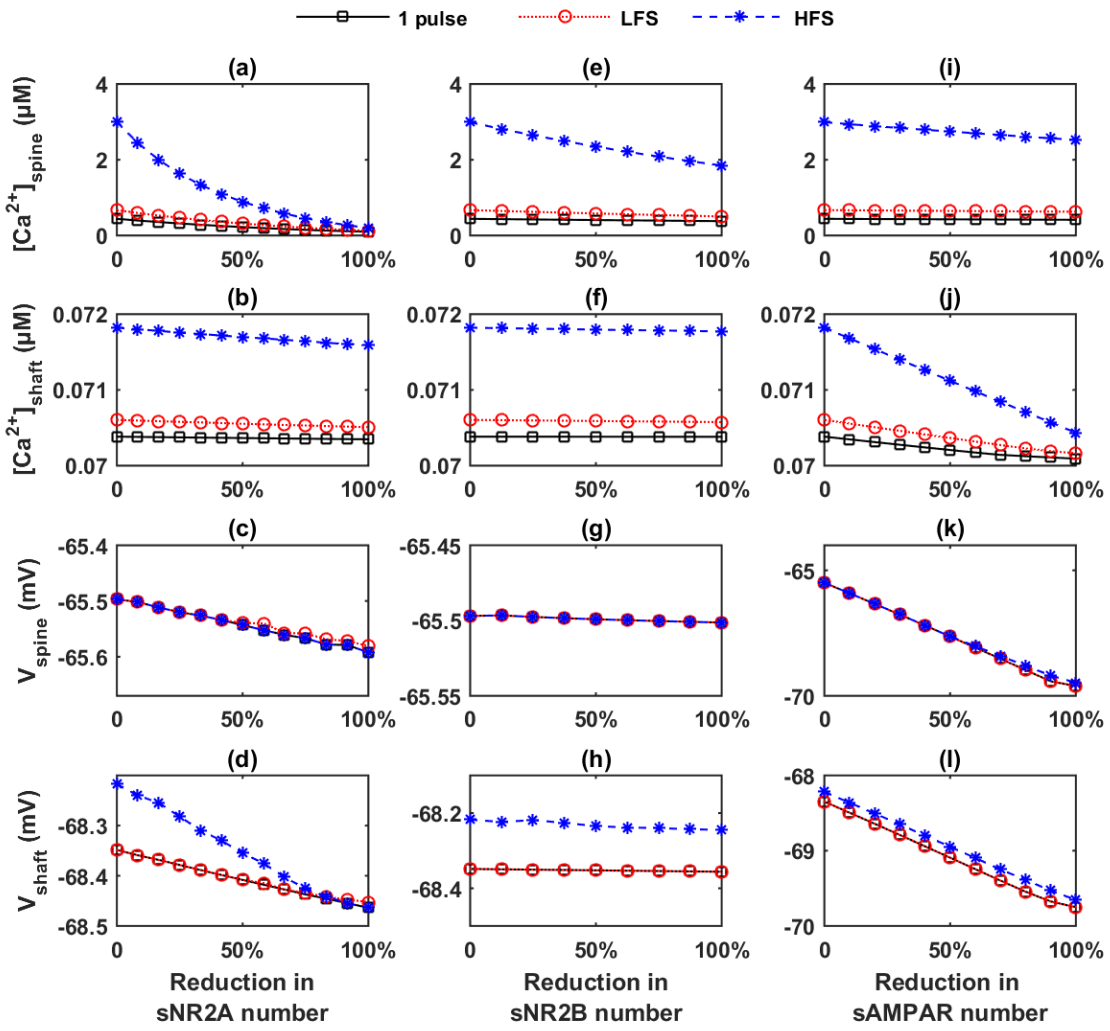

Figure 3.24. Effects of reduction on the number of synaptic glutamate receptors on the amplitudes of Ca^{2+} transient and membrane depolarisation in the spine head and dendrite shaft.

3.4.2.2 Reduction in desensitisation of synaptic receptors

Under healthy conditions, NMDARs undergo desensitisation in response to prolonged presence of their agonists, to prevent excess Ca^{2+} influx (Mayer, Vyklicky et al. 1989). Slowed of NMDAR desensitisation has been observed in transgenic mice that overexpress large amounts of $A\beta_{1-42}$ within neurons (You, Tsutsui et al. 2012). To investigate the inhibition of the desensitisation of synaptic glutamate receptors by Aβ, we decrease the desensitisation related parameters of each receptor by 0% to 100% of the standard value to mimic the degree of inhibition in their desensitisation in response to presynaptic glutamate release.

The inhibition of the desensitisation of sNR2A-NMDAR and sNR2B-NMDAR shows no obvious or minor effects on the on the Ca^{2+} transient and membrane depolarization in the spine head under a 1 pulse stimulus and LFS (Figure 3.25 A (a)-(h), B and C). Under HFS, the peak of Ca^{2+} transient increases significantly from 2.9 μM to 17.9 μM with the increase in the inhibition level of the sNR2A-NMDAR desensitisation (Figure 3.25 A (a)). When the desensitisation of sNR2A-NMDAR is fully inhibited, the cytosolic Ca^{2+} concentration in the spine head maintains at a high level after reaching a peak through the stimulation period (Figure 3.25 B). The inhibition of the sNR2B-NMDAR desensitisation also positively affect the Ca^{2+} transient in the spine head under HFS (Figure 3.25 A (e) and C). It leads to about 2 μM increase in the $[Ca^{2+}]_{peak}$ when the sNR2B-NMDAR desensitisation is fully inhibited. However, cytosolic Ca^{2+} concentration fails to maintain at a high level after reaching a peak (Figure 3.25 C). This is because of the desensitisation of sNR2A-NMDAR.

The inhibition of the sAMPAR desensitisation has minor effects on the $[Ca^{2+}]_{peak}$ (Figure 3.25 A (i) and (j)) and it mainly affects the amplitude of the membrane depolarisation both in the spine head and the dendrite shaft. When its desensitisation is fully inhibited, it results in about a 1-2 mV and 0.5-1 mV increase in the V_{peak} in comparison with the control conditions in the spine head and dendritic shaft membrane, respectively (Figure 3.25 A (k) and (l)).

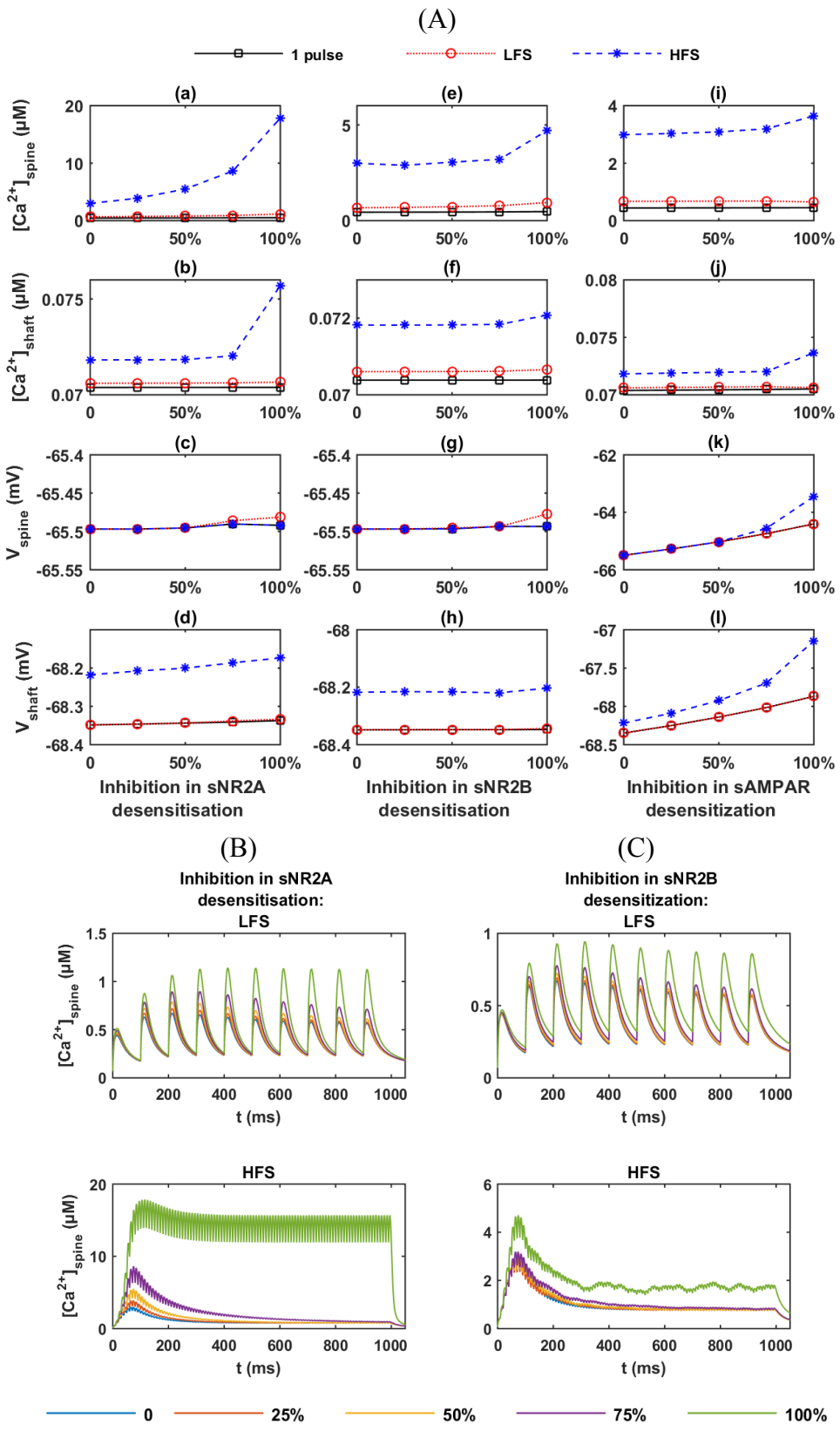

Figure 3.25. (A) Effects of inhibition of the desensitisation of synaptic glutamate receptors on the amplitudes of Ca^{2+} transient and membrane depolarisation in the spine head and dendrite shaft. The Ca^{2+} time course in the spine head under LFS and HFS, with the desensitisation inhibition of sNR2A-NMDAR (B) and sNR2B-NMDAR (C), respectively.

3.4.3 Global sensitivity analysis

Aβ is proposed to disturb the cytosolic Ca^{2+} dynamics through multiple targets. In this section, we study the difference in importance of the various factors globally. We select 15 factors which have been tested in previous sections and eight outputs which represent the postsynaptic neuron response to presynaptic stimulation (Table 3.8). Two thousand perturbed factor sets are generated using Latin hypercube sampling (LHS) (McKay et al., 1979) according the range in Table 3.8. LHS makes sure each factor is evenly distributed in the given range and effectively reduces the correlation among the factors.

We use a partial rank correlation coefficient (PRCC) to identify the most important or sensitive factors (Marino, Hogue et al. 2008). PRCC is useful to measure the nonlinear but monotonic relationships between outputs and parameters (see Appendix F.2 for the explanation). Therefore, the factor ranges are chosen according to Sections 3.4.1 and 3.4.2, to ensure there is not a non-monotonicity relationship between the selected factors and outputs. In each realisation, we run the model with one set from the factor matrix generated by LHS while keeping other parameters at the standard values. Both the LFS and HFS conditions are simulated.

We calculate the PRCC value and the corresponding p-value for each factor against each output using a PRCC Matlab toolbox (Marino, Hogue et al. 2008). PRCC results if its corresponding p-value is greater than 0.05, which fails to reject the null hypothesis that no relationship exists between the factor and the output. The PRCC results are shown in Figure 3.26. Generally, we assume there is a correlation between the factor and the output when the absolute PRCC value is greater than 0.5. Based on this, we modified the results and, therefore, in Figure 3.26, the white colour denotes that there is no correlation between corresponding factor and output.

From the point of view of parameter contributions (read the Figure 3.26 in a vertical direction), all outputs, but not the Ca^{2+} ion number entering through sNR2B-NMDAR, are very sensitive to the amount of presynaptic released glutamate. The correlation levels decrease under HFS in comparison with under LFS, with the only exception being that the Ca^{2+} ion numbers entered through eNR2B-NMDAR show the highest correlation (PRCC = 0.95) with the glutamate release number under both conditions. The resting extrasynaptic glutamate level positively contributes to the Ca^{2+} influx through eNR2B-NMDAR under LFS but not under HFS. The resting extrasynaptic glutamate level negatively contributes to the

Ca^{2+} influx through pNR2B-NMDAR under HFS, suggesting an elevation in $[Glu]_{rest}$ will cause a stronger desensitisation of pNR2B-NMDAR in response to HFS from rather than LFS. Only sNR2A-NMDAR is sensitive to sAMPAR, which infers that only sNR2A-NMDAR, but not NR2A-NMDAR, is sensitive to membrane depolarisation under LFS and HFS. The transporter concentration, desensitisation of eNR2B-NMDAR and the eAMPAR show no relationship with any output, which suggests they are of less importance in the postsynaptic response to presynaptic stimulation while the other NR2B, including NMRDARs, show no relationship with the AMPARs.

From the point of view of output sensitivity (read Figure 3.26 in a horizontal direction), the Ca^{2+} transient in the spine head is most sensitive to sNR2A-NMDAR followed by sNR2B-NMDAR. Under HFS, the importance of sNR2B-NMDAR decreases, which suggests a relatively lower activity of sNR2B-NMDAR in HFS than under LFS. The AMPAR number becomes more important in comparison to LFS, indicating that depolarisation by HFS brings more Ca^{2+} ions into the spine head. The Ca^{2+} transient in the dendritic shaft is mostly sensitive to the amount of glutamate release, while eNR2B is only important under LFS. Surprisingly, it is also sensitive to the sNR2A-NMDAR number. This suggests that under HFS, large amounts of Ca^{2+} ion influx from NR2A, either by the increased release of glutamate numbers and/or activity or numbers of sNR2A-NMDAR, may lead to more ions diffusing to the dendritic shaft. Moreover the membrane depolarisation in the spine head and the dendritic shaft are determined by the glutamate release and sAMPMR numbers, with no dendritic receptor involved. This indicates that the dendritic receptors may be less involved in information transduction under presynaptic stimulation than the synaptic receptors.

Table 3.8. Fifteen factors and eight outputs selected for PRCC. (A) Factors and their biological meaning, standard values and ranges for PRCC; (B) Outputs and their biological meaning for PRCC.

A.

Factor	Biological meaning	Standard value	PRCC ranges
G0	Glutamate number per release	1500	500-10000
Grest	Rest extrasynaptic glutamate concentration	0.25 uM	0 – 1 uM
TP	Glutamate transporter concentration	0.5 mM	0 – 1 uM
Ds2A	Inhibition on desensitisation of sNR2A-NMDAR	0	0-1
Ds2B	Inhibition on desensitisation of sNR2B-NMDAR		
DsAMPAR	Inhibition on desensitisation of sAMPAR		
Dp2B	Inhibition on desensitisation of pNR2B-NMDAR		
De2B	Inhibition on desensitisation of eNR2B-NMDAR		
DeAMPAR	Inhibition on desensitisation of eAMPAR		
sNR2A	sNR2A-NMDAR number	12	6-18
sNR2B	sNR2B-NMDAR number	8	4-12
AMPAR	sAMPAR number	85	43-130
pNR2B	pNR2B-NMDAR number	3	1-5
eNR2B	eNR2B-NMDAR number	8	4-12
eAMPAR	eAMPAR number	20/μm^2	15 – 30 /μm^2

B.

Output	Biological meaning
Ca^{2+} by sNR2A	Ca^{2+} ions entered through of sNR2A-NMDAR
Ca^{2+} by sNR2B	Ca^{2+} ions entered through of sNR2B-NMDAR
Ca^{2+} by pNR2B	Ca^{2+} ions entered through of pNR2B-NMDAR
Ca^{2+} by eNR2B	Ca^{2+} ions entered through of eNR2B-NMDAR
Peak Ca2@spine	Peak concentration of Ca^{2+} transint in spine head
Peak Ca2@shaft	Peak concentration of Ca^{2+} transint in dendritic shaft
PeakB@spine	Peak membrane potential in spine head
PeakB@shaft	Peak membrane potential in dendritic shaft

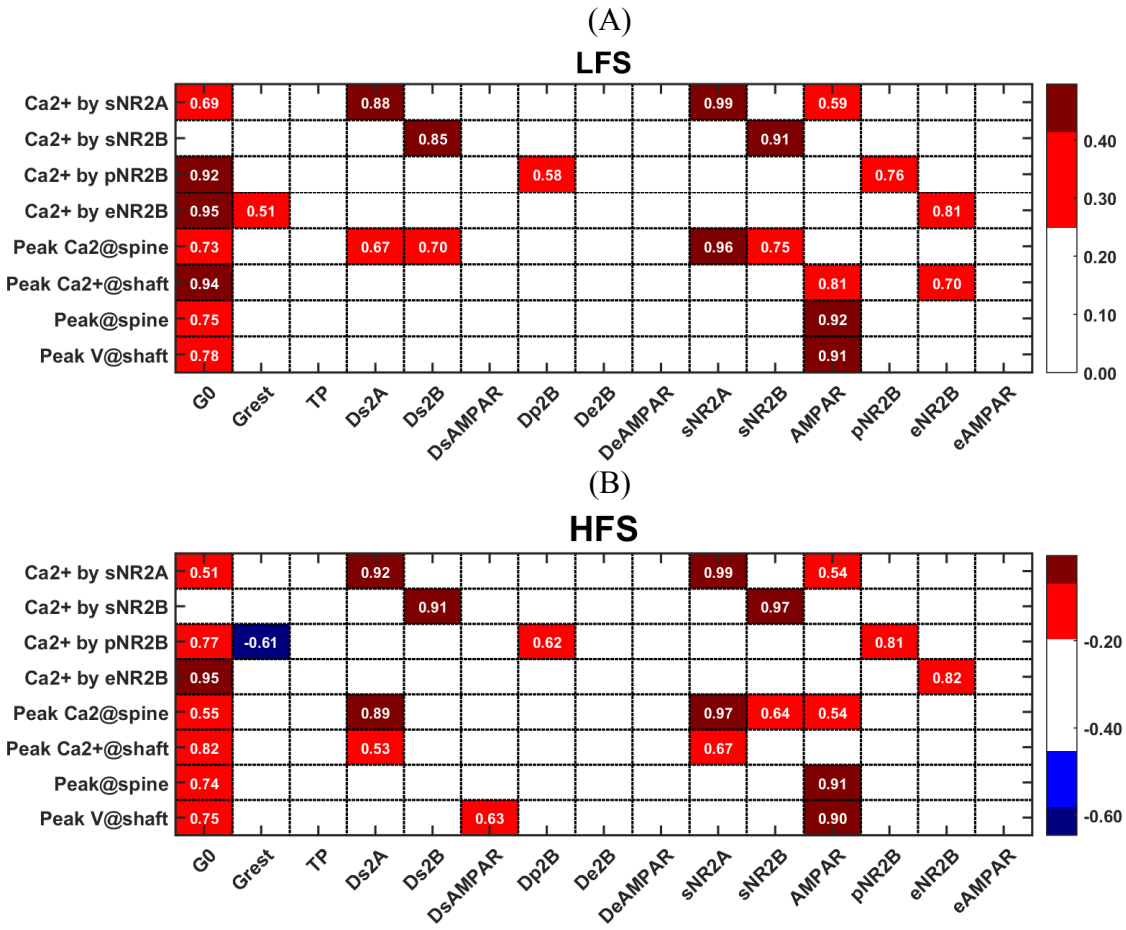

Figure 3.26. Heat maps of PRCC results for the model in response to (A) LFS and (B) HFS. The PRCC values for 15 factors against eight outputs are represented by colours, with the corresponding PRCC values written in white. Red and blue denote the positive and negative correlations, respectively. Only PRCCs greater than 0.5 and with p-value < 0.05 are shown in the figures. The white colour means there is no relationship between the corresponding factor and the output.

3.5 Discussion and conclusions

In this chapter, we present a computational model of Ca^{2+} dynamics in the dendritic spine in response to the presynaptic stimulation, which is carefully developed according to the characteristics of the CA1 pyramidal dendritic spine. This model integrates three aspects: (1) AP-induced presynaptic glutamate release and diffusion; (2) glutamate receptor activation; and (3) Ca^{2+} dynamics within a single dendritic spine and its parent dendrite shaft for a CA1 pyramidal neuron. We use this model to investigate the effects of Aβ-dependent disturbances on activation patterns of NMDARs with different subunit composition and at different locations and NMDAR-mediated Ca^{2+} dynamics in the dendritic spine and its parent dendrite shaft.

Our model shows that the increase in the numbers of glutamate released leads to different levels of increases in the availability of glutamate to receptors at tested location. It predicts that increased glutamate availability in the synaptic cleft and perisynaptic zone after presynaptic stimulation leads to higher Ca^{2+} responses in the spine head. Global sensitivity analysis suggests a great sensitivity of the postsynaptic response to the glutamate amount released during presynaptic stimulation. This confirms that the Aβ-induced increase in synaptic glutamate release may play a major role in the over excitation and Ca^{2+} overload of postsynaptic neurons. However, the spill-over effect of glutamate from the synaptic cleft shows much lower effects on activation patterns of extrasynaptic NMDARs than perisynaptic NMDARs. This is because of the fast diffusion of glutamate and the uptake by glial glutamate transporters before it reaches to eNMDAR. Therefore, it suggests that Aβ-induced multiple vesicle releases from presynaptic terminal alone may not be sufficient to cause an overactivation of the extrasynaptic receptors.

In contrast, the results show that the inhibition of the ability to uptake extrasynaptic glutamate only affects peri- and extrasynaptic receptors in our model experiments. Furthermore, on a longer time scale, this inhibition may cause an accumulation of the glutamate released from the presynaptic neurons and astrocytes in the extrasynaptic space. Therefore, it may contribute to a gradual increase in the resting level of extrasynaptic glutamate.

We have shown that elevation in the resting extrasynaptic glutamate concentration reduces the sensitivity of the postsynaptic neurons to the presynaptic signals, as a result of increased background opening under conditions of rest. The large background opening of eNMDARs will cause an especially high level of net Ca^{2+} ion influx into the dendritic shaft. As well, the

Aβ-induced astrocytic glutamate release also lead to a high level of Ca^{2+} ion influx in the absence of presynaptic stimulation. These findings are consistent with experimental observations, which show excitotoxicity results from Aβ-induced over activation of the extrasynaptic NMDAR, but not the synaptic NMDAR (Sobczyk, Scheuss et al. 2005), which may also, in turn, promote Aβ production (Bordji, Becerril-Ortega et al. 2010). Even though these abnormal Ca^{2+} influxes have failed to induce large amplitudes of Ca^{2+} transient in the dendritic shaft, due the dilution of its relatively large volume, it still may induce downstream pathways by affecting proteins located close to the receptors. Over a long time span, this may contribute to the Ca^{2+} overload and neuronal death in AD (Hardingham and Bading 2010).

The experimental observations suggest that Aβ induced the internalisation of surface glutamate receptors, especially sNR2B-NMDAR, which may affect the synaptic transmission (Snyder, Nong et al. 2005, Li, Jin et al. 2011). Our simulation shows that sNR2B-NMDAR contributes less to the synaptic Ca^{2+} transient compared to sNR2A-NMDAR. Even when removing all sNR2B-NMDAR, the sNR2A-NMDAR can still lead to considerable Ca^{2+} transients. This seems to be in conflict with the experimental observations. In fact, besides its role as a Ca^{2+} channel, sNR2B-NMDAR binds to Ca^{2+} /calmodulin-dependent protein kinase II (CaMKII), a critical protein in LTP formation and, therefore, sNR2B-NMDAR are involved in downstream pathways mediating synapse strength and plasticity (Bayer, De Koninck et al. 2001). Reducing the functional surface of sNR2B-NMDAR may affect the accessibility of CaMKII which, consequently, disturbs information transmission and memory formation. We discuss this further by combining the current model with a CaMKII transition model in Chapter 5.

Chapter 4
Computational modelling of disturbances in the ER using an extended model

The dendritic smooth endoplasmic reticulum (ER) extends into the spine head through the spine neck and in some spine head, forms a specialised organelle called the spine apparatus, which comprises a stack of membrane discs (Spacek and Harris 1997, Holbro, Grunditz et al. 2009). About 20% of the pyramidal dendritic spine contains ER and these ER-containing spines tend to have much larger volumes than other spines (Cooney, Hurlburt et al. 2002, Holbro, Grunditz et al. 2009). Experimental studies suggest that the spine apparatus may be involved in the synaptic signalling through modifying Ca^{2+} influx from extracellular space in response to stimulation (Emptage, Bliss et al. 1999, Matsuzaki, Honkura et al. 2004). ER releases Ca^{2+} to cytosol through receptor-mediated Ca^{2+}-induced Ca^{2+} release (CICR) and membrane Ca^{2+} leakage and uptakes cytosol Ca^{2+} by SERCA pumps. The opposed Ca^{2+} fluxes lead to a dual role of ER that functions as a Ca^{2+} source and functions as a Ca^{2+} sink (Friel and Tsien 1992).

In research on Alzheimer's disease, the alterations in ER function have been observed in AD and are suggested to contribute to AD pathophysiology (reviewed in section 2.4 in Chapter 2). In the dendritic spine of the pyramidal neuron in the hippocampus, these alterations may partly account for the disturbance in synaptic Ca^{2+} signalling in AD by abnormal responses to Ca^{2+} influx via NMDAR (Goussakov, Miller et al. 2010, Supnet and Bezprozvanny 2010) (Figure 4.1).The dysregulation of ER Ca^{2+} handling is suggested to cause defects in the structure of the spine head or synaptic function which, ultimately, synapse loss, neuronal death and cognitive deficits seen in AD (Popugaeva and Bezprozvanny 2013, Liang, Kulasiri et al. 2015). For instance, studies of cultured hippocampal neurons have shown that the increase in Ca^{2+} responses by RyR causes mitochondrial fragmentation and neuronal death (Chan, Mayne et al. 2000). Besides, the Bezprozvanny research group (Popugaeva, Supnet et al. 2012, Bezprozvanny and Hiesinger 2013) proposes that alterations in the contribution of ER to Ca^{2+} signalling in ageing and AD relate to a shift in the balance from CaMKII-mediated "LTP-like" synaptic signalling to CaN-mediated "LTD-like" synaptic signalling. The latter signal weakens and destabilises the synapse and, consequently, leads to memory deficits.

It is important to understand the role of dysregulated ER in Ca^{2+} signalling in the dendritic

spine in AD pathology. In particular, how different alterations affect the NMDAR-mediated Ca^{2+} signalling and how these effects may contribute to synapse dysfunction. In this chapter, we select three major alterations of ER reported in AD: (1) ER Ca^{2+} overload; (2) up-regulation of RyR expression; and (3) reduction in SERCA pumps. Therefore, we investigate these alterations by plugging the ER submodel into the model described in Chapter 3. Using the extended model, we examine the interactions among the different Ca^{2+} sources between the healthy condition and the AD condition. By analysing the computational experimental results, it provides insights into the contribution of external and internal Ca^{2+} sources in synaptic transmission and how dysregulation of the ER function affects the postsynaptic Ca^{2+} response.

In this chapter, we first describe the ER submodel in Section 4.1. In Section 4.2, we give the details of the model integration, including parameter calibration and estimation, and present the model performance under healthy condition. In Section 4.3, we investigate the effects of the ER Ca^{2+} overload and dysregulations in RyR and SERCA in AD conditions using the extended model and, in Section 4.4, we give a brief discussion and the conclusions.

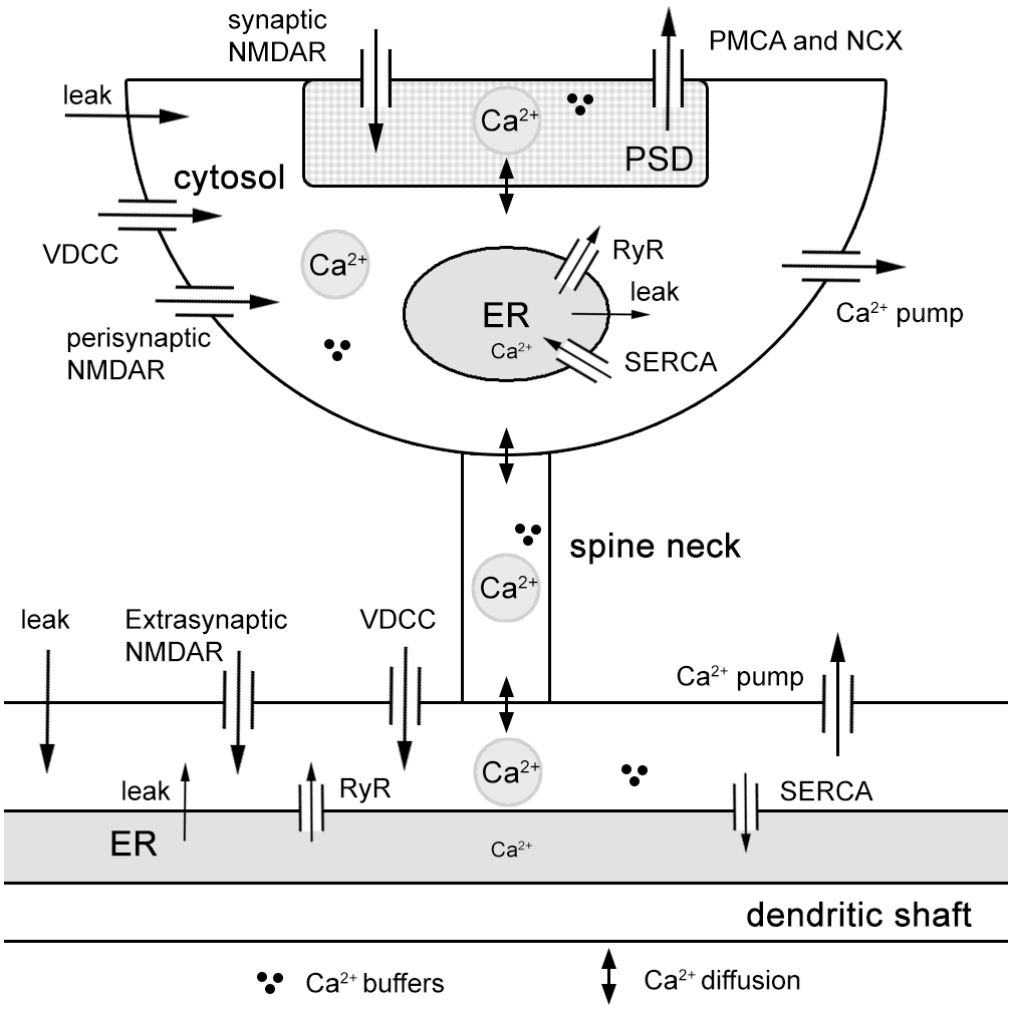

Figure 4.1. Ca^{2+} signalling in an ER-containing spine. Ca^{2+} transient in the dendritic spine head is a production of Ca^{2+} fluxes from the external and internal Ca^{2+} sources via membrane Ca^{2+} channels (external: NMDAR and VDCC; internal RyR in this case), passive membrane leaking, binding of intracellular Ca^{2+} buffers and extrusion by membrane Ca^{2+} pumps (external: PMCA and NCX; internal SERCA).

4.1 Model development

We extend the Ca^{2+} model from Chapter 3 with an intracellular ER component, as described in Figure 4.2. The ER consists of three parts: (1) Ca^{2+} release to the cytosol via membrane receptors and (2) membrane leaking, and (3) Ca^{2+} uptake by SERCA pumps. In hippocampal pyramidal CA1 neurons, RyRs are expressed throughout the axons, dendritic shaft and spines, whereas IP3Rs are primarily present in dendritic shafts and cell bodies, but absent in dendritic spines (Sharp, McPherson et al. 1993, Sabatini, Maravall et al. 2001, Hertle and Yeckel 2007). Therefore, we set the location of RyRs in ER in the compartments of the spine head and dendritic shaft. We did not include IP_3Rs in the dendritic shaft compartment in this model. This is because the presynaptic stimulation cannot induce high enough increase in the IP_3 concentration to induce IP_3R opening in the dendritic shaft.

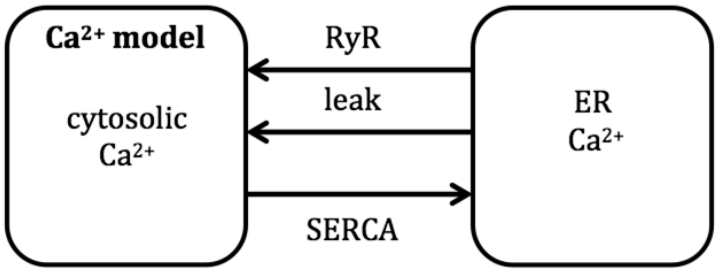

Figure 4.2. The conceptual framework of the extended model by including ER into the Ca^{2+} model in Chapter 3.

We place the ER in the spine head compartment and in the adjacent dendritic shaft compartment. For reasons of simplicity, we assume there is no store in the spine neck compartment. To take the ER into consideration, we modified Eq. (3.12) by adding a new term, $J_{ER,j}$, to govern the Ca^{2+} dynamics in the spine head and dendritic shaft:

$$\frac{d[Ca^{2+}]_j}{dt} = J_{I_{Ca},j} + J_{mem,j} + J_{diffusion,j} - J_{buffer,j} + J_{ER,j}, \quad (4.1)$$

where j = 2 or 4, indicates the compartment index (j =2, cytosol; 4, dendritic shaft). $J_{ER,j}$ denotes the net ER Ca^{2+} flux to the cytosol, and is the balance between the outward Ca^{2+} flux via RyRs (J_{RyR}) and membrane leakage (J_{leakER}), and the inward Ca^{2+} flux via SERCA pumps (J_{SERCA}):

$$J_{ER,j} = J_{RyR,j} - J_{SERCA,j} + J_{leakER,j}, \mathrm{j} = 2, 4. \quad (4.2)$$

The Ca^{2+} dynamics of ERs are governed as follows:

$$\frac{d[Ca^{2+}]_{ER,j}}{dt} = \rho\, J_{ER,j}, \tag{4.3}$$

where ρ is the ratio of ER volume to the cytosol volume. Parameters used in this section are summarised in Table 4.1.

4.1.1 The RyR gating

We simulate the RyR mediated CICR as:

$$J_{\mathrm{RyR,i}} = \mathrm{V}_{RyR,j} Po_{RyR,j}\left([Ca^{2+}]_{ER} - [Ca^{2+}]_j\right), \tag{4.4}$$

where V_{RyR} is the rate constant of RyRs and is proportional to the number of RyRs. The opening of RyR by Ca^{2+} is simulated using the four-state model developed by Keizer and Levine (1996) (Figure 4.3).

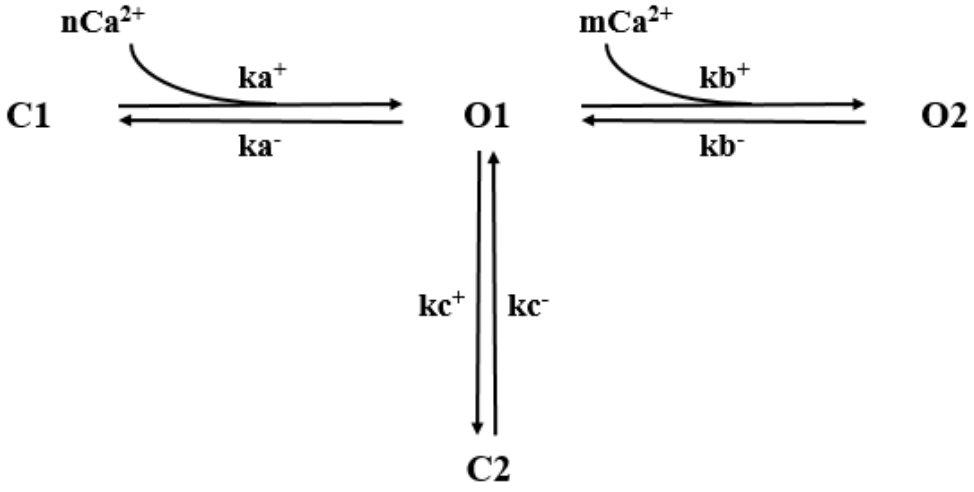

Figure 4.3. Schematic diagram of the model of RyR developed by Keizer and Levine (1996). This model contains two closed states, C1 and C2, and two open states, O1 and O2. The two open states are assumed to have the same single channel conductance. Therefore, the fraction of RyRs in the open state is the summation of the fraction of RyRs that are in state O1 and O2. The transition from C1 → O1and O1 → O2 are Ca^{2+} dependent. The transitions between C1 and O1 and between O1 and O2 are assumed to be fast (in milliseconds), and reach equilibrium rapidly. In contrast, the transition between C2 and O1 is assumed to be slow (in seconds).

$Po_{RyR,j}$ is the fraction of RyR that is opened by cytosolic Ca^{2+}:

$$Po_{RyR,j} = w_j \frac{1 + \left(\frac{[Ca^{2+}]_i}{\mathrm{K}_b}\right)^3}{1 + \left(\frac{\mathrm{K}_a}{[Ca^{2+}]_j}\right)^4 + \left(\frac{[Ca^{2+}]_j}{\mathrm{K}_b}\right)^3}, \tag{4.5}$$

where w_j denotes the fraction of channels not in state C_2, and the three dissociation constants, K_i, are ${\mathrm{K}_a}^4 = \frac{k_{ab}}{k_{af}}$, ${\mathrm{K}_b}^3 = \frac{k_{bb}}{k_{bf}}$, and $\mathrm{K}_c = \frac{k_{cb}}{k_{cf}}$. The change in w_j with time is calculated as

$$\frac{dw_j}{dt} = \frac{1}{\tau_w([Ca^{2+}]_j)}(w_\infty([Ca^{2+}]_j) - w_j), \tag{4.6}$$

where

$$w_\infty([Ca^{2+}]_j) = \frac{1 + \frac{{\mathrm{K}_a}^4}{[Ca^{2+}]_j{}^4} + \frac{[Ca^{2+}]_j{}^3}{{\mathrm{K}_b}^3}}{1 + \frac{1}{\mathrm{K}_c} + \frac{{\mathrm{K}_a}^4}{[Ca^{2+}]_j{}^4} + \frac{[Ca^{2+}]_j{}^3}{{\mathrm{K}_b}^3}} \; and \; \tau_w([Ca^{2+}]_j) = \frac{w_\infty([Ca^{2+}]_j)}{k_{cb}}.$$

4.1.2 The SERCA pump

The activity of SERCA pump is modelled by a Hill equation with a Hill coefficient of 2 (Lytton, Westlin et al. 1992):

$$J_{SERCA,j} = v_{SERCA} \frac{[Ca^{2+}]_j^2}{K_{SERCA}^2 + [Ca^{2+}]_i^2} \tag{4.7}$$

where v_{SERCA} is the maximum rate of Ca^{2+} uptake by ER via the SERCA pump, and K_{SERCA} is the affinity of the SERCA pump for Ca^{2+} ions (see Appendix C.4 for the explanation). The value v_{SERCA} is proportional to the availability of SERCA and is estimated in the next section.

4.1.3 Ca^{2+} passive leak

The flux of the passive Ca^{2+} leak from the ER is described as:

$$J_{leak,j} = v_{leak,ER}\left([Ca^{2+}]_{ER,j} - [Ca^{2+}]_j\right) \tag{4.8}$$

where $v_{leak,ER}$ is the leak rate constant of ER.

Therefore, we substitute Eq (4.4), (4.7) and (4.8) into Eq. (4.2) and get

$$J_{ER,j} = V_{RyR} Po_{RyR,i}\left(\left[Ca^{2+}\right]_{ER} - \left[Ca^{2+}\right]_j\right) - v_{SERCA}\frac{\left[Ca^{2+}\right]_j^2}{K_{SERCA}^2 + \left[Ca^{2+}\right]_j^2} + v_{leak,ER}\left(\left[Ca^{2+}\right]_{ER,j} - \left[Ca^{2+}\right]_j\right), \quad (4.9)$$

where j = 2 or 4. At the resting state ($J_{ER,j} = 0$), the Ca^{2+} leaking flux together with RyR-mediated Ca^{2+} release balances the Ca^{2+} influx by the SERCA pumps, according to which we can calculate the corresponding value of $v_{leak,ER}$.

Table 4.1. Parameters values used in this chapter under healthy condition.

Description	Symbol	Value	Reference
Ratio of ER volume to the cytosol volume	ρ	0.032	(Cooney, Hurlburt et al. 2002)
RyR Ca^{2+} release rate	$V_{RyR,2}$	0.005 ms^{-1}	(Keizer and Levine 1996)
RyR kinetic constants	k_{af}	1.5 μM^{-4} ms^{-1}	
	k_{ab}	0.0288 ms^{-1}	
	k_{bf}	1.5 μM^{-3} ms^{-1}	
	k_{bb}	0.3859 ms^{-1}	
	k_{cf}	0.00175 ms^{-1}	
	k_{cb}	0.0001 ms^{-1}	
Maximum rate of SERCA	v_{SERCA}	0.9003 μM/ms	MCMC estimated
Dissociation constant for SERCA	K_{SERCA}	0.27 μM	(Lytton, Westlin et al. 1992)
Leak rate constant of ER	$v_{leak,ER}$	0.0004 ms^{-1}	MCMC estimated

4.2 Model parameter estimation and calibration

Keizer and Levine (1996) used different values for the relevant parameters for small and large ER, respectively. The ρ they use for small ER, 0.02, is close to the ratio observed experimentally (3.2±0.2% (Cooney, Hurlburt et al. 2002)). Assuming the basal Ca2+ concentration of cytosol ($[Ca^{2+}]_{cyto0}$) is 0.07 μM, then the basal Ca2+ concentration of ER ($[Ca^{2+}]_{ER0}$) is between 56.2 and 66.2 μM for different sized ERs, and is calculated based on these constraints as

$$[Ca^{2+}]_{ER0} = \frac{1}{\rho}\left(\left[Ca^{2+}\right]_{cyto0} - \left[Ca^{2+}\right]_{total}\right),$$

where $[Ca^{2+}]_{total}$ is the total Ca^{2+} concentration in the dendrites. We choose $[Ca^{2+}]_{ER0}$ to be 60 μM under control conditions and ρ to be 0.032, which gives $[Ca^{2+}]_{total}$ as 1.99 μM. This is slightly higher than the value for the small ER used in the model of Keizer and Levine (1996),

1.2 μM, since the value for ρ in our model is slightly higher than that in their model.

We assume the densities of RyR and SERCA pump and the surface area to volume ratios of ER are the same in the spine head and the dendritic shaft. Therefore, the rate constants of RyRs, V_{RyR}, in Eq. (4.4) shaft are the same in the spine head and dendritic shaft, which is assumed to be 0.005 ms^{-1} (Keizer and Levine 1996). The maximum rate of Ca^{2+} uptake by SERCA, v_{SERCA}, can be calculated by

$$v_{SERCA,j} = V_{max} Ps_{SERCA} \frac{A_j}{V_j},$$

where V_{max} is the maximum turnover rate of Ca^{2+} by SERCA, Ps_{SERCA} is its surface density and $\frac{A_j}{V_j}$ is the ratio of surface area to the volume of compartment j. Based on our assumption, the value of v_{SERCA} in the spine head and the dendritic shaft are identical.

4.2.1 Estimate parameter values using MCMC

In Chapter 3, we estimate ten parameters using MCMC from the experimental data. The estimation is based on the assumption of the absence of ER, therefore, we need to re-estimate their values by considering the presence of ER.

Sabatini, Oertner et al. (2002) observed that in response to a single bAP, about 30% of the Ca^{2+} ions are extruded from the cytosol via SERCA in the spine, while the rest are via PMCA and NCX. We add this as an additional target in the experimental data listed in Table 3.6 in Chapter 3 to estimate the value for v_{SERCA} as well as the other ten parameters (Table 4.2). The range of v_{SERCA} is from 0.1 to 1 μM ms^{-1} (Keizer and Levine 1996). The procedure for estimation is the same as described in Section 3.2.4 in Chapter 3. The means of MCMC samples and the parameter set with the lowest MAPE are listed in the last two columns in Table 4.3. The simulation results show that the model with the parameter set with the lowest MAPE performs much better than the one using the mean of MCMC samples (Table 4.2). Therefore, we choose parameters with the lowest MAPE for our model under control conditions.

Table 4.2. Values of target experimental data, means of MCMC samples and the parameter set with the lowest mean absolute percentage error (MAPE)

Target experimental data	Target value	Mean of MCMC samples	Set with the lowest MAPE
$\Delta[Ca]_{bAP}$ in spine (μM)	1.7 (±0.6)	1.257	1.647
$\Delta[Ca]_{bAP}$ in dendrite (μM)	1.5 (±0.5)	1.277	1.606
τ_{decay} in spine (ms)	12 (±4)	14.731	12.486
τ_{decay} in dendrite (ms)	15 (±5)	17.803	14.862
$\frac{[Ca]_{PMCA}}{[Ca]_{NCX}}$ in spine	1.070	2.464	1.200
$\frac{[Ca]_{PMCA}}{[Ca]_{NCX}}$ in dendrite	0.825	1.425	0.826
$\frac{[Ca^{2+}]_{SERCA}}{[Ca^{2+}]_{SERCA}+[Ca^{2+}]_{PMCA}+[Ca^{2+}]_{NCX}}$	0.3	0.168	0.307
MAPE		0.377	0.040

Table 4.3. Parameter ranges for MCMC and the values estimated by MCMC

Parameter	Range for MCMC	Mean of MCMC samples	Set with the lowest MAPE
VDCC density in spine head	2.23 - 4.66 μm^{-2}	3.630 μm^{-2}	3.169 μm^{-2}
VDCC density in shaft	7.29 – 14.57 μm^{-2}	11.661 μm^{-2}	10.188 μm^{-2}
PMCA density in spine head	200 - 2000 μm^{-2}	555.014 μm^{-2}	283.878 μm^{-2}
PMCA density in shaft	200 - 2000 μm^{-2}	979.994 μm^{-2}	490.837 μm^{-2}
NCX density in spine head	10 - 700 μm^{-2}	0.350 μm^{-2}	0.410 μm^{-2}
NCX density in shaft	100 -1000 μm^{-2}	508.219 μm^{-2}	433.938 μm^{-2}
Immobile buffer concentration in spine head	50 - 200 μM	115.779 μM	83.871 μM
Immobile buffer concentration in shaft	50 - 200 μM	130.911 μM	102.409 μM
Forward rate constant of immobile buffer	0.05 – 1 $\mu M^{-1}ms^{-1}$	0.267$\mu M^{-1}ms^{-1}$	0.227 $\mu M^{-1}ms^{-1}$
Backward rate constant of immobile buffer	0.05 – 1 ms^{-1}	0.520 ms^{-1}	0.509 ms^{-1}
Maximum rate of SERCA	0.1 - 1 μM ms^{-1}	0.684 μM ms^{-1}	0.903 μM ms^{-1}

4.2.2 Model performance under control conditions

In this section, we present the simulation results of the ER-included model under control conditions, using parameter values from Table 4.1. We evaluate the model performance in response to different types of presynaptic stimulation from aspects of the Ca^{2+} dynamics in the spine head and its parent dendritic shaft, and the contributions of the different Ca^{2+} sources to the Ca^{2+} dynamics.

4.2.2.1 A single bAP stimulation

Sabatini, Oertner et al. (2002) applied the cyclopiazonic acid (CPA) to block the SERCA pumps to study the relative contribution of SERCA in Ca^{2+} transient in the spine head induced by a single bAP. The CPA is a specific inhibitor of SERCA pumps, and it will deplete the Ca^{2+} content of the ER. We mimic the block of SERCA pumps by CPA by letting vSERCA be zero and running the model long enough to let all variables reach their steady levels. We then use these steady levels as the initial values of each variable. The model is simulated under the conditions of the absence (immobile buffer only) and presence of mobile buffers (CaM and CaD), respectively. After the application of CPA, the peaks of the Ca^{2+} transients evoked by a single bAP in the spine head and shaft are not affected under either conditions (Figure 4.4 A) and the decay time constants to resting values are increased.These results are consistent with the experimental observations in Sabatini, Oertner et al. (2002).

Figure 4.4 B show that the model performs well in predicting the contribution of different Ca^{2+} sources to the Ca^{2+} transients in response to a single bAP in comparison to the experimental observations (Sabatini, Oertner et al. 2002). The increase of cytosolic Ca^{2+} is mainly via VDCC in the spine head and shaft. There is only a minor Ca^{2+} release from ER by RyRs to the cytosolic Ca^{2+} transients (Figure 4.4 B middle), which is very similar to the experimental observation that CICR does not contribute to the Ca^{2+} elevation stimulated by bAP (Emptage, Bliss et al. 1999, Sabatini, Oertner et al. 2002). Moreover, about 30% and 35% of cytosolic Ca^{2+} extrusion are taken up by ER during the transient in the spine head and shaft, respectively (Figure 4.4 B bottom).

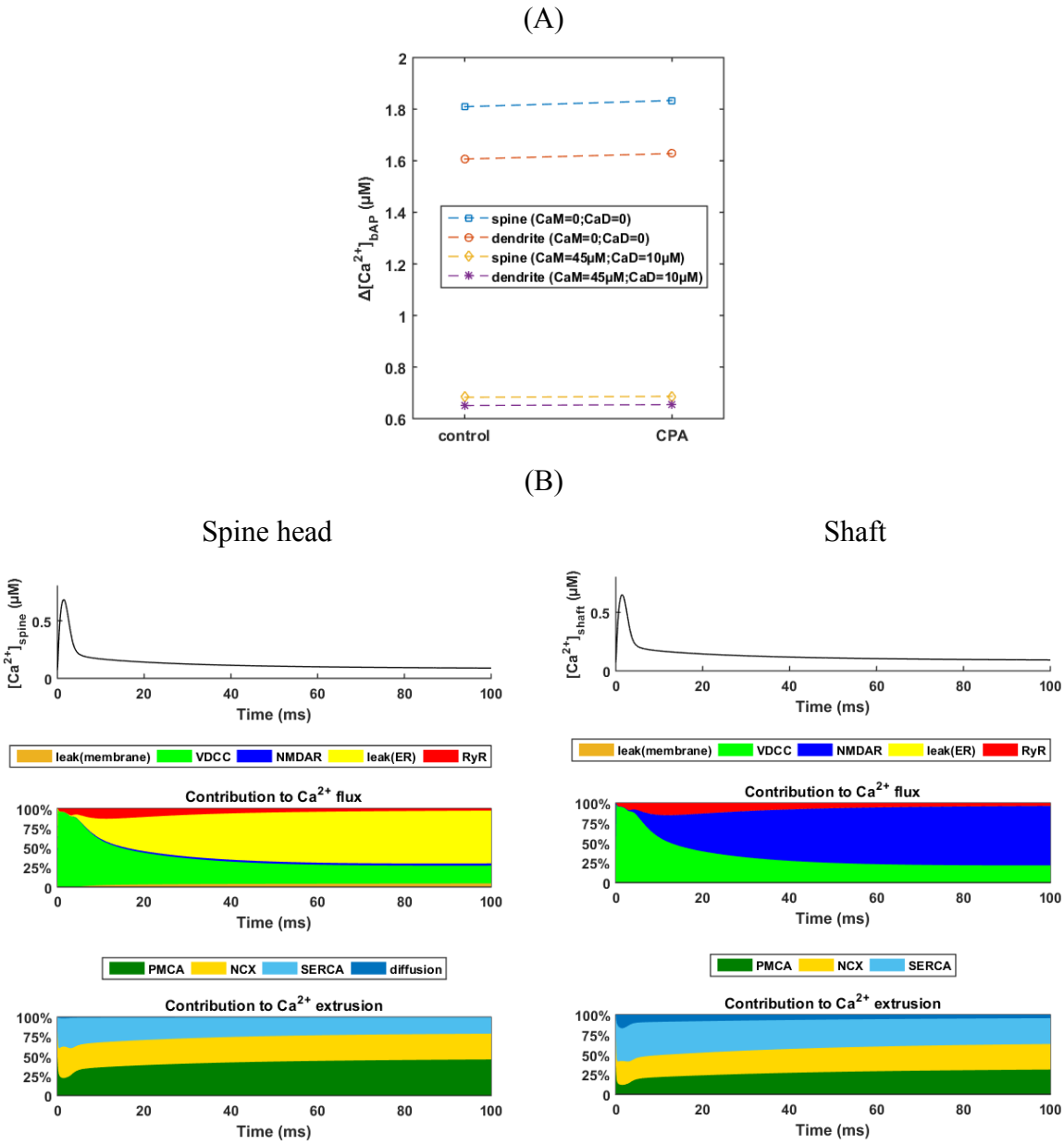

Figure 4.4. Ca^{2+} response in the spine head and the adjacent dendritic shaft evoked by a single bAP. (A) Effects of block of Ca^{2+} uptake into ER via SERCA pumps in response to a single bAP. (B) Ca^{2+} trainsient (top), fractional contribution of Ca^{2+} influx from different sources (middle) and Ca^{2+} extrusion by different mechanisms (bottom) to the cytosolic Ca^{2+} transients in the spine head and the adjacent dendritic shaft.

4.2.2.2 1 s of presynaptic stimulation

CICR by ER can be triggered by Ca^{2+} influx via NMDAR in response to the presynaptic stimulation (Emptage, Bliss et al. 1999). We use the model to simulate the Ca^{2+} dynamics in a dendritic spine in response to 1 s of presynaptic stimulation at 1 Hz (1 pulse), 10 Hz (10 pulses) and 100 Hz (100 pulses), respective, under healthy condition. At a 1 Hz stimulation,

the peak Ca^{2+} transient is about 0.48 μM in the spine head (Figure 4.5 A left) at the presence of mobile buffers, which is located in the range estimated under experimental conditions (Sterratt, Graham et al. 2011). The Ca^{2+} elevation is mainly by the Ca^{2+} influx via NMDARs and RyRs and ER membrane leakage show higher contributions to the Ca^{2+} elevation in response to a single presynaptic stimulation (Figure 4.5 B left) than in response to a single bAP stimulation (Figure 4.4 B and C). VDCCs does not contribute to the Ca^{2+} elevation because the small membrane depolarization is not sufficient to open them. About one-third of cytosolic Ca^{2+} ions is removed by SERCA pumps during the Ca^{2+} transient, while the rest is by the membrane pumps (PMCA and NCX) (Figure 4.5 C left). The Ca^{2+} response in the dendritic shaft is relatively less noticeable (Figure 4.5 A right), showing that the Ca^{2+} response to a single presynaptic stimulation is highly restricted to the spine head (Nevian and Sakmann 2004). Therefore, in following sections, we only focus on the Ca^{2+} dynamics in the spine hand.

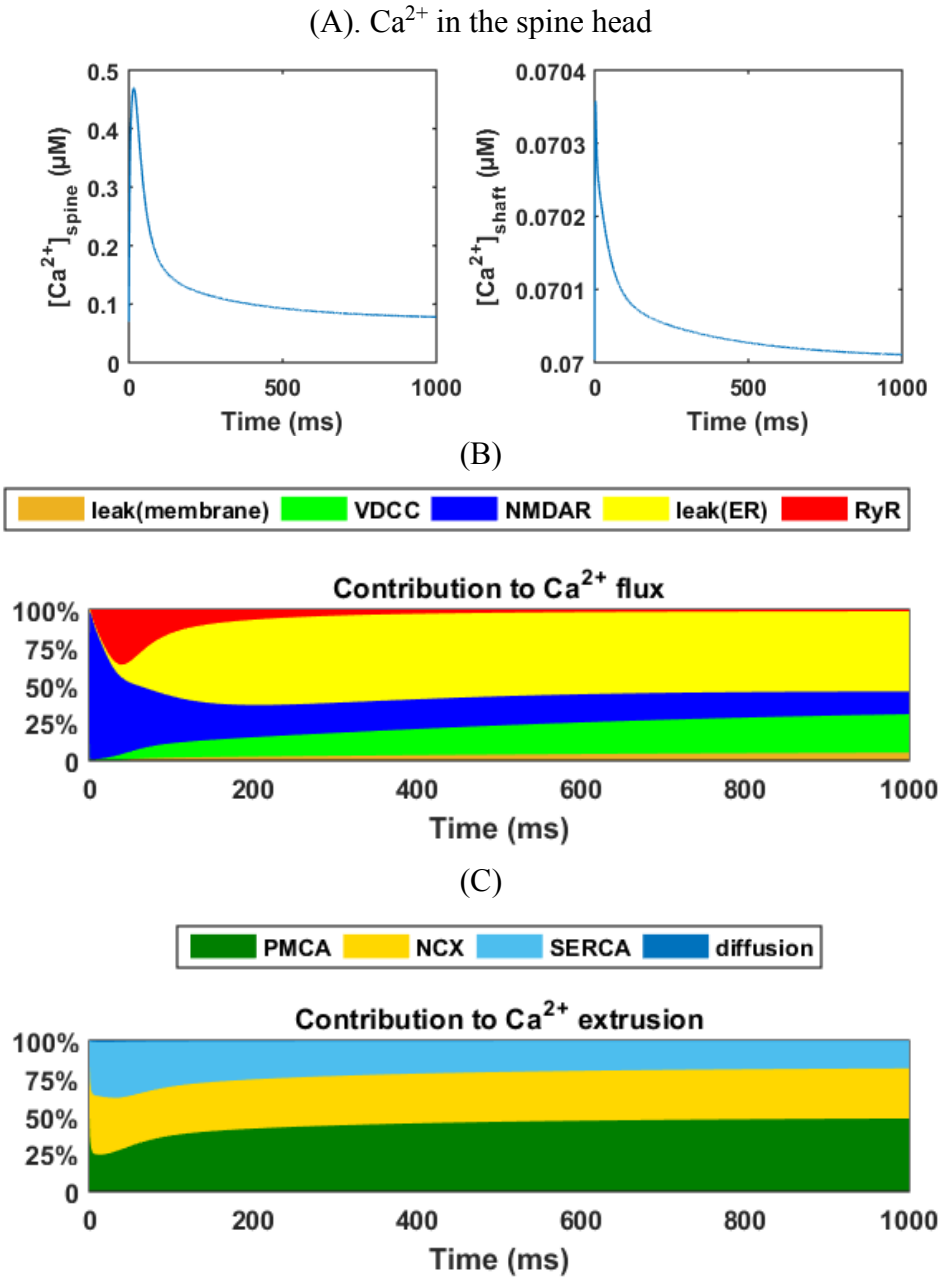

Figure 4.5. Ca^{2+} response in the spine head and the adjacent dendritic shaft evoked by a single presynaptic stimulation. (A) Ca^{2+} concentration in the spine head and the adjacent dendritic shaft. Contributions of Ca^{2+} influx from different sources (B) and Ca^{2+} extrusion by different mechanisms (C) to the cytosolic Ca^{2+} transients in the spine head.

At 10 and 100 Hz stimulation, the maximum Ca^{2+} levels are about 0.83 and 3.7 μM, respectively (Figure 4.6 A top and B top). At the 100 Hz stimulation, after reaches a peak, the Ca^{2+} concentration decreases and stays on a plateau at a lower level (about 1.1 μM) until the end of stimulation, which because of the large desensitisation of synaptic NMDAR by high-frequency stimulation. RyRs show a larger contribution to the cytosolic Ca^{2+} transients at the

decay phase at a 10 stimulation than at a 100 one (Figure 4.6 A middle and B middle). The contribution of Ca^{2+} extrusion by different mechanisms to the cytosolic Ca^{2+} transients are very similar between at 10 and 100 Hz stimulation (Figure 4.6 A bottom and B bottom).

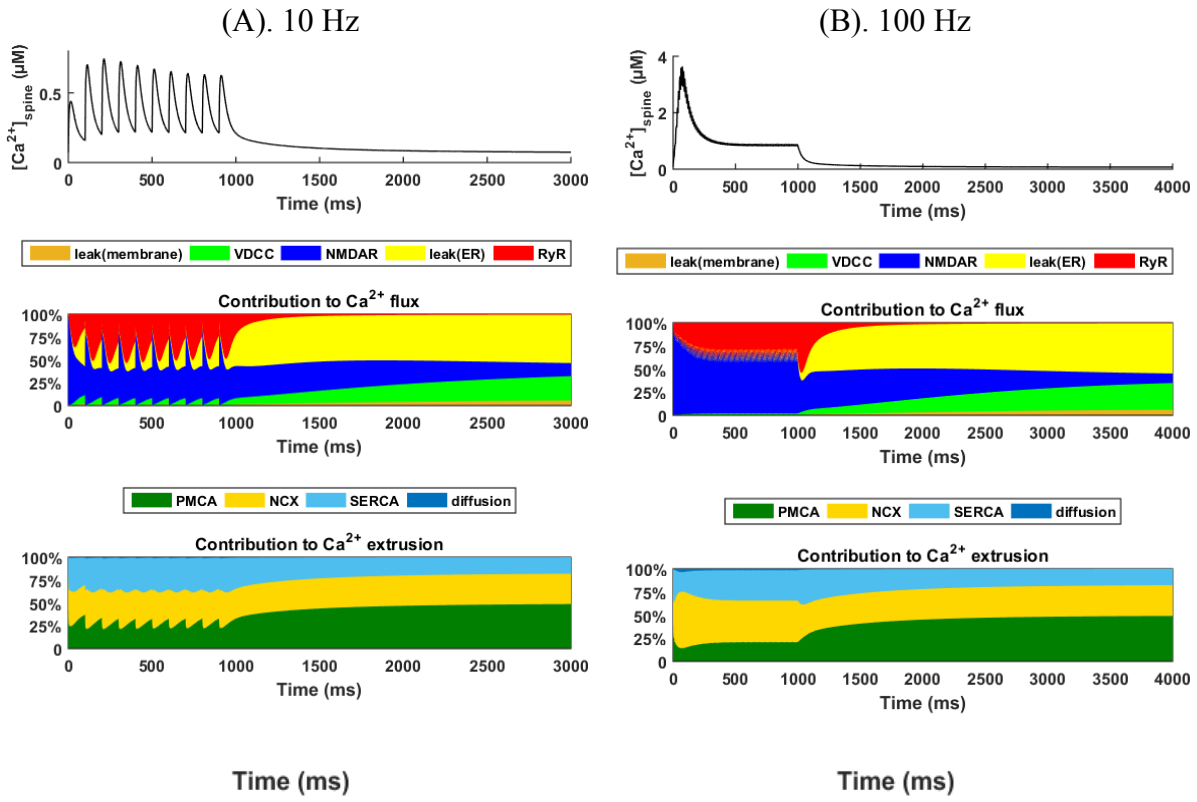

Figure 4.6. Ca^{2+} response in the spine head and the adjacent dendritic shaft evoked by 1s of stimulation at 10 Hz (A) and 100 Hz (B), respectively. (Top) Ca^{2+} concentration in the spine head. The fractional contribution of Ca^{2+} influx from different sources (middle) and Ca^{2+} extrusion by different mechanisms (bottom) to the cytosolic Ca^{2+} transients in the spine head.

4.3 Computational experiments

We investigate the three selected effects of ER alterations on Ca^{2+} signalling in the dendritic spine individually and collectively, by simulating the model under the following four conditions: (1) ER Ca^{2+} overload (Section 4.3.1); (2) upregulation in RyR response (Section 4.3.2); (3) combination effects of (1),(2) (Section 4.3.3); (4) SERCA pumps (Section 4.3.4); and (5) combination effects of (1),(4) (Section 4.3.5). Simulations are carried in response to a 1 s presynaptic stimulation at 1 Hz (1 pulse), 10 Hz (10 pulses) and 100 Hz (100 pulses),

respectively. The results are compared with those of the control produced by the parameters in Table 4.1 and the ones used in Chapter 3.

The outputs we choose to collect after simulation are as follows:

(1) Ca^{2+} elevation in the spine head ($[Ca^{2+}]_{cyto}$). This includes $[Ca^{2+}]_{cyto}$ peaks in response to each stimulation pulse.

(2) Ca^{2+} responses of RyR (J_{RyR}; positive outward flux) and the SERCA pump (J_{SERCA}; negative, inward flux), ER membrane leaking (J_{leakER}; positive outward flux), and the net Ca^{2+} flux from the ER to the cytosol (J_{ER}) (Eq.(4.9)). This indicates the role ER plays in the cytosolic Ca^{2+} dynamics. A positive J_{ER} indicates that the ER mainly acts as a Ca^{2+} source and a negative J_{ER} indicates it acts as a Ca^{2+} sink.

(3) The fraction of RyRs (Po_{RyR}) opened by cytosolic Ca^{2+} and the total open time. The total open time of RyR is calculated from the area under the Po_{RyR} curve against time.

(4) The ratio of total Ca^{2+} ions enters via RyR to those via the NMDAR ($[Ca^{2+}]_{RyR}$: $[Ca^{2+}]_{NMDAR}$ ratio). This indicates the contribution between the internal and external Ca^{2+} sources to cytosolic Ca^{2+} elevation. The total Ca^{2+} ions is calculated from the area under the Ca^{2+} flux curve against time.

4.3.1 ER Ca^{2+} overload

An increase in the resting Ca^{2+} level of ER has been observed in AD neurons as well as in ageing neurons (Popugaeva and Bezprozvanny 2013). Several researches have linked the ER Ca^{2+} overload to mutations in PS (see Section 2.2.4.2 in Chapter 2). PS is suggested to serve as a Ca^{2+}leak channel on the ER membrane, which balances the activity of the SERCA pumps and RyRs to maintain Ca^{2+} homeostasis of the ER at the resting level (Tu, Nelson et al. 2006). Therefore, PS mutation will diminish its leak function, leading to a Ca^{2+} overload in the ER and an alteration in Ca^{2+} homeostasis (Tu, Nelson et al. 2006, Nelson, Tu et al. 2007, Zhang, Sun et al. 2010, Nelson, Supnet et al. 2011). We mimic the alteration in ER Ca^{2+} by varying the resting Ca^{2+} of the ER ($[Ca^{2+}]_{ER0}$) from 30 μM to 600 μM ($[Ca^{2+}]_{ER0}$ as the healthy condition is assumed to be 150 μM), and keep other parameters at standard values.

The ER Ca^{2+} leak rate constant, $v_{leak,ER}$, is calculated by rearranging Eq.(4.9):

$$v_{leakER} = \mathrm{V}_{RyR} Po_{RyR} - v_{SERCA} \frac{\left[Ca^{2+}\right]_{cyto}^{2}}{K_{SERCA}^{2} + \left[Ca^{2+}\right]_{cyto}^{2}} \frac{1}{\left[Ca^{2+}\right]_{ER} - \left[Ca^{2+}\right]_{cyto}}. \quad (4.10)$$

For fixed values of RyR and the SERCA pump-related parameter and resting cytosolic Ca^{2+} concentration ($[Ca^{2+}]_{cyto}$), v_{leakER} is negatively depending on the concentration gradient between the cytosol and ER $\left(\left[Ca^{2+}\right]_{ER} - \left[Ca^{2+}\right]_{cyto}\right)$ under resting conditions (Figure 4.7).

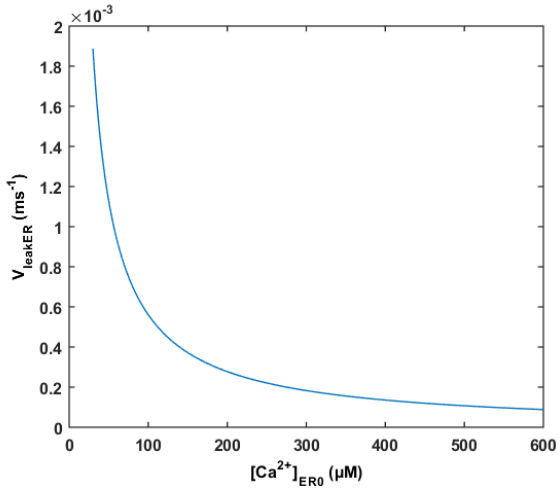

Figure 4.7. The membrane Ca^{2+} leak rate constant of ER (v_{leakER}) at various levels of resting Ca^{2+} levels of ER ($[Ca^{2+}]_{ER0}$). The values of v_{leakER} is calculated using Eq. (4.10). V_{RyR} = 0.005 ms^{-1}. v_{SERCA} = 0.9 μM ms^{-1}. K_{SERCA} = 0.27 μM. $[Ca^{2+}]_{cyto}$ = 0.07 μM. Po_{RyR} is calculated from Eq.(4.5) and Eq.(4.6) at steady state.

The peak of $[Ca^{2+}]_{cyto}$ evelation in the postsynaptic spine head in response to a 1 Hz presynaptic stimulation increases with the rise in $[Ca^{2+}]_{ER0}$ (Figure 4.8 A), from 0.32 μM at standard $[Ca^{2+}]_{ER0}$ to 0.42 μM when $[Ca^{2+}]_{ER0}$ increases to 600 μM. At the standard and lower level of $[Ca^{2+}]_{ER0}$, the net ER Ca^{2+} flux is negative/inward during the rising of $[Ca^{2+}]_{cyto}$ and becomes positive during the Ca^{2+} decay stage. In contrast, at high levels of

$[Ca^{2+}]_{ER0}$ (300 and 600 μM), a positive peak appears during the rising stage of $[Ca^{2+}]_{cyto}$(Figure 4.8 B). This is mainly contributed to by the increasing level of RyR response (Figure 4.8 B and Figure 4.8 C). The peak RyR response increases linearly with increases in $[Ca^{2+}]_{ER0}$ while the peak activity of the SERCA pump is nearly unaffected across the range of $[Ca^{2+}]_{ER0}$ tested (Figure 4.8 C). This suggests that under a single presynaptic stimulation, when the ER is overfilled with Ca^{2+} at the resting level, it shifts its role from a Ca^{2+} sink, which attenuates the rising of $[Ca^{2+}]_{cyto}$, to an internal Ca^{2+} source in addition to the extracellular one.

When we apply 1 s presynaptic stimulations at 10 Hz and 100 Hz, respectively, the increase in normalised peak of $[Ca^{2+}]_{cyto}$ with $[Ca^{2+}]_{ER0}$ is attenuated from the second pulse onward (Figure 4.9 A and B). Under 100 Hz stimulation, there is no difference in peak $[Ca^{2+}]_{cyto}$ upon simulation with different $[Ca^{2+}]_{ER0}$ after the 10th pulse (Figure 4.9 B). When $[Ca^{2+}]_{ER0}$ is 150 μM and higher, the net ER Ca^{2+} flux shows a positive spike in response to each stimulation pulse with a decrease in amplitude against time at a 10 Hz stimulation (Figure 4.9 C). The spike amplitudes in response to each stimulation pulse increase with $[Ca^{2+}]_{ER0}$. Under a 100 Hz stimulation, the net Ca^{2+} flux fluctuates around zero from the second pulse onward, without obvious differences between different levels of $[Ca^{2+}]_{ER0}$ (Figure 4.9 D). Moreover, the $[Ca^{2+}]_{RyR}$: $[Ca^{2+}]_{NMDAR}$ ratio increases with the level of $[Ca^{2+}]_{ER0}$ (Figure 4.9 E). The increment is slightly affected by the stimulation frequency. Under a 1 Hz stimulation, the $[Ca^{2+}]_{RyR}$: $[Ca^{2+}]_{NMDAR}$ ratio shows a linear increase with V_{RyR}, whereas, the increment in the $[Ca^{2+}]_{RyR}$: $[Ca^{2+}]_{NMDAR}$ ratio by V_{RyR} is attenuated under 10 Hz and 100 Hz stimulations.

Under a 1 Hz stimulation, the peak of Po_{RyR} increases from around 0.38 at $[Ca^{2+}]_{ER0}$= 30 μM to around 0.67 at $[Ca^{2+}]_{ER0}$= 300 μM (Figure 4.10 A insert). At a 10 Hz stimulation, the Po_{RyR} reaches a peak in response to the second stimulation pulse, and afterwards, the increase in Po_{RyR} with $[Ca^{2+}]_{ER0}$ is attenuated (Figure 4.10 B). At a 100 Hz stimulation, more than 90% of RyRs open in response to the second pulse and gradually decrease to around 30% through the stimulation (Figure 4.10 C). There is no obvious difference in Po_{RyR} among the different values of $[Ca^{2+}]_{ER0}$. The total open time of RyR increases with $[Ca^{2+}]_{ER0}$ at 1 Hz and 10 Hz stimulations, whereas at a 100 Hz stimulation, it decreases and rises again between 451.2 and 453.5 ms (Figure 4.10 D).

The reasons cause these differences are the fast activation and slow inactivation of RyRs. Once a presynaptic stimulation pulse arrives at a resting synapse, it leads to a rapid Ca^{2+} elevation and immediate RyR response. When the time duration between the two stimulation pulses shortens under the higher frequency stimulation, this allows a fraction of RyR that is activated by the previous pulse to be still open when the next pulse arrives. This explains why higher Po_{RyR} peaks are obtained at a 100 Hz stimualtion (Figure 4.10 C) than at a 10 Hz stimualtion (Figure 4.10 B).

(A)

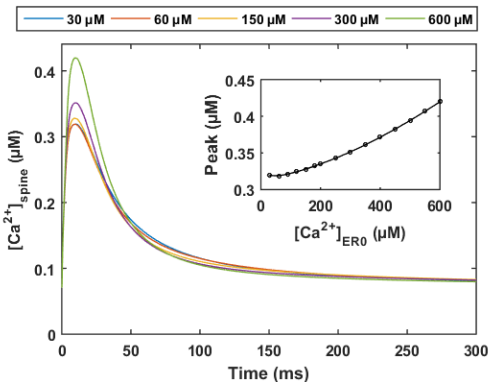

(B)

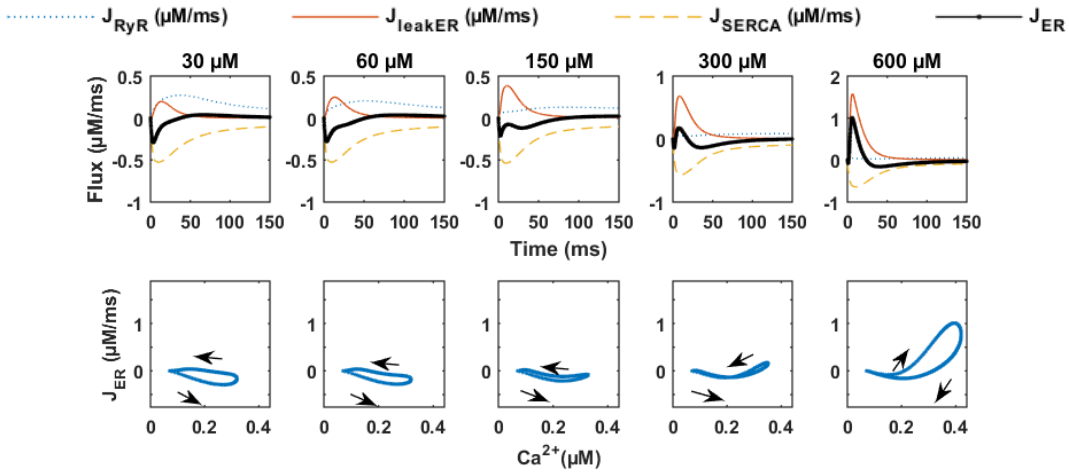

(C)

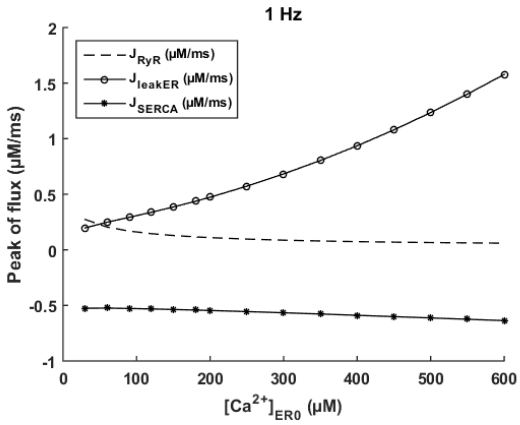

Figure 4.8. Effects of rising $[Ca^{2+}]_{ER0}$ on postsynaptic response by a single presynaptic stimulation pulse (1 Hz). (A) The $[Ca^{2+}]_{cyto}$ dynamics in the spine head and the relationship between $[Ca^{2+}]_{ER0}$ and the $[Ca^{2+}]_{cyto}$ peaks (insert). The corresponding Ca^{2+} responses of RyR (J_{RyR}) and the SERCA pump (J_{SERCA}), ER membrane leaking (J_{leakER}), and the net Ca^{2+} flux from the ER to the cytosol (J_{ER}) are shown in (B). Arrows in the bottom panel indicate the direction of time flow. The peaks of J_{RyR}, J_{SERCA} and J_{leakER} at different levels of $[Ca^{2+}]_{ER0}$ are in (C).

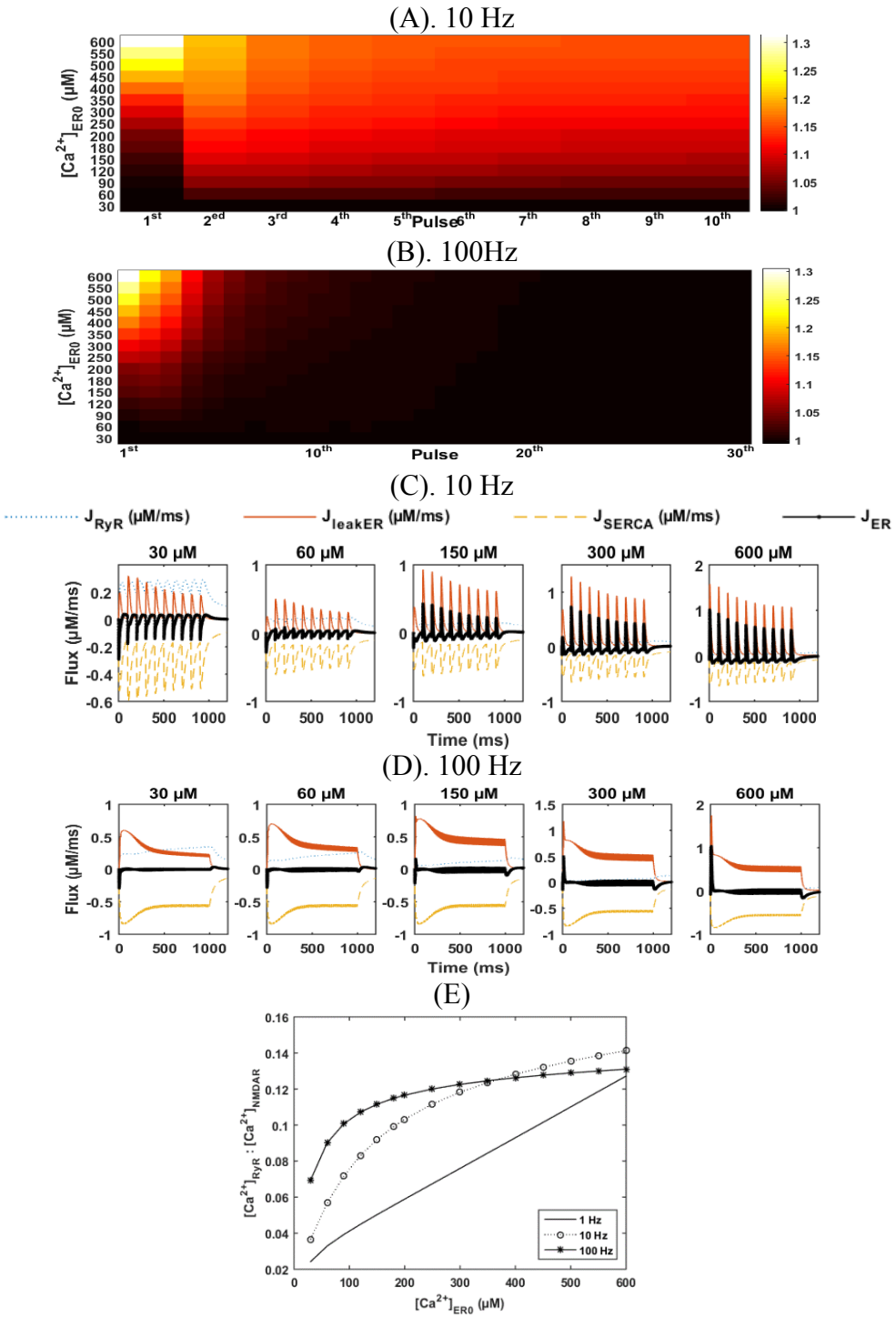

Figure 4.9. Effects of rising $[Ca^{2+}]_{ER0}$ on postsynaptic response under 1 s presynaptic stimulation at 10 Hz and 100 Hz, respectively. The $[Ca^{2+}]_{cyto}$ peaks in response to different stimulation pulses at a 10 Hz (A) and a 100 Hz stimulation (B), respectively are normalised to the one with the lowest $[Ca^{2+}]_{ER0}$ at each pulse. The colour density represents the values of $[Ca^{2+}]_{cyto}$ peaks in the spine head. Under the 100 Hz stimulation, only the first 30 pulses are shown in the figure since there is no difference afterwards. The corresponding Ca^{2+} responses of RyR (J_{RyR}) and the SERCA pump (J_{SERCA}), ER membrane leaking (J_{leakER}), and the net Ca^{2+} flux from the ER to the cytosol (J_{ER}) are shown in (C) and (D), respectively. (E) Effects of rising $[Ca^{2+}]_{ER0}$ on $[Ca^{2+}]_{RyR}$: $[Ca^{2+}]_{NMDAR}$ ratio.

(A). 1 Hz

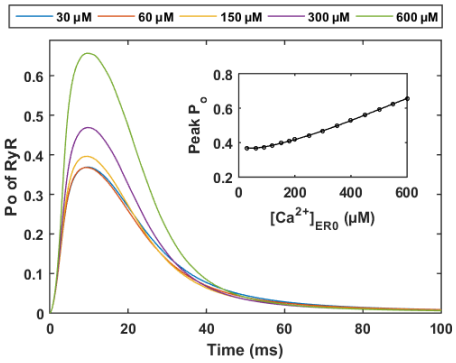

(B). 10 Hz

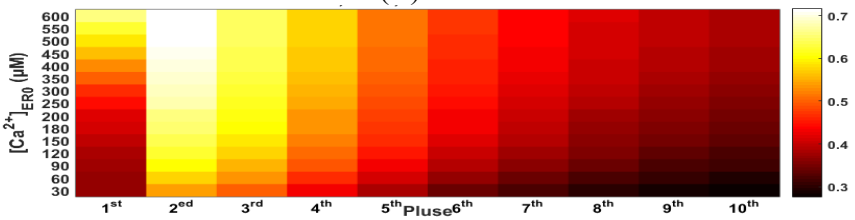

(C). 100 Hz

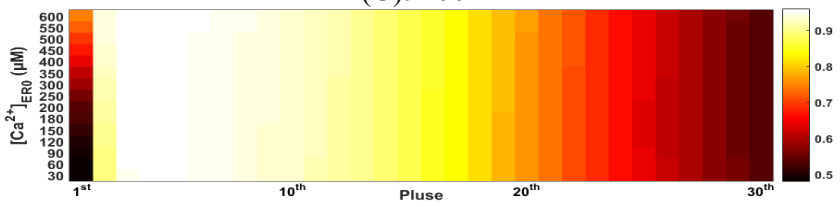

(D)

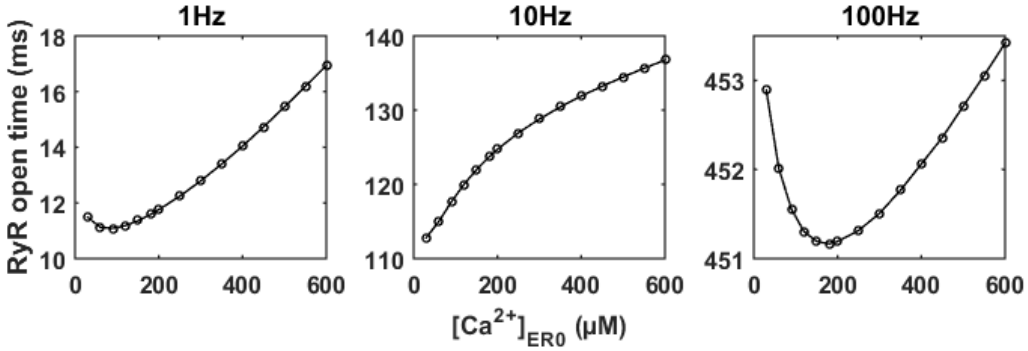

Figure 4.10. Effects of rising $[Ca^{2+}]_{ER0}$ on RyR opening. (A) The Po_{RyR} with time in the spine head and the relationship between $[Ca^{2+}]_{ER0}$ and the Po_{RyR} peaks (insert) at a 1 Hz stimulation. The heatmaps show the maximums of Po_{RyR} in response to different stimulation pulses at a 10 Hz (B) and a 100 Hz stimulation (C), respectively. The colour density represents the values of Po_{RyR} peaks in the spine head. Under the 100 Hz stimulation, only the first 30 pulses are shown in the figure since there is no difference afterwards. (D) The corresponding total opening times of RyR at stimulations with different frequencies.

4.3.2 Enhanced Ca^{2+} release via RyRs

For a fixed maximum rate of a single receptor, the maximum rate of total RyRs is in proportion to the number of RyRs. In this section, we mimic the upregulation in RyR expression by increasing V_{RyR} from its standard level of 0.005 ms^{-1} to 0.3 ms^{-1}. We also include lower levels of V_{RyR} (below 0.005 ms^{-1}) in the computational experiments.

Under a 1 Hz stimulation, the peak of $[Ca^{2+}]_{cyto}$ increases from 0.3 μM, when V_{RyR} is 0.001 ms^{-1} , to around 0.37 μM, when V_{RyR} is 0.03 ms^{-1} (Figure 4.11 A). Further increases in V_{RyR} do not lead to a higher $[Ca^{2+}]_{cyto}$ elevation. ER contributes mainly as a Ca^{2+} sink at standard and lower levels of V_{RyR}, while, with an increase in V_{RyR} , it is more like as an internal Ca^{2+} source during stimulation (Figure 4.11 B). The peak Ca^{2+} flux via RyR, increases dramatically with the value of V_{RyR} and fluxtuates at high level of V_{RyR}, whereas the peak activity of the SERCA pumps is not affected (Figure 4.11 C).

Under a 10 Hz stimulation, from the second pulse onward, both the normalised $[Ca^{2+}]_{cyto}$ peak (Figure 4.12 A) and the Po_{RyR} peak (Figure 4.13 B) show a maximum value when V_{RyR} is between 0.05 to 0.03 ms^{-1}. Positive spikes in the net Ca^{2+} flux from ER, J_{RyR}, appear during stimulation (Figure 4.12 C). At 100 Hz, from the second pulse onward, the degree of increase in $[Ca^{2+}]_{cyto}$ peaks with V_{RyR} being attenuated over time (Figure 4.12 B). There is no difference in $[Ca^{2+}]_{cyto}$ dynamics across the testing range of V_{RyR} values after the 15th pulse. J_{ER} fluctuates around zero (Figure 4.12 D) and shows a balance between release and uptake of Ca^{2+} by ER.The Po_{RyR} does not show differences in response to a 100 Hz stimulation across the tested ranges the testing ranges of V_{RyR} from the second pulse onward (Figure 4.13 C). Moreoever, at all types of stimulation, the open time increases sharply with V_{RyR} and when V_{RyR} is below 0.01 ms^{-1} (Figure 4.13 C). At 1 Hz and 100 Hz, the total open time is almost stable with minor increases whereas, at 10 Hz, it decreases gradually from 129 ms to 122s while V_{RyR} increases from 0.01 ms^{-1} to 0.3 ms^{-1}.

The $[Ca^{2+}]_{RyR}$: $[Ca^{2+}]_{NMDAR}$ ratio generally increases with V_{RyR}, indicating a increasing contribution of RyR in Ca^{2+} entering the cytosol against NMDAR(Figure 4.12 E). Under 10 Hz and 100 Hz stimulations, it dramatically rises to around 0.13 and 0.14, respectively, when increasing V_{RyR} to 0.03 ms^{-1}, and then it gradually approaches 0.2 and 0.16, respectively. This suggests upregulation in RyR expression can increase the contribution of RyR to Ca^{2+} dynamics and the increase is larger at a lower frequency stimulation in comparison to a higher

one.

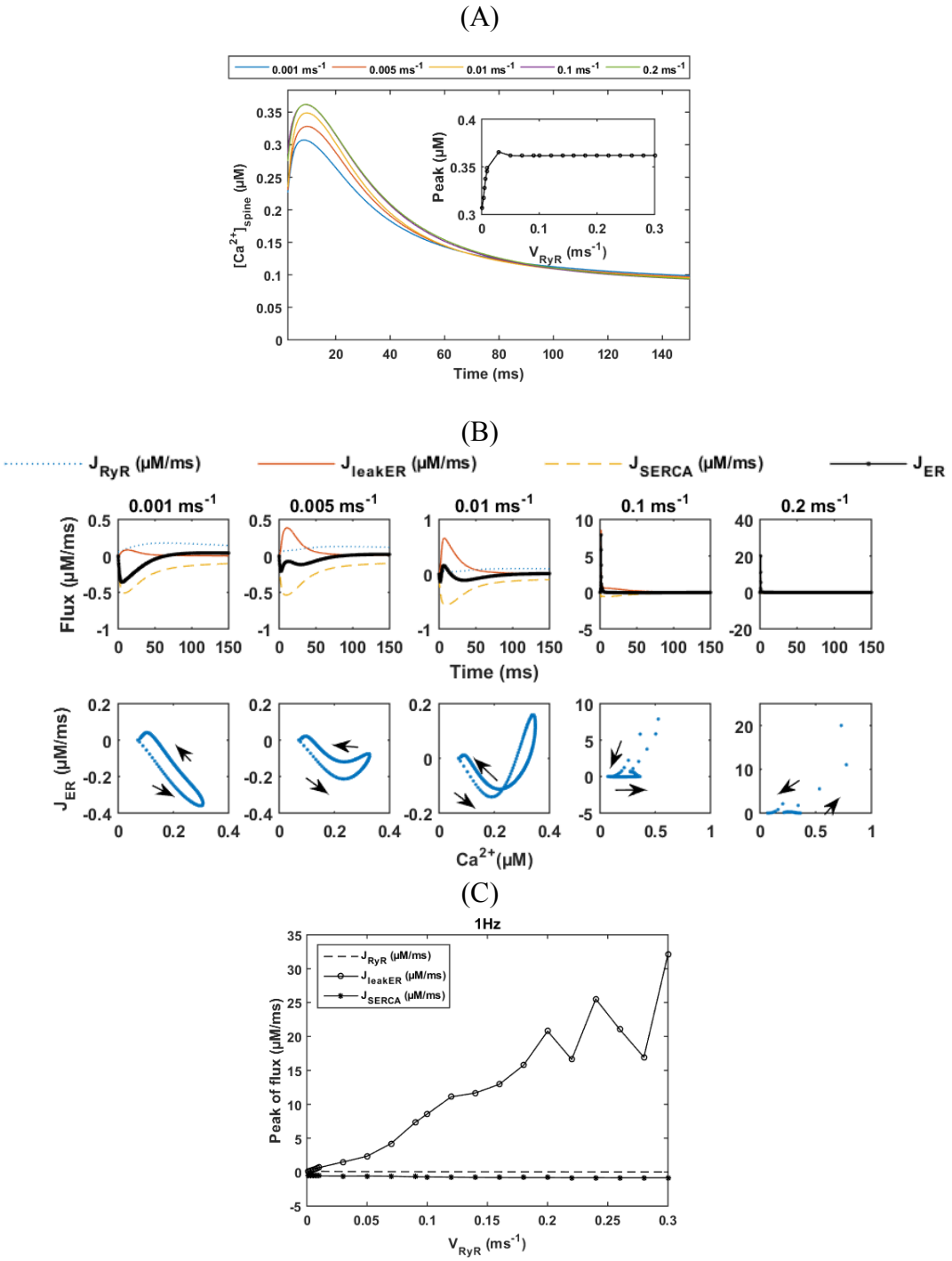

Figure 4.11. Effects of V_{RyR} on postsynaptic response by a single presynaptic stimulation pulse (1 Hz). (A) The $[Ca^{2+}]_{cyto}$ dynamics in the spine head and the relationship between V_{RyR} and the $[Ca^{2+}]_{cyto}$ peaks (insert). The corresponding Ca2+ responses of RyR (J_{RyR}) and the SERCA pump (J_{SERCA}), ER membrane leaking (J_{leakER}), and the net Ca2+ flux from the ER to the cytosol (J_{ER}) are shown in (B). Arrows in the bottom panel indicate the direction of time flow. The peaks of J_{RyR}, J_{SERCA} and J_{leakER} at different levels of V_{RyR} are in (C).

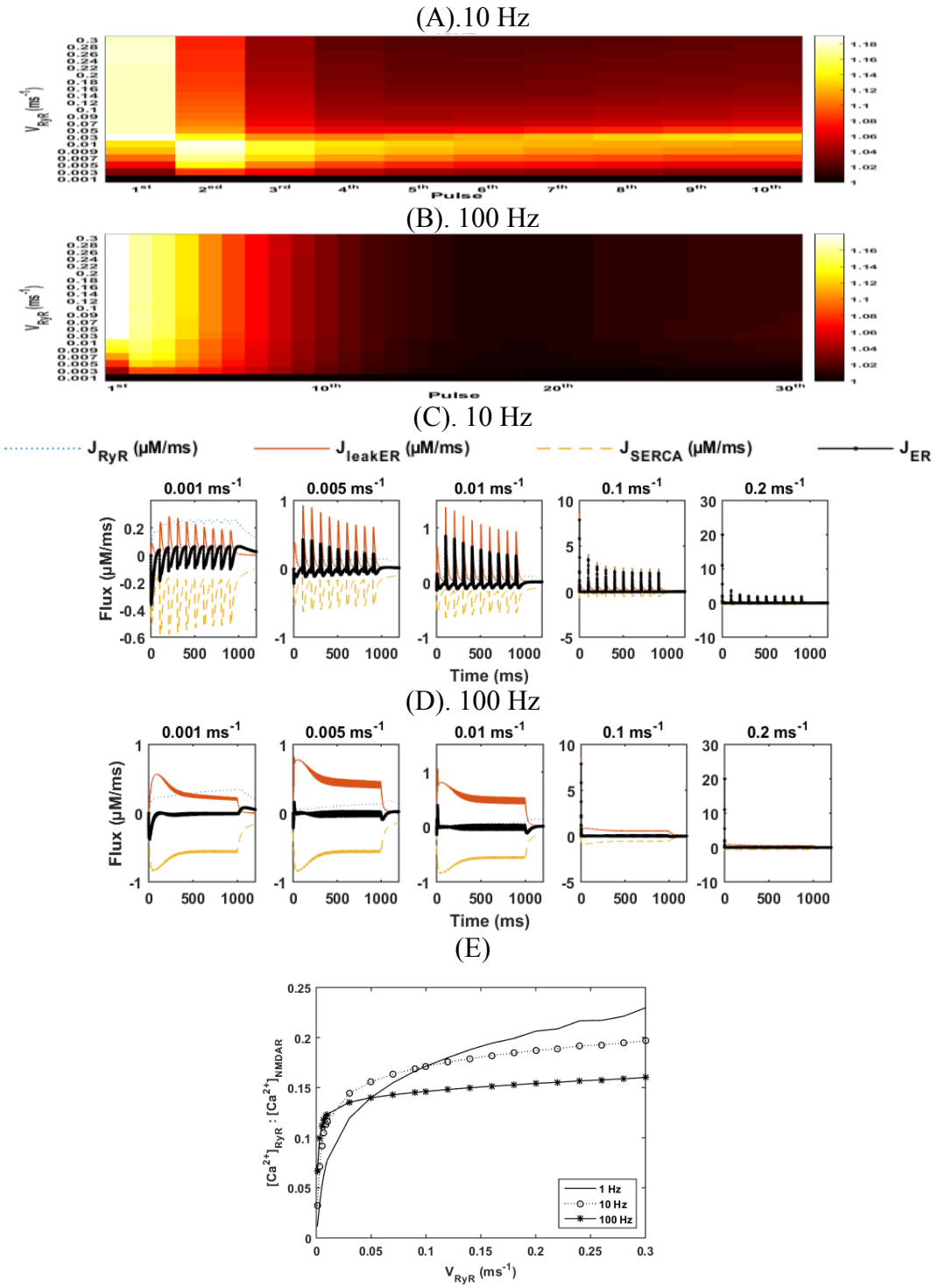

Figure 4.12. Effects of V_{RyR} on postsynaptic response under 1 s presynaptic stimulation at 10 Hz and 100 Hz, respectively. The $[Ca^{2+}]_{cyto}$ peaks in response to different stimulation pulses at a 10 Hz (A) and a 100 Hz stimulation (B), respectively are normalised to the one with the lowest V_{RyR} at each pulse. The colour density represents the values of $[Ca^{2+}]_{cyto}$ peaks in the spine head. Under the 100 Hz stimulation, only the first 30 pulses are shown in the figure since there is no difference afterwards. The corresponding Ca2+ responses of RyR (J_{RyR}) and the SERCA pump (J_{SERCA}), ER membrane leaking (J_{leakER}), and the net Ca2+ flux from the ER to the cytosol (J_{ER}) are shown in (C) and (D), respectively. (E) Effects of rising V_{RyR} on $[Ca^{2+}]_{RyR}$: $[Ca^{2+}]_{NMDAR}$ ratio.

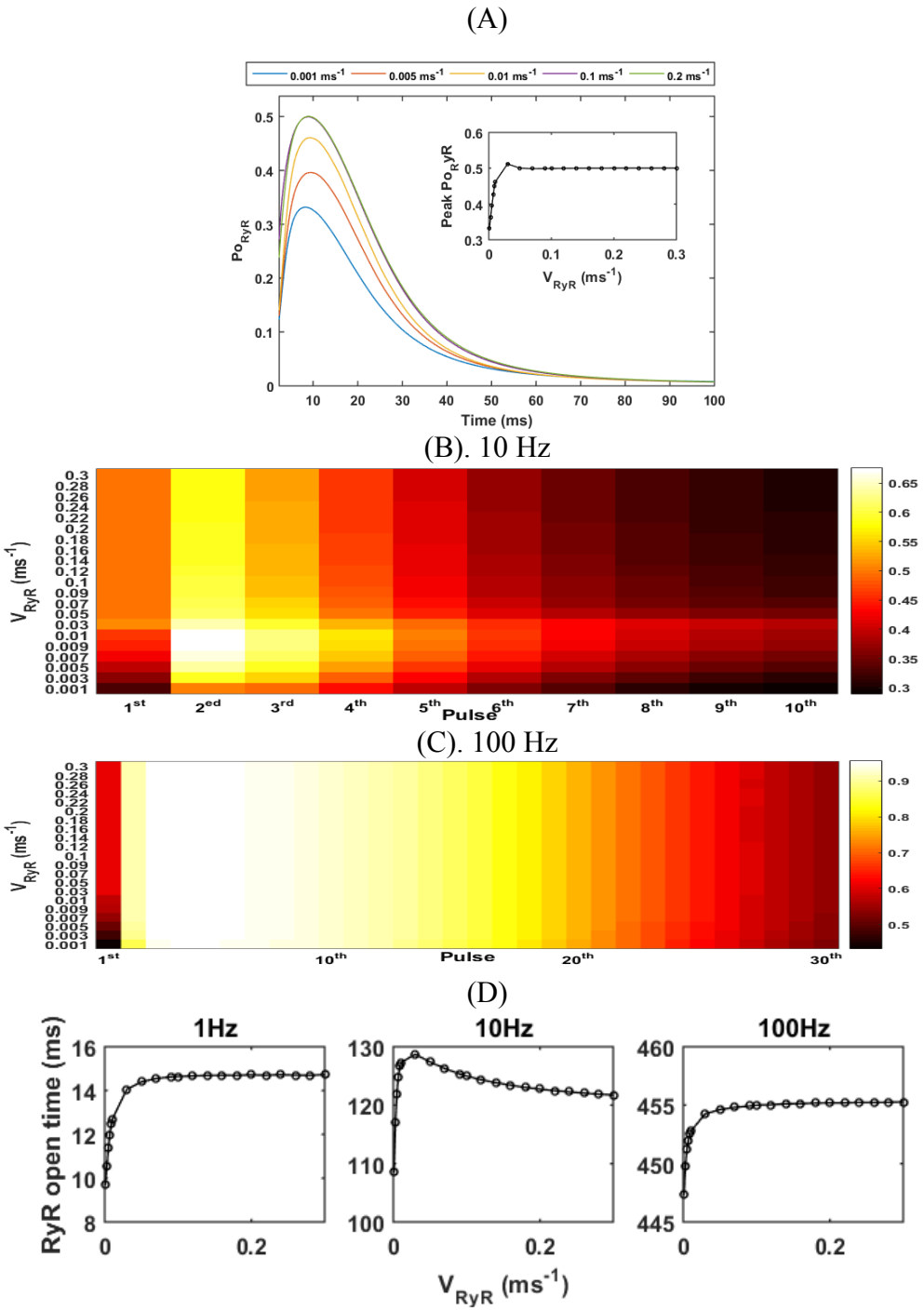

Figure 4.13. Effects of V_{RyR} on RyR opening. (A) The Po_{RyR} with time in the spine head and the relationship between V_{RyR} and the Po_{RyR} peaks (insert) at a 1 Hz stimulation. The heatmaps show the maximums of Po_{RyR} in response to different stimulation pulses at a 10 Hz (B) and a 100 Hz stimulation (C), respectively. The colour density represents the values of Po_{RyR} peaks in the spine head. Under the 100 Hz stimulation, only the first 30 pulses are shown in the figure since there is no difference afterwards. (D) The corresponding total opening times of RyR at stimulations with different frequencies.

4.3.3 RyR upregulation at ER with various Ca^{2+} load

Experiments with AD animal models suggest that the increase in RyRs expression may be because the neurons attempt to compensate for the ER Ca^{2+} overload (Zhang, Sun et al. 2010). However, the upregulation of RyR expression can cause pathogenic cytosol Ca^{2+} elevation by increasing the Ca^{2+} release from ER. Therefore, we examine the system responses at various levels of $[Ca^{2+}]_{ER0}$ (30 – 600 μM) and V_{RyR} (0.001 - 0.15 ms^{-1}).

At a 1 Hz stimulation or the stimulation by the first pulse of multi-pulse stimulation, the $[Ca^{2+}]_{cyto}$ peak generally increases with higher levels of $[Ca^{2+}]_{ER0}$ and V_{RyR} (Figure 4.14A). At a 10 Hz stimulation, the $[Ca^{2+}]_{cyto}$ peak increases with V_{RyR} and reaches the first maximum level when V_{RyR} is around 0.02 ms^{-1} (Figure 4.14B). It then decreases with further increases in V_{RyR}; then when $[Ca^{2+}]_{ER0}$ is above 200 μM, it increases again with V_{RyR}. The $[Ca^{2+}]_{cyto}$ peak-V_{RyR} relationship is transformed from a single-peak to a double-peak, with the increase of the $[Ca^{2+}]_{ER0}$. Under a 100 Hz stimulation the $[Ca^{2+}]_{cyto}$ peaks show similar patterns in response to different simulation pulses from the second pulse onward (Figure 4.14C). At each degree of $[Ca^{2+}]_{ER0}$, the $[Ca^{2+}]_{cyto}$ peak increases with V_{RyR} when V_{RyR} is below 0.02 ms^{-1}, and is not affected by V_{RyR} when V_{RyR} is greater. In contrast, as the degree of $[Ca^{2+}]_{ER0}$ becomes higher, the $[Ca^{2+}]_{cyto}$ peaks increase across the tested ranges of V_{RyR}.

(A). 1 HZ or 1 pulse of multi-pulse stimulation

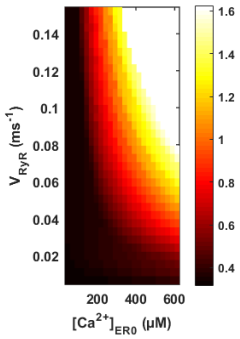

(B). 10 HZ

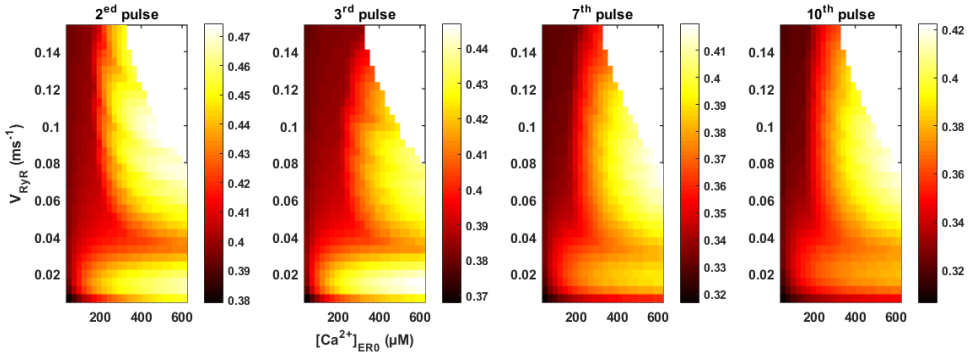

(C). 100 HZ

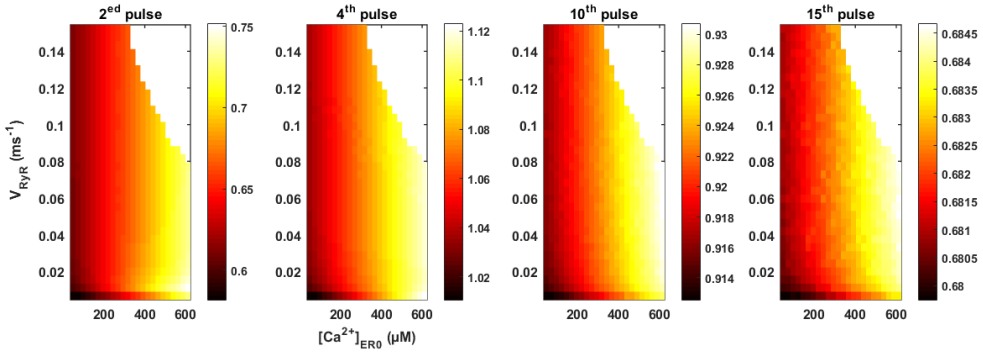

Figure 4.14. Ca^{2+} response at various level of $[Ca^{2+}]_{ER0}$ and V_{RyR} at a (A) 1 Hz (A), (B) 10 Hz and (C) 100 Hz stimulation. Figures (B) and (C) show $[Ca^{2+}]_{cyto}$ peaks at selected stimulation pulse. The colour density represents the values of $[Ca^{2+}]_{cyto}$ peaks in the spine head.

The $[Ca^{2+}]_{RyR}$: $[Ca^{2+}]_{NMDAR}$ ratio increases with $[Ca^{2+}]_{ER0}$ and V_{RyR} at all tested stimulation frequencies (Figure 4.15 A). As the frequency is higher, the $[Ca^{2+}]_{RyR}$: $[Ca^{2+}]_{NMDAR}$ ratio is easier to obtain a higher level than at a lower degree of $[Ca^{2+}]_{ER0}$ and V_{RyR}. This suggests that ER, as the internal Ca^{2+} source, makes a high contribution to the cytosolic response under conditions of RyR expression and ER Ca^{2+} overload. The results of the total open time of RyR under presynaptic stimulation (Figure 4.15 B) show similar pattern to ones of the $[Ca^{2+}]_{cyto}$ peaks in Figure 4.14. Under 10 Hz

stimulation, a peak value appears when V_{RyR} is around 0.02 ms^{-1}. At 100 Hz, RyR opens for a longer time as the increase in the $[Ca^{2+}]_{ER0}$ and V_{RyR}, where when V_{RyR} is above 0.03 ms^{-1}, it does not affect the open time with a fixed $[Ca^{2+}]_{ER0}$.

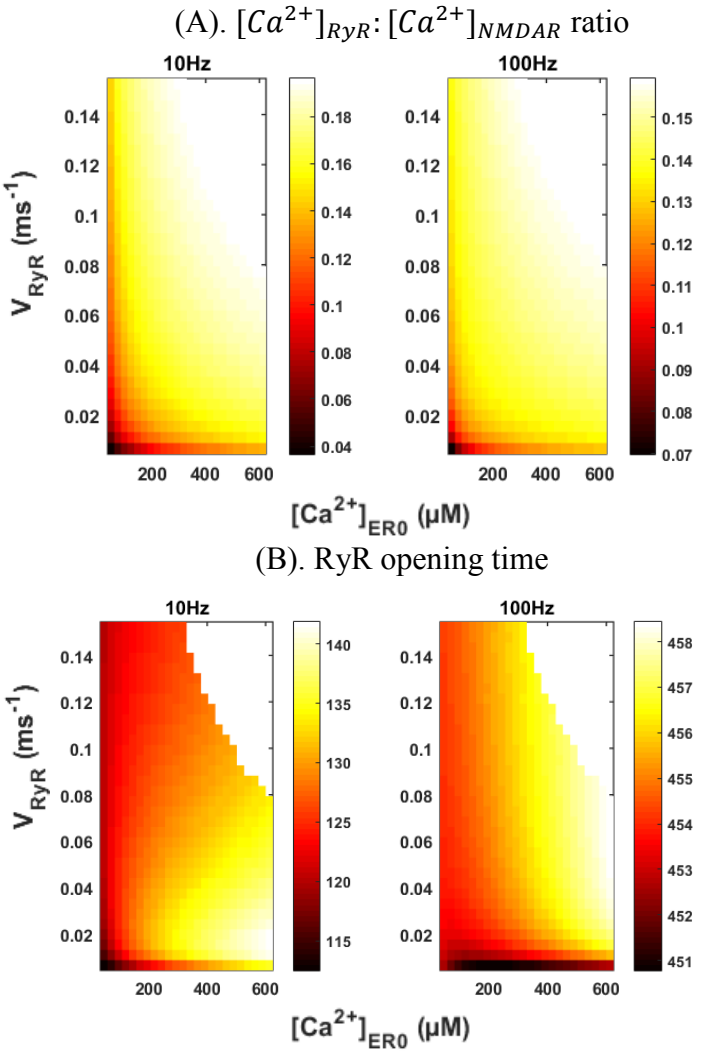

Figure 4.15. (A)$[Ca^{2+}]_{RyR}$: $[Ca^{2+}]_{NMDAR}$ ratio and (B) RyR opening time at various level of $[Ca^{2+}]_{ER0}$ and V_{RyR}. The colour density represents the values of the $[Ca^{2+}]_{RyR}$: $[Ca^{2+}]_{NMDAR}$ ratio and the RyR opening time in the spine head, respectively.

4.3.4 SERCA pump reduction

We manipulate the maximum rate of SERCA pump, v_{SERCA}, to see the effect of Ca^{2+} uptake by ER on Ca^{2+} response. The $[Ca^{2+}]_{cyto}$ peak decreases from 0.37 μM to 0.3 μM when the v_{SERCA} increases from 0.01 to 1.5 μM/ms (Figure 4.16 A) at 1 Hz stimulation. The net ER

Ca^{2+} flux is negative but has a lower amplitude as the value of v_{SERCA} increases (Figure 4.16 B). The Ca^{2+} fluxes via SERCA pump as well as via RyR and membrane leaking are enhanced by larger v_{SERCA} (Figure 4.16 C). Under a 10 Hz stimulation, the normalised $[Ca^{2+}]_{cyto}$ peak slightly increases with v_{SERCA} from the second pulse onward (Figure 4.17 A), whereas with a 100 Hz stimulation, a reduced degree of reduction in the $[Ca^{2+}]_{cyto}$ peak with v_{SERCA} from the second pulse onward, and after the 4th pulse, there is no obvious difference in $[Ca^{2+}]_{cyto}$ peak with v_{SERCA} (Figure 4.17 B). The net ER Ca^{2+} flux is negative with decreasing amplitude when v_{SERCA} is below 0.9 under a 10 Hz stimulation (Figure 4.17 C). At a high level of v_{SERCA} (1.5 μM/ms), positive spikes in the net ER Ca^{2+} flux appear from the second stimulation pulse onward. This is because the RyR response to Ca^{2+} is greatly enhanced by a larger v_{SERCA} in comparison with the Ca^{2+} flux via SERCA pumps and membrane leaking (Figure 4.17 E). In contrast, with a 100 Hz stimulation, the peak Ca^{2+} flux via SERCA pumps stays at around -1.5 μM/ms across the testing range of v_{SERCA} value (Figure 4.17 F), which is around -1 μM/ms at the 1 and 10 Hz stimulations. This is because of the high Ca^{2+} influx via NMDAR under a 100 Hz stimulation. which leads to a high inward net Ca^{2+} flux from the cytosol to the ER. The peak of the net flux decreases with v_{SERCA} (Figure 4.17 D). Moreover, the $[Ca^{2+}]_{RyR}$: $[Ca^{2+}]_{NMDAR}$ ratio shows a linear increase with v_{SERCA} at all frequencies of stimulation, with a larger slope at the higher frequency (Figure 4.18).

The fraction of RyR opened by the 1 Hz stimulation shows a decrease in the peak, from 0.5 to 0.34, when v_{SERCA} increases from 0.01 to 1.5 μM/ms (Figure 4.19 A). At 100 Hz, the maximum Po_{RyR} increases to a peak of around 95% from the second stimulation pulse to the eighth one, and decreases gradually afterwards. There is no difference in the maximum of Po_{RyR} from different Po_{RyR} (Figure 4.19 C). However, under the 10 Hz stimulation, the pattern of maximum Po_{RyR} switches to increasing with v_{SERCA} from the second pulse onward (Figure 4.19 B). The total open time of RyR decreases by 4.4 ms and 5.3 ms when increasing v_{SERCA} from 0.01 to 1.5 μM/ms at 1 and 100 Hz stimulations, respectively (Figure 4.19 D). Under 10 Hz stimulation, a bell-shaped relationship between the RyR open time and v_{SERCA}, with the peak value, appears when v_{SERCA} is around 0.6 μM/ms.

(A)

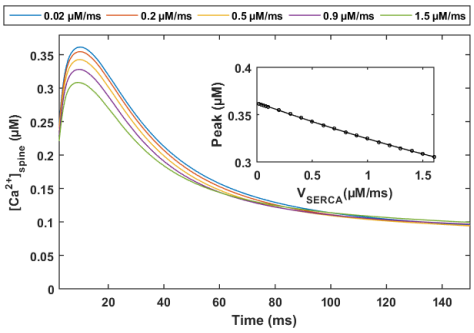

(B).

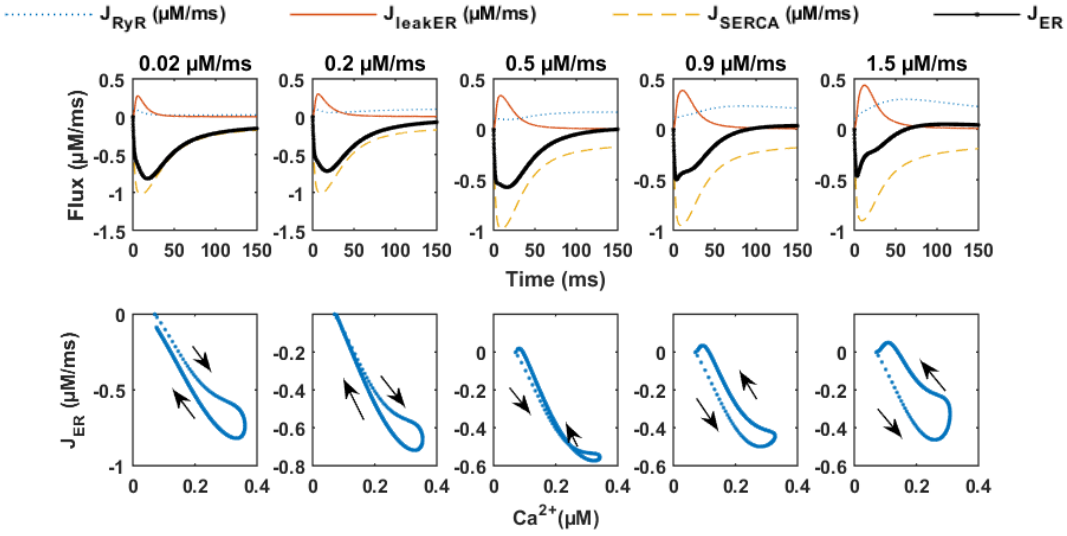

(C)

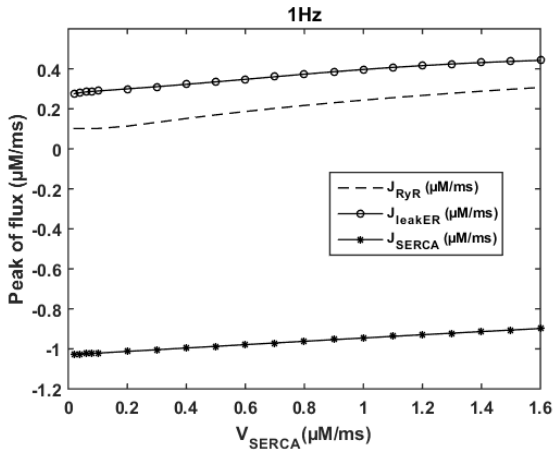

Figure 4.16. Effects of v_{SERCA} on postsynaptic response by a single presynaptic stimulation pulse (1 Hz). (A) The $[Ca^{2+}]_{cyto}$ dynamics in the spine head and the relationship between v_{SERCA} and the $[Ca^{2+}]_{cyto}$ peaks (insert). The corresponding Ca^{2+} responses of RyR (J_{RyR}) and the SERCA pump (J_{SERCA}), ER membrane leaking (J_{leakER}), and the net Ca^{2+} flux from the ER to the cytosol (J_{ER}) are shown in (B). Arrows in the bottom panel indicate the direction of time flow. The peaks of J_{RyR}, J_{SERCA} and J_{leakER} at different levels of v_{SERCA} are in (C).

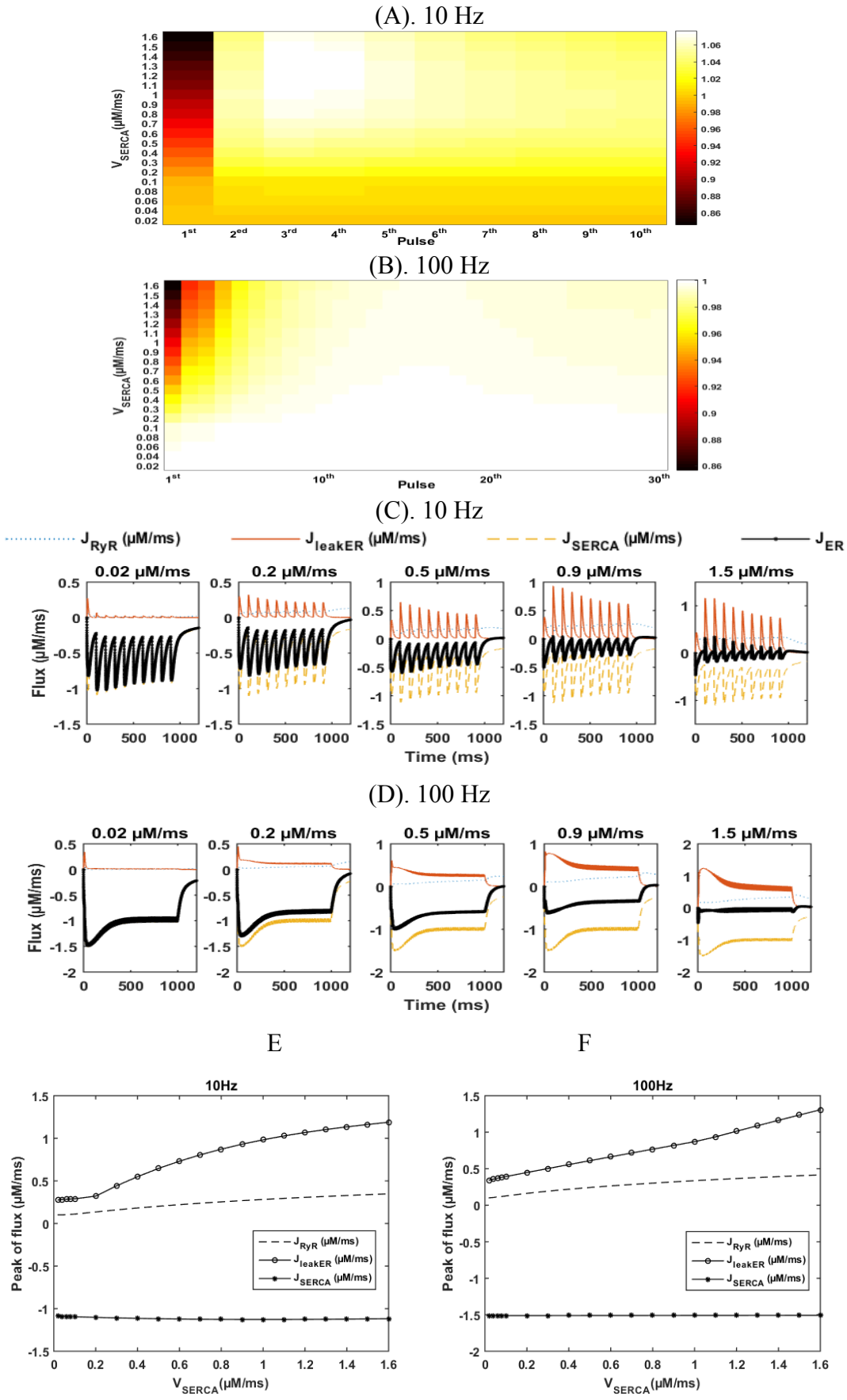

Figure 4.17. Effects of v_{SERCA} on postsynaptic response under 1 s presynaptic stimulation at 10 Hz and 100 Hz, respectively. The $[Ca^{2+}]_{cyto}$ peaks in response to

different stimulation pulses at a 10 Hz (A) and a 100 Hz stimulation (B), respectively are normalised to the one with the lowest v_{SERCA} at each pulse. The colour density represents the values of $[Ca^{2+}]_{cyto}$ peaks in the spine head. Under the 100 Hz stimulation, only the first 30 pulses are shown in the figure since there is no difference afterwards. The corresponding Ca^{2+} responses of RyR (J_{RyR}) and the SERCA pump (J_{SERCA}), ER membrane leaking (J_{leakER}), and the net Ca^{2+} flux from the ER to the cytosol (J_{ER}) are shown in (C) and (D), respectively. The peaks of J_{RyR}, J_{SERCA} and J_{leakER} at different levels of v_{SERCA} are in (E) and (F).

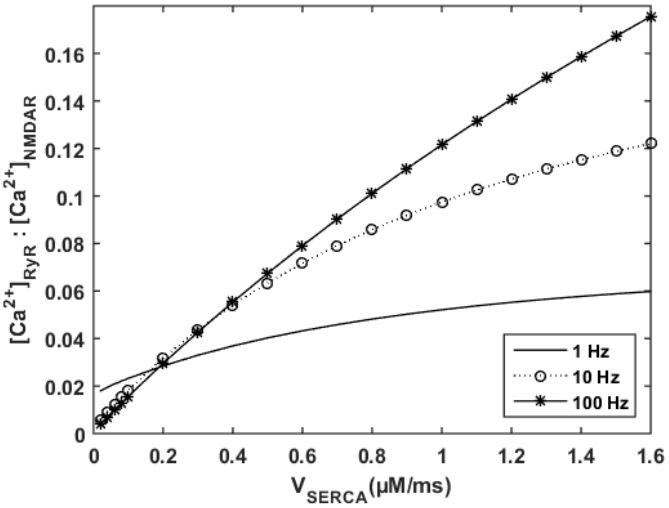

Figure 4.18. Effects of v_{SERCA} on $[Ca^{2+}]_{RyR}$: $[Ca^{2+}]_{NMDAR}$ ratio at 1 Hz, 10 Hz and 100 Hz stimulation, respectively.

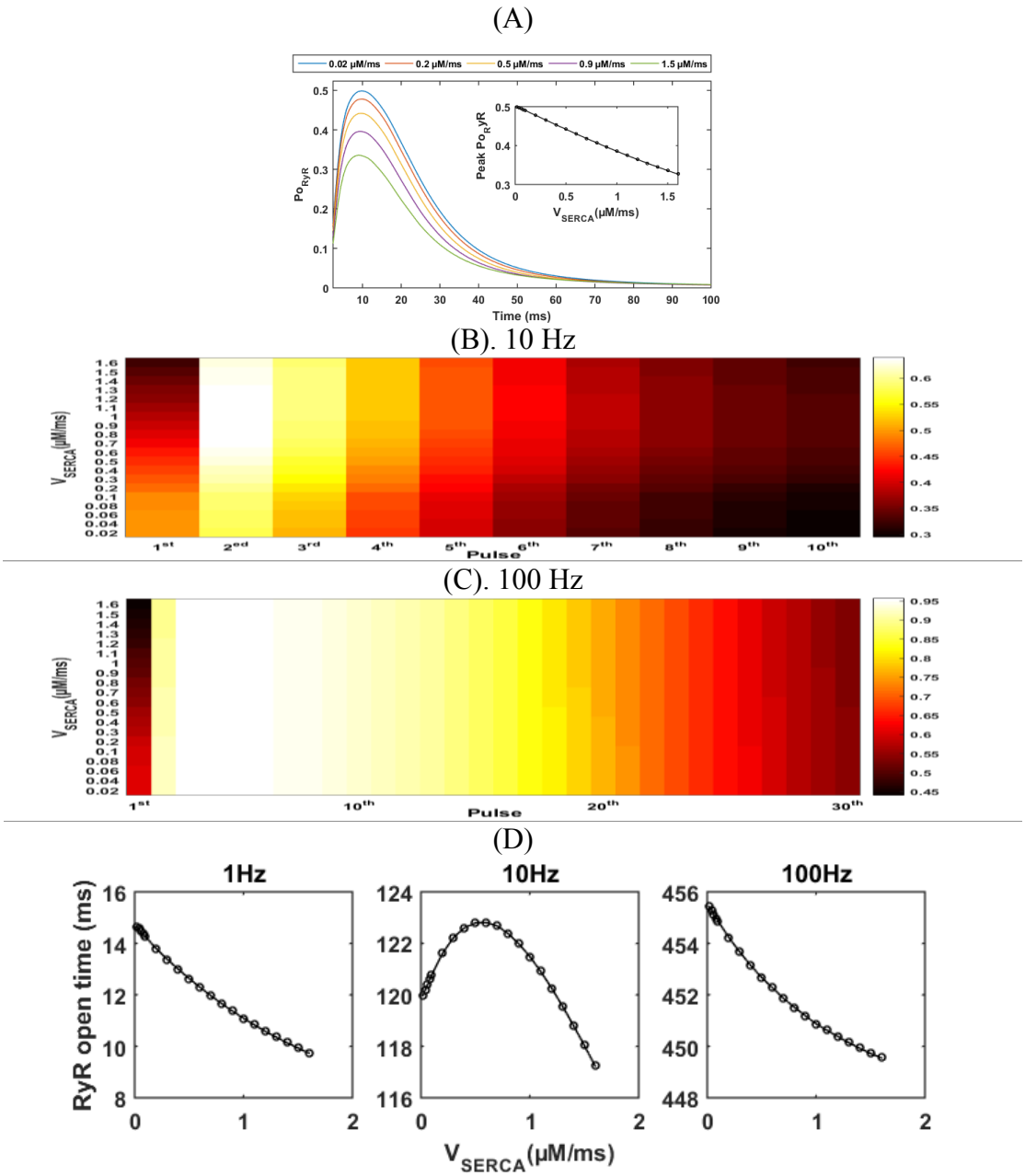

Figure 4.19. Effects of v_{SERCA} on RyR opening. (A) The Po_{RyR} with time in the spine head and the relationship between v_{SERCA} and the Po_{RyR} peaks (insert) at a 1 Hz stimulation. The heatmaps show the maximums of Po_{RyR} in response to different stimulation pulses at a 10 Hz (B) and a 100 Hz stimulation (C), respectively. The colour density represents the values of Po_{RyR} peaks in the spine head. Under the 100 Hz stimulation, only the first 30 pulses are shown in the figure since there is no difference afterwards. (D) The corresponding total opening times of RyR at stimulations with different frequencies.

4.3.5 Alteration in SERCA pumps at ER with various Ca^{2+} load

Green, Demuro et al. (2008) reported that PS interacts with SERCA pump to modulate its function and lack of PS impaires the SERCA pumps function in *Xenopus laevis* oocytes. However, it is not clear how the PS mutation in AD will affect SERCA pumping. However, Brunello, Zampese et al. (2009) produced opposite results that both wild-type and mutant PS2 could reduce SERCA activity. Therefore, we examine the system responses at various levels of $[Ca^{2+}]_{ER0}$ (30 – 600 μM) and $\boldsymbol{v_{SERCA}}$ (0.01 – 1.2 μM/ms), to investigate the possible contribution of SERCA alteration in the Ca^{2+} elevation in the spine head.

At a 1 Hz stimulation or the stimulation by the first pulse of multi-pulse stimulation, the $[Ca^{2+}]_{cyto}$ peak increases with higher levels of $[Ca^{2+}]_{ER0}$ and lower levels of v_{SERCA} (Figure 4.20 A). The results show similar pattern inresponse to the second pulse onward at 100 Hz stimulation, and C). In contrast, at a 10 Hz stimulation, the $[Ca^{2+}]_{cyto}$ peak from the second pulse onward increases with the decrease in $\boldsymbol{v_{SERCA}}$ when $[Ca^{2+}]_{ER0}$ belows 150 μM and shift to decrease with the decrease in $\boldsymbol{v_{SERCA}}$ at higher levels of $[Ca^{2+}]_{ER0}$ (Figure 4.20 B).

At both 10 and 100 Hz stimulations, the $[Ca^{2+}]_{RyR}$: $[Ca^{2+}]_{NMDAR}$ ratio increases with v_{SERCA}, but only increases with $[Ca^{2+}]_{ER0}$ at lower levels of $[Ca^{2+}]_{ER0}$(Figure 4.21A). This suggests that the expression level of SERCA pumps promotes the role as an internal Ca^{2+} source by ER at variouse resting Ca^{2+} level of ER. Figure 4.21B shows that the results of the RyR opening time have simlar pattern to ones of the $[Ca^{2+}]_{cyto}$ peaks in Figure 4.20, in response to different simulation pulses. At 10 Hz stimualtion, lower levels of v_{SERCA} lead to higher levels of $[Ca^{2+}]_{RyR}$: $[Ca^{2+}]_{NMDAR}$ when $[Ca^{2+}]_{ER0}$ belows 150 μM, while, at higer levels of $[Ca^{2+}]_{ER0}$, higher levels of v_{SERCA} lead to higher levels of $[Ca^{2+}]_{RyR}$: $[Ca^{2+}]_{NMDAR}$. At a 100 Hz stimualtion, the RyR opening time generally increases with $[Ca^{2+}]_{ER0}$ and decreases with v_{SERCA}.

(A). 1 HZ or 1 pulse of multi-pulse stimulation

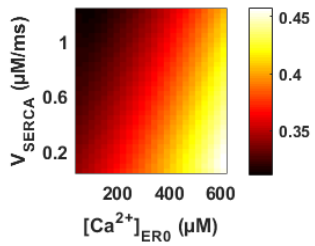

(B). 10 HZ

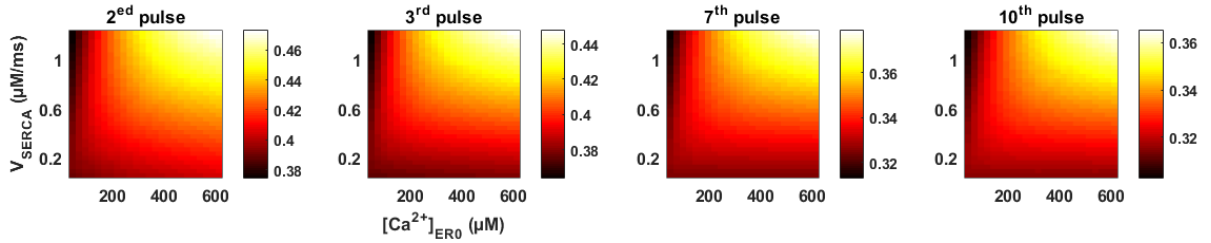

(C). 100 HZ

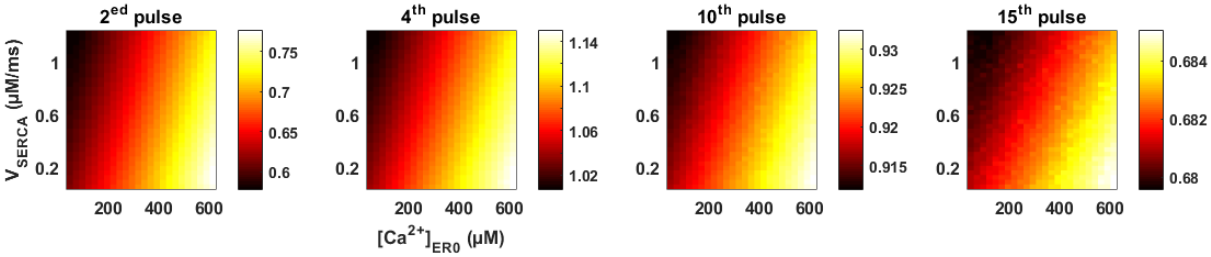

Figure 4.20. Ca^{2+} response at various level of $[Ca^{2+}]_{ER0}$ and v_{SERCA} at a (A) 1 Hz (A), (B) 10 Hz and (C) 100 Hz stimulation. Figures (B) and (C) show $[Ca^{2+}]_{cyto}$ peaks at selected stimulation pulse. The colour density represents the values of $[Ca^{2+}]_{cyto}$ peaks in the spine head.

(A). $[Ca^{2+}]_{RyR}$: $[Ca^{2+}]_{NMDAR}$ ratio

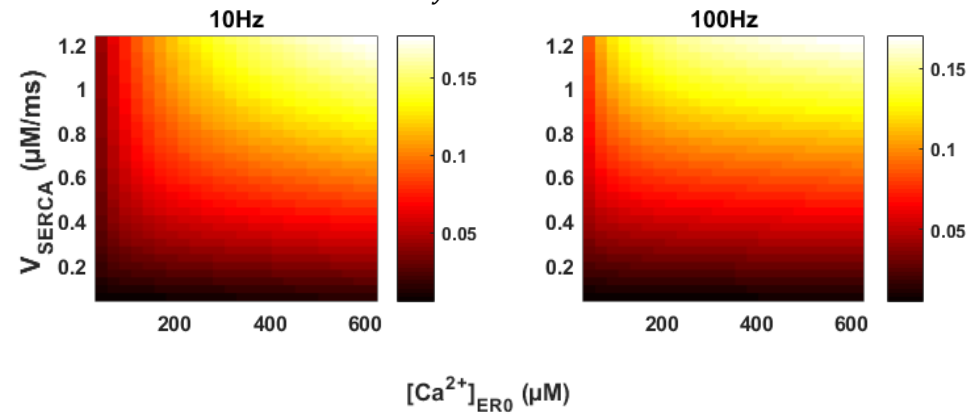

(B). RyR opening time

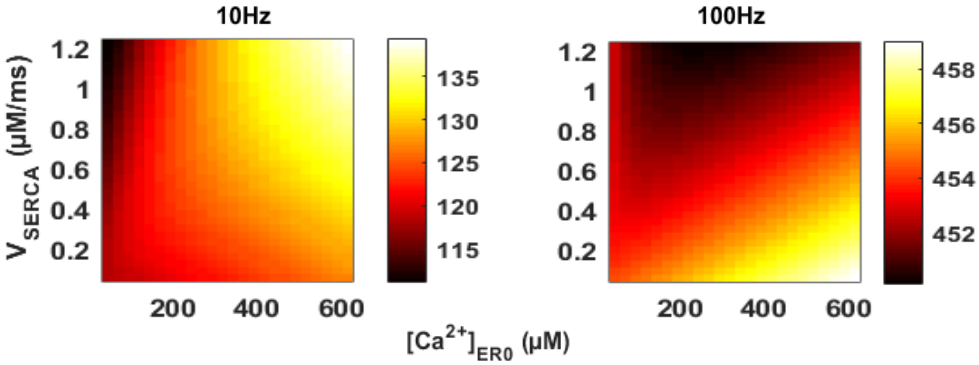

Figure 4.21. (A) RyR opening time and (A)$[Ca^{2+}]_{RyR}$: $[Ca^{2+}]_{NMDAR}$ ratio at various levels of $[Ca^{2+}]_{ER0}$ and v_{SERCA}. The colour density represents the values of the $[Ca^{2+}]_{RyR}$: $[Ca^{2+}]_{NMDAR}$ ratio and the RyR opening time in the spine head, respectively.

4.4 Discussion and conclusions

In this chapter, we use an extended model from the one in Chapter 3 to investigate the effects of the alteration of several of the main factors in ER in the postsynaptic response. We look at the relationship of Ca^{2+} transient levels, net ER Ca^{2+} fluxes, RyR opening and its contribution to cytosolic Ca^{2+} elevation and the relationship between them and selected alterations of ER function, as reported in AD.

The simulation predicts that the ER Ca^{2+} overload and up-regulation in RyR expression will enhance its role as an internal Ca^{2+} source to amplify the external Ca^{2+} influx. This is on account of the longer open times of RyR or the reduction in Ca^{2+} uptake by SERCA pumps. The increase in RyR response suggests a reduced CICR threshold, which means RyR shows higher sensitivity to the NMDAR-mediated Ca^{2+} signal under these conditions. This alteration can promote the processing of amyloid precursor protein (APP) to facilitate the production of Aβ peptides (Querfurth, Jiang et al. 1997). In addition, experimental studies suggest that up-regulation of RyR expression may be a compensatory mechanism to the Ca^{2+} overload in the ER in the early stages of AD (Del Prete, Checler et al. 2014). Our simulation predicts that at high levels of ER Ca^{2+}, low levels of up-regulation in RyR expression will increase all outputs. However, when the up-regulation in RyR expression is higher, it shows less effect on all outputs. This suggests that, although an increase in RyR expression may be beneficial to ease the stress of ER from Ca^{2+} overloading, it may, however, make the cell more vulnerable by amplifying the cytosolic Ca^{2+} level.

A stimulation frequency-dependant effects in the outputs has been observed when applying multiple stimulation pulses at various stimulation frequencies. The overall enhanced effect on the postsynaptic Ca^{2+} response is higher under low-frequency stimulation (10 Hz) in comparison with high-frequency stimulation (100 Hz). For example, manipulating the selected factors shows no obvious effects on the peak of Ca^{2+} elevation and maximum fraction of RyR opened in response to presynaptic stimulation at 100 Hz from the second pulse onward; whereas a clear pattern with the level of selected factors can be observed under 10 Hz stimulation. This implies that the alteration is more likely to amplify the NMDAR-mediated Ca^{2+} signal with a lower frequency and lower amplitude, consistent with the experimental observations (Chakroborty, Goussakov et al. 2009). This will affect the basal synaptic transmission or may bring the basal synaptic transmission to a long-term depression.

Less is studied on the alteration of SERCA pumps than of RyRs and ER Ca^{2+} load in ER. Green, Demuro et al. (2008) and Brunello, Zampese et al. (2009) suggest opposites effects on SERCA pumps by PS and PS mutation in AD. Here, we predict opposite effects by the alteration of SERCA pumps in the Ca^{2+} signalling in the spine head, which shows an interesting frequency-dependence. Higher levels of SERCA pumps can increase the Ca^{2+} uptake by ER. At the same time, it leads to a faster refilling of Ca^{2+} by ER and thus, promotes the Ca^{2+} release from ER at the same time. At high-frequency stimulation, an increase in the level of SERCA pumps causes a shorter opening for RyR; however, it speeds up the replenishment of ER with Ca^{2+}, leading to a higher Ca^{2+} release via RyR from ER. Even though the increase in SERCA will lead to an exceeding amount of Ca^{2+} ions removed from the cytosol to ER, this overcomes the effect of increasing Ca^{2+} release by RyR and accounts for the decreasing in the elevation of cytosol Ca^{2+} transients. At low-frequency stimulation, because the Ca^{2+} influx via NMDAR is lower than at high frequency, the Ca^{2+} uptake by ER enhanced by the upregulation in the SERCA pumps is not high enough to compromise the increasing Ca^{2+} release from ER. Therefore, the cytosolic Ca^{2+} signal is amplified by the upregulation in SERCA pumps.

The simulation results suggest that inhibit SERCA pumps may rescue the spine head from dysregulation in Ca^{2+} signalling by ER Ca^{2+} overload. At low-level stimulation, inhibition of SERCA pumps will reduce the Ca^{2+} from ER by attenuating the refilling of Ca^{2+} by ER. At high stimulation, although inhibit SERCA pumps will increase the Ca^{2+} release from ER, long-term inhibition will decrease the Ca^{2+} load of ER. Besides, Green, Demuro et al. (2008) reported that decrease the SERCA function can reduce the production of Aβ, which may be a consequence of reduced ER Ca^{2+} signalling.

Chapter 5
Modelling and analysis of NMDAR-dependent State Transition of CaMKII under AD condition

NMDAR-dependent LTP (NMDAR-LTP) is a widely studied form of LTP which can be found in the glutamatergic synapse in the hippocampus (Isaac, Nicoll et al. 1995, Durand, Kovalchuk et al. 1996, Lüscher and Malenka 2012). Recent studies suggest the roles of NMDAR in synaptic plasticity are determined by their subunit composition and location of NMDARs (Barria and Malinow 2005, Paoletti, Bellone et al. 2013). There have been contradictory experimental observations made about which subunit composition predominantly mediates the NMDAR-LTP. For instance, preferential blocking of NR2A-NMDARs inhibits LTP in slices of the hippocampal CA1 area (Liu, Wong et al. 2004) and the perirhinal cortex of rats (Massey, Johnson et al. 2004). Blocking NR2B by ifenprodil abolishes LTD but does not affect LTP, suggesting that NR2B-NMDAR is only required for LTD induction (Liu, Wong et al. 2004). However, overexpression of NR2B in the transgenic mouse forebrain shows enhanced LTP in response to stimulation at 10-100 Hz (Tang, Shimizu et al. 1999). Knock-down of the NR2B subunit in the hippocampus of young rats suppresses LTP formation (Clayton, Mesches et al. 2002). These conflicting results may arise from the differences in the types and concentrations of the antagonists, the experimental conditions, the developmental stages and the location of brain regions of the experimental materials.

One possible reason underlying the different contributions of NR2A- and NR2B-NMDAR to the synaptic plasticity may be because of the different kinetic properties of NR2A-NMDAR and NR2B-NMDAR (Erreger, Dravid et al. 2005, Paoletti, Bellone et al. 2013). Moreover, the different preferences by other key molecular players in synaptic plasticity may also determine their different contributions (Barria and Malinow 2005). Therefore, it is important to investigate the different roles of NMDAR collectively. In this chapter, we explore the effects of disturbances on NMDAR availability under AD conditions on the Ca^{2+} signalling and downstream CaMKII activation, a key event in NMDAR-LTP induction and maintenance (Malenka, Nicoll et al. 1999).

NMDAR-LTP in the hippocampus is induced by the NMDAR-mediated Ca^{2+} influx in the dendritic spine. The transient Ca^{2+} signal is then transferred into a long-lasting enhancement

of synaptic strength, which is believed to contribute to memory formation (Malenka, Nicoll et al. 1999). The induction of LTP as a long-lasting increase in synaptic strength requires CaMKII activation; however, the mechanism of its maintenance is under debate (Barria and Malinow 2005, Lee, Escobedo-Lozoya et al. 2009, Lisman, Yasuda et al. 2012). The autophosphorylation of CaMKII, and its translation into the PSD in the CA1 region of hippocampal slices, have been observed after NMDAR-mediated Ca^{2+} transients (Fukunaga, Muller et al. 1995, Strack and Colbran 1998, Merrill, Chen et al. 2005). CaMKII is a holoenzyme consisting of 12 subunits that are autoinhibited at resting Ca^{2+} levels. The Ca^{2+} ions entering the cytosol will bind to calmodulin (CaM) to form the fully-bound Ca_4CaM complex, Ca_4CaM, which can activate CaMKII by binding to its CaM footprint. This leads to the exposure of the threonine 286 (Thr286) site of CaMKII and the subunit can then be autophosphorylated by active neighbouring subunits (Lisman, Schulman et al. 2002). The autophosphorylated CaMKII is CaM-independent and shows persistent activity long after the Ca^{2+} transients (Kennedy, Bennett et al. 1990, Hudmon and Schulman 2002).

The translocation of CaMKII into PSD is also mediated by Ca_4CaM. This process is reversible, while autophosphorylation of CaMKII at Thr286 can persist its presence in the PSD for a longer time. CaMKII in PSD can phosphorylate synaptic AMPARs, which can enhance their conductance and increase their numbers in the PSD by mediating their trafficking (Lisman, Schulman et al. 2002). This will, consequently, lead to an enhanced AMPAR-mediated transmission during LTP (Derkach, Barria et al. 1999). Once the CaMKII is translocated into the PSD, it can also bind to synaptic NR2B at the T-site (Bayer, LeBel et al. 2006). The CaMKII-NMDAR complex anchors AMPAR by creating new anchoring sites for additional synaptic AMPAR (Lisman and Zhabotinsky 2001, Sanhueza and Lisman 2013). We do not consider the binding of CaMKII to NR2A-NMDAR because of its lower affinity in comparison to NR2B-NMDAR (Barria and Malinow 2005).

The role of synaptic NR2B in forming CaMKII-NMDAR complex in the PSD is independent from its role as a Ca^{2+} channel (Foster, McLaughlin et al. 2010). Given the dual role of NR2B-NMDAR in NMDAR-LTP formation and the differential disturbances in NR2A- and NR2B NMDARs in AD, it raises questions: how different disturbances of NMDAR reported in AD affect CaMKII ST? Which disturbance predominantly suppresses NMDAR-LTP formation? What pathological consequences in AD may these effects link to? To answer these questions, we incorporate a CaMKII state transition (ST) model into our Ca^{2+} model (Figure 5.1A). In this chapter, we use the term Ca^{2+} model to refer to the model we present in Chapter

3 and 4.The simulation results show that both NR2A- and NR2B-NMDAR are necessary for CaMKII ST and it requires cooperation between them. The model provides insights into the potential contribution of the different roles of NMDAR in the formation of NMDAR-mediated-LTP. The simulation results also suggest that the disturbance in synaptic NMDAR in AD could be a potential cause of other critical changes in the pathology of the disease, which are related to the learning and memory deficit in AD patients.

In this chapter, we briefly introduce the CaMKII ST model by He, Kulasiri et al. (2015) and the integration of it to our Ca^{2+} model in Section 5.1. In Section5.2, we analyse the disturbance of the synaptic NMDAR numbers in the CaMKII-NMDAR complex formation and, in Section 5.3, we give a brief discussion and summary of the results.

5.1 Model integration

5.1.1 CaMKII state transition (ST) model

The CaMKII ST model developed by He, Kulasiri et al. (2015) simulates the formation of the CaMKII-NMDAR complex in PSD in response to presynaptic stimulation. It consists of a series of key events: (1) formation of Ca_4CaM complex; (2) activation and autophosphorylation of the CaMKII subunit; (3) translocation of the CaMKII holoenzyme into PSD; and (4) the formation of CaMKII-NMDAR complex in PSD. These events are downstream events of Ca^{2+} influx via NMDAR after stimulation. We have already included the event (1) in our Ca^{2+} model. Therefore, the Ca_4CaM complex is a link between our Ca^{2+} model and the CaMKII ST model (Figure 5.1). Besides, the other link between the two model is the postsynaptic NR2B-NMDAR, which serves as a Ca^{2+} channel in the Ca^{2+} model and as a CaMKII binding partner in the CaMKII ST model. The complete CaMKII ST model and the parameters are in Appendix H.

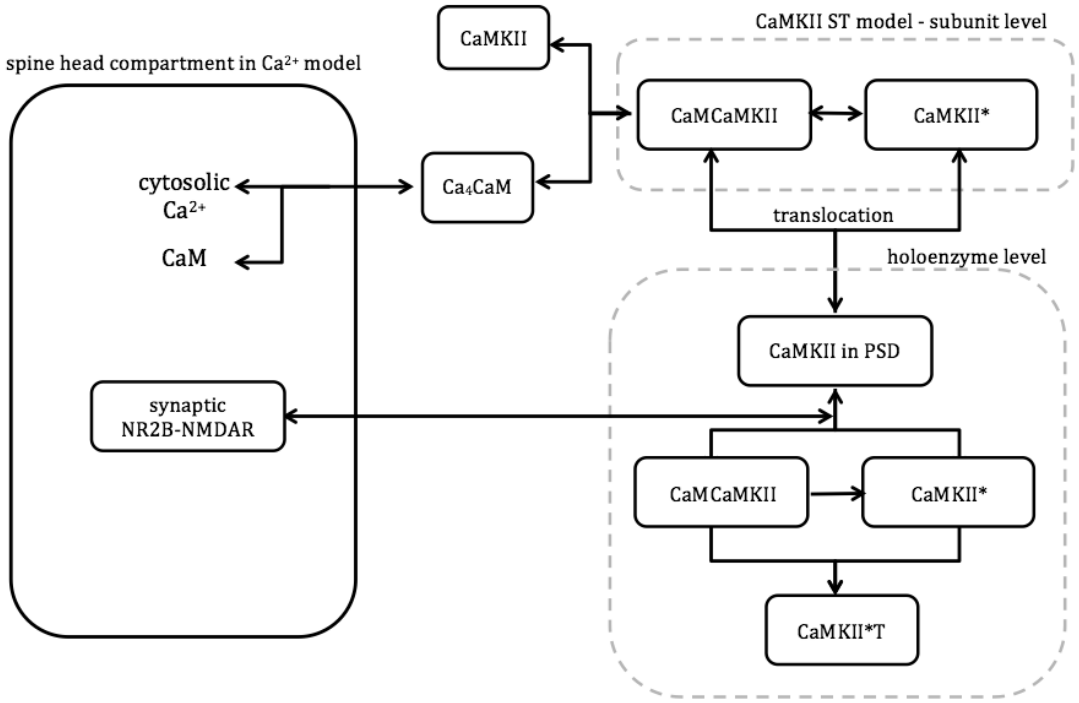

Figure 5.1. Schematics of the model integration. Schematic diagram of the CaMKII state transition (ST) model. (He, Kulasiri et al. 2015)

5.1.2 Adjustments and testing for model integration

The stimulation patterns used in the CaMKII ST model are a tetanus of 100 pulses at low-frequency (1, 10 Hz) and high-frequency (100 Hz), respectively. The Ca^{2+} dynamics in the dendritic spine ($[Ca^{2+}]_{cyto}$) in response to a stimulation tetanus is governed by

$$[Ca^{2+}]_{cyto} = [Ca^{2+}]_{rest} + A\sum_{i=1}^{n} \exp\left(-\frac{i}{f\tau}\right) \tag{5.1}$$

where $[Ca^{2+}]_{rest}$ is the cytosolic Ca^{2+} concentration at the resting level, A is the amplitude of Ca^{2+} concentration induced by one stimulation pulse, τ is the decay time constant, f is the stimulation frequency and n is the total number of the stimulation pulses (Zhabotinsky 2000). The intracellular Ca^{2+} dynamics in response to a 100-pulse tetanus at 100 Hz is in Figure 5.2 A. The Ca^{2+} level increases with time during the stimulation until it reaches a maximum level of about 20 μM, and after the last pulse, it decreases exponentially back to the resting level exponentially (τ = 200 ms). We apply a high-frequency presynaptic stimulation (HFS; 100 pulses at 100 Hz) and a high-frequency presynaptic stimulation paired with postsynaptic

stimulation (pairing HFS; 100 pulses at 100 Hz) to our Ca^{2+} model, respectively, and the results of the Ca^{2+} dynamics are shown in Figure 5.2 B. We use a paired pre/postsynaptic stimulation protocol because experimental evidence showed that postsynaptic membrane depolarisation triggered by presynaptic stimulation alone was not sufficient to induce LTP (Pike, Meredith et al. 1999, Mansvelder and McGehee 2000). Paired stimulation at both the presynaptic and postsynaptic neurons are used to create pairing of the EPSP and the bAP, which leads to a large depolarisation and Ca^{2+} elevation by NMDAR in the postsynaptic spine head (Caporale and Dan 2008). When simulate the pairing HFS protocol, a 2 ms-delayed bAP is introduced after each presynaptic stimulus pulse (the fomula for bAP was introduced in Chapter 3).

The result produced by Eq. (5.1) did not show any desensitisation of NMDARs (Figure 5.2 A). This may be because of assumptions that NMDARs are not the major Ca^{2+} channels, or that NMDARs recover from desensitisation completely between two pulses. Both of these assumptions conflict with the setting of our model that NMDARs are the major Ca^{2+} channels in the spine head and the experimental observation that both NR2A-NMDAR and NR2B-NMDAR will be desensitised under high-frequency stimulation (Erreger, Dravid et al. 2005). The Ca^{2+} response of Ca^{2+} model to HFS and pairing HFS reaches a peak level, decreases, then stays on a plateau at a lower level until the end of stimulation, which reflects the large desensitisation of synaptic NMDAR by high-frequency stimulation (Figure 5.2 B). Under the HFS, the elevation in $[Ca^{2+}]_{cyto}$ in much less than in the original Ca^{2+} reponse. In contrast, under the pairing HFS, although the peak level of $[Ca^{2+}]_{cyto}$ can be above 40 μM and is higher than in the maximum $[Ca^{2+}]_{cyto}$ fo the original Ca^{2+} response (around 20 μM), the plateau level (around 5 μM) is much lower than of the original response during the same stimulation time period.

We next compare the levels of the CaMKII-NMDAR complex in the original and our Ca^{2+} results. Before simulation, we have made several adjustments before connecting the Ca^{2+} model to the CamKII ST model. In the CaMKII ST model all proteins are in units of particle numbers (#). The time-dependent changes in the concentration of these proteins are calculated in particle numbers and all concentration-based rate constants are in $\#^{-1}s^{-1}$. Therefore, we convert the Ca_4CaM concentration (in μM) from Ca^{2+} model into particle numbers (in #) before calculating the translocation of CaMKII. The conversion is according to the following formula

$$particle\ number\ = concentration\ \times\ N_A \times\ Vol,$$

where N_A is the Avogadro constant (6.022140857×10^{23} mol^{-1}) and Vol is the volume of the spine head (0.1fL).

The rate constants used in the CaMKII ST model are based on 37°C, therefore, we adjust them to 34°C using a Q_{10} of 2.15 (Chiba, Schneider et al. 2008) to be consistent with the conditions in the previous chapters. The details of temperature correction on reaction rate constants are in Section 3.2.1. The simulation results of CaMKII ST model show a minor difference in the level of CaMKII-NMDAR complex formation at 34°C and 37°C (Figure 5.2 C).

Furthermore, we adjust the NR2B number in the CaMKII ST model from 20 to 8, which is the standard value based on our previous assumptions in Chapter 3. This decreases the level of the CaMKII-NMDAR complex by CaMKII ST model at t =300s by 1 (Figure 5.2 C). In contrast, the level of the CaMKII-NMDAR complex by our Ca^{2+} model in response to pairing HFS is about 0.7 (Figure 5.2 D) lower than in response to the original Ca^{2+} input (Figure 5.2 C). The difference is because a larger fraction of NMDARs are desensitised during pairing HFS and this leads to fewer Ca^{2+} ions entering the spine than the original input in CaMKII ST. There is no CaMKII-NMDAR formation in response to presynaptic HFS alone, because fo the insufficient amount of Ca^{2+} ion entered into the cytosol.

Moreover, we also use theta-burst stimulation (TBS) as an optional stimulation protocol in this chapter (See Appendix G.1 for the detail of TBS). In a train of TBS, pulses are grouped into several bursts, and the time duration (200 ms) between two bursts allows desensitised NMDARs to partially recover. TBS is considered to be a more physiologically relevant stimulus, which is close to the frequency of the endogenous hippocampal rhythm that triggers LTP (Lee, Barbarosie et al. 2000, Raymond 2007). One train of TBS consists of 10 stimulus bursts at 5 Hz (200 ms separation between bursts) and each burst consists of four pulses at 100 Hz. A 2 ms-delayed bAP is introduced into the model after each presynaptic stimulus pulse. Four trains of TBS are delivered at 0.1 Hz (10 s separation between trains), which is used to induce LTP experimentally (Lee, Barbarosie et al. 2000). The changes of Ca^{2+} level in the spine head by four trains of TBS and the corresponding production of CaMKII-NMDAR complex are shown in Figure 5.2 E and Figure 5.2 F, respectively. The level of the CaMKII-NMDAR complex shows a good agreement to that produced by the original Ca^{2+} input (Figure 5.2C).

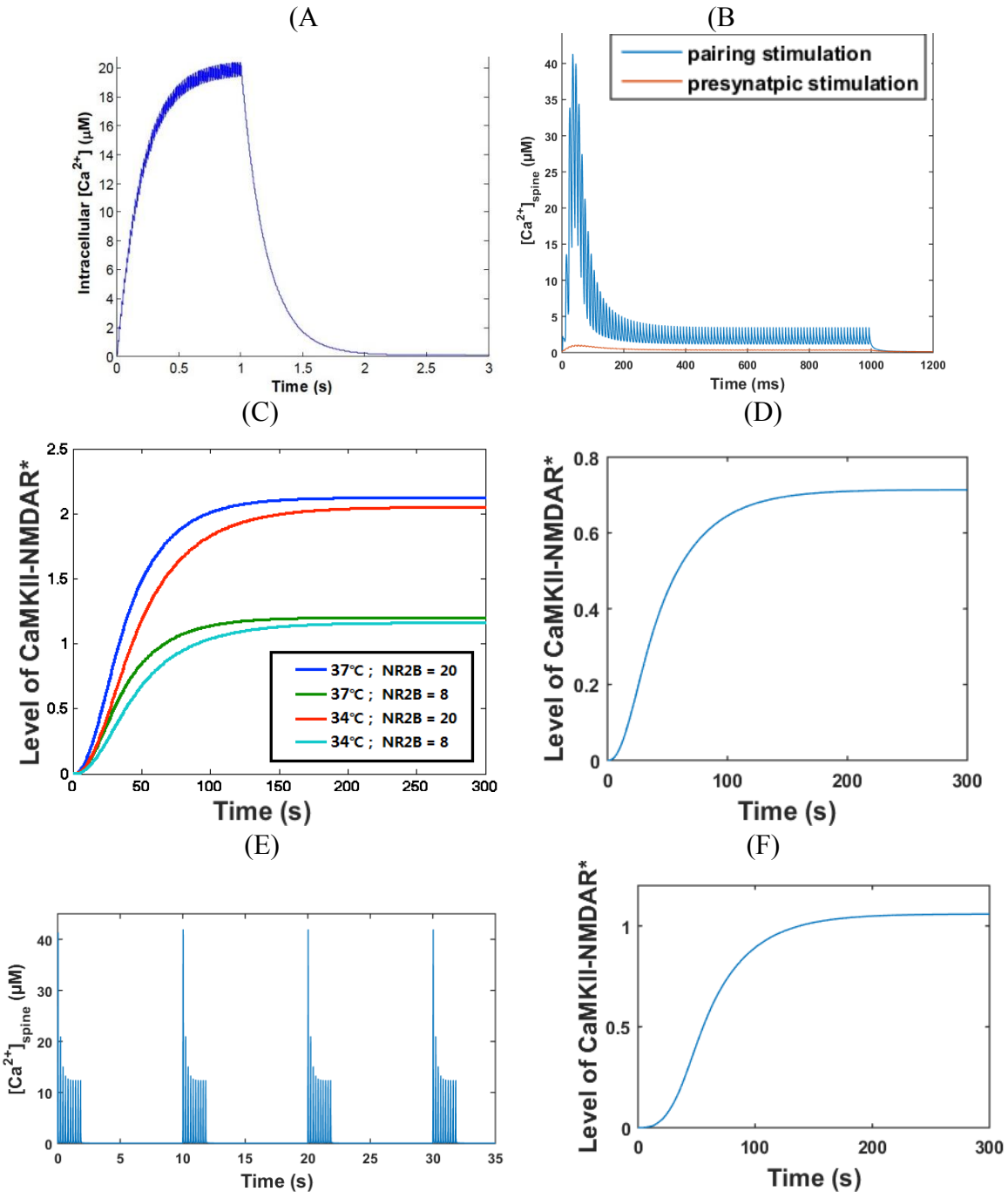

Figure 5.2. Ca^{2+} elevation and CaMKII-NMDAR complex formation in the spine head in response to presynaptic stimulation. Ca^{2+} dynamics in the spine head in response to Ca^{2+} by Eq. (5.1) (A), HFS and paring HFS (B) and 4 trains of TBS (E), respectively, and the coresponding CaMKII-NMDAR complex production (C, D and F).

5.2 Computational experiments

In this section, we mimic disturbances in the availability of synaptic NMDAR in AD to investigate the consequential effects on CaMKII ST and study the contribution of NMDARs with different subunit compositions in CaMKII ST. For each experiment, we run the model under 1 s of pairing HFS (100 pulses at 100 Hz) and 4 trains of paring TBS (4 TBS), respectively. In both stimulation protocols, a 2 ms-delayed bAP is introduced into the model after each presynaptic stimulus pulse. All simulations are run for 300 s.

After each simulation, we collect the Ca^{2+} elevation in the spine head ($[Ca^{2+}]_{spine}$) and 4 key outputs from the downstream events as following:

(1) Numbers of Ca_4CaM complexes. This is a determining factor for CaMKII activation and, subsequently, autophosphorylation.

(2) Numbers of autophosphorylated CaMKII subunits. Because once a CaMKII is autophosphorylated, its activity is independent from CaM and it shows persistent activity after the removal of stimulation. This is critical for the induction and maintenance of LTP, which requires a much longer time course in comparison with the stimulation.

(3) Numbers of CaMKII in PSD. Because CaMKII needs to be translocated into the PSD to affect its target, AMPAR, and bind to NR2B-NMDAR, once a CaMKII enters into the PSD, its autophosphorylation is suggested to be irreversible (Mullasseril, Dosemeci et al. 2007). The level of translocated CaMKII can be an indicator of the potential ability to form CaMKII-NMDAR complexes.

(4) Numbers CaMKII-NMDAR complex in PSD at time t = 300 s. The persistent localisation of CaMKII in PSD is suggested to be a critical factor for LTP induction and maintenance, and NR2B may play a key role in the synaptic CaMKII maintenance and recruitment (Bayer, LeBel et al. 2006). Therefore, the level of CaMKII-NMDAR complex numbers is an important output that can provide insights into the induction and maintenance of NMDAR-LTP.

5.2.1 NR2A/NR2B-NMDAR

The numbers of NR2A-NMDAR and NR2B-NMDAR in PSD under healthy conditions are assumed to be 12 and 8, respectively, to be consistent with the conditions in the previous chapters. We decrease the number of one of them from the standard value to zero to mimic

the increasing degree of reduction in the availability of a particular NMDAR type in the PSD.

Reduction in the numbers of NR2A-NMDAR in PSD greatly reduces the maximum amplitude of Ca^{2+} elevation during the first 10 stimulation pulses of pairing HFS, and this effect diminishes as more pulses arrive (Figure 5.3 A). The decrease in the Ca^{2+} elevation level during first few stimulation pulses reduces all the other four outputs (Figure 5.3 B). The amplitudes of Ca^{2+} elevation in response to 4 TBS show similar decreases with the degree of reduction in the NR2A-NMDAR number (Figure 5.4 A). During both stimulation protocols, a 50% reduction (6 NR2A-NMDAR left in the PSD) can block all downstream events (Figure 5.3 C and Figure 5.4 C). Especially, the formation of CaMKII-NMDAR is mostly sensitive to NR2A-NMDAR reduction, a 25% reduction (9 NR2A-NMDAR left in the PSD) can lead to no production of CaMKII-NMDAR. Even 8% reductions (11 NR2A-NMDAR left) can reduce the level of CaMKII-NMDAR formation by 60% (pairing HFS; Figure 5.3 B and Figure 5.3 C) and 75% (4 TBS; Figure 5.4 B and Figure 5.4 C), respectively.

In contrast, a reduction in NR2B-NMDAR numbers affects all outputs more lightly than the reduction in NR2A-NMDAR numbers. Even when reducing the NR2B-NMDAR from 8 to 1 (88% reduction), the amplitude of Ca^{2+} elevation only decreases by about 35% (from 42 μM to 27.3 μM) (Figure 5.5 A and Figure 5.6 A). This decrease is not able to fully block most downstream events, except for the formation of CaMKII-NMDAR complex(Figure 5.5 C and Figure 5.6 C). The level of Ca_4CaM formation, CaMKII autophosphorylation and translocation are reduced by about 65%, 78 % and 75%, respectively (Figure 5.5 B and C and Figure 5.6 B and C). The formation of CaMKII-NMDAR complex is largely reduced by the reduction in NR2B-NMDAR numbers, that reduce the NR2B-NMDAR numbers by 50% leads to a 70% reduction in the final level CaMKII-NMDAR complex at t =300 s.

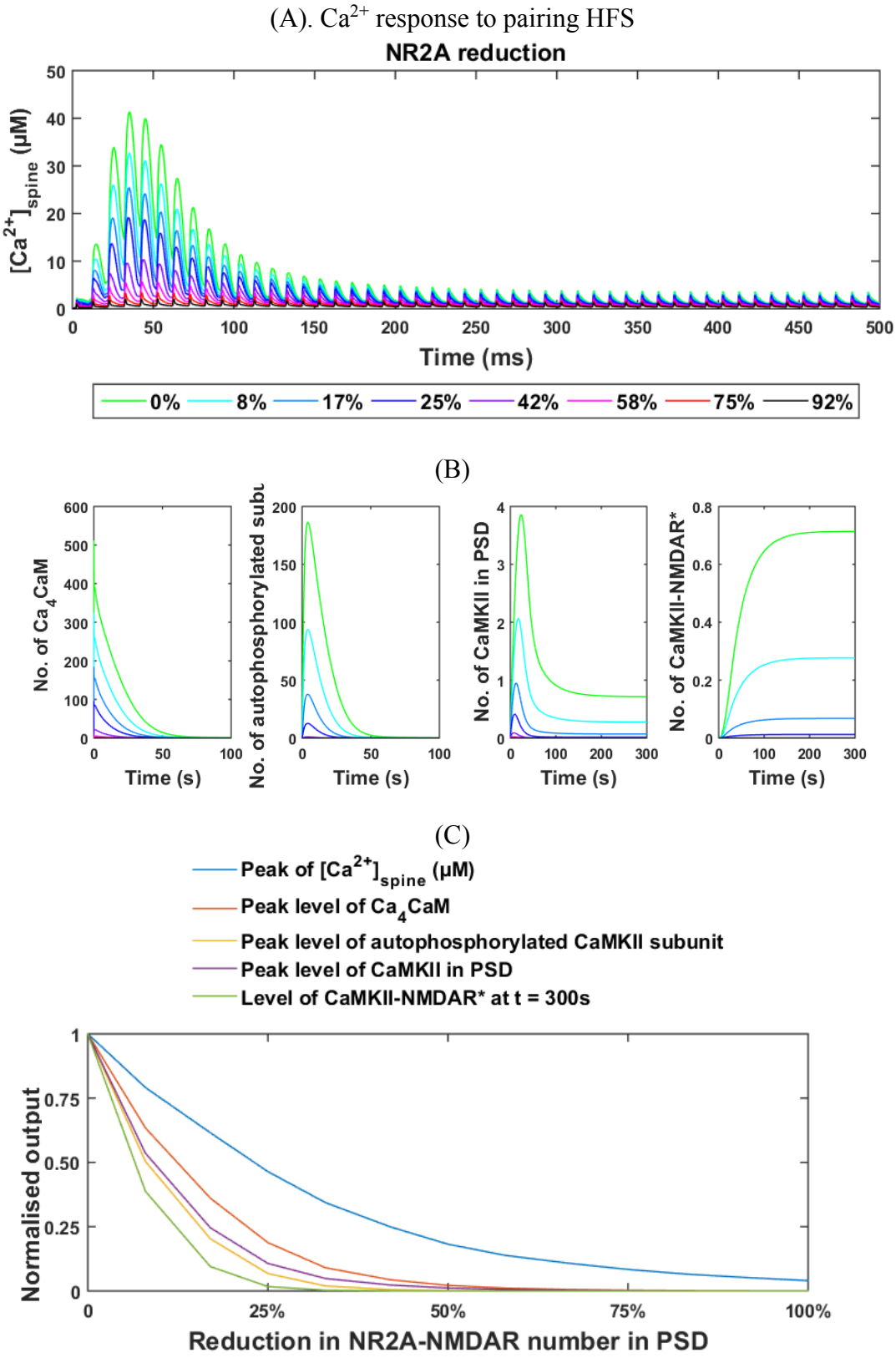

Figure 5.3. Effects of reduction in NR2A-NMDAR numbers in response to pairing HFS. (A) Ca^{2+} responses in spine head and (B) four outputs from downstream events with a different level of reduction in NR2A-NMDAR. (C)The relationship between the reduction level in NR2A-NMDAR numbers and selected typical values of the outputs. The results are normalised to those at the healthy condition (NR2A-NMDAR = 12; 0% reduction).

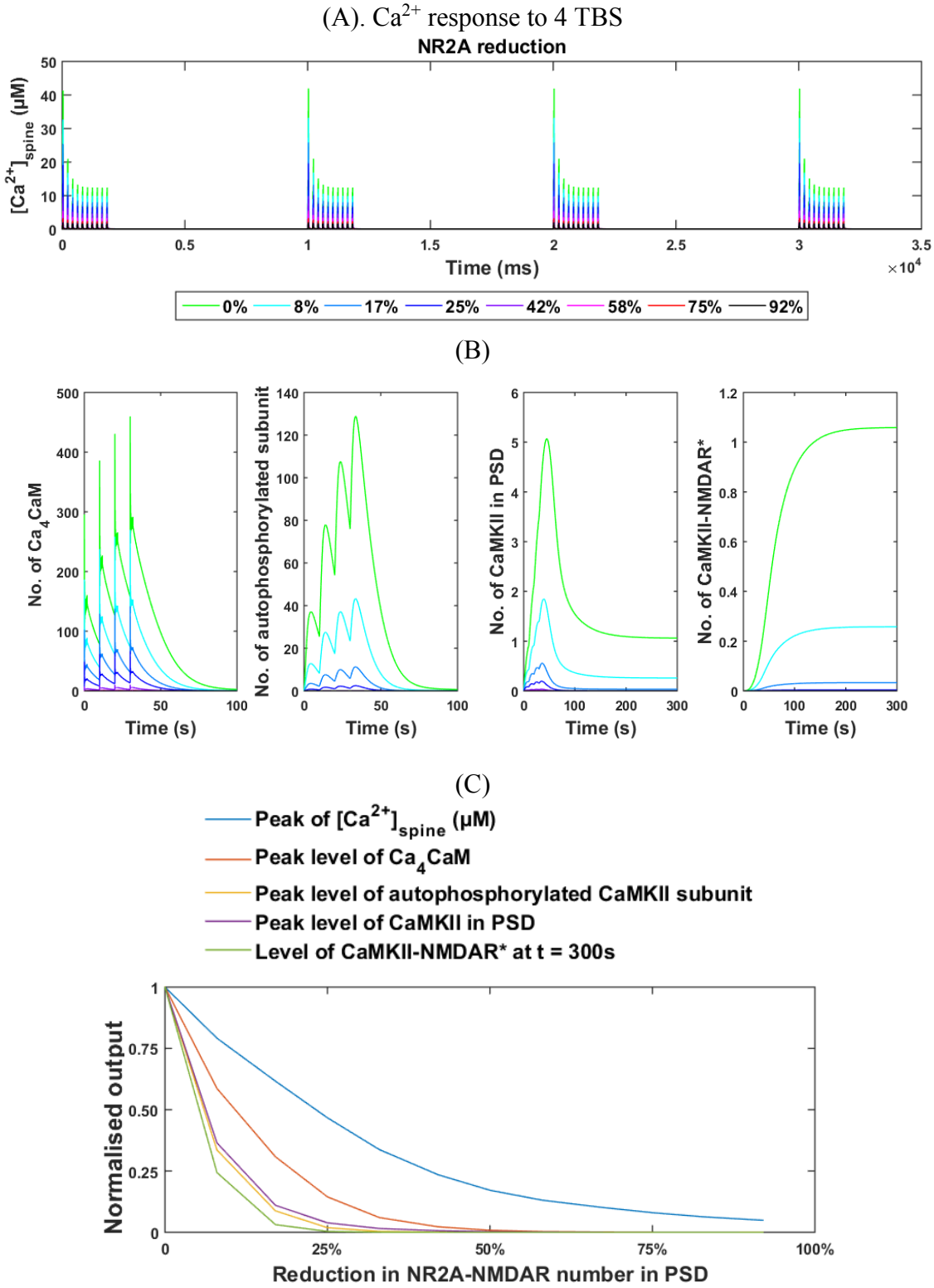

Figure 5.4. Effects of reduction in NR2A-NMDAR numbers in response to 4 TBS. (A) Ca^{2+} responses in spine head and (B) four outputs from downstream events with a different level of reduction in NR2A-NMDAR. (C)The relationship between the reduction level in NR2A-NMDAR numbers and selected typical values of the outputs. The results are normalised to those at the healthy condition (NR2A-NMDAR = 12; 0% reduction).

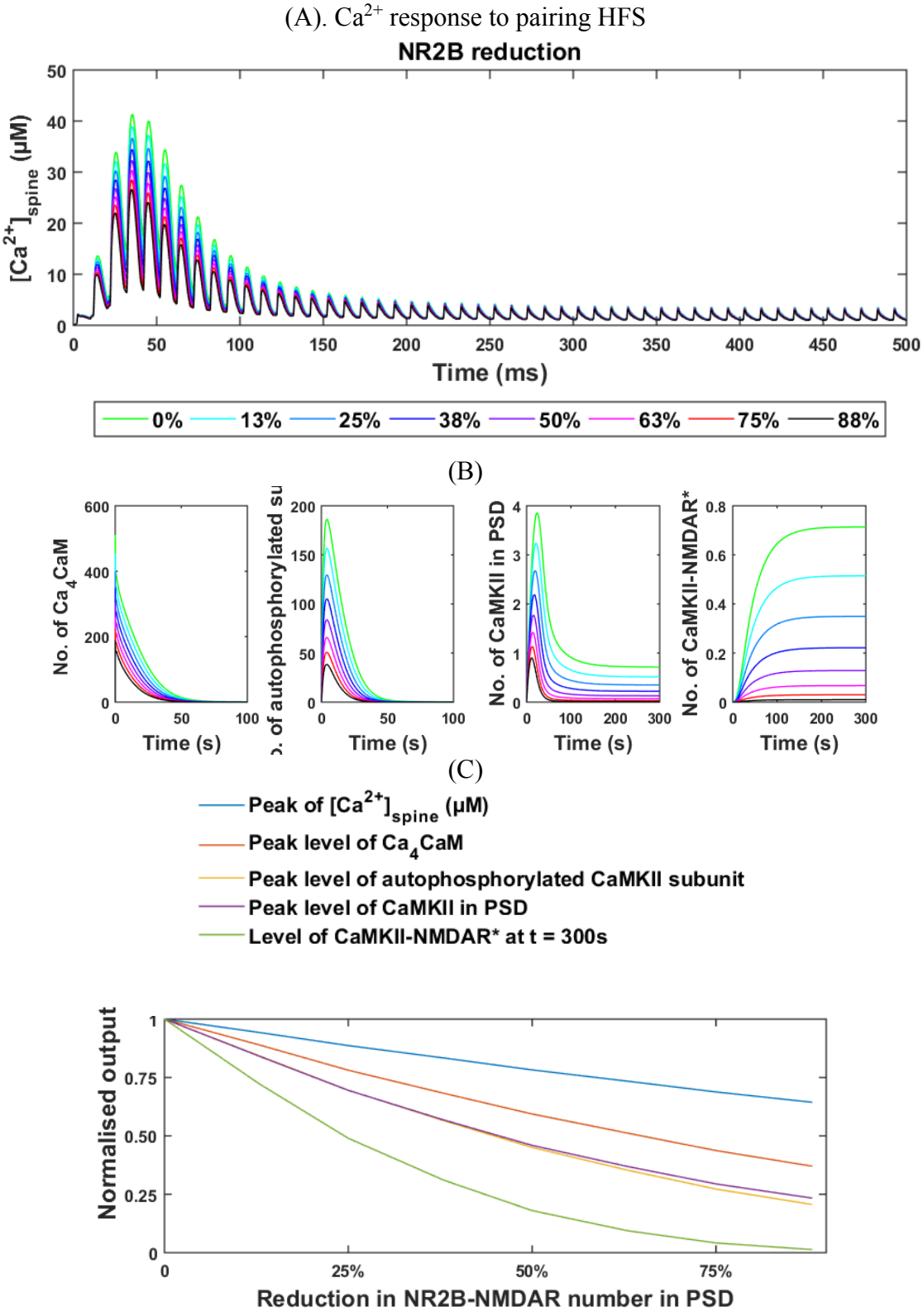

Figure 5.5. Effects of reduction in NR2B-NMDAR numbers in response to pairing HFS. (A) Ca^{2+} responses in spine head and (B) four outputs from downstream events with a different level of reduction in NR2B-NMDAR. (C)The relationship between the reduction level in NR2B-NMDAR numbers and selected typical values of the outputs. The results are normalised to those at the healthy condition (NR2B-NMDAR = 8; 0% reduction).

(A). Ca2+ response to 4 TBS (first three bursts)

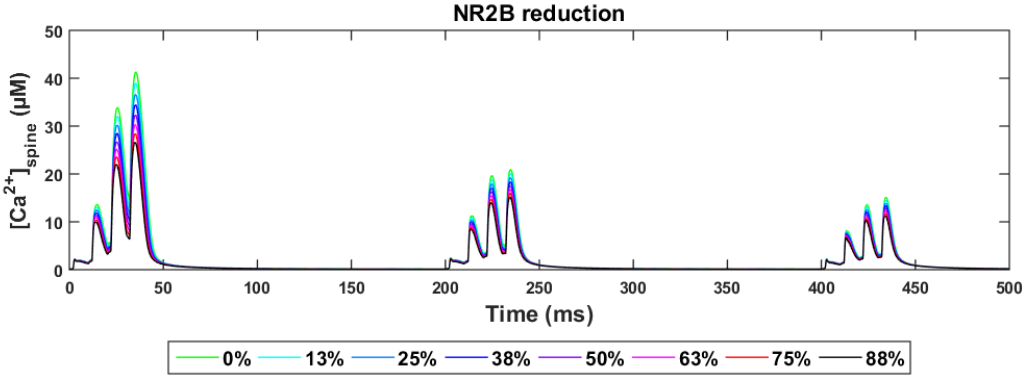

(B)

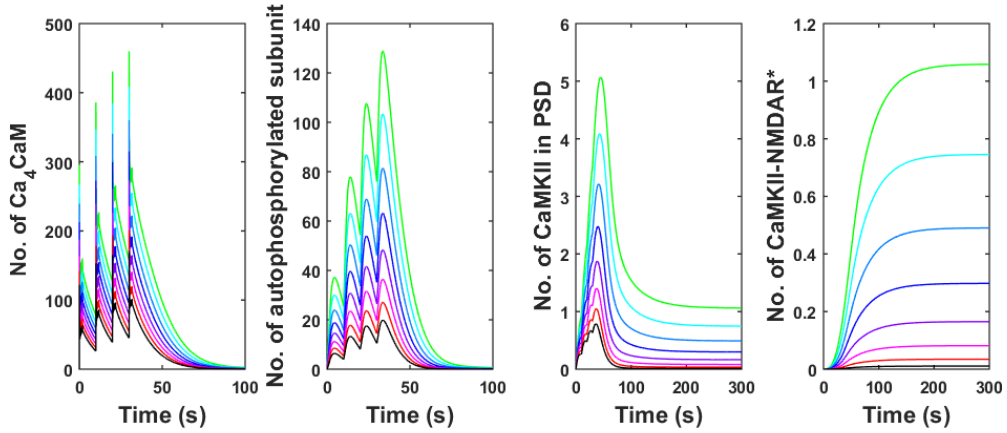

(C)

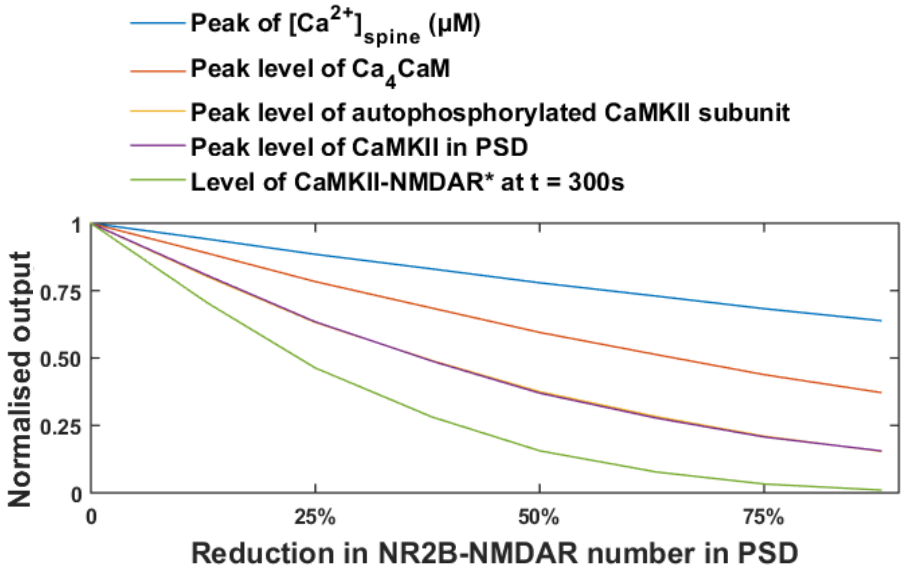

Figure 5.6. Effects of reduction in NR2B-NMDAR numbers in response to 4 TBS. (A) Ca^{2+} responses in spine head (only first three bursts are shown here to display the difference clearly). (B) Four outputs from downstream events with a different level of reduction in NR2B-NMDAR. (C)The relationship between the reduction level in NR2B-NMDAR numbers and selected typical values of the outputs. The results are normalised to those at the healthy condition (NR2B-NMDAR = 8; 0% reduction).

5.2.2 The ratio of NR2B:NR2A

The ratio of NR2A- to NR2B-NMDAR (NR2A/NR2B ratio) is precisely regulated by the production, trafficking and degradation of NMDARs, and the different ratios are linked to the preferences in the induction of different types of synaptic plasticity (Yashiro and Philpot 2008). Therefore, we investigate the effects of a disturbance on the NR2A/NR2B ratio in the CaMKII-NMDAR complex formation by keeping the total number of NMDARs in PSD constant (20 NMDARs) and varying the NR2A/NR2B ratio from 1: 19 to 19:1.

The amplitude of $[Ca^{2+}]_{spine}$ by stimulation increases with the NR2A/NR2B ratio (Figure 5.7A and Figure 5.8 B). When the NR2A/NR2B ratio belows 6:14, the peak $[Ca^{2+}]_{spine}$ in responses to each stimulation pulse are the same, and are less than with the standard NR2A/NR2B ratio (12:8). Productions of the other four outputs are blocked when the NR2A/NR2B ratio belows 6:14 (Figure 5.7 B and C and Figure 5.8 B and C). With the increase in the NR2A/NR2B ratio peak levels of all outputs, but not the production of CaMKII-NMDAR complex, rise with different slopes in response to a pairing HFS (Figure 5.7). The results from the 4TBS simulation show similar trends, but higher increases in comparison with the ones from the pairing HFS (Figure 5.8C). In contrast, the normalised final level of CaMKII-NMDAR after stimulation increases to a maximum level of 1.69 (pairing HFS) and 2.04 (pairing TBS), respectively, at the NR2A/NR2B ratio of 15:5, and decreases afterwards (Figure 5.9). This suggests the existence of an optimal NR2A/NR2B ratio in generation CaMKII-NMDAR complex.

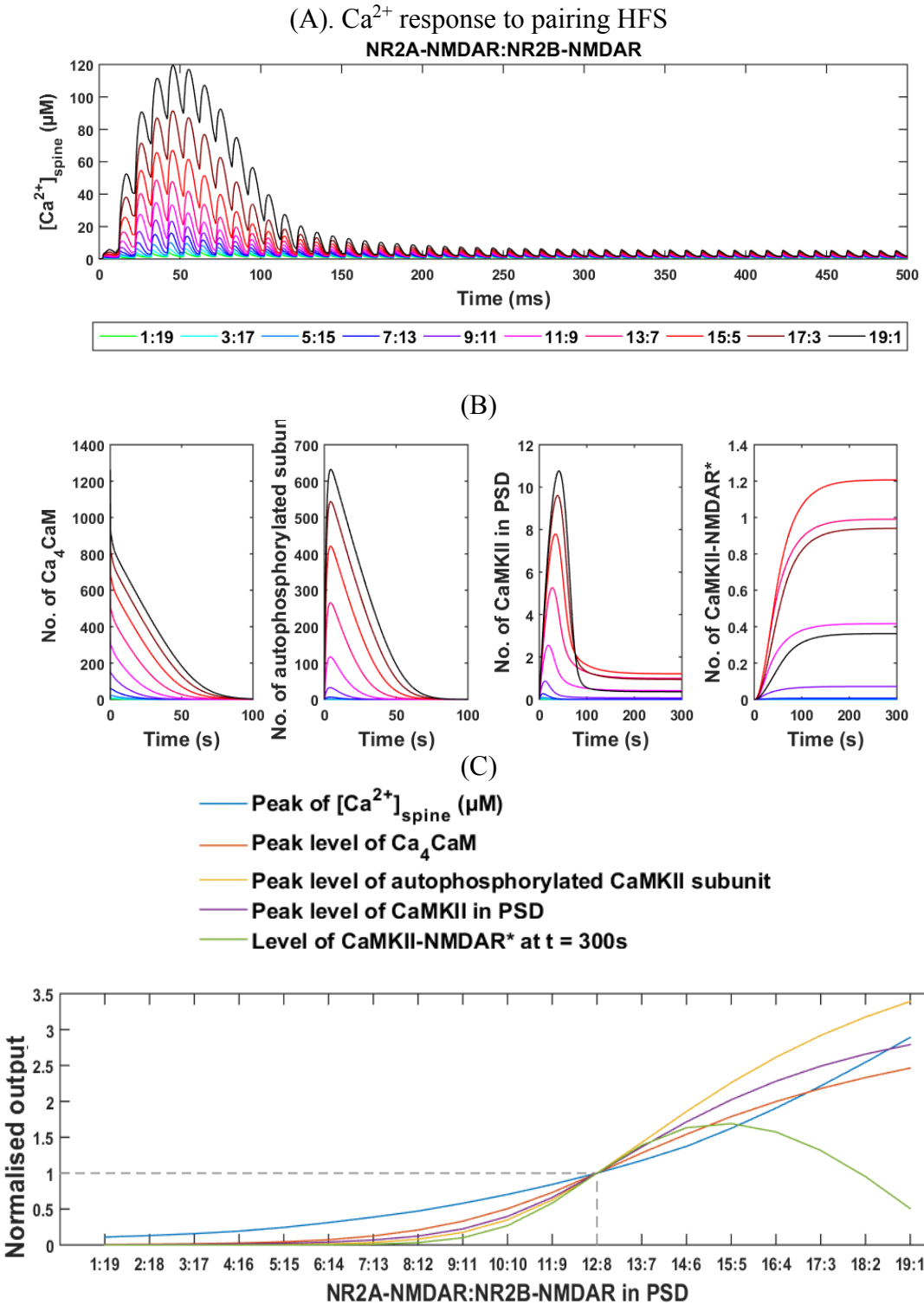

Figure 5.7. Effects of variation in the NR2A/NR2B ratio in response to pairing HFS. (A) Ca^{2+} responses in spine head and (B) four outputs from downstream events with different NR2A/NR2B ratio. (C)The relationship between the NR2A/NR2B ratio and selected typical values of the outputs. The results are normalised to those at the healthy condition (NR2A-NMDAR:NR2B-NMDAR = 12:8).

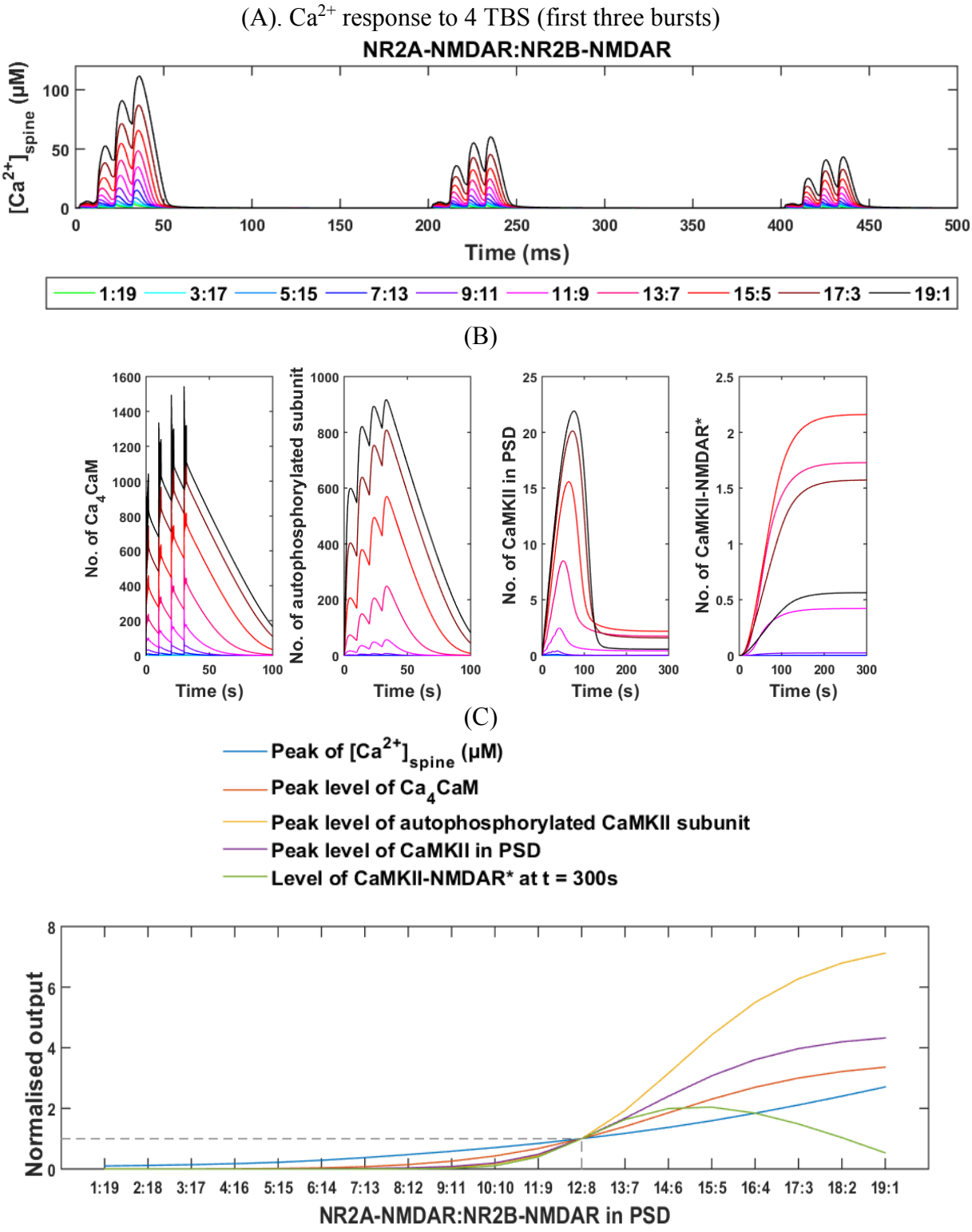

Figure 5.8. Effects of variation in the NR2A/NR2B ratio in response to 4TBS. (A) Ca^{2+} responses in spine head (only first three bursts are shown here to display the difference clearly). (B) Four outputs from downstream events with different NR2A/NR2B ratio. (C)The relationship between the NR2A/NR2B ratio and selected typical values of the outputs. The results are normalised to those at the healthy condition (NR2A-NMDAR:NR2B-NMDAR = 12:8).

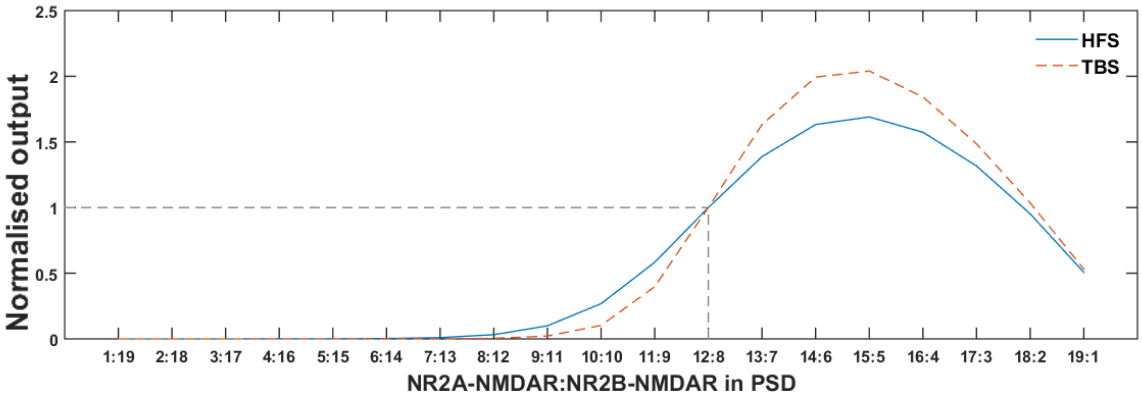

Figure 5.9. Effect of variation in the NR2A/NR2B ratio on the level of CaMKII-NMDAR complex production.

5.3 Discussion and summary

In this chapter, we extend our Ca^{2+} model presented in the previous chapter with a CaMKII TS model, to investigate the roles of NMDARs in Ca^{2+} transients in the dendritic spine head and the subsequent CaMKII TS in response to repeated paired pre/postsynaptic stimulation. We simulate the model under the conditions of the dysregulated level of NMDARs to study their role as Ca^{2+} channels (NR2A- and NR2B-NMDAR) and as a scaffold in PSD to anchor CaMKII. We also predict their contributions to a series of selected downstream events leading to CaMKII-NMDAR complex formation. The simulation results of the levels of the selected outputs are useful to gain insights into the different contributions of NR2A- and NR2B-NMDAR in the induction of LTP and the ability for maintenance later on. It also helps us to better understand the potential outcomes of the disturbances in NMDAR observed in AD and to explain the possible linkages between those disturbances and the pathology of the disease.

Simulation of the reduction in NR2A- and NR2B-NMDAR show negative effects on the activation, autophosphorylation and translocation of CaMKII and the formation of CaMKII-NMDAR complexes at different degrees. This suggests that both types of NMDAR are necessary for LTP formation, while contributing to its induction and maintenance in different ways. Specifically, the role of NR2A-NMDARs is to allow sufficient Ca^{2+} influx to trigger the downstream Ca^{2+}-CaM interaction, which determines the activation of CaMKII. NR2B-NMDAR contributes less as a Ca^{2+} channel than NR2A-NMDAR and itself alone is insufficient to trigger the activation of CaMKII. However, it is required to function as a scaffold in PSD that anchors CaMKII by forming a CaMKII-NMDAR complex. This is

consistent with the experimental findings and hypothesis that the opening of NR2B-NMDAR may not be necessary for LTP induction (Kim, Dunah et al. 2005, Foster, McLaughlin et al. 2010). Simulation with different NR2A/NR2B ratios suggests that although a high NR2A/NR2B ratio facilities activation, autophosphorylation and translocation of CaMKII, it still requires a certain level of NR2B-NMDAR to anchor CaMKII in the PSD. Overall, these results provide a clearer picture that NMDAR-LTP may require cooperation between the NR2A- and NR2B-NMDAR.

The internalisation of synaptic NMDAR seen in AD (Snyder, Nong et al. 2005, Li, Jin et al. 2011) could underly some of the critical alterations in the pathology of the disease. For instance, in AD transgenic mice, it has been observed that Aβ can alter the CaMKII distribution and reduce the synaptic CaMKII level, which may be the mechanism by which Aβ induces the loss of synaptic AMPARs (Gu, Liu et al. 2009). It is unclear how the distribution of CaMKII is altered by Aβ. Here, the simulation results predict that a reduction in synaptic NMDARs by Aβ can reduce the CaMKII-NMDAR formation in PSD by affecting the upstream Ca^{2+} response to stimulation or the scaffold function of NR2B-NMDAR. Consequently, this may contribute to the deficits of LTP and loss of synapse in AD (Townsend, Mehta et al. 2007, Koffie, Hyman et al. 2011).

Chapter 6
Conclusion and Future Directions

In this thesis, we use mathematical modelling to advance our understanding of Ca^{2+} dysregulation in the spine head under AD conditions. We investigate selected major alterations reported in AD and evaluate their effects on the postsynaptic Ca^{2+} responses. We also extend our research of synaptic Ca^{2+} signalling to the downstream CaMKII state transition to gain insights into the disturbances from alterations in synaptic NMDAR in the emergence of LTP in AD. In this chapter, we give a general overview of our work, summarise the major contributions and suggest several future directions that can follow this work.

6.1 Overview of the study

The first objective is to investigate the effects of Aβ-dependent disturbances on NMDAR-mediated Ca^{2+} dynamics in the dendritic spine (Chapter 3). To accomplish this target, we first develop a mathematical model according to the characteristics of the CA1 pyramidal dendritic spine. This model integrates three aspects, representing three sequencing events: (1) glutamate release, diffusion and uptake; (2) glutamate receptor state transition; and (3) Ca^{2+} dynamics in the spine head and its adjacent dendritic shaft. We estimate and calibrate the uncertain parameters according to data obtained from experiments to ensure that the model can perform well under healthy conditions. We then use this model to investigate the proposed disturbances of Aβ in: (1) glutamate uptake by glutamate transporters; (2) glutamate vesicle release from the presynaptic terminal and astrocytes; and (3) availability of functional glutamate receptors at membrane surface. We analyse the responses of NMDAR with different subunit compositions and at different locations, and also the Ca^{2+} dynamics in the postsynaptic spine and the adjacent dendritic shaft in response to different stimulation patterns.

The model predicts that an increase in the glutamate release from the presynaptic terminal by Aβ mostly promotes more Ca^{2+} ions to flux into the cytosol via synaptic NMDARs in comparison to the extrasynaptic ones, whereas a decrease in the glutamate uptake facilitates more Ca^{2+} ions to enter via extrasynaptic NMDAR in comparison to the synaptic ones. Elevation in the resting levels of the extrasynaptic glutamate causes a large fraction of extrasynaptic NMDARs at the open state and decreases their response to the presynaptic

stimulations in comparison to the resting level. The model also predicts that the internalisation of synaptic NR2B-NMDAR has fewer effects on the synaptic Ca^{2+} response in comparison to the internalisation of synaptic NR2A-NMDAR, suggesting the dysregulation by synaptic NR2B-NMDAR internalisation observed in the AD condition may be because of disturbances in the other roles of NR2B-NMDAR.

Furthermore, we use PRCC to analyse the global sensitivities of these parameters and predict the most vulnerable target of Aβ to disturb the postsynaptic Ca^{2+} response. The results suggest that the glutamate amount released by presynaptic stimulation is the most sensitive factor and an Aβ-induced increase in synaptic glutamate release may play a major role in the overexcitation and Ca^{2+} overload of postsynaptic neurons in comparison to other factors in our test.

The second objective is to investigate the effects of disturbances of ER Ca^{2+} handling in AD on the NMDAR-mediated Ca^{2+} dynamics in the spine head (Chapter 4). We extend the Ca^{2+} model by adding the internal ER components. We use this model to investigate effects in the postsynaptic Ca^{2+} response by three reported alterations in AD: (1) ER Ca^{2+} overload; (2) upregulation of RyR; and (3) disturbances of SERCA pumps in ER. We analyse and compare the contributions of ER in the postsynaptic Ca^{2+} response between the healthy condition and the AD condition. The simulation predicts both an ER Ca^{2+}overload and RyR upregulation will promote Ca^{2+} release from the ER over Ca^{2+} uptake and amplify the external Ca^{2+} signal. Multipulse simulations at different frequencies show a frequency-dependant effect on the postsynaptic response.The model also predicts and suggests that inhibition of the SERCA pumps may protect the spine head from Ca^{2+} dysregulation by an ER Ca^{2+} overload.

The third objective is to investigate the effects of Ca^{2+} dysregulation in one of the key downstream events, CaMKII-NMDAR complex formation (Chapter 5). We add a CaMKII ST model (He, Kulasiri et al. 2015) downstream of our Ca^{2+} model to study the different roles of NMDARs collectively. We simulate conditions that alter the availability of different types of synaptic NMDAR and in the ratio of NR2A- to NR2B-NMDAR and analyse their effects on the Ca^{2+} response and CaMKII state transition. The model predicts that a reduction in NR2A-NMDAR predominantly decreases the postsynaptic Ca^{2+} elevation and subsequent CaMKII state transition while a reduction in NR2B-NMDAR mostly only affects the CaMKII-NMDAR complex formation. Simulations with changes in the ratio of NR2A- to NR2B-NMDAR suggest cooperation between the two is required for LTP induction.

6.2 Contributions

The major contributions of this thesis are:

- Development of an integration model representing an average CA1 pyramidal dendritic spine, with and without the presence of the ER component.
- Advancement of our understanding of Aβ-dependent disturbances in NMDAR-mediated Ca^{2+} dynamics in the dendritic spine. Predict the most vulnerable target of Aβ among those that affect the Ca^{2+} response in the synaptic spines.
- Advancement of our understanding of the effects of ER dysfunction under the AD condition in response to NMDAR-mediated Ca^{2+} elevation in the dendritic spine.
- Extendsion of the Ca^{2+} model with a state transition model of CaMKII to advance our understanding of the subunit-specific roles of NMDAR in the postsynaptic response and CaMKII state transition.
- Prediction of the consequences of the internalisation of NMDAR with different subunit compositions as seen in AD in NMDAR-LTD induction and maintenance. Revelation that cooperation and a balance between NR2A- and NR2B-NMDAR is necessary for NMDAR-LTD.

6.3 Policy Implication

A number of therapy research on the AD is mainly focused on reducing the concentration of Aβ or inhibiting Ca^{2+} overload of a neuron. For example, memantine is one of the popular drugs that is used to block NMDARs, however, there are adverse effects that could arise in both the brain and the body (Areosa et al, 2005). Our research suggests that selective inhibition on the internalisation of synaptic NR2B-NMDARs in AD can be a useful therapeutic approach that may prevent the loss of synapses and memory decline. Besides, the extracellular glutamate concentration could be an indicator of AD and therapeutic research can be carried out on controlling the extracellular glutamate level to avoid the excess activation of extrasynaptic NMDARs.

6.4 Future Directions

We suggest several future directions that can follow the current work:

- Release of glutamate vesicles from the presynaptic terminal induced by APs is a highly stochastic process and is mediated by different functional pools, Ca^{2+} dynamics in the presynaptic terminal and the frequency of APs (Nadkarni, Bartol et al. 2010, Alabi and Tsien 2012). It is very unlikely that each presynaptic stimulation can successfully induce a vesicle release under certain conditions, such as readily releasable pool size is very small. Therefore, a model of the vesicle release probability can be add to the upstream of our Ca^{2+} model to decide whether there is a release event in response to each presynaptic stimulation at various frequencies.

- The dendritic spines are remarkably dynamic over time, and the morphology of spines can be altered by synaptic activity (Hering and Sheng 2001, Holtmaat, Wilbrecht et al. 2006, Roberts, Tschida et al. 2010). In this research, we fix the geometry of the dendritic spine to represent an average CA1 pyramidal dendritic spine. Therefore, the model can be extended by taking consideration of the variation and changes in the geometry of the spine, to test how it will affect the results.

- The modelling strategies in this research are all based on deterministic approaches. However, the Ca^{2+} dynamics in the dendritic spine are actually stochastic in realistic biological systems, because of its small volume and the low copy numbers of the reactants in it. For instance, the concentration of Ca^{2+} near its channels may be at a higher level than other sites when taking Ca^{2+} diffusion into account (Keener 2006). Therefore, instead of simulating the diffusion of glutamate and Ca^{2+} using PDE or between neighbouring compartments, stochastic modelling, such as a Brownian motion random walk, can be applied (Grewer, Gameiro et al. 2008). Morover, the binding of ligands to a single receptor can be treated stochastically.

- The dendritic shaft compartments can be extended and modified to study Ca^{2+} dysregulation in the dendrites in AD. IP_3R can be included because it is an important factor in Ca^{2+} oscillation and propagation in the dendrites (Bezprozvanny 2005), and under AD conditions, a disturbance in IP3R has been reported (see Section 2.2.4). Another factor related to ER Ca^{2+} handling is the store-operated Ca^{2+} channels, which are also reported to be affected in AD. Therefore, these two aspects can be added to the ER component in the dendritic compartment in a future study.

- Ca^{2+}-sensitive phosphatase 2B (PP2B) is sensitive to Ca^{2+} more than CaM and indirectly contributes to the dephosphorylation of CaMKII (Klee 1991, Colbran 2004). PP2B activity is found to increase in the aging brain and the presence of Aβ can further increase its activity (Zhao, Watson et al. 2004, O'Dwyer, Lamberton et al. 2012). This may because of the alteration in the NMDAR-induced Ca^{2+} influx by Aβ, and, consequently, it impairs NMDAR-LTP induction (Chen, Wei et al. 2002). Therefore, the model of Ca^{2+} dynamics and CaMKII ST in Chapter 5 can be extended to incorporate PP2B to investigate the Aβ disturbance in NMDAR-LTP.

6.5 Conclusions

The Ca^{2+} dysregulation reported in AD can be a result of alterations of multiple factors in Ca^{2+} signalling. It is important to understand how these alterations individually and collectively affect the system. However, it is challenging and expensive to study these effects experimentally. Mathematical modelling and computational simulation provide great opportunities to explore the network and investigate the dysregulations by conducting simulation experiments with models. In this thesis, we develop an integration mathematical model of a CA1 pyramidal dendritic spine and investigate the various alterations that are reported in AD. We analyse the Ca^{2+} response in the spine head at different levels for each alteration. We also extend our study by including an important Ca^{2+} downstream event, the CaMKII state transition, in the induction of LTP. We use the model to investigate how alterations in the different composition of NMDARs affect the Ca^{2+} responses as well as the autophosphorylation, and the formation of CaMKII-NMDAR and to provide important insights into how NMDAR-mediated LTP gets disturbed in AD.

Appendix A. Simulation tools

Table A. 1. Simulation tools

A. General purpose simulation tools

Tool	Freeware	Website
MATLAB		http://www.mathworks.com
Mathematica		http://www.wolfram.com/mathematica
Python	√	https://www.python.org
XPPAUT	√	https://www.math.pitt.edu/~bard/xpp/xpp.html

B. Biological specific simulation tools

Tool	Simulation algorithm		Interface for model development	Freeware	Website
	Deterministic	Stochastic			
CellDesigner	√		GUI	√	http://www.celldesigner.org
COPASI	√		GUI	√	http://www.copasi.org
VCell	√	√	GUI	√	http://www.nrcam.uchc.edu
MCell		√	CellBlender	√	http://www.mcell.org
Smoldyn		√	CLI	√	http://www.smoldyn.org
STEPS		√	Python	√	http://steps.sourceforge.net
Chemesis	√		GENESIS	√	http://krasnow1.gmu.edu/CENlab/software.html
MOOSE	√	√	Python	√	http://moose.ncbs.res.in
NEURON	√	√*	GUI; CLI	√	http://www.neuron.yale.edu
NeuroRD		√	xml files	√	http://krasnow1.gmu.edu/CENlab/software.html

*Channel states and total conductance can be deterministic or stochastic (Brette, Rudolph et al. 2007).

(A)

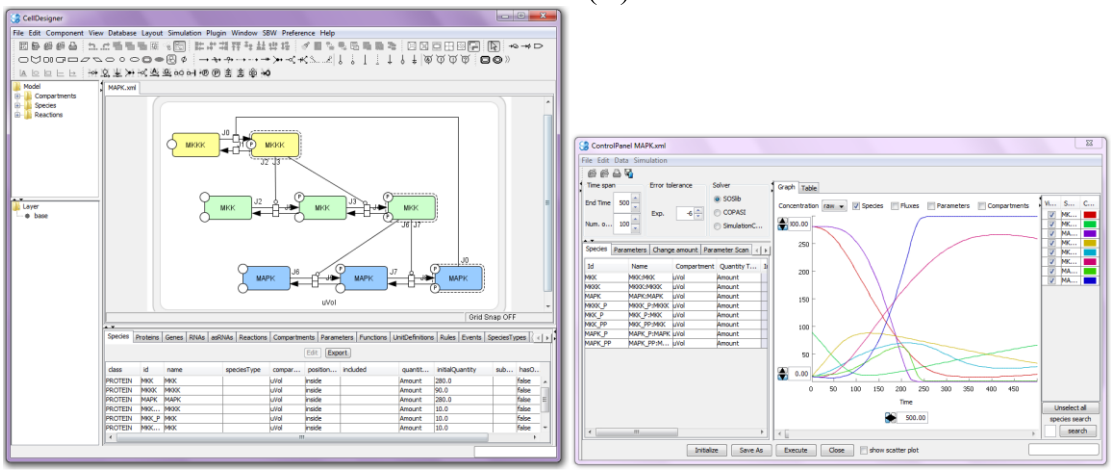

(B)

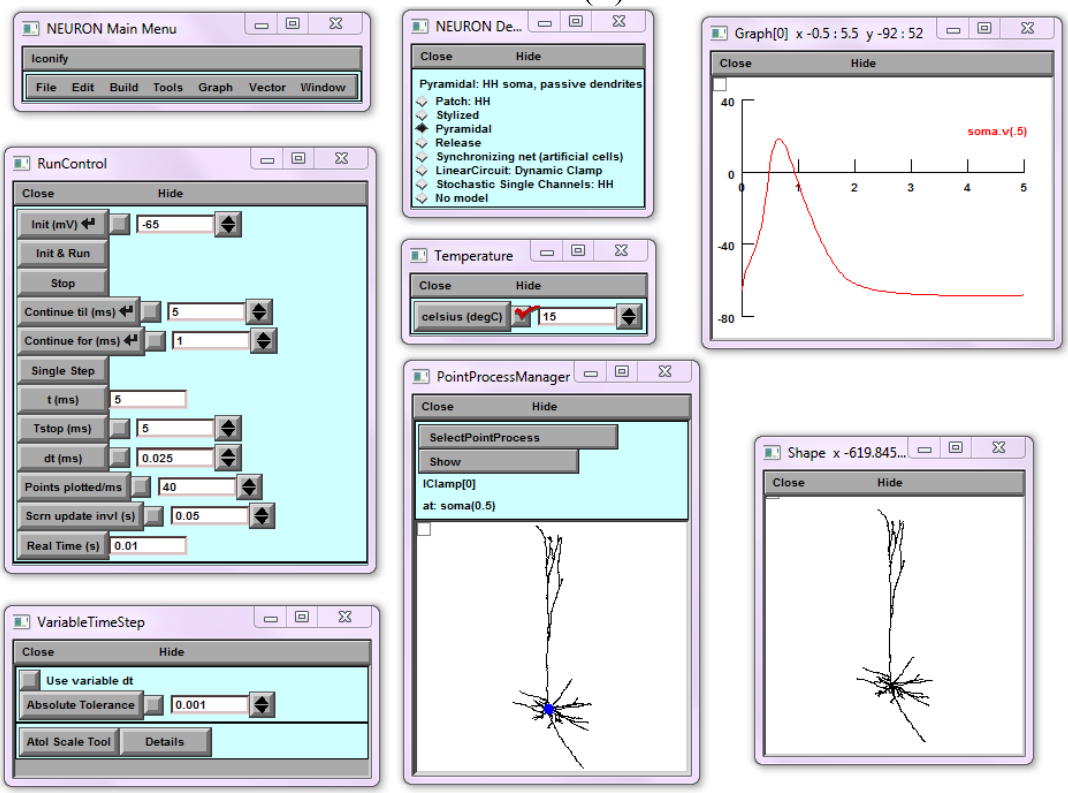

Figure A. 1. Interface captures of simulation tools. Biological simulation tools (e.g., CellDesigner) with user-friendly GUI allow users to draw biochemical networks of their model (A, left) and run models with simulation control panel (A. right). Neuronal simulation tools (e.g., NEURON (B)) provide several built-in builders, with which users can set the precise parameters of neuronal specific features for their model. (A) CellDesigner interface capture for a sample model (MAPK.xml). (B) NEURON interface capture of a sample demonstration of a hippocampal pyramidal neuron. All sample models in this figure are pre-assembled in these software.

Appendix B. Glutamate Diffusion Model

B.1 Fick's first law

Adolf Fick was the first one to describe diffusion process quantitatively (Fick 1855). Fick's first law states that the diffusion flux is proportional to the concentration gradient and the rate of concentration change at a point in space is proportional to the second derivative of concentration with space. For example, Fick's law in one dimension is:

$$J(x,t) = -D\frac{\partial C(x,t)}{\partial x}, \tag{B. 1}$$

where $J(x,t)$ is the diffusion flux (the amount of a substance crossing through a unit area per unit time), D is the diffusion coefficient, $C(x,t)$ is the concentration of substance at position x at time t. The negative sign before D denotes the diffusion is from a higher concentration to a lower one.

Consider the diffusion space is separated into a series of compartments. In each compartment, the substance is well mixed. Therefore, its concentration in compartment i is changed by the diffusion between neighbour compartments i-1 and i+1:

$$\frac{dC_i}{dt} = \frac{J_{i,i-1} + J_{i,i+1}}{V_i} = -\frac{D}{V_i}[\left(\frac{A}{\delta}\right)_{i,i-1}(C_i - C_{i-1}) - \left(\frac{A}{\delta}\right)_{i+1,i}(C_{i+1} - C_i)], \tag{B. 2}$$

where $\left(\frac{A}{\delta}\right)_{p,q} = \frac{A_{pq}}{\Delta l_{pq}}$ describes the movement of Ca^{2+} ions from compartment p to q, where A_{pq} is the cross-sectional area of the two compartments and Δl_{pq} is the distance between the midpoints of compartments p and q.

B.2 Diffusion inside the synaptic cleft

The synaptic cleft is divided into N concentric cylindrical rings, with a thinness of ΔR=20 nm. Therefore, the dynamics of glutamate in the i-th ring is

$$\frac{d[Glu_i]}{dt} = -\frac{\mathrm{D_{Glu}}}{V_i}\left[\left(\frac{A}{\delta}\right)_{i,i-1}([Glu_i] - [Glu_{i-1}]) - \left(\frac{A}{\delta}\right)_{i+1,i}([Glu_{i+1}] - [Glu_{ii-1}])\right], \tag{B.3}$$

where $V_i = h\pi[(\Delta Ri]^2 - h\pi[(\Delta R(i-1)]^2$ and $\left(\frac{A}{\delta}\right)_{p,q} = \frac{2h\pi\Delta Rq}{\Delta R}$.

B.3 Diffusion in the extrasynaptic space

Diffusion in the extrasynaptic space is modified from the model of Rusakov (2001). The coordinate origin is set at the centre of synaptic cleft, the space compartments runs in the radial direction with step ΔR_2 and in the tangential direction with an angular step $\Delta\theta$ (Figure D.1). Each ring-shaped *(i,j)*-th compartment have four interfaces with adjacent compartments. In the tangential direction, the interface area is $S_T(i,j) = 2\pi i\Delta R_2 sin\theta(j)\Delta\theta$. In the radial direction, the interface are is $S_R(i,j) = 2\pi(i\Delta R_2)^2[cos\theta(j) - cos\theta(j-1)]$. Its compartment volume is $\mathrm{V}(i,j) = \frac{1}{2}[\,S_T(i,j) + \,S_T(i-1,j)]\Delta R_2$. In our simulation, ΔR_2 = 20 nm and $\Delta\theta = \frac{\pi}{9}$.

The dynamic of gluatamate concentraiton in compartment *(i,j)* is

$$\frac{d[Glu_{i,j}]}{dt} = -\frac{\mathrm{D_{Glu}}^*}{V_{i,j}}\left(\sum J_R(i,j)S_R + \sum J_T(i,j)\,S_T\right), \tag{B.3}$$

where $\mathrm{D_{Glu}}^*$is the effective diffusion coefficient in the extrasynaptic space, $\sum J_R(i,j)$ and $\sum J_T(i,j)$ are the summation of fluxes through radial and tangetial interfaces, respectively. The diffusion fluxe between two adjacent compartment *n* and *n+1* can be calculated calculate them using the Fick's ist law (Eq. (B.2)) and obtain:

$$J_{n,n+1} = \frac{1}{\delta_{n,n+1}}\left([Glu_n] - [Glu_{\mathrm{n+1}}]\right),$$

where $\delta_{n,n+1}$ is the spatial distance between compartment *n* and *n+1*.

Appendix C. Mathematical expressions for rate laws

C.1 Mass Action Based Models

The law of mass action is a fundamental law of a chemical reaction, which defines that the rates of a chemical reation at constant temperature are proportional to the product of the reactant concentrations (Guldberg and Waage 1864). A signle step reaciton follows the mass action kinetics is called elementary reaction. Based on the number of reactant species, there are unimolecular, bimolecular and termolecular reactions. For example, the following simple bimolecular elementary reation:

$$A + B \overset{k}{\rightarrow} C, \tag{C. 1}$$

where A and B are the reactants, C is the product and k is the reaction rate constant or proportionality rate. Based on the law of mass action, the rate of this reaction, V, is propotional to [A][B], and therefore,

$$V = k[A][B], \tag{C. 2}$$

where [A] and [B] represent the concentrations of reactant A and B, respectively. (In the following section, we use [x] to denote the concentration of x). The concentration changes of A, B and C over time can be described by a set of differential equations (ODEs):

$$\frac{d[A]}{dt} = -k[A][B] = -V, \tag{C. 3}$$

$$\frac{d[B]}{dt} = -k[A][B] = -V, and \tag{C. 4}$$

$$\frac{d[C]}{dt} = k[A][B] = V. \tag{C. 5}$$

An elementary reaction can be reversible, such as the following reaction

$$A + B \overset{k_1;\, k_{-1}}{\longleftrightarrow} C \tag{C. 6}$$

can be treated as two simultaneous reactions: one forward and one backward reaction, where k_1 and k_{-1} denote the forward and backward reaction rate constants, respectively. According to the law of mass action, the forward reaction rate, V_1, is

$$V_1 = k_1[A][B], \tag{C. 7}$$

and the backward reaction rate, V_{-1}, is

$$V_{-1} = k_{-1}[C]. \tag{C. 8}$$

The concentration changes of all species in this system over time can be described three ODEs:

$$\frac{d[A]}{dt} = -k_1[A][B] + k_{-1}[C] = -V_1 + V_{-1} \tag{C. 9}$$

$$\frac{d[B]}{dt} = -k_1[A][B] + k_{-1}[C] = -V_1 + V_{-1}, and \tag{C. 10}$$

$$\frac{d[C]}{dt} = k_1[A][B] - k_{-1}[C] = V_1 - V_{-1}. \tag{C. 11}$$

Many complex reactions contain multiple steps, and each step is an elementary reaction. For example, the following chain reaction

$$A \overset{k_1}{\rightarrow} B \overset{k_2}{\rightarrow} C \tag{C. 12}$$

consist of two elementary reaction: $A \overset{k_1}{\rightarrow} B$ and $B \overset{k_2}{\rightarrow} C$, with reaction rate constant $k1$ and $k2$, respectively. In the first reaction step, the reactant A converts into an intermediate, B, and the reaction rate, V_1, is

$$V_1 = k_1[A]. \tag{C. 13}$$

In the second reaction step, the intermediate B converts into the final product C, and the reaction rate, V_2, is

$$V_2 = k_2[B]. \tag{C. 14}$$

Therefore, the ODEs for the concentration changes of all species in this system over time are

$$\frac{d[A]}{dt} = -k_1[A] = -V_1, \tag{C. 15}$$

$$\frac{d[B]}{dt} = k_1[A] - k_2[B] = V_1 - V_2, and \tag{C. 16}$$

$$\frac{d[C]}{dt} = k_2[B] = V_2. \quad \text{(C. 17)}$$

C.2 Michaelis-Menten model

C.2.1 Equilibrium approximation

The Michaelis-Menten model is a classic more for enzyme kinetic (Michaelis and Menten 1913). In an enzyme-catalysed reactions:

$$E + S \overset{k_1; k_{-1}}{\longleftrightarrow} ES \overset{k_2}{\longrightarrow} E + P, \quad \text{(C. 18)}$$

a substrate, S, reversibly binds to an enzyme, E, to form a substrate-enzyme complex, ES, with the forwar reaction rate constant, k_1, and the backward reaction rate constant, k_{-1}. Then, ES irreversibly converts into the production, P, with rate constant k_2 and releases E at the same time. Therefore, based on the law of mass action, the concentration changes of all species in this system can be described by four ODEs:

$$\frac{d[S]}{dt} = -k_1[E][S] + k_{-1}[ES], \quad \text{(C. 19)}$$

$$\frac{d[E]}{dt} = -k_1[E][S] + (k_{-1} + k_2)[ES], \quad \text{(C. 20)}$$

$$\frac{d[ES]}{dt} = k_1[E][S] - (k_{-1} + k_2)[ES], and \quad \text{(C. 21)}$$

$$\frac{d[P]}{dt} = k_2[ES]. \quad \text{(C. 22)}$$

The total concentration of the enzyme (E_0) is a constant, where

$$[E_0] = [E] + [ES]. \quad \text{(C. 23)}$$

The original assumption by Michaelis and Menten (1913) was that the substrate-enzyme complex, ES reaches its equilibrium instantly ($k_1[E][S] = k_{-1}[ES]$). Therefore, the concentration of the substrate-enzyme complex is given by

$$[ES] = \frac{k_1}{k_{-1}}[E][S]. \quad \text{(C. 24)}$$

According to the Eq. (C.23), Eq. (C.24) is modified to

$$[ES] = \frac{k_1}{k_{-1}}[S]([E_0] - [ES]). \quad \text{(C. 25)}$$

Let $K_d = \frac{k_{-1}}{k_1}$ represent the dissociation constant of the ES complex. Substiute $K_d = \frac{k_{-1}}{k_1}$ in to Eq. (C.25) and rearrage it to

$$[ES] = \frac{[S][E_0]}{K_d + [S]}. \quad \text{(C. 26)}$$

Therefore, the reaction rate of the final production P (Eq. (22)), V, is given by

$$V = \frac{d[P]}{dt} = k_2[ES] = k_2\frac{[S][E_0]}{K_d + [S]}. \quad \text{(C. 27)}$$

Let $V_{max} = k_2[E_0]$ represent the maximum reaction rate the system can reach at a saturating substrate concentration. Then, Eq. (C.27) becomes

$$V = V_{max}\frac{[S]}{K_d + [S]}. \quad \text{(C. 28)}$$

When [S] = K_d, $V = \frac{1}{2}V_{max}$. This equilibrium approximation is valid when the reversible reaction is much faster than the irreversible reaction ($k_{-1} \gg k_2$), and thus, the reaction rate of the production P is limited by the irreversible reaction limites.

C.2.2 Quasi-steady-state approximation

Briggs and Haldane (1925) suggested an alternative approximation, the quasi-steady-state approximation, which assumes the concentration of the intermediate substrate-enzyme complex ES does not change during the production of P. Therefore, $\frac{d[ES]}{dt} = 0$ and rearrange the Eq. (21) to

$$[ES] = \frac{k_1}{k_{-1} + k_2}[E][S]. \quad \text{(C. 29)}$$

Based on the conservation of the enzyme in Eq. (C.23), Eq. (C.29) is modified to

$$[ES] = \frac{[S][E_0]}{K_M + [S]}, \quad \text{(C. 30)}$$

where $K_M = \frac{k_{-1}+k_2}{k_1}$ is called Michaelis-Menten constant.

Substitue Eq. (C.30) into Eq. (C.22), the reaction rate of the final production P, V, is given by

$$V = \frac{d[P]}{dt} = k_2[ES] = k_2 \frac{[S][E_0]}{K_M + [S]} = V_{max} \frac{[S]}{K_M + [S]}. \quad \text{(C. 31)}$$

The quasi-steady-state approximation is valid when $[E_0] \ll [S_0]$, where $S_0$is the total substrate concentration ($[S_0] = [S] + [ES]$). Eq. (C.31) is very similar to Eq. (C.28), with the only difference that the equilibrium approximation uses K_M (Eq. (C.31)) whereas the equilibrium approximation uses K_{max} (Eq. (C.28)). To be notice, when $k_{-1} \gg k_2$, $K_M \approx K_{max}$ and these two approximation will produce similar results.

C.3 Hill model

The Hill model is a type of model that describes the cooperativity cooperative binding of ligands to receptors (Hill 1910). It is widely used as the mathematically formulate to quantify the binding between ligands and receptors by expressing the fraction of the bound receptor as a function of the ligand concentration (Weiss 1997). The Hill model provides a way to describe the dependence between chemical substances in modelling the cooperative activation or inhibition in complex biochemical systems.

Consider an receport protein consists of n subunits and each subunits contains one binding site for a ligand. The binding of the ligands to the receptor can be seperated into n reversible elementary reaction steps as follows:

$$L + R + \overset{k_1;\, k_{-1}}{\longleftrightarrow} LR, \tag{C. 32}$$

$$L + LR \overset{k_2;\, k_{-2}}{\longleftrightarrow} L_2R, \tag{C. 33}$$

...

$$L + L_{n-1}R \overset{k_n;\, k_{-n}}{\longleftrightarrow} d\ L_nR, \tag{C. 34}$$

where L is the ligand, R is the free receptor, L_nR is the n-ligand bound receptor, and k_n and k_{-n} are the forward and backward reaction for the n-th elementary reaction steps, respectively. Besides, the rate of ions enter through this recepoter is propotianl to the concentration of the full bound receport, L_nR, with a rate constant of k_{ion}. Let [x] be the concentration of x. The dynamics of all species in this system can be governed by a set of ODEs:

$$\frac{d[R]}{dt} = -k_1[R][L] + k_{-1}[LR], \tag{C. 35}$$

$$\frac{d[LR]}{dt} = k_1[R][L] - k_{-1}[LR] - k_2[LR][L] + k_{-2}[L_2R], \tag{C. 36}$$

$$\frac{d[L_2R]}{dt} = k_2[LR][L] - k_{-2}[L_2R] - k_3[L_2R][L] + k_{-3}[L_3R], \tag{C. 37}$$

...

$$\frac{d[L_{n-1}R]}{dt} = k_{n-1}\left[L_{(n-2)}R\right][L] - k_{-(n-1)}[L_{n-1}R] - k_n[L_{n-1}R][L] + k_{-n}[L_nR], \quad \text{(C. 38)}$$

$$\frac{d[L_nR]}{dt} = k_n[L_{n-1}R][L] - k_{-n}[L_nR], and \quad \text{(C. 39)}$$

$$\frac{d[L]}{dt} = -(k_1[R] + k_2[LR] + k_3[L_2R] + \cdots + k_n[L_{n-1}R])[L] + (k_{-1}[LR] + k_{-2}[L_2R] + k_{-3}[L_3R] + k_{-n}[L_nR]). \quad \text{(C. 40)}$$

The ion flux rate through this receptor is $f = k_{ion}[L_nR]$. Assume there is no change in the concentraions of all binding states ($LR, L_2R, \dots, L_nR$) over the timescale of f, thus, Eq. (C.36) to Eq. (C.39) become zeros and obtain:

$$[LR] = \frac{[R][L]}{K_1}, \quad \text{(C. 41)}$$

$$[L_2R] = \frac{[R][L]^2}{K_1K_2}, \quad \text{(C. 42)}$$

...

$$[L_nR] = \frac{[R][L]^n}{K_1K_2 \dots K_n}, \quad \text{(C. 43)}$$

where $K_1 = \frac{k_{-1}}{k_1}$, $K_2 = \frac{k_{-2}}{k_2}$, … and $K_n = \frac{k_{-n}}{k_n}$.

Let R_0 be the total concentration of the receptor, $[R_0] = [R] + [LR] + [L_2R] + \cdots + [L_nR]$ besed on the law of conservation of mass. Therefore, we can calculate the fraction of receptor that has been full-bound by *n* ligands:

$$\frac{[L_nR]}{[R_0]} = \frac{[L_nR]}{[R] + [LR] + [L_2R] + \cdots + [L_nR]} = \frac{\frac{[R][L]^n}{K_1K_2 \dots K_n}}{[R] + \frac{[R][L]}{K_1} + \frac{[R][L]^2}{K_1K_2} + \cdots + \frac{[R][L]^n}{K_1K_2 \dots K_n}} = \frac{[L]^n}{K_1K_2 \dots K_n + K_2 \dots K_n[L] + K_3 \dots K_n[L]^2 + \cdots + [L]^n}. \quad \text{(C. 44)}$$

If we assume the first ligand binding is slow, but once one site is occupied, binding to the rest site is fast and the binding affinity for the remaining sites are changed by the first binding and ligands can bind to them simultaneously. This can be modelled as $k_1 \to 0$, $k_2 to\ k_n \to \infty$ and $k_1 k_2 \dots k_n$ is fixed. Therefore, $K_1 \to \infty$, $K_2 \dots K_n \to 0$ and $K_1 K_2 \dots K_n$ is a constant. Let ${K_a}^n = K_1 K_2 \dots K_n$, which discribes the ligand concentration producting half occupation of all binding sites. Eq. (C.44) can be simplified to

$$\frac{[L_n R]}{[R_0]} = \frac{[L]^n}{{K_a}^n + [L]^n}. \tag{C. 45}$$

The Eq. (C.45) is the classic form of Hill equation, and n is called Hill coefficient. Hill equation can also be written as

$$\frac{[L_n R]}{[R_0]} = \frac{[L]^n}{K_d + [L]^n}, \tag{C. 46}$$

where $K_d = {K_a}^n$ denotes the apparent dissociation constant which can be derived from the law of mass action.

Rearrange the Eq. (C.46), the concentration of $L_n R$ becomes a function of the ligand concentration:

$$[L_n R] = \frac{[R_0][L]^n}{{K_a}^n + [L]^n}. \tag{C. 47}$$

Therefore, the ion flux rate through this receptor is $f = k_{ion}[L_n R]$.

$$f = V_{max} \frac{[L]^n}{{K_a}^n + [L]^n}, \tag{C. 48}$$

where $V_{max} = k_{ion}[R_0]$ is the maximum flux rate when all receptors are full bound by ligands.

The modified hill model (Eq. (B.48)) describes a sigmoid relationship between the flux rate f and the ligand concentration $[L]$ (Figure C.1). The curve of f versus $[L]$ has an "S" shape (sigmoid curve). The Hill coefficient n determines the steepness of the sigmoid curve. When n = 1, the Hill model becomes Michaelis-Menten model, which shows no cooperativity binding. This is valid when each ligand binding site is independent from each other and the binding affinity for a ligand to a binding site is not affected if the receport is already bound by other ligands.

When n >1, the Hill model describes a positively cooperative binding process that once a ligand is bound to the receptor, the affinity for the rest ligands increases. On the contrary, when n < 1, the Hill model describes a negatively cooperative binding that the binding affinity decreases once a ligand is bound to the receptor.

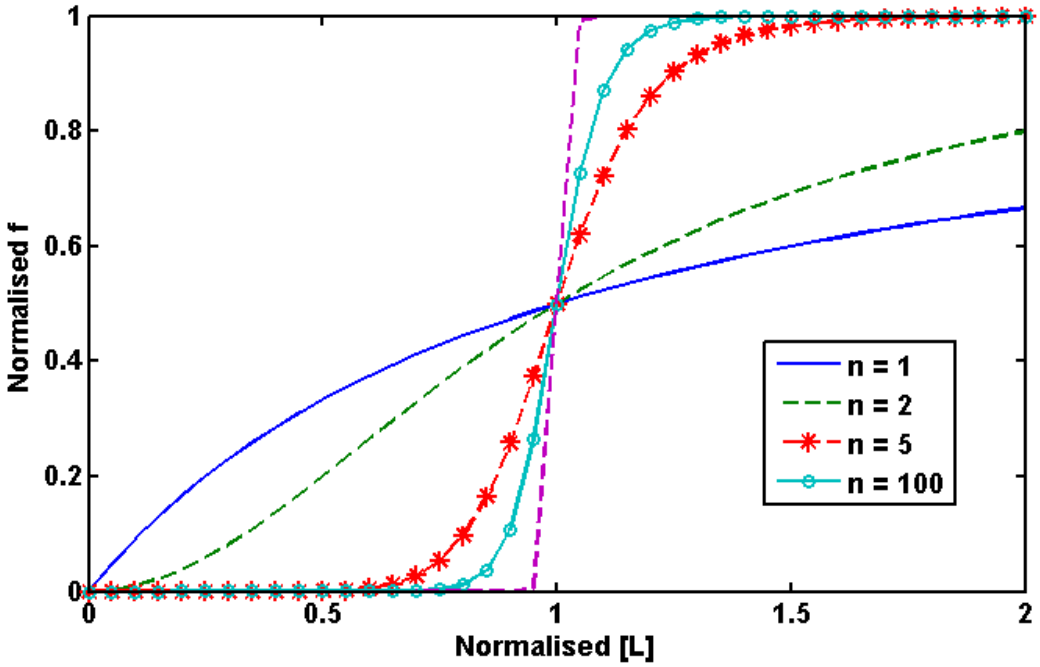

Figure C.1. The normalised flux rate from a Hill model. The flux rate is normalised to the V_{max}. The ligand concentration $[L_n]$ is normalised to the K_a.

C.4 Application of Michaelis-Menten model to simulation of Ca^{2+} extrusion mechanisms

The intracellular Ca^{2+} ions are removed from the cytosol by membrane exchangers or pumps, which can be assumed as two steps: (1) intracellular Ca^{2+} binds to the Ca^{2+} pump or and (2) the Ca^{2+} pump or exchanger releases the bound Ca^{2+} to the extracellular space

$$Ca_i^{2+} + P \overset{k_1;\, k_{-1}}{\longleftrightarrow} CaP \xrightarrow{k_2} Ca_0^{2+} + P, \tag{C. 49}$$

where Ca_i^{2+} and Ca_o^{2+} denotes intracellular and extracellular Ca^{2+}, respectively. P and CaP denotes the free and intermediate Ca^{2+}-bound Ca^{2+} pumps or exchangers, respectively. The Ca^{2+} pumps in membrane of internal Ca^{2+} stores, such as ER or mitochondrion, can be represented in a similar way. The only difference is that Ca_o^{2+} represents the the Ca^{2+} in internal Ca^{2+} store. The Ca^{2+} binding step is reveserble, with forward rate constant, k_1, and backward rate constant, k_{-1}, respectively. The release step, with release time constant k_2, is irreverseble when assuming the $Ca_0^{2+}$is a constant. Ca^{2+} normally bind to the pump with a high affinity, and the release process is relatively much slower than the Ca^{2+} binding process ($k_{-1} \gg k_2$). Therefore, the Ca^{2+} flux via the Ca^{2+} pump or exchanger can be described by a Michaelis-Menten model:

$$J_{pump} = V_{pump} \frac{[Ca^{2+}]_i}{K_{pump} + [Ca^{2+}]_i}, \tag{C. 50}$$

where J_{pump} denotes the pump Ca^{2+} flux (in units of conerntration per unit time), V_{pump} denotes the maximum pump velocity, K_{pump} is Michaelis-Menten constant, which denotes the Ca^{2+} concentration with half V_{pump}, and $[Ca^{2+}]_i$ denotes the intracellualr Ca^{2+} concentration. V_{pump} can be calculated from the maximum velocity and the total pump number:

$$V_{pump} = k_2 Ps \frac{A}{V},$$

where Ps is the surface density of the pump (in units of molecue number per unit area of membrane), A is the suface area of membrane and V is the volume of the cytosol. According to Eq. (C.30), $K_{pump} = \frac{k_{-1}+k_2}{k_1}$, in the unit of concentrations.

In some literature, SERCA pump is simulated using a Hill model with with a Hill coefficient

greater than 1 (offen use 2) (Lytton, Westlin et al. 1992). The SERCA pump in the smooth ER membrane binds to two Ca^{2+} ions for each ATP molecule, and can be modelled as two sequentially binding steps:

$$Ca_i^{2+} + P \overset{k_1;\, k_{-1}}{\longleftrightarrow} CaP \xrightarrow{k_{r1}} Ca_{ER}^{2+} + P, \tag{C. 51}$$

$$Ca_i^{2+} + CaP \overset{k_2;\, k_{-2}}{\longleftrightarrow} Ca_2P \xrightarrow{k_{r2}} Ca_{ER}^{2+} + CaP, \tag{C. 52}$$

where Ca_{ER}^{2+} denotes the Ca^{2+} in the ER, k_1 and k_2 are the forward rate constants and k_{-1} and k_{-2} are the backward rate constants, of the each reveserble Ca^{2+} binding step, respectively. k_{r1} and k_{r2} are the release time constant. The total concentration of SERCA, P_0, is a constant that $P_0 = [P] + [Ca_2P]$. Assume the concentration of CaP and Ca_2P reach to the equilibriums instantly, then the Ca^{2+} flux via the SERCA pump can be described by a hill model:

$$J_{pump} = V_{pump} \frac{[Ca^{2+}]_i{}^n}{K_{pump}{}^n + [Ca^{2+}]_i{}^n}, \tag{C. 53}$$

where the Hill coefficient $n = 2$ (Lytton, Westlin et al. 1992).

Appendix D. ODEs for Tr, CaD and CaM

D.1 Gluatmate tranporter (Tr).

Glutamate uptake by glial transporters can be represented as a follwing simple kinetic scheme (Rusakov and Kullmann 1998):

$$Glu + Tr \overset{k_{1f};\, k_{1b}}{\longleftrightarrow} Glu - Tr \overset{k_2}{\rightarrow} Tr,$$

where Glu is the glutamate, Tr is the unbound surface transporter and $Glu - Tr$ is the glutamate-transporter complex (See section 3.1.1 for the explanation). The dynamics of all species in the model can be described by three ODEs (Appendix C.1):

$$\frac{d[Glu]}{dt} = -k_{1f}[Glu][Tr] + k_{1b}[Glu - Tr], \quad \text{(D. 1)}$$

$$\frac{d[Tr]}{dt} = -k_{1f}[Glu][Tr] + (k_{1b} + k_2)[Glu - Tr], and \quad \text{(D. 2)}$$

$$\frac{d[Glu - Tr]}{dt} = k_{1f}[Glu][Tr] - (k_{1b} + k_2)[Glu - Tr]. \quad \text{(D. 3)}$$

According to the law of conservation of mass, $[Tr_{total}] = [Tr] + [Glu - Tr]$, $[Tr_{total}]$ is the total concentration of the transporter, therefore Eq. (D.1) to Eq. (D.3) can be simplified to two ODEs:

$$\frac{d[Glu]}{dt} = -k_{1f}[Glu][Tr] + k_{1b}([Tr_{total}] - [Tr]), and \quad \text{(D. 4)}$$

$$\frac{d[Tr]}{dt} = -k_{1f}[Glu][Tr] + (k_{1b} + k_2)([Tr_{total}] - [Tr]). \quad \text{(D. 5)}$$

D.2 Buffers

Dynamics of the immobile buffer and CaD are governded by a same ODE:

$$\frac{d[B]_j}{dt} = -k_{bf}[Ca^{2+}]_j[B]_j + k_{bb}\left([B]_{total} - [B]_j\right), \tag{D. 6}$$

where k_{bf} and k_{bb} are the forward and backward buffer rate constants, respectively, and $[B]_{total,j}$ is the total concentration of immobile buffer or CaD in compartment j.

One CaM can bind four Ca^{2+} ions:

$$Ca^{2+} + CaM \overset{k_1;\, k_{-1}}{\longleftrightarrow} CaCaM,$$

$$Ca^{2+} + CaCaM \overset{k_2;\, k_{-2}}{\longleftrightarrow} Ca_2CaM,$$

$$Ca^{2+} + Ca_2CaM \overset{k_3;\, k_{-3}}{\longleftrightarrow} Ca_3CaM, \text{ and}$$

$$Ca^{2+} + Ca_4CaM \overset{k_4;\, k_{-4}}{\longleftrightarrow} Ca_4CaM.$$

The dynamics of all species in the model can be described by four ODEs (Appendix C.1):

$$\frac{d[CaCaM]}{dt} = k_1[Ca^{2+}][CaM] - k_{-1}[CaCaM] - k_2[Ca^{2+}][CaCaM] + k_{-2}[Ca_2CaM] \tag{D. 7}$$

$$\frac{d[Ca_2CaM]}{dt} = k_2[Ca^{2+}][CaCaM] - k_{-2}[Ca_2CaM] - k_3[Ca^{2+}][Ca_2CaM] + k_{-3}[Ca_3CaM] \tag{D. 8}$$

$$\frac{d[Ca_3CaM]}{dt} = k_3[Ca^{2+}][Ca_2CaM] - k_{-3}[Ca_3CaM] - k_4[Ca^{2+}][Ca_3CaM] + k_{-4}[Ca_4CaM] \tag{D. 9}$$

$$\frac{d[Ca_4CaM]}{dt} = k_4[Ca^{2+}][Ca_3CaM] - k_{-4}[Ca_4CaM] \tag{D. 10}$$

where $[CaM] = [CaM]_{total} - [CaCaM] - [Ca_2CaM] - [Ca_3CaM] - [Ca_4CaM]$ ($[CaM]_{total}$ is the total concentration of CaM).

Appendix E. Markov State Models of Ca^{2+} channels

E.1 Markov kinetic models for a single ligand-gated ion channel

Most voltage- and ligand-gated ion channels go through multiple conformational changes during gating (Tombola, Pathak et al. 2006). Markov kinetic model is widely used to capture the stransition dynamics of between different states and the ligand dependece of voltage- and ligand-gated ion channels (Destexhe, Mainen et al. 1994). The Markov kinetic model consists of a seriers of discrete states, such as open, close, desensitisation and ligand-bound states, and discribes the transition pathways among these states with specific rate constants, dependent or independent of voltage and/or ligand, accordingly. The state transition in a Markov kinetic model is memoryless, only depends on the state the channels in, not on time or its previous transitions.

The rate constants can be estimated by fiting experimental single-channel data to proposed Markov kinetic schemes. The experimental single-channel data by single-channel recording techniques describles the dwell times single channels spent in open or closed states. The frequency distribution of dwell-times can be discribed as a sum of exponential decay components by fitting the dwell-time histgrams to multiple exponential functions (Colquhoun and Hawkes 1982). Fit the dwell-time distributions to the Markov kinetic model to estimate values of each rate constant (Qin and Li 2004).

The deterministic interpretation of the Markov kinetic scheme can be represented as a set of ODEs (Stevens 1978). For example, the following simple four-state model of a ligand-gated channel is:

$$C + L \overset{k_1;\, k_{-1}}{\longleftrightarrow} LC_1 \overset{k_2;\, k_{-2}}{\longleftrightarrow} CL_2 \overset{k_3;\, k_{-3}}{\longleftrightarrow} O, \qquad \text{(E. 2)}$$

where C, LC_1, and LC_2 represtent close state and two ligand-bound close state, L denotes the ligand and O denotes the open state. k_1 and k_{-1} are the forward and backward rate constants for the ligand binding step, respectively. k_2 and k_{-2} are rate constants for the state transition between LC_1, and LC_2. k_3 and k_{-3} are the rate constants of opening and the open state inactivation back to LC_2, respectively.

Let [x] represents the fraction of a single channe in x state. The dynamics can be described by

a set of ODEs as following:

$$\frac{d[L]}{dt} = -k_1[C][L] + k_{-1}[LC_1], \tag{E. 3}$$

$$\frac{d[C]}{dt} = -k_1[C][L] + k_{-1}[LC_1], \tag{E. 4}$$

$$\frac{d[LC_1]}{dt} = k_1[C][L] - k_{-1}[LC_1] - k_2[LC_1] + k_{-2}[LC_2], \tag{E. 5}$$

$$\frac{d[LC_2]}{dt} = k_2[LC_1] - k_{-2}[LC_2] - k_3[LC_2] + k_{-3}[O], \text{and} \tag{E. 6}$$

$$\frac{d[O]}{dt} = k_3[LC_2] - k_{-3}[O]. \tag{E. 7}$$

Because of $[C] + [LC_1] + [LC_2] + [O] = 1$, the fraction of channel in state C is:

$$[C] = 1 - [LC_1] - [LC_2] - [O]. \tag{E. 8}$$

Therefore, Eq. (E.3) can be removed and Eq. (E.4) becomes:

$$\frac{d[LC_1]}{dt} = k_1[L](1 - [LC_1] - [LC_2] - [O]) - k_{-1}[LC_1] - k_2[LC_1] + k_{-2}[LC_2] \tag{E. 9}$$

When the total concentration of the ligand is much greater than the number of channels, $[L]$ can be approximated to be unaffected by the binding step. Therefore, the dynamics of the four-state Markov model in Eq. (E.1) are governed by three ODEs: Eq. (E.5) , Eq. (E.6), and Eq. (E.8)

E.2 Eight-state NMDAR model

The Markov kinetic scheme of NMDAR in Figure 3.4A contains eight states (Erreger, Dravid et al. 2005). Let [X] denotes the fraction of a single NMDAR in state X, and, thus, $[R_N] + [R_NG] + [R_NG_2] + [R_NG_2F] + [R_NG_2S] + [D_1] + [D_2] + [O_N] = 1$. We assume the glutamate concentration is not affected by the binding processes. The parameters of the reaction rates are summarised in Table 3.2. The dynamics of this Markov model are governed by seven ODEs:

$$\frac{d[R_NG]}{dt} = 2k_{on}[R_N][G] - k_{off}[R_NG] - k_{on}[R_NG][G] + 2k_{off}[R_NG_2], \quad \text{(E. 10)}$$

$$\begin{aligned}\frac{d[R_NG_2]}{dt} = {} & k_{on}[R_NG][G] - 2k_{off}[R_NG_2] - k_{d1+}[R_NG_2] + k_{d1-}[D_1] \\ & - k_{d2+}[R_NG_2] + k_{d2-}[D_2] - k_{f+}[R_NG_2] + k_{f-}[R_NG_2F] \\ & - k_{s+}[R_NG_2] + k_{s-}[R_NG_2S],\end{aligned} \quad \text{(E. 11)}$$

$$\frac{d[R_NG_2F]}{dt} = k_{f+}[R_NG_2] - k_{f-}[R_NG_2F] - k_{s+}[R_NG_2F] + k_{s-}[O_N], \quad \text{(E. 12)}$$

$$\frac{d[R_NG_2S]}{dt} = k_{s+}[R_NG_2] - k_{s-}[R_NG_2S] - k_{f+}[R_NG_2S] + k_{f-}[O_N], \quad \text{(E. 13)}$$

$$\frac{d[D_1]}{dt} = k_{d1+}[R_NG_2] - k_{d1-}[D_1], \quad \text{(E. 14)}$$

$$\frac{d[D_2]}{dt} = k_{d2+}[R_NG_2] - k_{d2-}[D_2], and \quad \text{(E. 15)}$$

$$\frac{d[O_N]}{dt} = k_{s+}[R_NG_2F] - k_{s-}[O_N] + k_{f+}[R_NG_2S] - k_{f-}[O_N], \quad \text{(E. 16)}$$

where $[R_N] = 1 - [R_NG] - [R_NG_2] - [R_NG_2F] - [R_NG_2S] - [D_1] - [D_2] - [O_N]$. The fraction of a single NMDAR in the open state at time t is $Po_{NMDAR}(t) = [O_N](t)$.

E.3 Seven-state AMPAR model

The Markov kinetic scheme of AMPAR in Figure 3.4B contains seven states (Jonas, Major et al. 1993). Let [X] denotes the fraction of a single AMPAR in state X, and, thus, $[R_A] + [R_AG_1] + [R_AG_2] + [D_1] + [D_2] + [DO_A] + [O_A] = 1$. We assume the glutamate concentration is not affected by the binding processes. The parameters of the reaction rates are summarised in Table 3.2. The dynamics of this Markov model are governed by six ODEs:

$$\frac{d[R_AG_1]}{dt} = k_{11}[R_A][G] - k_{10}[R_AG_1] - k_{21}[R_AG_1][G] + k_{20}[R_AG_2] - \alpha_1[R_AG_1] + \beta_1[D_1], \quad \text{(E. 17)}$$

$$\frac{d[R_AG_2]}{dt} = k_{21}[R_AG_1][G] - k_{20}[R_AG_2] - \alpha[R_AG_2] + \beta[O_A] - \alpha_2[R_AG_2] + \beta_2[D_2], \quad \text{(E. 18)}$$

$$\frac{d[D_1]}{dt} = \alpha_1[R_AG_1] - \beta_1[D_1] - k_{31}[D_1][G] + k_{30}[D_2], \quad \text{(E. 19)}$$

$$\frac{d[D_2]}{dt} = k_{31}[D_1][G] - k_{30}[D_2] + \alpha_2[R_AG_2] - \beta_2[D_2] - \alpha_4[D_2] + \beta_4[DO_A], \quad \text{(E. 20)}$$

$$\frac{d[DO_A]}{dt} = \alpha_4[D_2] - \beta_4[DO_A] + \alpha_3[O_A] - \beta_3[DO_A], and \quad \text{(E. 21)}$$

$$\frac{d[O_A]}{dt} = \alpha[R_AG_2] - \beta[O_A] - \alpha_3[O_A] + \beta_3[DO_A], \quad \text{(E. 22)}$$

where $[R_A] = 1 - [R_AG_1] - [R_AG_2] - [D_1] - [D_2] - [DO_A] - [O_A]$.The fraction of a single AMPAR in the open state at time t is $Po_{AMPAR}(t) = [O_A](t)$.

Appendix F. MCMC and PRCC

F.1 MCMC for parameter estimation

Markov chain Monte Carlo (MCMC) is a general sampling strategy. It is always used in solving problems with high-dimensional spaces, such as parameter estimation in a multi-dimensional system (Andrieu, De Freitas et al. 2003). In this research, we estimate the values of parameters using an MCMC Matlab toolboxes downloaded from http://helios.fmi.fi/~lainema/mcmc/.

A Markov chain is a discrete random process that consists of a finite number of states. The probability of being at a state only depends on the previous states. Suppose a Markov chain is a sequence of random variables $(X_0, X_1, \dots, X_N)$ at t = 0, 1, …, n, respectively, with a state space of $X = \{x_1, x_2, \dots, x_s\}$. Therefore, the probability of transifer from one state X_n at time n to next state X_{n+1} at time n+1 is

$$p\left(X_{n+1} = x_j \middle| X_n = x_{i_n}, X_{n-1} = x_{i_{n-1}}, \dots, X_0 = x_{i_0}\right) = p\left(X_{n+1} = x_j \middle| X_n = x_{i_n}\right), (n \in N, i_n, j \in s),$$

where $p\left(x_j \middle| x_i\right)$ denotes the probability of moving from state *i* to *j* at current time step. A transition matrix, T, describes the transition probabilities across the state space is

$$T = \begin{pmatrix} p(x_1|x_1) & p(x_1|x_2) & \dots & p\left(x_1|x_j\right) & \dots & p(x_1|x_s) \\ p(x_2|x_1) & p(x_2|x_2) & \dots & p\left(x_2|x_j\right) & \dots & p(x_2|x_s) \\ & & & \dots & & \\ p(x_i|x_1) & p(x_i|x_2) & \dots & p\left(x_i|x_j\right) & \dots & p(x_i|x_s) \\ & & & \dots & & \\ p(x_s|x_1) & p(x_s|x_2) & \dots & p\left(x_s|x_j\right) & \dots & p(x_s|x_s) \end{pmatrix}.$$

The total of the transition probabilities from a state x_i to the rest states in X is 1, therefore,

$$\sum_{i=1}^{s} p\left(x_j \middle| x_i\right) = 1.$$

For example, a simple Markov chain consists a state space of three discrete states($X = \{x_1, x_2, x_3\}$) and its transition matrix is

$$T = \begin{pmatrix} 0.5 & 0 & 0.5 \\ 0 & 0.4 & 0.6 \\ 0.1 & 0 & 0.9 \end{pmatrix}.$$

The probability distribution over states at time n is P_n at time, and

$$P_{n+1} = P_n T = (P_{n-1} T)T = \cdots = P_0 T^n,$$

where P_0 is the initial distribution. When n is large enough, that

$$\lim_{n\to\infty}(T)^n = \begin{pmatrix} 0.1667 & 0 & 0.8333 \\ 0.1667 & 0 & 0.8333 \\ 0.1667 & 0 & 0.8333 \end{pmatrix}.$$

Therefore, the chain converges to an invariant or stationary distribution, $(0.1667 \quad 0 \quad 0.8333)$, regardless the initial distribution P_0.

When an aperiodic Markov chain starts from any state and all the rest states of the state space are reachable within finite steps, the chain will converge to an invariant or stationary distribution (Andrieu, De Freitas et al. 2003). The MCMC is developed based on this convergence property of the Markov chain. The invariant or stationary distribution must have the following detailed balance:

$$P(x_i)T_{ij} = P(x_j)T_{ji}\ , (i, j = 1, \dots, s),$$

where $T_{ij} = p(x_i|x_j)$. Summing both sides of the above equation over x_j, thus

$$P(x_i) = \sum p(x_j)T_{ji}.$$

When we use MCMC to estimate parameter values, if we let the constructed Markov chain converging to the optimal distribution of parameters, then the optimal distribution of parameters can be directly generated from the converged chain.

The Metropolis-Hastings algorithm is one of the most general MCMC methods (Metropolis, Rosenbluth et al. 1953, Hastings 1970). For a given aperiodic and irreducible Markov chain, MC_1 with a discrete parameters space $X = \{x_1, x_2, \dots, x_s\}$. Its transition matrix Q is

$$Q = q(X_{n+1} = x_j | X_n = x_i) = Q_{ij}, (i, j = 1, \dots, s).$$

Suppose the optimal distribution of parameters is $P(X)$, and MC_1 does not converge to *P(X)*:

$$P(x_i)Q_{ij} \neq P(x_j)Q_{ji}\ , (i, j = 1, \dots, s).$$

If MC_1 can be transformed by a function A into MC_2 and MC_2 satisfies the detailed balance condition and converges to $P(X)$:

$$P(x_i)Q_{ij}A(x_i, x_j) = P(x_j)Q_{ji}A(x_j, x_i)\ , (i, j = 1, \dots, s).$$

Therefore, the simplest for of A satisfies $A(x_i, x_j) = P(x_j)Q_{ji}$ and $A(x_j, x_i) = P(x_i)Q_{ij}$. The function A is called the acceptance probability and it describes the probability of accepting the transition happens in MC_1 also occurs in MC_2.

Then the transition matrix of MC_2 is

$$Q' = q'(X_{n+1} = x_j | X_n = x_i) = Q'_{ij} = Q_{ij}Q_{ji}\,P(x_j), (i, j = 1, \dots, s).$$

If A is very small, it may take a long time for MC_2 to explore the whole parameter space to converge to $P(X)$. In that case, multiply A with a factor k where

$$kA(x_i, x_j) \leq 1, kA(x_j, x_i) \leq and\ k \geq 1.$$

Then we obtain a Markov chain MC_3 which can converge to $P(X)$ faster than MC_2:

$$P(x_i)Q_{ij}kA(x_i, x_j) = P(x_j)Q_{ji}kA(x_j, x_i)\,, (i, j = 1, \dots, s).$$

When $kA(x_i, x_j) = 1$ or $kA(x_j, x_i) = 1$, the convergence of MC_3 reaches to the maximum speed, and therefore, the maximum of $kA(x_i, x_j)$ is $\min\left[1, \frac{A(x_i, x_j)}{A(x_j, x_i)}\right]$.

With a given initial state x^0 ($x^0 \in X$), at iteration t (t = 1, 2, …, T), the Metropolis-Hastings algorithm follows the following steps:

(1) Draw y from X and generate a random number, u, from uniform distribution, U(0,1);

(2) If $u < \min\left[1, \frac{A(x_i, x_j)}{A(x_j, x_i)}\right]$, $x^t = y$;

Otherwise, $x^t = x^{t-1}$.

F.2 PRCC for global parameter sensitivity

The partial ranking correlation coefficient (PRCC) is one of popular global sensitivity analysis methods, which quantifies the sensitivity of the model output with respect to the variation of selected parameters. PRCC works well for nonlinear but monotonic relationships between outputs and inputs, therefore, it is important to check the monotonicity of the model parameters against the outputs (Marino, Hogue et al. 2008).

There is a number of sampling algorithms, such as Latin hypercube sampling (LHS) (McKay,

Beckman et al. 2000), which provides the model with a large number of parameter sets, varying within given ranges. For a given model, the correlation coefficient (CC) between a particular parameter, $x_j (j = 1,2, \dots n)$ and output, y, is calculated:

$$r_{x_j y} = \frac{\sum_{i=1}^{N}(x_{ij} - \bar{x})(y_i - \bar{y})}{\sqrt{\sum_{i=1}^{N}(x_{ij} - \bar{x})^2 \sum_{i=1}^{N}(y_i - \bar{y})^2}},$$

where N is the total number of sets of parameters. x_{ij}, $\bar{x}$ and $\bar{y}$ are the values of the i-th sample of x_j, the mean of samples x_j and the mean of outputs, repectively. The absolute value of $r_{x_j y}$ which is close to 1 indicates a strong correlation whereas $|r_{x_j y}|$ which is close to 0 indicates a poor correlation. The sign of $r_{x_j y}$ means negative correlation (-) or positive correlation (+). A p-value shows the significance level of its correspongding $r_{x_j y}$. Normally when p-value <0.05, it rejects the null hypothesis that x_j and y is uncorrelated.

We generate sample parameter set simultaneously according to certain percentage around their reference values. Therefore, CC results may be affected by the variation of parameters and the reference values. The partial correlation coefficient (PCC) removes the linear effects on output y of all parameters other than x_j and then quantifies the relation between x_j and y. The PCC between x_j and y is the CC between $(x_j - \hat{x}_j)$ and $(y - \hat{y})$, where $\hat{x}_j$ and $\hat{y}$ are calculated by following regression model:

$$\hat{x}_j = e_1 + \sum_{i=1, i\neq j}^{n} \alpha_i x_i \, , and$$

$$\hat{y} = e_2 + \sum_{i=1, i\neq j}^{n} \beta_i x_i,$$

where $e_1$and e_2 are error terms, α_i and β_i are the regression coefficients for x_i and y, repectively.

In the PRCC analysis, the parameter x_j and output y are first rank-transformed before calculating $\hat{x}_j$ and $\hat{y}$ according the linear regression models. The rank-transformed data is ranks (integers) which are transferred from real values. Therefore, PRCC can eliminate the effect by the variation of parameters as well as by the magnitude of the referece values on CC. The PRCC analysis in this research is using Matlab functions downloaded from http://malthus.micro.med.umich.edu/lab/usadata/.

Appendix G. Stimulation protocols

G.1 Presynaptic stimulation

When the presynaptic action potential (AP) reaches the presynaptic terminal it triggers the release of glutamate vesicles to the synaptic cleft. The glutamate receptors in the membrane of the postsynaptic spine are activated by the glutamate, resulting the EPSP. This presynaptic stimulation is simulated as the release events of glutamate vesicles, which is closely regulated by the stimulation patterns applied. There are four types of presynaptic stimulation patterns used in this research: (1) single stimulation (or 1 s of stimulation at 1 Hz; 1 pulse); (2) 1 s of low frequency stimulation (LFS) at 10 Hz (10 pulses); (3) 1 s of high frequency stimulation (HFS) at 100 Hz (100 pulses); and (4) theta burst stimulation (TBS) (Figure G.1). We use (1) to (3) in chapter 3 and 4, and (3) and (4) in Chapter 5.

(A) single stimulation

(B) LFS

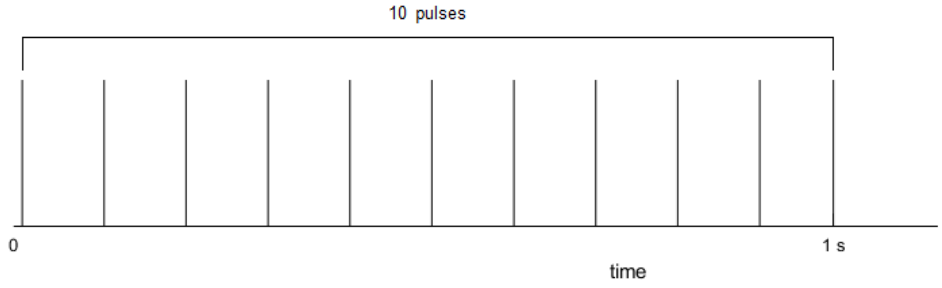

(C) HFS

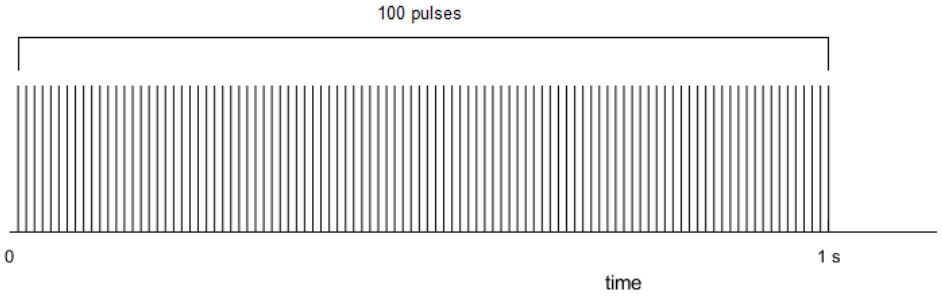

(D) TBS

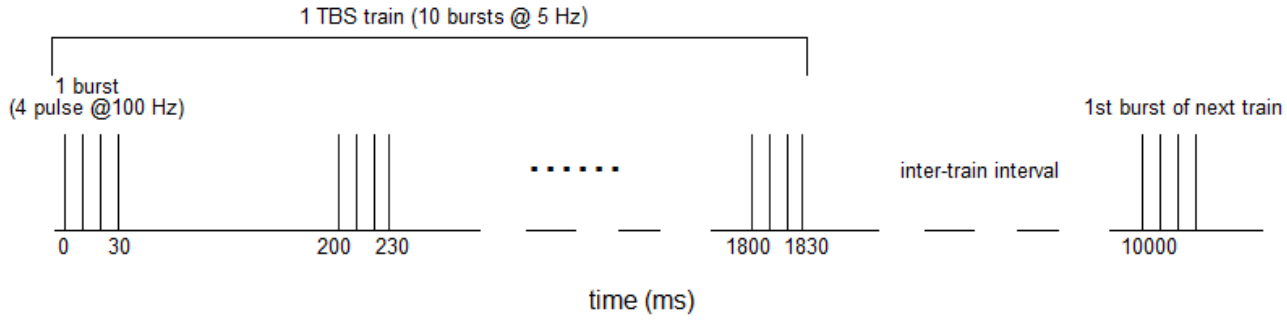

Figure G.1. Stimulation patterns. (1) A single pulse stimulation (or 1 s of stimulation at 1 Hz; 1 pulse); (2) 1 s of low frequency stimulation (LFS) at 10 Hz (10 pulses); (3) 1 s of high frequency stimulation (HFS) at 100 Hz (100 pulses); and (4) theta burst stimulation (TBS). One TBS train consists of 10 stimulus bursts at 5 Hz and each burst consists of four

pulses at 100 Hz. The TBS trains are delivered at 0.1 Hz (10 s separation between trains) (Lee, Barbarosie et al. 2000).

G.2 Postsynaptic stimulation

The action potential (AP) of a neuron travels along the axon and it has been found that AP can propagate back to the dendrites of the pyramidal neurons. This phenomenon is called backpropagation of action potentials (bAP). bAP can create a strong depolarisation on the dendritic membrane, with a brief duration. It activates VDCC to induce ions flux across the membrane (Sabatini, Oertner et al. 2002). We simulate the bAP by injecting a potential into the spine head and dendrite shaft to generate the bAP amplitudes of bAPs 66.4 and 66.7 mV, respectively (Palmer and Stuart 2009).

The decay of bAP is simulated by a simple function as

$$V_{bAP} = A(k_f\,\theta(t-t_i)e^{\frac{-(t-t_i)}{\tau_f}} + k_s\,\theta(t-t_i)e^{\frac{-(t-t_i)}{\tau_s}})$$

where A is the bAP amlitude, k_f = 75% and k_s = 25% are the proportions of fast and slow decay, respectively. τ_f= 3ms and τ_s = 25 ms are the time constants for fast and slow decay, respectively. $\theta(t-t_i)$ is a Heaviside function in which $\theta(st-t_i) = \begin{cases} 0, & if\ t < t_i, \\ 1, & if\ t \geq t_i. \end{cases}$ t is the current time and t_i is the time at when bAP occurs (t_i = 0 in this case). Parameter values are taken from (De Schutter and Bower 1994).

G.3 Pairing stimulation

Both EPSP and bAP themselves are not enough to induce significant depolarisation in the postsynaptic membrane. In the experiments, stimulation at both the presynaptic and postsynaptic neurons are used to create pairing of the bAP and the EPSP, which causes a large depolarisation and Ca^{2+} influx through the NMDARs (Caporale and Dan 2008) (Figure G.2). The interval between the pairing stimulation is a critical factor as it controls the significance of postsynaptic depolarisation (Shouval, Bear et al. 2002). The application of pairing stimulation is shown in Chapter 5.

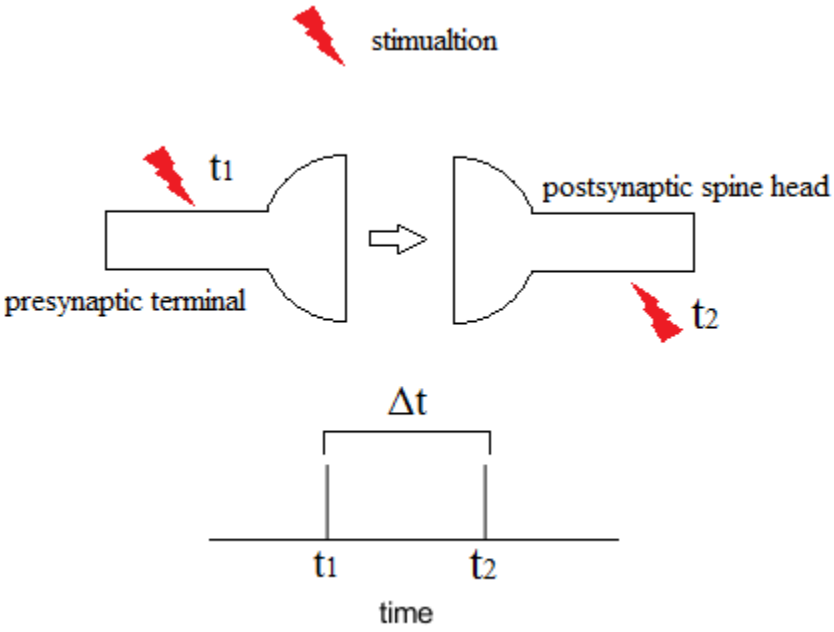

c

Figure G.2. Pairing stimualtion. A pairing stimulation contains a presynaptic stimualtion at time t_1 and a postsynaptic stimualtion at t_2. The time interval between the pairing stimulation is $t_2 - t_1 = \Delta t$.

Appendix H. Complete CaMKII ST model and Parameters

H.1 Reation rates

There are 7 (R_1~R_7) and 12 reaction rates (R_8~R_{19}) of the reactions governing the subunit state transitions and holoenzyme state transitions of CaMKII, respectively. All reation rates are given in a unit of # s^{-1}.

H.1.1 Subunit state transitions CaMKII

Ca^{2+} attaches to CaM to form CaCaM,

$$R_1 = k_{6f} Ca^{2+} \cdot CaM - k_{6b} CaCaM \ . \tag{H.1}$$

Ca^{2+} attaches to CaCaM to form Ca_2CaM,

$$R_2 = k_{7f} Ca^{2+} \cdot CaCaM - k_{7b} Ca_2 CaM \ . \tag{H.2}$$

Ca^{2+} attaches to Ca_2CaM to form Ca_3CaM,

$$R_3 = k_{8f} Ca^{2+} \cdot Ca_2 CaM - k_{8b} Ca_3 CaM \ . \tag{H.3}$$

Ca^{2+} attaches to Ca_3CaM to form Ca^{2+}/CaM complex,

$$R_4 = k_{9f} Ca^{2+} \cdot Ca_3 CaM - k_{9b} Ca_4 CaM \ . \tag{H.4}$$

Ca^{2+}/CaM complex binds to iCaMKII to form CaMKIICaM.

$$R_5 = k_{1f} Ca_4 CaM \cdot iCaMKII - k_{1b} CaMKIICaM \ . \tag{H.5}$$

Autophosphorylation of CaMKIICaM to form CaMKII* (Chiba, Schneider et al. 2008),

$$R_6 = \frac{K_{cat1} CaMKIICaM \cdot P \cdot ATP}{K_{m1} + ATP} \ , \tag{H.6}$$

where $P = 1 - \left(iCaMKII \Big/ CaMKII_{total} \right)^2$.

Dephosphorylation of CaMKII* into CaMKIICaM by PP1 (Chiba, Schneider et al. 2008),

$$R_7 = \frac{K_{cat2} CaMKII^* \cdot PP1}{K_{m2} + CaMKII^*} \quad . \tag{H.7}$$

H.1.2 Holoenzyme state transitions of CaMKII

Translocation of CaMKII into PSD

$$R_8 = k_{2f} EoPSD \frac{\Gamma_2 + \Gamma_3}{K_{m3} + \Gamma_2 + \Gamma_3} - k_{2b} EiPSD \frac{K_{m4}}{K_{m4} + \Gamma_3} \quad , \tag{H.8}$$

where Γ_2 and Γ_3 are the fraction of CaMKIICaM to the total number of unbound subunits and the fraction of CaMKII* to the total number of unbound subunits, respectively. (Γ_1 is the fraction of iCaMKII to the total number of unbound subunits).

$$\Gamma_1 = \frac{iCaMKII}{CaMKII_{Total} - \left(CaMKIIS + CaMKII^* S + CaMKII^* T \right)} \quad ,$$

$$\Gamma_2 = \frac{CaMKIICaM}{CaMKII_{Total} - \left(CaMKIIS + CaMKII^* S + CaMKII^* T \right)} \quad ,$$

$$\Gamma_3 = \frac{CaMKII^*}{CaMKII_{Total} - \left(CaMKIIS + CaMKII^* S + CaMKII^* T \right)} \quad , \text{and}$$

$$\Gamma_1 + \Gamma_2 + \Gamma_3 = 1$$

Binding between CaMKII and NMDAR to form CaMKII-NMDAR complex

$$R_9 = k_{3f} \Omega_1 EiPSD \cdot NMDAR - k_{3ba} CaMKIIS \quad , \tag{H.9}$$

$$R_{10} = k_{3f} \Omega_2 EiPSD \cdot NMDAR - k_{3bb} CaMKII^* S \quad , \tag{H.10}$$

where Ω_1 and Ω_2 are the modifier for average formation rate of CaMKIIS with respect to 91 possible conformations of CaMKII and the modifier for average formation rate of CaMKII*S with respect to 91 possible conformations of CaMKII,

$$\Omega_1 = \sum_{n=1}^{12} \frac{12!}{n!(12-n)!} \Gamma_2{}^n \sum_{m=0}^{12-n} \frac{(12-n)!}{m!(12-n-m)!} \Gamma_3{}^m \Gamma_1{}^{12-m-n} \frac{1-P_b}{(m-1)P_b+1} \cdot \frac{n}{(n-1)P_b+1},$$

$$\Omega_2 = \sum_{m=1}^{12} \frac{12!}{m!(12-m)!} \Gamma_3{}^m \sum_{n=0}^{12-m} \frac{(12-m)!}{n!(12-n-m)!} \Gamma_2{}^n \Gamma_1{}^{12-m-n} \frac{1-P_b}{(n-1)P_b+1} \cdot \frac{m}{(m-1)P_b+1},$$

where n is the number of CaM-pBS and m is the number of T286-pBS, P_b is the probability of S site mediated binding between CaMKII and NMDAR and $P_b = \frac{CaMKIIS + CaMKII^*S}{NMDAR_{Total}}$.

Transfers of the S site binding to the T site

$$R_{11} = k_4 CaMKIIS, \tag{H.11}$$

$$R_{12} = k_4 CaMKII^*S, \tag{H.12}$$

Autophosphorylating CaMKIIS to CaMKII*S

$$R_{13} = \frac{K_{cat1} CaMKIIS \cdot P \cdot ATP}{K_{m1} + ATP}. \tag{H.13}$$

CaMKII Turnover

$$R_{14} = k_5 CaMKIICaM, \tag{H.14}$$

$$R_{15} = k_5 CaMKII^*, \tag{H.15}$$

$$R_{16} = k_5 EiPSD, \tag{H.16}$$

$$R_{17} = k_5 CaMKIIS, \tag{H.17}$$

$R_{18} = k_5 CaMKII^*S$, and (H.18)

$$R_{19} = k_5 CaMKII^*T. \tag{H.19}$$

H.2 ODEs

The time-dependent changes of the states of CaMKII are goven by 10 ODEs based on above 19 reation rates:

Ca^{2+}/CaM complex formation:

$$\frac{dCaCaM}{dt} = R_1 - R_2 , \tag{H.20}$$

$$\frac{dCa_2CaM}{dt} = R_2 - R_3 , \tag{H.21}$$

$$\frac{dCa_3CaM}{dt} = R_3 - R_4 , \text{ and} \tag{H.22}$$

$$\frac{dCa_4CaM}{dt} = R_4 - R_5 . \tag{H.23}$$

Changes in IS of CaMKII:

$$\frac{dCaMKIICaM}{dt} = R_5 - R_6 + R_7 - R_{14} , \text{ and} \tag{H.24}$$

$$\frac{dCaMKII^*}{dt} = R_6 - R_7 - R_{15} . \tag{H.25}$$

CaMKII-NMDAR formation – Changes in HS of CaMKII:

$$\frac{dEiPSD}{dt} = R_8 - R_9 - R_{10} - R_{16} , \tag{H.26}$$

$$\frac{dCaMKIIS}{dt} = R_9 - R_{11} - R_{13} - R_{17} , \tag{H.27}$$

$$\frac{dCaMKII^*S}{dt} = R_{10} - R_{12} + R_{13} - R_{18} , \quad \text{and} \tag{H.28}$$

$$\frac{dCaMKII^*T}{dt} = R_{11} + R_{12} - R_{19} . \tag{H.29}$$

Constraints due to the conserved molecular numbers:

$$iCaMKII = CaMKII_{Total} - CaMKIICaM - CaMKII^{*} - CaMKIIS - CaMKII^{*}S - CaMKII^{*}T \ ,$$

$$CaM = CaM_{Total} - CaCaM - Ca_2CaM - Ca_3CaM - Ca_4CaM - \left(CaMKII_{Total} - iCaMKII\right) \ ,$$

$$NMDAR = NMDAR_{Total} - CaMKIIS - CaMKII^{*}S - CaMKII^{*}T \ , \text{ and}$$

$$EoPSD = CaMKII_{Total}/12 - EiPSD - \left(NMDAR_{Total} - NMDAR\right) \ .$$

H.3 Variables

Table H.1. Definition of the states/variables associated with inner state transition of CaMKII subunit of CaMKII

States (#)	Definition
Ca^{2+}	Intracellular Ca^{2+} ion
CaCaM	one Ca^{2+} ion binds to CaM
Ca_2CaM	two Ca^{2+} ions bind to CaM
Ca_3CaM	three Ca^{2+} ions binds to CaM
Ca_4CaM	Ca^{2+}/CaM complex
iCaMKII	Inhibited CaMKII subunit
CaMKIICaM	CaM bound CaMKII subunit
$CaMKII^{*}$	Autophosphorylated CaMKII subunit

H.4 Parameters and constants

Table H.1 Parameters and constants: their biological meaning, values and sources where the values are obtained.

Parameter	Biological Meaning	Value	Source
k_{1f}	Binding rate of Ca_4CaM and iCaMKII	0.035 $\#^{-1}$ s^{-1}	(Chiba, Schneider et al. 2008)
k_{1b}	Dissociation rate of CaMKIICaM into Ca_4CaM and iCaMKII	0.14 s^{-1}	
k_{2f}	Translocation rate of EoPSD into PSD	0.0088 s^{-1}	(He, Kulasiri et al. 2015)
k_{2b}	Dissociation rate of EiPSD out of PSD	0.247 s^{-1}	
k_{3f}	Binding rate of elementary CaMKII to NMDAR at the S site	0.008 $\#^{-1}s^{-1}$	
k_{3ba}	Dissociation rate of CaMKIIS into EiPSD and NMDAR	0.38 s^{-1}	
k_{3bb}	Dissociation rate of $CaMKII^*S$ into EiPSD and NMDAR	0.024 s^{-1}	
k_4	Transfer rate of NMDAR binding from S site to T site	0.01 s^{-1}	
k_5	Turnover rate of CaMKII	1/108000 s^{-1}	(Ehlers 2003)
k_{6f}	Binding rate of Ca^{2+} and CaM to form CaCaM	0.0415 $\#^{-1}$ s^{-1}	(Chiba, Schneider et al. 2008)
k_{6b}	Dissociation rate of CaCaM into Ca^{2+} and CaM	50 s^{-1}	
k_{7f}	Binding rate of Ca^{2+} and CaCaM to form Ca_2CaM	1.45 $\#^{-1}s^{-1}$	
k_{7b}	Dissociation rate of Ca_2CaM into Ca^{2+} and CaCaM	50 s^{-1}	
k_{8f}	Binding rate of Ca^{2+} and CaCaM to form Ca_3CaM	0.2 $\#^{-1}$ s^{-1}	
k_{8b}	Dissociation rate of Ca_3CaM into Ca^{2+} and Ca_2CaM	1250 s^{-1}	
k_{9f}	Binding rate of Ca^{2+} and CaCaM to form Ca_4CaM	4.15 $\#^{-1}$ s^{-1}	
k_{9b}	Dissociation rate of Ca_4CaM into Ca^{2+} and Ca_3CaM	1250 s^{-1}	
K_{cat1}	Autophosphorylation rate of CaMKIICaM into $CaMKII^*$	0.9 s^{-1}	
K_{cat2}	Dephosphorylation rate of CaMKII* by PP1	1.72 s^{-1}	
K_{m1}	Michaelis constant of the autophosphorylation	1150 $\#^{-1}$	
K_{m2}	Michaelis constant of the dephosphorylation by PP1	660 $\#^{-1}$	
K_{m3}	Fraction of active CaMKII subunits at half maximal translocation rate	0.39	(He, Kulasiri et al. 2015)

K_{m4}	Fraction of autophosphorylated CaMKII subunits at half maximal dissociation rate	0.019	
Constant	**Biological Meaning**	**Value (#)**	**Source**
$CaMKII_{Total}$	Total number of CaMKII subunits	1200	(Ribrault, Sekimoto et al. 2011)
CaM_{Total}	Total number of CaM molecule	consistent with the Ca^{2+} model	
$NMDAR_{Total}$	Total number of NMDAR (or NR2B)		
ATP	Total number of ATP	240000	(Coultrap and Bayer 2012)
PP1	Total number of PP1	145	(He, Kulasiri et al. 2015)

References

Abramov, E., I. Dolev, H. Fogel, G. D. Ciccotosto, E. Ruff and I. Slutsky (2009). "Amyloid-beta as a positive endogenous regulator of release probability at hippocampal synapses." Nat Neurosci **12**(12): 1567-1576.

Adasme, T., P. Haeger, A. C. Paula-Lima, I. Espinoza, M. M. Casas-Alarcón, M. A. Carrasco and C. Hidalgo (2011). "Involvement of ryanodine receptors in neurotrophin-induced hippocampal synaptic plasticity and spatial memory formation." Proceedings of the National Academy of Sciences **108**(7): 3029-3034.

Alabi, A. A. and R. W. Tsien (2012). "Synaptic Vesicle Pools and Dynamics." Cold Spring Harbor Perspectives in Biology **4**(8): a013680.

Alberdi, E., M. V. Sanchez-Gomez, F. Cavaliere, A. Perez-Samartin, J. L. Zugaza, R. Trullas, M. Domercq and C. Matute (2010). "Amyloid beta oligomers induce Ca2+ dysregulation and neuronal death through activation of ionotropic glutamate receptors." Cell Calcium **47**(3): 264-272.

Allan, L. E., G. Bultynck, T. Luyten, H. Amijee, M. D. Bootman and H. L. Roderick (2013). "Alzheimer's Disease-associated peptide Aß42 mobilises ER Ca^{2+} via InsP3R-dependent and -independent mechanisms." Frontiers in Molecular Neuroscience **6**.

Allbritton, N. L., T. Meyer and L. Stryer (1992). "Range of messenger action of calcium ion and inositol 1,4,5-trisphosphate." Science **258**(5089): 1812-1815.

Alves, R., F. Antunes and A. Salvador (2006). "Tools for kinetic modeling of biochemical networks." Nat Biotech **24**(6): 667-672.

Ambert, N., R. Greget, O. Haeberle, S. Bischoff, T. W. Berger, J. M. Bouteiller and M. Baudry (2010). "Computational studies of NMDA receptors: differential effects of neuronal activity on efficacy of competitive and non-competitive antagonists." Open Access Bioinformatics **2**: 113-125.

Andrieu, C., N. De Freitas, A. Doucet and M. I. Jordan (2003). "An introduction to MCMC for machine learning." Machine learning **50**(1-2): 5-43.

Aqdam, M. J., K. Kamali, M. Rahgozar, M. Ohadi, M. Manoochehri, A. Tahami, L. Bostanshirin and H. R. Khorshid (2010). "Association of CALHM1 Gene Polymorphism with Late Onset Alzheimer's Disease in Iranian Population." Avicenna J Med Biotechnol **2**(3): 153-157.

Araya, R., J. Jiang, K. B. Eisenthal and R. Yuste (2006). "The spine neck filters membrane potentials." Proc Natl Acad Sci U S A **103**(47): 17961-17966.

Area-Gomez, E., A. J. de Groof, I. Boldogh, T. D. Bird, G. E. Gibson, C. M. Koehler, W. H. Yu, K. E. Duff, M. P. Yaffe, L. A. Pon and E. A. Schon (2009). "Presenilins are enriched in endoplasmic reticulum membranes associated with mitochondria." Am J Pathol **175**(5): 1810-1816.

Area-Gomez, E., M. Del Carmen Lara Castillo, M. D. Tambini, C. Guardia-Laguarta, A. J. de Groof, M. Madra, J. Ikenouchi, M. Umeda, T. D. Bird, S. L. Sturley and E. A. Schon (2012). "Upregulated function of mitochondria-associated ER membranes in Alzheimer disease." Embo j **31**(21): 4106-4123.

Arendt, T. (2009). "Synaptic degeneration in Alzheimer's disease." Acta Neuropathol **118**(1): 167-179.

Arias, C., I. Arrieta and R. Tapia (1995). "β‐Amyloid peptide fragment 25‐35 potentiates the calcium‐dependent release of excitatory amino acids from depolarized hippocampal slices." Journal of neuroscience research **41**(4): 561-566.

Augustine, G. J. (2001). "How does calcium trigger neurotransmitter release?" Curr Opin Neurobiol **11**(3): 320-326.

Bandara, S., S. Malmersjo and T. Meyer (2013). "Regulators of Calcium Homeostasis Identified by Inference of Kinetic Model Parameters from Live Single Cells Perturbed by siRNA." Sci Signal **6**(283): ra56.
Banke, T. G. and S. F. Traynelis (2003). "Activation of NR1/NR2b NMDA Receptors." Nature neuroscience **6**(2): 144-152.
Barbour, B. and M. Häusser (1997). "Intersynaptic diffusion of neurotransmitter." Trends Neurosci **20**(9): 377-384.
Barger, S. W. and A. S. Basile (2001). "Activation of microglia by secreted amyloid precursor protein evokes release of glutamate by cystine exchange and attenuates synaptic function." Journal of neurochemistry **76**(3): 846-854.
Barria, A. and R. Malinow (2005). "NMDA receptor subunit composition controls synaptic plasticity by regulating binding to CaMKII." Neuron **48**(2): 289-301.
Bartus, R. T., R. L. Dean, 3rd, B. Beer and A. S. Lippa (1982). "The cholinergic hypothesis of geriatric memory dysfunction." Science **217**(4558): 408-414.
Bayer, K. U., P. De Koninck, A. S. Leonard, J. W. Hell and H. Schulman (2001). "Interaction with the NMDA receptor locks CaMKII in an active conformation." Nature **411**(6839): 801-805.
Bayer, K. U., É. LeBel, G. L. McDonald, H. O'Leary, H. Schulman and P. De Koninck (2006). "Transition from reversible to persistent binding of CaMKII to postsynaptic sites and NR2B." The Journal of neuroscience **26**(4): 1164-1174.
Berridge, M. J. (1997). "Elementary and global aspects of calcium signalling." J Physiol **499 (Pt 2)**: 291-306.
Berridge, M. J. (2010). "Calcium hypothesis of Alzheimer's disease." Pflugers Arch **459**(3): 441-449.
Berridge, M. J. (2013). "Dysregulation of neural calcium signaling in Alzheimer disease, bipolar disorder and schizophrenia." Prion **7**(1): 2-13.
Berridge, M. J. (2014). "Calcium regulation of neural rhythms, memory and Alzheimer's disease." The Journal of Physiology **592**(2): 281-293.
Berridge, M. J., M. D. Bootman and H. L. Roderick (2003). "Calcium signalling: dynamics, homeostasis and remodelling." Nat Rev Mol Cell Biol **4**(7): 517-529.
Bezprozvanny, I. (1994). "Theoretical analysis of calcium wave propagation based on inositol (1,4,5)-trisphosphate (InsP3) receptor functional properties." Cell Calcium **16**(3): 151-166.
Bezprozvanny, I. (2005). "The inositol 1,4,5-trisphosphate receptors." Cell Calcium **38**(3-4): 261-272.
Bezprozvanny, I. (2013). "Presenilins and calcium signaling--systems biology to the rescue." Sci Signal **6**(283): pe24.
Bezprozvanny, I. and P. R. Hiesinger (2013). "The synaptic maintenance problem: membrane recycling, Ca2+homeostasis and late onset degeneration." Molecular Neurodegeneration **8**(1): 1-14.
Blackwell, K. T. (2013). "Approaches and tools for modeling signaling pathways and calcium dynamics in neurons." Journal of Neuroscience Methods **220**(2): 131-140.
Blackwell, K. T. and J. Kotaleski (2003). Modeling The Dynamics of Second Messenger Pathways. Neuroscience Databases. R. Kötter, Springer US**:** 63-79.
Blaustein, M. P. and W. J. Lederer (1999). "Sodium/Calcium Exchange: Its Physiological Implications." Physiological Reviews **79**(3): 763-854.
Bloodgood, B. L. and B. L. Sabatini (2007). "Nonlinear regulation of unitary synaptic signals by CaV(2.3) voltage-sensitive calcium channels located in dendritic spines." Neuron **53**(2): 249-260.
Boada, M., C. Antunez, J. Lopez-Arrieta, J. J. Galan, F. J. Moron, I. Hernandez, J. Marin, P. Martinez-Lage, M. Alegret, J. M. Carrasco, C. Moreno, L. M. Real, A. Gonzalez-Perez, L.

Tarraga and A. Ruiz (2010). "CALHM1 P86L polymorphism is associated with late-onset Alzheimer's disease in a recessive model." J Alzheimers Dis **20**(1): 247-251.
Bobich, J. A., Q. Zheng and A. Campbell (2004). "Incubation of nerve endings with a physiological concentration of Aβ_ {1-42} activates CaV2. 2 (N-Type)-voltage operated calcium channels and acutely increases glutamate and noradrenaline release." Journal of Alzheimer's Disease **6**(3): 243-255.
Bojarski, L., J. Herms and J. Kuznicki (2008). "Calcium dysregulation in Alzheimer's disease." Neurochem Int **52**(4-5): 621-633.
Bojarski, L., P. Pomorski, A. Szybinska, M. Drab, A. Skibinska-Kijek, J. Gruszczynska-Biegala and J. Kuznicki (2009). "Presenilin-dependent expression of STIM proteins and dysregulation of capacitative Ca^{2+} entry in familial Alzheimer's disease." Biochimica et Biophysica Acta (BBA) - Molecular Cell Research **1793**(6): 1050-1057.
Bondarenko, V. E., G. P. Szigeti, G. C. Bett, S. J. Kim and R. L. Rasmusson (2004). "Computer model of action potential of mouse ventricular myocytes." Am J Physiol Heart Circ Physiol **287**(3): H1378-1403.
Bordji, K., J. Becerril-Ortega and A. Buisson (2011). "Synapses, NMDA receptor activity and neuronal Abeta production in Alzheimer's disease." Rev Neurosci **22**(3): 285-294.
Bordji, K., J. Becerril-Ortega, O. Nicole and A. Buisson (2010). "Activation of Extrasynaptic, But Not Synaptic, NMDA Receptors Modifies Amyloid Precursor Protein Expression Pattern and Increases Amyloid-β Production." The Journal of Neuroscience **30**(47): 15927-15942.
Braak, H. and E. Braak (1991). "Neuropathological stageing of Alzheimer-related changes." Acta Neuropathol **82**(4): 239-259.
Brette, R., M. Rudolph, T. Carnevale, M. Hines, D. Beeman, J. M. Bower, M. Diesmann, A. Morrison, P. H. Goodman, F. C. Harris, Jr., M. Zirpe, T. Natschlager, D. Pecevski, B. Ermentrout, M. Djurfeldt, A. Lansner, O. Rochel, T. Vieville, E. Muller, A. P. Davison, S. El Boustani and A. Destexhe (2007). "Simulation of networks of spiking neurons: a review of tools and strategies." J Comput Neurosci **23**(3): 349-398.
Briggs, G. E. and J. B. S. Haldane (1925). "A note on the kinetics of enzyme action." Biochemical journal **19**(2): 338.
Brunello, L., E. Zampese, C. Florean, T. Pozzan, P. Pizzo and C. Fasolato (2009). "Presenilin-2 dampens intracellular Ca2+ stores by increasing Ca2+ leakage and reducing Ca2+ uptake." J Cell Mol Med **13**(9b): 3358-3369.
Brunkan, A. L. and A. M. Goate (2005). "Presenilin function and γ-secretase activity." Journal of Neurochemistry **93**(4): 769-792.
Bruno, A. M., J. Y. Huang, D. A. Bennett, R. A. Marr, M. L. Hastings and G. E. Stutzmann (2012). "Altered ryanodine receptor expression in mild cognitive impairment and Alzheimer's disease." Neurobiology of Aging **33**(5): 1001.e1001-1001.e1006.
Buchholz, J. N., J. N. Pottorf, C. K. Vanterpool, E. J. Behringer and S. P. Duckles (2012). Calcium Regulation in Neuronal Function with Advancing Age: Limits of Homeostasis. Senescence. T. Nagata, InTech**:** 531-558.
Butterfield, D. A. and C. B. Pocernich (2003). "The glutamatergic system and Alzheimer's disease." CNS drugs **17**(9): 641-652.
Buxbaum, J. D., A. A. Ruefli, C. A. Parker, A. M. Cypess and P. Greengard (1994). "Calcium regulates processing of the Alzheimer amyloid protein precursor in a protein kinase C-independent manner." Proc Natl Acad Sci U S A **91**(10): 4489-4493.
Caporale, N. and Y. Dan (2008). "Spike timing-dependent plasticity: a Hebbian learning rule." Annu Rev Neurosci **31**: 25-46.
Carafoli, E. (1992). "The Ca2+ pump of the plasma membrane." J Biol Chem **267**(4): 2115-2118.

Casley, C. S., V. Lakics, H. G. Lee, L. M. Broad, T. A. Day, T. Cluett, M. A. Smith, M. J. O'Neill and A. E. Kingston (2009). "Up-regulation of astrocyte metabotropic glutamate receptor 5 by amyloid-beta peptide." Brain Res.
Chakroborty, S., C. Briggs, M. B. Miller, I. Goussakov, C. Schneider, J. Kim, J. Wicks, J. C. Richardson, V. Conklin, B. G. Cameransi and G. E. Stutzmann (2012). "Stabilizing ER Ca^{2+} channel function as an early preventative strategy for Alzheimer's disease." PLoS One **7**(12): e52056.
Chakroborty, S., I. Goussakov, M. B. Miller and G. E. Stutzmann (2009). "Deviant Ryanodine Receptor-Mediated Calcium Release Resets Synaptic Homeostasis in Presymptomatic 3xTg-AD Mice." The Journal of Neuroscience **29**(30): 9458-9470.
Chakroborty, S., J. Kim, C. Schneider, C. Jacobson, J. Molgó and G. E. Stutzmann (2012). "Early Presynaptic and Postsynaptic Calcium Signaling Abnormalities Mask Underlying Synaptic Depression in Presymptomatic Alzheimer's Disease Mice." The Journal of Neuroscience **32**(24): 8341-8353.
Chan, S. L., M. Mayne, C. P. Holden, J. D. Geiger and M. P. Mattson (2000). "Presenilin-1 mutations increase levels of ryanodine receptors and calcium release in PC12 cells and cortical neurons." J Biol Chem **275**(24): 18195-18200.
Chan, S. L., M. Mayne, C. P. Holden, J. D. Geiger and M. P. Mattson (2000). "Presenilin-1 Mutations Increase Levels of Ryanodine Receptors and Calcium Release in PC12 Cells and Cortical Neurons." Journal of Biological Chemistry **275**(24): 18195-18200.
Chen, Q.-S., W.-Z. Wei, T. Shimahara and C.-W. Xie (2002). "Alzheimer Amyloid β-Peptide Inhibits the Late Phase of Long-Term Potentiation through Calcineurin-Dependent Mechanisms in the Hippocampal Dentate Gyrus." Neurobiology of Learning and Memory **77**(3): 354-371.
Cheng, D., C. C. Hoogenraad, J. Rush, E. Ramm, M. A. Schlager, D. M. Duong, P. Xu, S. R. Wijayawardana, J. Hanfelt, T. Nakagawa, M. Sheng and J. Peng (2006). "Relative and Absolute Quantification of Postsynaptic Density Proteome Isolated from Rat Forebrain and Cerebellum." Molecular & Cellular Proteomics **5**(6): 1158-1170.
Cheung, K. H., L. Mei, D. O. Mak, I. Hayashi, T. Iwatsubo, D. E. Kang and J. K. Foskett (2010). "Gain-of-function enhancement of IP3 receptor modal gating by familial Alzheimer's disease-linked presenilin mutants in human cells and mouse neurons." Sci Signal **3**(114): ra22.
Cheung, K. H., D. Shineman, M. Muller, C. Cardenas, L. Mei, J. Yang, T. Tomita, T. Iwatsubo, V. M. Lee and J. K. Foskett (2008). "Mechanism of Ca2+ disruption in Alzheimer's disease by presenilin regulation of InsP3 receptor channel gating." Neuron **58**(6): 871-883.
Chiba, H., N. S. Schneider, S. Matsuoka and A. Noma (2008). "A simulation study on the activation of cardiac CaMKII δ-isoform and its regulation by phosphatases." Biophysical journal **95**(5): 2139-2149.
Chin, J. H., L. Ma, D. MacTavish and J. H. Jhamandas (2007). "Amyloid β protein modulates glutamate-mediated neurotransmission in the rat basal forebrain: involvement of presynaptic neuronal nicotinic acetylcholine and metabotropic glutamate receptors." The Journal of Neuroscience **27**(35): 9262-9269.
Chivet, M., F. Hemming, K. Pernet-Gallay, S. Fraboulet and R. Sadoul (2012). "Emerging Role of Neuronal Exosomes in the Central Nervous System." Frontiers in Physiology **3**: 145.
Christen, Y. (2000). "Oxidative stress and Alzheimer disease." The American Journal of Clinical Nutrition **71**(2): 621s-629s.
Christensen, R. A., A. Shtifman, P. D. Allen, J. R. Lopez and H. W. Querfurth (2004). "Calcium dyshomeostasis in beta-amyloid and tau-bearing skeletal myotubes." J Biol Chem **279**(51): 53524-53532.
Chua, J. J. E., S. Kindler, J. Boyken and R. Jahn (2010). "The architecture of an excitatory synapse." Journal of Cell Science **123**(6): 819-823.

Chuang, D., X.-M. Gao and S. M. Paul (1992). "N-methyl-D-aspartate exposure blocks glutamate toxicity in cultured cerebellar granule cells." Molecular pharmacology **42**(2): 210-216.
Clayton, D. A., M. H. Mesches, E. Alvarez, P. C. Bickford and M. D. Browning (2002). "A hippocampal NR2B deficit can mimic age-related changes in long-term potentiation and spatial learning in the Fischer 344 rat." The Journal of neuroscience **22**(9): 3628-3637.
Colbran, R. J. (2004). "Protein phosphatases and calcium/calmodulin-dependent protein kinase II-dependent synaptic plasticity." The Journal of neuroscience **24**(39): 8404-8409.
Collingridge, G. L., J. T. Isaac and Y. T. Wang (2004). "Receptor trafficking and synaptic plasticity." Nature Reviews Neuroscience **5**(12): 952-962.
Colquhoun, D. and A. G. Hawkes (1982). "On the stochastic properties of bursts of single ion channel openings and of clusters of bursts." Philosophical Transactions of the Royal Society of London B: Biological Sciences **300**(1098): 1-59.
Cooney, J. R., J. L. Hurlburt, D. K. Selig, K. M. Harris and J. C. Fiala (2002). "Endosomal Compartments Serve Multiple Hippocampal Dendritic Spines from a Widespread Rather Than a Local Store of Recycling Membrane." The Journal of Neuroscience **22**(6): 2215-2224.
Costa, R. O., P. N. Lacor, I. L. Ferreira, R. Resende, Y. P. Auberson, W. L. Klein, C. R. Oliveira, A. C. Rego and C. M. F. Pereira (2012). "Endoplasmic reticulum stress occurs downstream of GluN2B subunit of N-methyl-D-aspartate receptor in mature hippocampal cultures treated with amyloid-β oligomers." Aging Cell **11**(5): 823-833.
Coultrap, S. J. and K. U. Bayer (2012). "CaMKII regulation in information processing and storage." Trends in neurosciences **35**(10): 607-618.
Cowburn, R. F., B. Wiehager and E. Sundström (1995). "β-amyloid peptides enhance binding of the calcium mobilising second messengers, inositol(1,4,5)trisphosphate and inositol-(1,3,4,5)tetrakisphosphate to their receptor sites in rat cortical membranes." Neuroscience Letters **191**(1–2): 31-34.
Craig, L. A., N. S. Hong and R. J. McDonald (2011). "Revisiting the cholinergic hypothesis in the development of Alzheimer's disease." Neuroscience & Biobehavioral Reviews **35**(6): 1397-1409.
Crews, L. and E. Masliah (2010). "Molecular mechanisms of neurodegeneration in Alzheimer's disease." Hum Mol Genet **19**(R1): R12-20.
Cruts, M., J. Theuns and C. Van Broeckhoven (2012). "Locus-specific mutation databases for neurodegenerative brain diseases." Human Mutation **33**(9): 1340-1344.
Cui, P. J., L. Zheng, L. Cao, Y. Wang, Y. L. Deng, G. Wang, W. Xu, H. D. Tang, J. F. Ma, T. Zhang, J. Q. Ding, Q. Cheng and S. D. Chen (2010). "CALHM1 P86L polymorphism is a risk factor for Alzheimer's disease in the Chinese population." J Alzheimers Dis **19**(1): 31-35.
Cull-Candy, S. G. (2001). NMDA Receptors. eLS, John Wiley & Sons, Ltd.
Danbolt, N. C. (2001). "Glutamate uptake." Progress in Neurobiology **65**(1): 1-105.
Danysz, W. and C. G. Parsons (2012). "Alzheimer's disease, beta-amyloid, glutamate, NMDA receptors and memantine--searching for the connections." Br J Pharmacol **167**(2): 324-352.
Dawson, A. P., E. J. Lea and R. F. Irvine (2003). "Kinetic model of the inositol trisphosphate receptor that shows both steady-state and quantal patterns of Ca^{2+} release from intracellular stores." Biochem J **370**(Pt 2): 621-629.
De Caluwé, J. and G. Dupont (2013). "The progression towards Alzheimer's disease described as a bistable switch arising from the positive loop between amyloids and Ca^{2+}." Journal of Theoretical Biology **331**(0): 12-18.
De Felice, F. G., P. T. Velasco, M. P. Lambert, K. Viola, S. J. Fernandez, S. T. Ferreira and W. L. Klein (2007). "Aβ oligomers induce neuronal oxidative stress through an N-methyl-D-aspartate receptor-dependent mechanism that is blocked by the Alzheimer drug memantine." Journal of Biological Chemistry **282**(15): 11590-11601.

De Schutter, E. and J. M. Bower (1994). "An active membrane model of the cerebellar Purkinje cell II. Simulation of synaptic responses." Journal of Neurophysiology **71**(1): 401-419.
De Schutter, E. and P. Smolen (1998). "Calcium dynamics in large neuronal models." Methods in neuronal modeling: From ions to networks **2**.
De Strooper, B., T. Iwatsubo and M. S. Wolfe (2012). "Presenilins and gamma-secretase: structure, function, and role in Alzheimer Disease." Cold Spring Harb Perspect Med **2**(1): a006304.
De Young, G. W. and J. Keizer (1992). "A single-pool inositol 1,4,5-trisphosphate-receptor-based model for agonist-stimulated oscillations in Ca^{2+} concentration." Proceedings of the National Academy of Sciences **89**(20): 9895-9899.
Del Prete, D., F. Checler and M. Chami (2014). "Ryanodine receptors: physiological function and deregulation in Alzheimer disease." Molecular Neurodegeneration **9**: 21-21.
Demuro, A., E. Mina, R. Kayed, S. C. Milton, I. Parker and C. G. Glabe (2005). "Calcium dysregulation and membrane disruption as a ubiquitous neurotoxic mechanism of soluble amyloid oligomers." J Biol Chem **280**(17): 17294-17300.
Demuro, A. and I. Parker (2013). "Cytotoxicity of intracellular abeta42 amyloid oligomers involves Ca^{2+} release from the endoplasmic reticulum by stimulated production of inositol trisphosphate." J Neurosci **33**(9): 3824-3833.
Derkach, V., A. Barria and T. R. Soderling (1999). "Ca2+/calmodulin-kinase II enhances channel conductance of α-amino-3-hydroxy-5-methyl-4-isoxazolepropionate type glutamate receptors." Proceedings of the National Academy of Sciences **96**(6): 3269-3274.
Destexhe, A., Z. F. Mainen and T. J. Sejnowski (1994). "Synthesis of models for excitable membranes, synaptic transmission and neuromodulation using a common kinetic formalism." Journal of computational neuroscience **1**(3): 195-230.
Dewachter, I., R. K. Filipkowski, C. Priller, L. Ris, J. Neyton, S. Croes, D. Terwel, M. Gysemans, H. Devijver, P. Borghgraef, E. Godaux, L. Kaczmarek, J. Herms and F. Van Leuven (2009). "Deregulation of NMDA-receptor function and down-stream signaling in APP[V717I] transgenic mice." Neurobiology of Aging **30**(2): 241-256.
Dingledine, R., K. Borges, D. Bowie and S. F. Traynelis (1999). "The Glutamate Receptor Ion Channels." Pharmacological Reviews **51**(1): 7-62.
Doi, T., S. Kuroda, T. Michikawa and M. Kawato (2005). "Inositol 1,4,5-trisphosphate-dependent Ca^{2+} threshold dynamics detect spike timing in cerebellar Purkinje cells." J Neurosci **25**(4): 950-961.
Dreses-Werringloer, U., J. C. Lambert, V. Vingtdeux, H. Zhao, H. Vais, A. Siebert, A. Jain, J. Koppel, A. Rovelet-Lecrux, D. Hannequin, F. Pasquier, D. Galimberti, E. Scarpini, D. Mann, C. Lendon, D. Campion, P. Amouyel, P. Davies, J. K. Foskett, F. Campagne and P. Marambaud (2008). "A polymorphism in CALHM1 influences Ca^{2+} homeostasis, Abeta levels, and Alzheimer's disease risk." Cell **133**(7): 1149-1161.
Durand, G. M., Y. Kovalchuk and A. Konnerth (1996). "Long-term potentiation and functional synapse induction in developing hippocampus."
Duyckaerts, C., B. Delatour and M.-C. Potier (2009). "Classification and basic pathology of Alzheimer disease." Acta Neuropathologica **118**(1): 5-36.
Ehlers, M. D. (2003). "Activity level controls postsynaptic composition and signaling via the ubiquitin-proteasome system." Nature neuroscience **6**(3): 231-242.
Elbaz, Y. and M. Schuldiner (2011). "Staying in touch: the molecular era of organelle contact sites." Trends Biochem Sci **36**(11): 616-623.
Emilsson, L., P. Saetre and E. Jazin (2006). "Alzheimer's disease: mRNA expression profiles of multiple patients show alterations of genes involved with calcium signaling." Neurobiology of Disease **21**(3): 618-625.

Emptage, N., T. V. P. Bliss and A. Fine (1999). "Single Synaptic Events Evoke NMDA Receptor–Mediated Release of Calcium from Internal Stores in Hippocampal Dendritic Spines." Neuron **22**(1): 115-124.
Engelman, H. S. and A. B. MacDermott (2004). "Presynaptic ionotropic receptors and control of transmitter release." Nature Reviews Neuroscience **5**(2): 135-145.
Ermak, G. and K. J. A. Davies (2002). "Calcium and oxidative stress: from cell signaling to cell death." Molecular Immunology **38**(10): 713-721.
Erreger, K., S. M. Dravid, T. G. Banke, D. J. A. Wyllie and S. F. Traynelis (2005). "Subunit-specific gating controls rat NR1/NR2A and NR1/NR2B NMDA channel kinetics and synaptic signalling profiles." The Journal of Physiology **563**(Pt 2): 345-358.
Fellin, T., O. Pascual, S. Gobbo, T. Pozzan, P. G. Haydon and G. Carmignoto (2004). "Neuronal synchrony mediated by astrocytic glutamate through activation of extrasynaptic NMDA receptors." Neuron **43**(5): 729-743.
Fernández-Tomé, P., B. Brera, M. a.-A. Arévalo and M. a. L. de Ceballos (2004). "β-Amyloid 25-35 inhibits glutamate uptake in cultured neurons and astrocytes: modulation of uptake as a survival mechanism." Neurobiology of disease **15**(3): 580-589.
Ferreira, I. L., L. M. Bajouco, S. I. Mota, Y. P. Auberson, C. R. Oliveira and A. C. Rego (2012). "Amyloid beta peptide 1–42 disturbs intracellular calcium homeostasis through activation of GluN2B-containing N-methyl-d-aspartate receptors in cortical cultures." Cell Calcium **51**(2): 95-106.
Ferreira, S. T., J. R. Clarke, T. R. Bomfim and F. G. De Felice (2014). "Inflammation, defective insulin signaling, and neuronal dysfunction in Alzheimer's disease." Alzheimer's & Dementia **10**(1, Supplement): S76-S83.
Ferreiro, E., C. R. Oliveira and C. Pereira (2004). "Involvement of endoplasmic reticulum Ca^{2+} release through ryanodine and inositol 1,4,5-triphosphate receptors in the neurotoxic effects induced by the amyloid-beta peptide." J Neurosci Res **76**(6): 872-880.
Ferreiro, E., R. Resende, R. Costa, C. R. Oliveira and C. M. F. Pereira (2006). "An endoplasmic-reticulum-specific apoptotic pathway is involved in prion and amyloid-beta peptides neurotoxicity." Neurobiology of Disease **23**(3): 669-678.
Fick, A. (1855). "Ueber Diffusion." Annalen der Physik **170**(1): 59-86.
Fink, C. C., B. Slepchenko, I. I. Moraru, J. Watras, J. C. Schaff and L. M. Loew (2000). "An Image-Based Model of Calcium Waves in Differentiated Neuroblastoma Cells." Biophysical Journal **79**(1): 163-183.
Floyd, R. A. and K. Hensley (2002). "Oxidative stress in brain aging: Implications for therapeutics of neurodegenerative diseases." Neurobiology of Aging **23**(5): 795-807.
Foskett, J. K., C. White, K. H. Cheung and D. O. Mak (2007). "Inositol trisphosphate receptor Ca^{2+} release channels." Physiol Rev **87**(2): 593-658.
Foster, K. A., N. McLaughlin, D. Edbauer, M. Phillips, A. Bolton, M. Constantine-Paton and M. Sheng (2010). "Distinct Roles of NR2A and NR2B Cytoplasmic Tails in Long-Term Potentiation." The Journal of Neuroscience **30**(7): 2676-2685.
Francis, P. T., A. M. Palmer, M. Snape and G. K. Wilcock (1999). "The cholinergic hypothesis of Alzheimer's disease: a review of progress." Journal of Neurology, Neurosurgery & Psychiatry **66**(2): 137-147.
Friel, D. D. and R. W. Tsien (1992). "A caffeine- and ryanodine-sensitive Ca2+ store in bullfrog sympathetic neurones modulates effects of Ca2+ entry on [Ca2+]i." The Journal of Physiology **450**: 217-246.
Fukunaga, K., D. Muller and E. Miyamoto (1995). "Increased Phosphorylation of Ca/Calmodulin-dependent Protein Kinase II and Its Endogenous Substrates in the Induction of Long Term Potentiation." Journal of Biological Chemistry **270**(11): 6119-6124.
Furukawa, H., S. K. Singh, R. Mancusso and E. Gouaux (2005). "Subunit arrangement and function in NMDA receptors." Nature **438**(7065): 185-192.

Galeotti, N., E. Vivoli, A. Bartolini and C. Ghelardini (2008). "A gene-specific cerebral types 1, 2, and 3 RyR protein knockdown induces an antidepressant-like effect in mice." Journal of Neurochemistry **106**(6): 2385-2394.
Gallego-Sandin, S., M. T. Alonso and J. Garcia-Sancho (2011). "Calcium homoeostasis modulator 1 (CALHM1) reduces the calcium content of the endoplasmic reticulum (ER) and triggers ER stress." Biochem J **437**(3): 469-475.
Garaschuk, O., R. Schneggenburger, C. Schirra, F. Tempia and A. Konnerth (1996). "Fractional Ca2+ currents through somatic and dendritic glutamate receptor channels of rat hippocampal CA1 pyramidal neurones." The Journal of Physiology **491**(Pt 3): 757-772.
Ghidoni, R., A. Paterlini, V. Albertini, M. Glionna, E. Monti, L. Schiaffonati, L. Benussi, E. Levy and G. Binetti (2011). "Cystatin C is released in association with exosomes: a new tool of neuronal communication which is unbalanced in Alzheimer's Disease." Neurobiology of aging **32**(8): 1435-1442.
Ghosh, A. and M. E. Greenberg (1995). "Calcium signaling in neurons: molecular mechanisms and cellular consequences." Science **268**(5208): 239.
Giacomello, M., L. Barbiero, G. Zatti, R. Squitti, G. Binetti, T. Pozzan, C. Fasolato, R. Ghidoni and P. Pizzo (2005). "Reduction of Ca^{2+} stores and capacitative Ca^{2+} entry is associated with the familial Alzheimer's disease presenilin-2 T122R mutation and anticipates the onset of dementia." Neurobiol Dis **18**(3): 638-648.
Gin, E., V. Kirk and J. Sneyd (2006). "A bifurcation analysis of calcium buffering." Journal of Theoretical Biology **242**(1): 1-15.
Goedert, M. and M. G. Spillantini (2006). "A Century of Alzheimer's Disease." Science **314**(5800): 777-781.
Golde, T. E. (2003). "Alzheimer disease therapy: can the amyloid cascade be halted?" The Journal of clinical investigation **111**(1): 11-18.
Good, T. A. and R. M. Murphy (1996). "Effect of beta-amyloid block of the fast-inactivating K+ channel on intracellular Ca^{2+} and excitability in a modeled neuron." Proc Natl Acad Sci U S A **93**(26): 15130-15135.
Goto, Y., T. Niidome, A. Akaike, T. Kihara and H. Sugimoto (2006). "Amyloid β-peptide preconditioning reduces glutamate-induced neurotoxicity by promoting endocytosis of NMDA receptor." Biochemical and Biophysical Research Communications **351**(1): 259-265.
Gouras, G. K., J. Tsai, J. Naslund, B. Vincent, M. Edgar, F. Checler, J. P. Greenfield, V. Haroutunian, J. D. Buxbaum, H. Xu, P. Greengard and N. R. Relkin (2000). "Intraneuronal Abeta42 accumulation in human brain." Am J Pathol **156**(1): 15-20.
Goussakov, I., M. B. Miller and G. E. Stutzmann (2010). "NMDA-Mediated Ca2+ Influx Drives Aberrant Ryanodine Receptor Activation in Dendrites of Young Alzheimer's Disease Mice." The Journal of Neuroscience **30**(36): 12128-12137.
Goussakov, I., M. B. Miller and G. E. Stutzmann (2010). "NMDA-mediated Ca(2+) influx drives aberrant ryanodine receptor activation in dendrites of young Alzheimer's disease mice." J Neurosci **30**(36): 12128-12137.
Green, K. N., A. Demuro, Y. Akbari, B. D. Hitt, I. F. Smith, I. Parker and F. M. LaFerla (2008). "SERCA pump activity is physiologically regulated by presenilin and regulates amyloid β production." The Journal of cell biology **181**(7): 1107-1116.
Grewer, C., A. Gameiro, Z. Zhang, Z. Tao, S. Braams and T. Rauen (2008). "Glutamate forward and reverse transport: From molecular mechanism to transporter-mediated release after ischemia." IUBMB life **60**(9): 609-619.
Gu, Z., W. Liu and Z. Yan (2009). "β-Amyloid Impairs AMPA Receptor Trafficking and Function by Reducing Ca(2+)/Calmodulin-dependent Protein Kinase II Synaptic Distribution." The Journal of Biological Chemistry **284**(16): 10639-10649.
Guldberg, C. M. and P. Waage (1864). "Studies concerning affinity." CM Forhandlinger: Videnskabs-Selskabet i Christiana **35**(1864): 1864.

Guo, Q., W. Fu, B. L. Sopher, M. W. Miller, C. B. Ware, G. M. Martin and M. P. Mattson (1999). "Increased vulnerability of hippocampal neurons to excitotoxic necrosis in presenilin-1 mutant knock-in mice." Nat Med **5**(1): 101-106.
Guo, Q., B. L. Sopher, K. Furukawa, D. G. Pham, N. Robinson, G. M. Martin and M. P. Mattson (1997). "Alzheimer's presenilin mutation sensitizes neural cells to apoptosis induced by trophic factor withdrawal and amyloid beta-peptide: involvement of calcium and oxyradicals." J Neurosci **17**(11): 4212-4222.
Haario, H., M. Laine, A. Mira and E. Saksman (2006) "DRAM: Efficient adaptive MCMC." Statistics and Computing **16**(4): 339-354.
Haario, H., E. Saksman and J. Tamminen (2001). "An adaptive Metropolis algorithm." Bernoulli, 223-242.
Hardingham, G. E. and H. Bading (2010). "Synaptic versus extrasynaptic NMDA receptor signalling: implications for neurodegenerative disorders." Nature reviews. Neuroscience **11**(10): 682-696.
Hardy, J. and D. J. Selkoe (2002). "The Amyloid Hypothesis of Alzheimer's Disease: Progress and Problems on the Road to Therapeutics." Science **297**(5580): 353-356.
Hardy, J. A. and G. A. Higgins (1992). "Alzheimer's disease: the amyloid cascade hypothesis." Science **256**(5054): 184-185.
Harris, A. Z. and D. L. Pettit (2007). "Extrasynaptic and synaptic NMDA receptors form stable and uniform pools in rat hippocampal slices." The Journal of Physiology **584**(Pt 2): 509-519.
Harris, K. M., F. E. Jensen and B. Tsao (1992). "Three-dimensional structure of dendritic spines and synapses in rat hippocampus (CA1) at postnatal day 15 and adult ages: implications for the maturation of synaptic physiology and long-term potentiation." J Neurosci **12**(7): 2685-2705.
Harris, M. E., J. M. Carney, P. S. Cole, K. Hensley, B. J. Howard, L. Martin, P. Bummer, Y. Wang, N. W. Pedigo, Jr. and D. A. Butterfield (1995). "beta-Amyloid peptide-derived, oxygen-dependent free radicals inhibit glutamate uptake in cultured astrocytes: implications for Alzheimer's disease." Neuroreport **6**(14): 1875-1879.
Harris, M. E., Y. Wang, N. W. Pedigo, K. Hensley, D. A. Butterfield and J. M. Carney (1996). "Amyloid β Peptide (25–35) Inhibits Na+ - Dependent Glutamate Uptake in Rat Hippocampal Astrocyte Cultures." Journal of neurochemistry **67**(1): 277-286.
Hastings, W. K. (1970). "Monte Carlo sampling methods using Markov chains and their applications." Biometrika **57**(1): 97-109.
Hayashi, T., R. Rizzuto, G. Hajnoczky and T. P. Su (2009). "MAM: more than just a housekeeper." Trends Cell Biol **19**(2): 81-88.
He, L. and G. J. Hannon (2004). "MicroRNAs: small RNAs with a big role in gene regulation." Nat Rev Genet **5**(7): 522-531.
He, Y., D. Kulasiri and S. Samarasinghe (2015). "Modelling the dynamics of CaMKII–NMDAR complex related to memory formation in synapses: The possible roles of threonine 286 autophosphorylation of CaMKII in long term potentiation." Journal of theoretical biology **365**: 403-419.
Hedskog, L., C. M. Pinho, R. Filadi, A. Ronnback, L. Hertwig, B. Wiehager, P. Larssen, S. Gellhaar, A. Sandebring, M. Westerlund, C. Graff, B. Winblad, D. Galter, H. Behbahani, P. Pizzo, E. Glaser and M. Ankarcrona (2013). "Modulation of the endoplasmic reticulum-mitochondria interface in Alzheimer's disease and related models." Proc Natl Acad Sci U S A **110**(19): 7916-7921.
Hering, H. and M. Sheng (2001). "Dentritic spines: structure, dynamics and regulation." Nature Reviews Neuroscience **2**(12): 880-888.
Herman, M. A. and C. E. Jahr (2007). "Extracellular glutamate concentration in hippocampal slice." J Neurosci **27**(36): 9736-9741.
Herms, J., I. Schneider, I. Dewachter, N. Caluwaerts, H. Kretzschmar and F. Van Leuven (2003). "Capacitive Calcium Entry Is Directly Attenuated by Mutant Presenilin-1, Independent

of the Expression of the Amyloid Precursor Protein." Journal of Biological Chemistry **278**(4): 2484-2489.
Hertle, D. N. and M. F. Yeckel (2007). "Distribution of inositol-1, 4, 5-trisphosphate receptor isotypes and ryanodine receptor isotypes during maturation of the rat hippocampus." Neuroscience **150**(3): 625-638.
Hidalgo, C., R. Bull, M. I. Behrens and P. Donoso (2004). "Redox regulation of RyR-mediated Ca^{2+} release in muscle and neurons." Biol Res **37**(4): 539-552.
Higgins, E. R., M. B. Cannell and J. Sneyd (2006). "A Buffering SERCA Pump in Models of Calcium Dynamics." Biophysical journal **91**(1): 151-163.
Hill, A. V. (1910). "The possible effects of the aggregation of the molecules of haemoglobin on its dissociation curves." J Physiol (Lond) **40**: 4-7.
Hoe, H.-S., Z. Fu, A. Makarova, J.-Y. Lee, C. Lu, L. Feng, A. Pajoohesh-Ganji, Y. Matsuoka, B. T. Hyman and M. D. Ehlers (2009). "The effects of amyloid precursor protein on postsynaptic composition and activity." Journal of Biological Chemistry **284**(13): 8495-8506.
Holbro, N., Å. Grunditz and T. G. Oertner (2009). "Differential distribution of endoplasmic reticulum controls metabotropic signaling and plasticity at hippocampal synapses." Proceedings of the National Academy of Sciences of the United States of America **106**(35): 15055-15060.
Holcman, D., Z. Schuss and E. Korkotian (2004). "Calcium Dynamics in Dendritic Spines and Spine Motility." Biophysical Journal **87**(1): 81-91.
Holmes, W. R. and W. B. Levy (1990). "Insights into associative long-term potentiation from computational models of NMDA receptor-mediated calcium influx and intracellular calcium concentration changes." J Neurophysiol **63**(5): 1148-1168.
Holtmaat, A., L. Wilbrecht, G. W. Knott, E. Welker and K. Svoboda (2006). "Experience-dependent and cell-type-specific spine growth in the neocortex." Nature **441**(7096): 979-983.
Hudmon, A. and H. Schulman (2002). "Structure–function of the multifunctional Ca2+/calmodulin-dependent protein kinase II." Biochemical Journal **364**(3): 593-611.
Iqbal, K., A. del C. Alonso, S. Chen, M. O. Chohan, E. El-Akkad, C.-X. Gong, S. Khatoon, B. Li, F. Liu, A. Rahman, H. Tanimukai and I. Grundke-Iqbal (2005). "Tau pathology in Alzheimer disease and other tauopathies." Biochimica et Biophysica Acta (BBA) - Molecular Basis of Disease **1739**(2–3): 198-210.
Isaac, J. T., R. A. Nicoll and R. C. Malenka (1995). "Evidence for silent synapses: implications for the expression of LTP." Neuron **15**(2): 427-434.
Isaacs, A. M., D. B. Senn, M. Yuan, J. P. Shine and B. A. Yankner (2006). "Acceleration of amyloid beta-peptide aggregation by physiological concentrations of calcium." J Biol Chem **281**(38): 27916-27923.
Ito, E., K. Oka, R. Etcheberrigaray, T. J. Nelson, D. L. McPhie, B. Tofel-Grehl, G. E. Gibson and D. L. Alkon (1994). "Internal Ca2+ mobilization is altered in fibroblasts from patients with Alzheimer disease." Proceedings of the National Academy of Sciences **91**(2): 534-538.
Jahr, C. E. and C. F. Stevens (1990). "Voltage dependence of NMDA-activated macroscopic conductances predicted by single-channel kinetics." J Neurosci **10**(9): 3178-3182.
Jiang, Q., C. Y. Lee, S. Mandrekar, B. Wilkinson, P. Cramer, N. Zelcer, K. Mann, B. Lamb, T. M. Willson, J. L. Collins, J. C. Richardson, J. D. Smith, T. A. Comery, D. Riddell, D. M. Holtzman, P. Tontonoz and G. E. Landreth (2008). "ApoE promotes the proteolytic degradation of Abeta." Neuron **58**(5): 681-693.
Jin, M., N. Shepardson, T. Yang, G. Chen, D. Walsh and D. J. Selkoe (2011). "Soluble amyloid β-protein dimers isolated from Alzheimer cortex directly induce Tau hyperphosphorylation and neuritic degeneration." Proceedings of the National Academy of Sciences **108**(14): 5819-5824.
Johansson, S., A.-C. Radesäter, R. F. Cowburn, J. Thyberg and J. Luthman (2006). "Modelling of amyloid β-peptide induced lesions using roller-drum incubation of hippocampal slice cultures from neonatal rats." Experimental brain research **168**(1-2): 11-24.

Jonas, P., G. Major and B. Sakmann (1993). "Quantal components of unitary EPSCs at the mossy fibre synapse on CA3 pyramidal cells of rat hippocampus." The Journal of Physiology **472**: 615-663.
Kabogo, D., G. Rauw, A. Amritraj, G. Baker and S. Kar (2010). "β-amyloid-related peptides potentiate K+-evoked glutamate release from adult rat hippocampal slices." Neurobiology of aging **31**(7): 1164-1172.
Kaftan, E. J., B. E. Ehrlich and J. Watras (1997). "Inositol 1,4,5-trisphosphate (InsP3) and calcium interact to increase the dynamic range of InsP3 receptor-dependent calcium signaling." J Gen Physiol **110**(5): 529-538.
Kamenetz, F., T. Tomita, H. Hsieh, G. Seabrook, D. Borchelt, T. Iwatsubo, S. Sisodia and R. Malinow (2003). "APP processing and synaptic function." Neuron **37**(6): 925-937.
Kampa, B. M., J. Clements, P. Jonas and G. J. Stuart (2004). "Kinetics of Mg(2+) unblock of NMDA receptors: implications for spike-timing dependent synaptic plasticity." The Journal of Physiology **556**(Pt 2): 337-345.
Karran, E., M. Mercken and B. D. Strooper (2011). "The amyloid cascade hypothesis for Alzheimer's disease: an appraisal for the development of therapeutics." Nat Rev Drug Discov **10**(9): 698-712.
Kasri, N. N., S. L. Kocks, L. Verbert, S. S. Hébert, G. Callewaert, J. B. Parys, L. Missiaen and H. De Smedt (2006). "Up-regulation of inositol 1,4,5-trisphosphate receptor type 1 is responsible for a decreased endoplasmic-reticulum Ca^{2+} content in presenilin double knock-out cells." Cell Calcium **40**(1): 41-51.
Kawahara, M., I. Ohtsuka, S. Yokoyama, M. Kato-Negishi and Y. Sadakane (2011). "Membrane Incorporation, Channel Formation, and Disruption of Calcium Homeostasis by Alzheimer's β-Amyloid Protein." International Journal of Alzheimer's Disease **2011**.
Keener, J. P. (2006). "Stochastic calcium oscillations." Math Med Biol **23**(1): 1-25.
Keizer, J. and L. Levine (1996). "Ryanodine receptor adaptation and Ca2+(-)induced Ca2+ release-dependent Ca2+ oscillations." Biophysical Journal **71**(6): 3477-3487.
Kelliher, M., J. Fastbom, R. F. Cowburn, W. Bonkale, T. G. Ohm, R. Ravid, V. Sorrentino and C. O'Neill (1999). "Alterations in the ryanodine receptor calcium release channel correlate with Alzheimer's disease neurofibrillary and beta-amyloid pathologies." Neuroscience **92**(2): 499-513.
Kelly, B. L. and A. Ferreira (2006). "beta-Amyloid-induced dynamin 1 degradation is mediated by N-methyl-D-aspartate receptors in hippocampal neurons." J Biol Chem **281**(38): 28079-28089.
Kennedy, M. B., M. K. Bennett, R. F. Bulleit, N. E. Erondu, V. R. Jennings, S. G. Miller, S. S. Molloy, B. L. Patton and L. J. Schenker (1990). "Structure and Regulation of Type II Calcium/Calmodulin-dependent Protein Kinase in Central Nervous System Neurons." Cold Spring Harbor Symposia on Quantitative Biology **55**: 101-110.
Kessels, H. W., S. Nabavi and R. Malinow (2013). "Metabotropic NMDA receptor function is required for beta-amyloid-induced synaptic depression." Proc Natl Acad Sci U S A **110**(10): 4033-4038.
Khachaturian, Z. S. (1987). "Hypothesis on the regulation of cytosol calcium concentration and the aging brain." Neurobiol Aging **8**(4): 345-346.
Khachaturian, Z. S. (1994). "Calcium hypothesis of Alzheimer's disease and brain aging." Ann N Y Acad Sci **747**: 1-11.
Kidd, J. and D. Sattelle (2006). "The effects of amyloid peptides on A-type K+ currents of Drosophila larval cholinergic neurons: modeled actions on firing properties." Invertebrate Neuroscience **6**(4): 207-213.
Kim, M. J., A. W. Dunah, Y. T. Wang and M. Sheng (2005). "Differential Roles of NR2A- and NR2B-Containing NMDA Receptors in Ras-ERK Signaling and AMPA Receptor Trafficking." Neuron **46**(5): 745-760.

Kirvell, S. L., M. Esiri and P. T. Francis (2006). "Down‐regulation of vesicular glutamate transporters precedes cell loss and pathology in Alzheimer's disease." Journal of neurochemistry **98**(3): 939-950.
Klee, C. B. (1991). "Concerted regulation of protein phosphorylation and dephosphorylation by calmodulin." Neurochemical research **16**(9): 1059-1065.
Koch, C. (1998). Biophysics of computation: information processing in single neurons, Oxford university press.
Koffie, R. M., B. T. Hyman and T. L. Spires-Jones (2011). "Alzheimer's disease: synapses gone cold." Molecular neurodegeneration **6**(1): 1.
Koppel, J., F. Campagne, V. Vingtdeux, U. Dreses-Werringloer, M. Ewers, D. Rujescu, H. Hampel, M. L. Gordon, E. Christen, J. Chapuis, B. S. Greenwald, P. Davies and P. Marambaud (2011). "CALHM1 P86L polymorphism modulates CSF Abeta levels in cognitively healthy individuals at risk for Alzheimer's disease." Mol Med **17**(9-10): 974-979.
Koran, M. E., T. J. Hohman and T. A. Thornton-Wells (2014). "Genetic interactions found between calcium channel genes modulate amyloid load measured by positron emission tomography." Hum Genet **133**(1): 85-93.
Kovalchuk, Y., J. Eilers, J. Lisman and A. Konnerth (2000). "NMDA Receptor-Mediated Subthreshold Ca2+ Signals in Spines of Hippocampal Neurons." The Journal of Neuroscience **20**(5): 1791-1799.
Kuchibhotla, K. V., S. T. Goldman, C. R. Lattarulo, H.-Y. Wu, B. T. Hyman and B. J. Bacskai (2008). "Aβ plaques lead to aberrant regulation of calcium homeostasis in vivo resulting in structural and functional disruption of neuronal networks." Neuron **59**(2): 214-225.
Kuchibhotla, K. V., C. R. Lattarulo, B. T. Hyman and B. J. Bacskai (2009). "Synchronous hyperactivity and intercellular calcium waves in astrocytes in Alzheimer mice." Science **323**(5918): 1211-1215.
Kurumatani, T., J. Fastbom, W. L. Bonkale, N. Bogdanovic, B. Winblad, T. G. Ohm and R. F. Cowburn (1998). "Loss of inositol 1,4,5-trisphosphate receptor sites and decreased PKC levels correlate with staging of Alzheimer's disease neurofibrillary pathology." Brain Research **796**(1–2): 209-221.
Kussius, C. L. and G. K. Popescu (2009). "Kinetic basis of partial agonism at NMDA receptors." Nature neuroscience **12**(9): 1114-1120.
Lacor, P. N., M. C. Buniel, P. W. Furlow, A. S. Clemente, P. T. Velasco, M. Wood, K. L. Viola and W. L. Klein (2007). "Aβ oligomer-induced aberrations in synapse composition, shape, and density provide a molecular basis for loss of connectivity in Alzheimer's disease." The Journal of Neuroscience **27**(4): 796-807.
LaFerla, F. M. (2002). "Calcium dyshomeostasis and intracellular signalling in alzheimer's disease." Nat Rev Neurosci **3**(11): 862-872.
LaFerla, F. M., K. N. Green and S. Oddo (2007). "Intracellular amyloid-beta in Alzheimer's disease." Nat Rev Neurosci **8**(7): 499-509.
Lambert, J. C., K. Sleegers, A. Gonzalez-Perez, M. Ingelsson, G. W. Beecham, M. Hiltunen, O. Combarros, M. J. Bullido, N. Brouwers, K. Bettens, C. Berr, F. Pasquier, F. Richard, S. T. Dekosky, D. Hannequin, J. L. Haines, G. Tognoni, N. Fievet, J. F. Dartigues, C. Tzourio, S. Engelborghs, B. Arosio, E. Coto, P. De Deyn, M. Del Zompo, I. Mateo, M. Boada, C. Antunez, J. Lopez-Arrieta, J. Epelbaum, B. M. Schjeide, A. Frank-Garcia, V. Giedraitis, S. Helisalmi, E. Porcellini, A. Pilotto, P. Forti, R. Ferri, M. Delepine, D. Zelenika, M. Lathrop, E. Scarpini, G. Siciliano, V. Solfrizzi, S. Sorbi, G. Spalletta, G. Ravaglia, F. Valdivieso, S. Vepsalainen, V. Alvarez, P. Bosco, M. Mancuso, F. Panza, B. Nacmias, P. Bossu, O. Hanon, P. Piccardi, G. Annoni, D. Mann, P. Marambaud, D. Seripa, D. Galimberti, R. E. Tanzi, L. Bertram, C. Lendon, L. Lannfelt, F. Licastro, D. Campion, M. A. Pericak-Vance, H. Soininen, C. Van Broeckhoven, A. Alperovitch, A. Ruiz, M. I. Kamboh and P. Amouyel (2010). "The CALHM1 P86L

polymorphism is a genetic modifier of age at onset in Alzheimer's disease: a meta-analysis study." J Alzheimers Dis **22**(1): 247-255.
LeBeau, A. P., D. I. Yule, G. E. Groblewski and J. Sneyd (1999). "Agonist-dependent phosphorylation of the inositol 1,4,5-trisphosphate receptor: A possible mechanism for agonist-specific calcium oscillations in pancreatic acinar cells." J Gen Physiol **113**(6): 851-872.
Lee, H.-K., M. Barbarosie, K. Kameyama, M. F. Bear and R. L. Huganir (2000). "Regulation of distinct AMPA receptor phosphorylation sites during bidirectional synaptic plasticity." Nature **405**(6789): 955-959.
Lee, S. J., Y. Escobedo-Lozoya, E. M. Szatmari and R. Yasuda (2009). "Activation of CaMKII in single dendritic spines during long-term potentiation." Nature **458**(7236): 299-304.
Lee, S. Y., D. Y. Hwang, Y. K. Kim, J. W. Lee, I. C. Shin, K. W. Oh, M. K. Lee, J. S. Lim, D. Y. Yoon, S. J. Hwang and J. T. Hong (2006). "PS2 mutation increases neuronal cell vulnerability to neurotoxicants through activation of caspase-3 by enhancing of ryanodine receptor-mediated calcium release." The FASEB Journal **20**(1): 151-153.
Leissring, M. A., Y. Akbari, C. M. Fanger, M. D. Cahalan, M. P. Mattson and F. M. LaFerla (2000). "Capacitative calcium entry deficits and elevated luminal calcium content in mutant presenilin-1 knockin mice." J Cell Biol **149**(4): 793-798.
Leissring, M. A., B. A. Paul, I. Parker, C. W. Cotman and F. M. LaFerla (1999). "Alzheimer's presenilin-1 mutation potentiates inositol 1,4,5-trisphosphate-mediated calcium signaling in Xenopus oocytes." J Neurochem **72**(3): 1061-1068.
Lesné, S., C. Ali, C. Gabriel, N. Croci, E. T. MacKenzie, C. G. Glabe, M. Plotkine, C. Marchand-Verrecchia, D. Vivien and A. Buisson (2005). "NMDA receptor activation inhibits α-secretase and promotes neuronal amyloid-β production." The Journal of neuroscience **25**(41): 9367-9377.
Lester, R. and C. E. Jahr (1992). "NMDA channel behavior depends on agonist affinity." The Journal of neuroscience **12**(2): 635-643.
Li, S., S. Hong, N. E. Shepardson, D. M. Walsh, G. M. Shankar and D. Selkoe (2009). "Soluble Oligomers of Amyloid β Protein Facilitate Hippocampal Long-Term Depression by Disrupting Neuronal Glutamate Uptake." Neuron **62**(6): 788-801.
Li, S., M. Jin, T. Koeglsperger, N. E. Shepardson, G. M. Shankar and D. J. Selkoe (2011). "Soluble Aβ oligomers inhibit long-term potentiation through a mechanism involving excessive activation of extrasynaptic NR2B-containing NMDA receptors." The Journal of neuroscience **31**(18): 6627-6638.
Li, X., S. Dang, C. Yan, X. Gong, J. Wang and Y. Shi (2013). "Structure of a presenilin family intramembrane aspartate protease." Nature **493**(7430): 56-61.
Li, Y.-X. and J. Rinzel (1994). "Equations for InsP3 Receptor-mediated [Ca^{2+}]i Oscillations Derived from a Detailed Kinetic Model: A Hodgkin-Huxley Like Formalism." Journal of Theoretical Biology **166**(4): 461-473.
Liang, J., D. Kulasiri and S. Samarasinghe (2015). "Ca 2+ dysregulation in the endoplasmic reticulum related to Alzheimer's disease: A review on experimental progress and computational modeling." Biosystems **134**: 1-15.
Lisman, J., H. Schulman and H. Cline (2002). "The molecular basis of CaMKII function in synaptic and behavioural memory." Nature Reviews Neuroscience **3**(3): 175-190.
Lisman, J., R. Yasuda and S. Raghavachari (2012). "Mechanisms of CaMKII action in long-term potentiation." Nature reviews. Neuroscience **13**(3): 169-182.
Lisman, J. E. and A. M. Zhabotinsky (2001). "A model of synaptic memory: a CaMKII/PP1 switch that potentiates transmission by organizing an AMPA receptor anchoring assembly." Neuron **31**(2): 191-201.
Liu, L., T. P. Wong, M. F. Pozza, K. Lingenhoehl, Y. Wang, M. Sheng, Y. P. Auberson and Y. T. Wang (2004). "Role of NMDA Receptor Subtypes in Governing the Direction of Hippocampal Synaptic Plasticity." Science **304**(5673): 1021-1024.

Lopez, J. R., A. Lyckman, S. Oddo, F. M. Laferla, H. W. Querfurth and A. Shtifman (2008). "Increased intraneuronal resting [Ca^{2+}] in adult Alzheimer's disease mice." J Neurochem **105**(1): 262-271.
Lüscher, C. and R. C. Malenka (2012). "NMDA receptor-dependent long-term potentiation and long-term depression (LTP/LTD)." Cold Spring Harbor perspectives in biology **4**(6): a005710.
Lytton, J., M. Westlin, S. E. Burk, G. E. Shull and D. H. MacLennan (1992). "Functional comparisons between isoforms of the sarcoplasmic or endoplasmic reticulum family of calcium pumps." Journal of Biological Chemistry **267**(20): 14483-14489.
Maes, O. C., H. M. Chertkow, E. Wang and H. M. Schipper (2009). "MicroRNA: Implications for Alzheimer Disease and other Human CNS Disorders." Current Genomics **10**(3): 154-168.
Mainen, Z. F., N. T. Carnevale, A. M. Zador, B. J. Claiborne and T. H. Brown (1996). "Electrotonic architecture of hippocampal CA1 pyramidal neurons based on three-dimensional reconstructions." J Neurophysiol **76**(3): 1904-1923.
Mak, D. O., S. McBride and J. K. Foskett (2001). "Regulation by Ca^{2+} and inositol 1,4,5-trisphosphate (InsP3) of single recombinant type 3 InsP3 receptor channels. Ca^{2+} activation uniquely distinguishes types 1 and 3 insp3 receptors." J Gen Physiol **117**(5): 435-446.
Malchiodi-Albedi, F., S. Paradisi, A. Matteucci, C. Frank and M. Diociaiuti (2011). "Amyloid oligomer neurotoxicity, calcium dysregulation, and lipid rafts." Int J Alzheimers Dis **2011**: 906964.
Malenka, R. C., Nicoll and R. A. (1999). "Long-Term Potentiation--A Decade of Progress?" Science **285**(5435): 1870-1874.
Manjarres, I. M., A. Rodriguez-Garcia, M. T. Alonso and J. Garcia-Sancho (2010). "The sarco/endoplasmic reticulum Ca(2+) ATPase (SERCA) is the third element in capacitative calcium entry." Cell Calcium **47**(5): 412-418.
Mansvelder, H. D. and D. S. McGehee (2000). "Long-Term Potentiation of Excitatory Inputs to Brain Reward Areas by Nicotine." Neuron **27**(2): 349-357.
Marino, S., I. B. Hogue, C. J. Ray and D. E. Kirschner (2008). "A Methodology For Performing Global Uncertainty And Sensitivity Analysis In Systems Biology." Journal of theoretical biology **254**(1): 178-196.
Masliah, E., M. Alford, M. Mallory, E. Rockenstein, D. Moechars and F. Van Leuven (2000). "Abnormal glutamate transport function in mutant amyloid precursor protein transgenic mice." Experimental neurology **163**(2): 381-387.
Masliah, E., L. Hansen, M. Alford, R. Deteresa and M. Mallory (1996). "Deficient glutamate tranport is associated with neurodegeneration in Alzheimer's disease." Annals of neurology **40**(5): 759-766.
Massey, P. V., B. E. Johnson, P. R. Moult, Y. P. Auberson, M. W. Brown, E. Molnar, G. L. Collingridge and Z. I. Bashir (2004). "Differential Roles of NR2A and NR2B-Containing NMDA Receptors in Cortical Long-Term Potentiation and Long-Term Depression." The Journal of Neuroscience **24**(36): 7821-7828.
Masugi-Tokita, M., E. Tarusawa, M. Watanabe, E. Molnar, K. Fujimoto and R. Shigemoto (2007). "Number and density of AMPA receptors in individual synapses in the rat cerebellum as revealed by SDS-digested freeze-fracture replica labeling." J Neurosci **27**(8): 2135-2144.
Matos, M., E. Augusto, C. R. Oliveira and P. Agostinho (2008). "Amyloid-beta peptide decreases glutamate uptake in cultured astrocytes: Involvement of oxidative stress and mitogen-activated protein kinase cascades." Neuroscience **156**(4): 898-910.
Matsuoka, S., N. Sarai, S. Kuratomi, K. Ono and A. Noma (2003). "Role of individual ionic current systems in ventricular cells hypothesized by a model study." Jpn J Physiol **53**(2): 105-123.
Matsuzaki, M., N. Honkura, G. C. Ellis-Davies and H. Kasai (2004). "Structural basis of long-term potentiation in single dendritic spines." Nature **429**(6993): 761-766.

Mattson, M. P. (2004). "Pathways towards and away from Alzheimer's disease." Nature **430**(7000): 631-639.
Mattson, M. P., F. M. LaFerla, S. L. Chan, M. A. Leissring, P. N. Shepel and J. D. Geiger (2000). "Calcium signaling in the ER: its role in neuronal plasticity and neurodegenerative disorders." Trends Neurosci **23**(5): 222-229.
Mattson, M. P., H. Zhu, J. Yu and M. S. Kindy (2000). "Presenilin-1 mutation increases neuronal vulnerability to focal ischemia in vivo and to hypoxia and glucose deprivation in cell culture: involvement of perturbed calcium homeostasis." J Neurosci **20**(4): 1358-1364.
Mayer, M. L., L. Vyklicky and J. Clements (1989). "Regulation of NMDA receptor desensitization in mouse hippocampal neurons by glycine." Nature **338**(6214): 425-427.
Mayer, M. L., G. L. Westbrook and P. B. Guthrie (1984). "Voltage-dependent block by Mg^{2+}; of NMDA responses in spinal cord neurones."
McKay, M. D., R. J. Beckman and W. J. Conover (2000). "A comparison of three methods for selecting values of input variables in the analysis of output from a computer code." Technometrics **42**(1): 55-61.
Meldrum, B. S. (2000). "Glutamate as a Neurotransmitter in the Brain: Review of Physiology and Pathology." The Journal of Nutrition **130**(4): 1007.
Merrill, M. A., Y. Chen, S. Strack and J. W. Hell (2005). "Activity-driven postsynaptic translocation of CaMKII." Trends in Pharmacological Sciences **26**(12): 645-653.
Metropolis, N., A. W. Rosenbluth, M. N. Rosenbluth, A. H. Teller and E. Teller (1953). "Equation of State Calculations by Fast Computing Machines." The Journal of Chemical Physics **21**(6): 1087-1092.
Michaelis, E. K. (1998). "Molecular biology of glutamate receptors in the central nervous system and their role in excitotoxicity, oxidative stress and aging." Progress in Neurobiology **54**(4): 369-415.
Michaelis, L. and M. L. Menten (1913). "Die kinetik der invertinwirkung."
Minster, R. L., F. Y. Demirci, S. T. DeKosky and M. I. Kamboh (2009). "No association between CALHM1 variation and risk of Alzheimer disease." Human Mutation **30**(4): E566-E569.
Mohamed, A. and E. Posse de Chaves (2011). "Aβ Internalization by Neurons and Glia." International Journal of Alzheimer's Disease **2011**.
Morse, T. M., N. T. Carnevale, P. G. Mutalik, M. Migliore and G. M. Shepherd (2010). "Abnormal Excitability of Oblique Dendrites Implicated in Early Alzheimer's: A Computational Study." Front Neural Circuits **4**.
Mota, S. I., I. L. Ferreira and A. C. Rego (2014). "Dysfunctional synapse in Alzheimer's disease - A focus on NMDA receptors." Neuropharmacology **76 Pt A**: 16-26.
Mucke, L. and D. J. Selkoe (2012). "Neurotoxicity of Amyloid β-Protein: Synaptic and Network Dysfunction." Cold Spring Harbor Perspectives in Medicine **2**(7): a006338.
Mullasseril, P., A. Dosemeci, J. E. Lisman and L. C. Griffith (2007). "A structural mechanism for maintaining the ‘on‐state’ of the CaMKII memory switch in the post‐synaptic density." Journal of neurochemistry **103**(1): 357-364.
Müller, M., K.-H. Cheung and J. K. Foskett (2011). "Enhanced ROS Generation Mediated by Alzheimer's Disease Presenilin Regulation of InsP(3)R Ca(2+) Signaling." Antioxidants & Redox Signaling **14**(7): 1225-1235.
Nadkarni, S., T. M. Bartol, T. J. Sejnowski and H. Levine (2010). "Modelling Vesicular Release at Hippocampal Synapses." PLoS Computational Biology **6**(11): e1000983.
Nakanishi, S. (1992). "Molecular diversity of glutamate receptors and implications for brain function." Science **258**(5082): 597-603.
Nakano, T., J. Yoshimoto and K. Doya (2013). "A model-based prediction of the calcium responses in the striatal synaptic spines depending on the timing of cortical and dopaminergic inputs and post-synaptic spikes." Frontiers in Computational Neuroscience **7**.

Nelson, O., C. Supnet, A. Tolia, K. Horre, B. De Strooper and I. Bezprozvanny (2011). "Mutagenesis mapping of the presenilin 1 calcium leak conductance pore." J Biol Chem **286**(25): 22339-22347.
Nelson, O., H. Tu, T. Lei, M. Bentahir, B. de Strooper and I. Bezprozvanny (2007). "Familial Alzheimer disease-linked mutations specifically disrupt Ca2+ leak function of presenilin 1." J Clin Invest **117**(5): 1230-1239.
Nevian, T. and B. Sakmann (2004). "Single Spine Ca2+ Signals Evoked by Coincident EPSPs and Backpropagating Action Potentials in Spiny Stellate Cells of Layer 4 in the Juvenile Rat Somatosensory Barrel Cortex." The Journal of Neuroscience **24**(7): 1689-1699.
Newpher, T. M. and M. D. Ehlers (2008). "Glutamate Receptor Dynamics in Dendritic Microdomains." Neuron **58**(4): 472-497.
Nielsen, T. A., D. A. DiGregorio and R. A. Silver (2004). "Modulation of Glutamate Mobility Reveals the Mechanism Underlying Slow-Rising AMPAR EPSCs and the Diffusion Coefficient in the Synaptic Cleft." Neuron **42**(5): 757-771.
Noda, M., H. Nakanishi and N. Akaike (1999). "Glutamate release from microglia via glutamate transporter is enhanced by amyloid-beta peptide." Neuroscience **92**(4): 1465-1474.
O'Donnell, C., M. F. Nolan and M. C. W. van Rossum (2011). "Dendritic Spine Dynamics Regulate the Long-Term Stability of Synaptic Plasticity." The Journal of Neuroscience **31**(45): 16142-16156.
O'Dwyer, L., F. Lamberton, A. L. Bokde, M. Ewers, Y. O. Faluyi, C. Tanner, B. Mazoyer, D. O'Neill, M. Bartley and D. R. Collins (2012). "Using support vector machines with multiple indices of diffusion for automated classification of mild cognitive impairment." PloS one **7**(2): e32441.
Oddo, S., A. Caccamo, I. F. Smith, K. N. Green and F. M. LaFerla (2006). "A dynamic relationship between intracellular and extracellular pools of Abeta." Am J Pathol **168**(1): 184-194.
Ondrejcak, T., I. Klyubin, N. W. Hu, A. E. Barry, W. K. Cullen and M. J. Rowan (2010). "Alzheimer's disease amyloid beta-protein and synaptic function." Neuromolecular Med **12**(1): 13-26.
Orellana, J. A., K. F. Shoji, V. Abudara, P. Ezan, E. Amigou, P. J. Sáez, J. X. Jiang, C. C. Naus, J. C. Sáez and C. Giaume (2011). "Amyloid β-induced death in neurons involves glial and neuronal hemichannels." The Journal of Neuroscience **31**(13): 4962-4977.
Oule`s, B., D. Del Prete, B. Greco, X. Zhang, I. Lauritzen, J. Sevalle, S. Moreno, P. Paterlini-Brechot, M. Trebak, F. Checler, F. Benfenati and M. Chami (2012). "Ryanodine receptor blockade reduces amyloid-beta load and memory impairments in Tg2576 mouse model of Alzheimer disease." J Neurosci **32**(34): 11820-11834.
Palmer, L. M. and G. J. Stuart (2009). "Membrane Potential Changes in Dendritic Spines during Action Potentials and Synaptic Input." The Journal of Neuroscience **29**(21): 6897-6903.
Palop, J. J. and L. Mucke (2010). "Amyloid-β Induced Neuronal Dysfunction in Alzheimer's Disease: From Synapses toward Neural Networks." Nature neuroscience **13**(7): 812-818.
Paoletti, P., C. Bellone and Q. Zhou (2013). "NMDA receptor subunit diversity: impact on receptor properties, synaptic plasticity and disease." Nature Reviews Neuroscience **14**(6): 383-400.
Papouin, T., L. Ladepeche, J. Ruel, S. Sacchi, M. Labasque, M. Hanini, L. Groc, L. Pollegioni, J. P. Mothet and S. H. Oliet (2012). "Synaptic and extrasynaptic NMDA receptors are gated by different endogenous coagonists." Cell **150**(3): 633-646.
Parpura-Gill, A., D. Beitz and E. Uemura (1997). "The inhibitory effects of β-amyloid on glutamate and glucose uptakes by cultured astrocytes." Brain Research **754**(1–2): 65-71.
Pasti, L., A. Volterra, T. Pozzan and G. Carmignoto (1997). "Intracellular Calcium Oscillations in Astrocytes: A Highly Plastic, Bidirectional Form of Communication between Neurons and Astrocytes In Situ." The Journal of Neuroscience **17**(20): 7817-7830.

Patneau, D. K. and M. L. Mayer (1991). "Kinetic analysis of interactions between kainate and AMPA: evidence for activation of a single receptor in mouse hippocampal neurons." Neuron **6**(5): 785-798.
Patterson, C., J. W. Feightner, A. Garcia, G. Y. R. Hsiung, C. MacKnight and A. D. Sadovnick (2008). "Diagnosis and treatment of dementia: 1. Risk assessment and primary prevention of Alzheimer disease." Canadian Medical Association Journal **178**(5): 548-556.
Petralia, R. S. (2012). "Distribution of Extrasynaptic NMDA Receptors on Neurons." The Scientific World Journal **2012**: 11.
Petralia, R. S., Y. X. Wang, F. Hua, Z. Yi, A. Zhou, L. Ge, F. A. Stephenson and R. J. Wenthold (2010). "Organization of NMDA receptors at extrasynaptic locations." Neuroscience **167**(1): 68-87.
Pierrot, N., P. Ghisdal, A.-S. Caumont and J.-N. Octave (2004). "Intraneuronal amyloid-β1-42 production triggered by sustained increase of cytosolic calcium concentration induces neuronal death." Journal of Neurochemistry **88**(5): 1140-1150.
Pike, F. G., R. M. Meredith, A. W. A. Olding and O. Paulsen (1999). "Postsynaptic bursting is essential for 'Hebbian' induction of associative long-term potentiation at excitatory synapses in rat hippocampus." The Journal of Physiology **518**(Pt 2): 571-576.
Pinheiro, P. S. and C. Mulle (2008). "Presynaptic glutamate receptors: physiological functions and mechanisms of action." Nature Reviews Neuroscience **9**(6): 423-436.
Popescu, G., A. Robert, J. R. Howe and A. Auerbach (2004). "Reaction mechanism determines NMDA receptor response to repetitive stimulation." Nature **430**(7001): 790-793.
Popugaeva, E. and I. Bezprozvanny (2013). "Role of endoplasmic reticulum Ca2+ signaling in the pathogenesis of Alzheimer disease." Frontiers in molecular neuroscience **6**: 29.
Popugaeva, E., C. Supnet and I. Bezprozvanny (2012). "Presenilins, deranged calcium homeostasis, synaptic loss and dysfunction in Alzheimer's disease." Messenger **1**(1): 53-62.
Prince, M., A. Comas-Herrera, M. Knapp, M. Guerchet and M. Karagiannidou (2016). "World Alzheimer report 2016: improving healthcare for people living with dementia: coverage, quality and costs now and in the future."
Puzzo, D., L. Privitera, E. Leznik, M. Fa, A. Staniszewski, A. Palmeri and O. Arancio (2008). "Picomolar amyloid-β positively modulates synaptic plasticity and memory in hippocampus." The Journal of neuroscience : the official journal of the Society for Neuroscience **28**(53): 14537-14545.
Qin, F. and L. Li (2004). "Model-Based Fitting of Single-Channel Dwell-Time Distributions." Biophysical Journal **87**(3): 1657-1671.
Querfurth, H. W., J. Jiang, J. D. Geiger and D. J. Selkoe (1997). "Caffeine Stimulates Amyloid β-Peptide Release from β-Amyloid Precursor Protein-Transfected HEK293 Cells." Journal of Neurochemistry **69**(4): 1580-1591.
Querfurth, H. W. and D. J. Selkoe (1994). "Calcium ionophore increases amyloid beta peptide production by cultured cells." Biochemistry **33**(15): 4550-4561.
Rahman, T. and C. W. Taylor (2009). "Dynamic regulation of IP_3 receptor clustering and activity by IP_3." Channels (Austin) **3**(4): 226-232.
Rajendran, L., M. Honsho, T. R. Zahn, P. Keller, K. D. Geiger, P. Verkade and K. Simons (2006). "Alzheimer's disease β-amyloid peptides are released in association with exosomes." Proceedings of the National Academy of Sciences of the United States of America **103**(30): 11172-11177.
Raymond, C. R. (2007). "LTP forms 1, 2 and 3: different mechanisms for the 'long' in long-term potentiation." Trends in Neurosciences **30**(4): 167-175.
Regehr, W. G. and D. W. Tank (1990). "Postsynaptic NMDA receptor-mediated calcium accumulation in hippocatnpal CAI pyramidal cell dendrites." Nature **345**.

Renner, M., P. N. Lacor, P. T. Velasco, J. Xu, A. Contractor, W. L. Klein and A. Triller (2010). "Deleterious effects of amyloid beta oligomers acting as an extracellular scaffold for mGluR5." Neuron **66**(5): 739-754.
Ribrault, C., K. Sekimoto and A. Triller (2011). "From the stochasticity of molecular processes to the variability of synaptic transmission." Nature Reviews Neuroscience **12**(7): 375-387.
Riera, J., R. Hatanaka, T. Uchida, T. Ozaki and R. Kawashima (2011). "Quantifying the uncertainty of spontaneous Ca^{2+} oscillations in astrocytes: particulars of Alzheimer's disease." Biophys J **101**(3): 554-564.
Roberts, T. F., K. A. Tschida, M. E. Klein and R. Mooney (2010). "Rapid spine stabilization and synaptic enhancement at the onset of behavioural learning." Nature **463**(7283): 948-952.
Rowland, A. A. and G. K. Voeltz (2012). "Endoplasmic reticulum-mitochondria contacts: function of the junction." Nat Rev Mol Cell Biol **13**(10): 607-625.
Rubin, J. E., R. C. Gerkin, G. Q. Bi and C. C. Chow (2005). "Calcium time course as a signal for spike-timing-dependent plasticity." J Neurophysiol **93**(5): 2600-2613.
Rusakov, D. A. (2001). "The role of perisynaptic glial sheaths in glutamate spillover and extracellular Ca 2+ depletion." Biophysical Journal **81**(4): 1947-1959.
Rusakov, D. A. and D. M. Kullmann (1998). "Extrasynaptic Glutamate Diffusion in the Hippocampus: Ultrastructural Constraints, Uptake, and Receptor Activation." The Journal of Neuroscience **18**(9): 3158-3170.
Ryan, K. A. and S. W. Pimplikar (2005). "Activation of GSK-3 and phosphorylation of CRMP2 in transgenic mice expressing APP intracellular domain." J Cell Biol **171**(2): 327-335.
Rybalchenko, V., S. Y. Hwang, N. Rybalchenko and P. Koulen (2008). "The cytosolic N-terminus of presenilin-1 potentiates mouse ryanodine receptor single channel activity." Int J Biochem Cell Biol **40**(1): 84-97.
Sabatini, B. L., M. Maravall and K. Svoboda (2001). "Ca 2+ signaling in dendritic spines." Current opinion in neurobiology **11**(3): 349-356.
Sabatini, B. L., T. G. Oertner and K. Svoboda (2002). "The Life Cycle of Ca2+ Ions in Dendritic Spines." Neuron **33**(3): 439-452.
Sachs, F., F. Qin and P. Palade (1995). "Models of Ca^{2+} release channel adaptation." Science **267**(5206): 2010-2011.
Saftenku, E., A. J. Williams and R. Sitsapesan (2001). "Markovian models of low and high activity levels of cardiac ryanodine receptors." Biophys J **80**(6): 2727-2741.
Sanhueza, M. and J. Lisman (2013). "The CaMKII/NMDAR complex as a molecular memory." Molecular brain **6**(1): 1.
Sanz-Arigita, E. J., M. M. Schoonheim, J. S. Damoiseaux, S. A. Rombouts, E. Maris, F. Barkhof, P. Scheltens and C. J. Stam (2010). "Loss of 'small-world' networks in Alzheimer's disease: graph analysis of FMRI resting-state functional connectivity." PLoS One **5**(11): e13788.
Sanz-Blasco, S., R. A. Valero, I. Rodríguez-Crespo, C. Villalobos and L. Núñez (2008). "Mitochondrial Ca 2+ overload underlies Aβ oligomers neurotoxicity providing an unexpected mechanism of neuroprotection by NSAIDs." PLoS One **3**(7): e2718.
Saura, C. A., S. Y. Choi, V. Beglopoulos, S. Malkani, D. Zhang, B. S. Shankaranarayana Rao, S. Chattarji, R. J. Kelleher, 3rd, E. R. Kandel, K. Duff, A. Kirkwood and J. Shen (2004). "Loss of presenilin function causes impairments of memory and synaptic plasticity followed by age-dependent neurodegeneration." Neuron **42**(1): 23-36.
Schapansky, J., K. Olson, R. Van Der Ploeg and G. Glazner (2007). "NF-κB activated by ER calcium release inhibits Aβ-mediated expression of CHOP protein: Enhancement by AD-linked mutant presenilin 1." Experimental Neurology **208**(2): 169-176.
Schiegg, A., W. Gerstner, R. Ritz and J. L. van Hemmen (1995). "Intracellular Ca2+ stores can account for the time course of LTP induction: a model of Ca2+ dynamics in dendritic spines." J Neurophysiol **74**(3): 1046-1055.

Schon, E. A. and E. Area-Gomez (2013). "Mitochondria-associated ER membranes in Alzheimer disease." Molecular and Cellular Neuroscience **55**(0): 26-36.
Schorge, S., S. Elenes and D. Colquhoun (2005). "Maximum likelihood fitting of single channel NMDA activity with a mechanism composed of independent dimers of subunits." The Journal of physiology **569**(2): 395-418.
Schuster, S., M. Marhl and T. Hofer (2002). "Modelling of simple and complex calcium oscillations. From single-cell responses to intercellular signalling." Eur J Biochem **269**(5): 1333-1355.
Sebollela, A., L. Freitas-Correa, F. F. Oliveira, A. C. Paula-Lima, L. M. Saraiva, S. M. Martins, L. D. Mota, C. Torres, S. Alves-Leon, J. M. de Souza, D. M. Carraro, H. Brentani, F. G. De Felice and S. T. Ferreira (2012). "Amyloid-β Oligomers Induce Differential Gene Expression in Adult Human Brain Slices." Journal of Biological Chemistry **287**(10): 7436-7445.
Selkoe, D. J. (1991). "The molecular pathology of Alzheimer's disease." Neuron **6**(4): 487-498.
Selkoe, D. J. and J. Hardy (2016). "The amyloid hypothesis of Alzheimer's disease at 25 years." EMBO Molecular Medicine **8**(6): 595-608.
Senn, W., H. Markram and M. Tsodyks (2001). "An algorithm for modifying neurotransmitter release probability based on pre-and postsynaptic spike timing." Neural Computation **13**(1): 35-67.
Shankar, G. M. and D. M. Walsh (2009). "Alzheimer's disease: synaptic dysfunction and Abeta." Mol Neurodegener **4**: 48.
Shannon, T. R., K. S. Ginsburg and D. M. Bers (2000). "Reverse mode of the sarcoplasmic reticulum calcium pump and load-dependent cytosolic calcium decline in voltage-clamped cardiac ventricular myocytes." Biophysical Journal **78**(1): 322-333.
Sharp, A. H., P. S. McPherson, T. M. Dawson, C. Aoki, K. P. Campbell and S. H. Snyder (1993). "Differential immunohistochemical localization of inositol 1,4,5-trisphosphate- and ryanodine-sensitive Ca2+ release channels in rat brain." J Neurosci **13**(7): 3051-3063.
Sheldon, A. L. and M. B. Robinson (2007). "The role of glutamate transporters in neurodegenerative diseases and potential opportunities for intervention." Neurochemistry International **51**(6–7): 333-355.
Shen, J. and R. J. Kelleher, 3rd (2007). "The presenilin hypothesis of Alzheimer's disease: evidence for a loss-of-function pathogenic mechanism." Proc Natl Acad Sci U S A **104**(2): 403-409.
Shilling, D., D. O. Mak, D. E. Kang and J. K. Foskett (2012). "Lack of evidence for presenilins as endoplasmic reticulum Ca2+ leak channels." J Biol Chem **287**(14): 10933-10944.
Shilling, D., M. Müller, H. Takano, D.-O. Daniel Mak, T. Abel, D. A. Coulter and J. K. Foskett (2014). "Suppression of InsP3 Receptor-Mediated Ca^{2+} Signaling Alleviates Mutant Presenilin-Linked Familial Alzheimer's Disease Pathogenesis." The Journal of Neuroscience **34**(20): 6910-6923.
Shouval, H. Z., M. F. Bear and L. N. Cooper (2002). "A unified model of NMDA receptor-dependent bidirectional synaptic plasticity." Proceedings of the National Academy of Sciences **99**(16): 10831-10836.
Shtifman, A., C. W. Ward, D. R. Laver, M. L. Bannister, J. R. Lopez, M. Kitazawa, F. M. LaFerla, N. Ikemoto and H. W. Querfurth (2010). "Amyloid-beta protein impairs Ca^{2+} release and contractility in skeletal muscle." Neurobiol Aging **31**(12): 2080-2090.
Smith, I. F., K. N. Green and F. M. LaFerla (2005). "Calcium dysregulation in Alzheimer's disease: Recent advances gained from genetically modified animals." Cell Calcium **38**(3–4): 427-437.
Sneyd, J. and M. Falcke (2005). "Models of the inositol trisphosphate receptor." Progress in Biophysics and Molecular Biology **89**(3): 207-245.
Sneyd, J., S. Girard and D. Clapham (1993). "Calcium wave propagation by calcium-induced calcium release: an unusual excitable system." Bull Math Biol **55**(2): 315-344.

Snyder, E. M., Y. Nong, C. G. Almeida, S. Paul, T. Moran, E. Y. Choi, A. C. Nairn, M. W. Salter, P. J. Lombroso, G. K. Gouras and P. Greengard (2005). "Regulation of NMDA receptor trafficking by amyloid-beta." Nat Neurosci **8**(8): 1051-1058.
Sobczyk, A., V. Scheuss and K. Svoboda (2005). "NMDA receptor subunit-dependent [Ca2+] signaling in individual hippocampal dendritic spines." J Neurosci **25**(26): 6037-6046.
Soboloff, J., B. S. Rothberg, M. Madesh and D. L. Gill (2012). "STIM proteins: dynamic calcium signal transducers." Nat Rev Mol Cell Biol **13**(9): 549-565.
Sorra, K. E. and K. M. Harris (2000). "Overview on the structure, composition, function, development, and plasticity of hippocampal dendritic spines." Hippocampus **10**(5): 501-511.
Spacek, J. and K. M. Harris (1997). "Three-dimensional organization of smooth endoplasmic reticulum in hippocampal CA1 dendrites and dendritic spines of the immature and mature rat." The Journal of neuroscience **17**(1): 190-203.
Spires-Jones, T. L., W. H. Stoothoff, A. de Calignon, P. B. Jones and B. T. Hyman (2009). "Tau pathophysiology in neurodegeneration: a tangled issue." Trends in neurosciences **32**(3): 150-159.
Spruston, N., P. Jonas and B. Sakmann (1995). "Dendritic glutamate receptor channels in rat hippocampal CA3 and CA1 pyramidal neurons." The Journal of Physiology **482**(Pt 2): 325-352.
Sterratt, D., B. Graham, A. Gillies and D. Willshaw (2011). Intracellular mechanisms. Principles of Computational Modelling in Neuroscience, Cambridge University Press.
Stevens, C. (1978). "Interactions between intrinsic membrane protein and electric field. An approach to studying nerve excitability." Biophysical journal **22**(2): 295.
Strack, S. and R. J. Colbran (1998). "Autophosphorylation-dependent Targeting of Calcium/Calmodulin-dependent Protein Kinase II by the NR2B Subunit of theN-Methyl-D-aspartate Receptor." Journal of Biological Chemistry **273**(33): 20689-20692.
Stutzmann, G. E., A. Caccamo, F. M. LaFerla and I. Parker (2004). "Dysregulated IP3 signaling in cortical neurons of knock-in mice expressing an Alzheimer's-linked mutation in presenilin1 results in exaggerated Ca2+ signals and altered membrane excitability." J Neurosci **24**(2): 508-513.
Stutzmann, G. E. and M. P. Mattson (2011). "Endoplasmic reticulum Ca(2+) handling in excitable cells in health and disease." Pharmacol Rev **63**(3): 700-727.
Stutzmann, G. E., I. Smith, A. Caccamo, S. Oddo, F. M. Laferla and I. Parker (2006). "Enhanced ryanodine receptor recruitment contributes to Ca2+ disruptions in young, adult, and aged Alzheimer's disease mice." J Neurosci **26**(19): 5180-5189.
Stutzmann, G. E., I. Smith, A. Caccamo, S. Oddo, I. Parker and F. Laferla (2007). "Enhanced ryanodine-mediated calcium release in mutant PS1-expressing Alzheimer's mouse models." Ann N Y Acad Sci **1097**: 265-277.
Sun, S., H. Zhang, J. Liu, E. Popugaeva, N. J. Xu, S. Feske, C. L. White, 3rd and I. Bezprozvanny (2014). "Reduced synaptic STIM2 expression and impaired store-operated calcium entry cause destabilization of mature spines in mutant presenilin mice." Neuron **82**(1): 79-93.
Supekar, K., V. Menon, D. Rubin, M. Musen and M. D. Greicius (2008). "Network Analysis of Intrinsic Functional Brain Connectivity in Alzheimer's Disease." PLoS Comput Biol **4**(6): e1000100.
Supnet, C. and I. Bezprozvanny (2010). "The dysregulation of intracellular calcium in Alzheimer disease." Cell calcium **47**(2): 183-189.
Supnet, C. and I. Bezprozvanny (2011). "Presenilins function in ER calcium leak and Alzheimer's disease pathogenesis." Cell Calcium **50**(3): 303-309.
Supnet, C., J. Grant, H. Kong, D. Westaway and M. Mayne (2006). "Amyloid-beta-(1-42) increases ryanodine receptor-3 expression and function in neurons of TgCRND8 mice." J Biol Chem **281**(50): 38440-38447.

Supnet, C., C. Noonan, K. Richard, J. Bradley and M. Mayne (2010). "Up-regulation of the type 3 ryanodine receptor is neuroprotective in the TgCRND8 mouse model of Alzheimer's disease." J Neurochem **112**(2): 356-365.
Takumi, Y., V. Ramirez-Leon, P. Laake, E. Rinvik and O. P. Ottersen (1999). "Different modes of expression of AMPA and NMDA receptors in hippocampal synapses." Nat Neurosci **2**(7): 618-624.
Talantova, M., S. Sanz-Blasco, X. Zhang, P. Xia, M. W. Akhtar, S.-i. Okamoto, G. Dziewczapolski, T. Nakamura, G. Cao, A. E. Pratt, Y.-J. Kang, S. Tu, E. Molokanova, S. R. McKercher, S. A. Hires, H. Sason, D. G. Stouffer, M. W. Buczynski, J. P. Solomon, S. Michael, E. T. Powers, J. W. Kelly, A. Roberts, G. Tong, T. Fang-Newmeyer, J. Parker, E. A. Holland, D. Zhang, N. Nakanishi, H.-S. V. Chen, H. Wolosker, Y. Wang, L. H. Parsons, R. Ambasudhan, E. Masliah, S. F. Heinemann, J. C. Piña-Crespo and S. A. Lipton (2013). "Aβ induces astrocytic glutamate release, extrasynaptic NMDA receptor activation, and synaptic loss." Proceedings of the National Academy of Sciences **110**(27): E2518-E2527.
Tan, E. K., P. Ho, S. Y. Cheng, Y. Yih, H. H. Li, S. Fook-Chong, W. L. Lee and Y. Zhao (2011). "CALHM1 variant is not associated with Alzheimer's disease among Asians." Neurobiology of Aging **32**(3): 546.e511-546.e512.
Tanaka, J.-i., M. Matsuzaki, E. Tarusawa, A. Momiyama, E. Molnar, H. Kasai and R. Shigemoto (2005). "Number and Density of AMPA Receptors in Single Synapses in Immature Cerebellum." The Journal of Neuroscience **25**(4): 799-807.
Tang, Y.-P., E. Shimizu, G. R. Dube, C. Rampon, G. A. Kerchner, M. Zhuo, G. Liu and J. Z. Tsien (1999). "Genetic enhancement of learning and memory in mice." Nature **401**(6748): 63-69.
Taufiq Ur, R., A. Skupin, M. Falcke and C. W. Taylor (2009). "Clustering of InsP3 receptors by InsP3 retunes their regulation by InsP3 and Ca^{2+}." Nature **458**(7238): 655-659.
Tempia, F., M. Kano, R. Schneggenburger, C. Schirra, O. Garaschuk, T. Plant and A. Konnerth (1996). "Fractional calcium current through neuronal AMPA-receptor channels with a low calcium permeability." J Neurosci **16**(2): 456-466.
Texidó, L., M. Martín-Satué, E. Alberdi, C. Solsona and C. Matute (2011). "Amyloid β peptide oligomers directly activate NMDA receptors." Cell Calcium **49**(3): 184-190.
Thibault, O., J. C. Gant and P. W. Landfield (2007). "Expansion of the calcium hypothesis of brain aging and Alzheimer's disease: minding the store." Aging Cell **6**(3): 307-317.
Thies, W. and L. Bleiler (2013). "World Alzheimer Report 2016." Alzheimers Dement **9**(2): 208-245.
Tiveci, S., A. Akin, T. Cakir, H. Saybasili and K. Ulgen (2005). "Modelling of calcium dynamics in brain energy metabolism and Alzheimer's disease." Comput Biol Chem **29**(2): 151-162.
Toescu, E. C. and A. Verkhratsky (2007). "The importance of being subtle: small changes in calcium homeostasis control cognitive decline in normal aging." Aging Cell **6**(3): 267-273.
Toivari, E., T. Manninen, A. K. Nahata, T. O. Jalonen and M. L. Linne (2011). "Effects of transmitters and amyloid-beta peptide on calcium signals in rat cortical astrocytes: Fura-2AM measurements and stochastic model simulations." PLoS One **6**(3): e17914.
Tombola, F., M. M. Pathak and E. Y. Isacoff (2006). "How does voltage open an ion channel?" Annu. Rev. Cell Dev. Biol. **22**: 23-52.
Townsend, M., T. Mehta and D. J. Selkoe (2007). "Soluble Aβ inhibits specific signal transduction cascades common to the insulin receptor pathway." Journal of Biological Chemistry **282**(46): 33305-33312.
Tu, H. P., O. Nelson, A. Bezprozvanny, Z. N. Wang, S. F. Lee, Y. H. Hao, L. Serneels, B. De Strooper, G. Yu and I. Bezprozvanny (2006). "Presenilins form ER Ca2+ leak channels, a function disrupted by familial Alzheimer's disease-linked mutations." Cell **126**(5): 981-993.

Turner, P. R., K. O'Connor, W. P. Tate and W. C. Abraham (2003). "Roles of amyloid precursor protein and its fragments in regulating neural activity, plasticity and memory." Prog Neurobiol **70**: 1 - 32.
Um, J. W., A. C. Kaufman, M. Kostylev, J. K. Heiss, M. Stagi, H. Takahashi, M. E. Kerrisk, A. Vortmeyer, T. Wisniewski, A. J. Koleske, E. C. Gunther, H. B. Nygaard and S. M. Strittmatter (2013). "Metabotropic glutamate receptor 5 is a coreceptor for Alzheimer abeta oligomer bound to cellular prion protein." Neuron **79**(5): 887-902.
Uttara, B., A. V. Singh, P. Zamboni and R. T. Mahajan (2009). "Oxidative Stress and Neurodegenerative Diseases: A Review of Upstream and Downstream Antioxidant Therapeutic Options." Current Neuropharmacology **7**(1): 65-74.
Van Dam, D. and P. P. De Deyn (2006). "Drug discovery in dementia: the role of rodent models." Nat Rev Drug Discov **5**(11): 956-970.
Van den Hove, D. L., K. Kompotis, R. Lardenoije, G. Kenis, J. Mill, H. W. Steinbusch, K.-P. Lesch, C. P. Fitzsimons, B. De Strooper and B. P. F. Rutten (2014). "Epigenetically regulated microRNAs in Alzheimer's disease." Neurobiology of Aging **35**(4): 731-745.
Vandenberg, R. J. and R. M. Ryan (2013). Mechanisms of Glutamate Transport.
Vargas-Caballero, M. and H. P. Robinson (2004). "Fast and slow voltage-dependent dynamics of magnesium block in the NMDA receptor: the asymmetric trapping block model." The Journal of neuroscience **24**(27): 6171-6180.
Ventura, R. and K. M. Harris (1999). "Three-dimensional relationships between hippocampal synapses and astrocytes." The Journal of Neuroscience **19**(16): 6897-6906.
Verkhratsky, A. (2005). "Physiology and pathophysiology of the calcium store in the endoplasmic reticulum of neurons." Physiol Rev **85**(1): 201-279.
Volfovsky, N., H. Parnas, M. Segal and E. Korkotian (1999). "Geometry of dendritic spines affects calcium dynamics in hippocampal neurons: theory and experiments." J Neurophysiol **82**(1): 450-462.
Wang, H.-Y., D. H. Lee, M. R. D'Andrea, P. A. Peterson, R. P. Shank and A. B. Reitz (2000). "β-Amyloid1–42 Binds to α7 Nicotinic Acetylcholine Receptor with High Affinity IMPLICATIONS FOR ALZHEIMER'S DISEASE PATHOLOGY." Journal of Biological Chemistry **275**(8): 5626-5632.
Wang, S. S. S., V. Kazantzi and T. A. Good (2003). "A Kinetic Analysis of the Mechanism of β-Amyloid Induced G Protein Activation." Journal of Theoretical Biology **221**(2): 269-278.
Weiss, J. N. (1997). "The Hill equation revisited: uses and misuses." The FASEB Journal **11**(11): 835-841.
Wilson, N. P., B. Gates and M. Castellanos (2013). "Modeling the short time-scale dynamics of β-amyloid–neuron interactions." Journal of Theoretical Biology **331**(0): 28-37.
Wischik, C. M., D. J. Wischik, J. M. D. Storey and C. R. Harrington (2010). Chapter 11 Rationale for Tau-Aggregation Inhibitor Therapy in Alzheimer's Disease and Other Tauopathies. Emerging Drugs and Targets for Alzheimer's Disease: Volume 1: Beta-Amyloid, Tau Protein and Glucose Metabolism, The Royal Society of Chemistry. **1:** 210-232.
Wu, B., H. Yamaguchi, F. A. Lai and J. Shen (2013). "Presenilins regulate calcium homeostasis and presynaptic function via ryanodine receptors in hippocampal neurons." Proc Natl Acad Sci U S A.
Wuytack, F., L. Raeymaekers and L. Missiaen (2002). "Molecular physiology of the SERCA and SPCA pumps." Cell Calcium **32**(5-6): 279-305.
Yano, K., O. H. Petersen and A. V. Tepikin (2004). "Dual sensitivity of sarcoplasmic/endoplasmic Ca^{2+}-ATPase to cytosolic and endoplasmic reticulum Ca^{2+} as a mechanism of modulating cytosolic Ca^{2+} oscillations." Biochem J **383**(Pt 2): 353-360.
Yashiro, K. and B. D. Philpot (2008). "Regulation of NMDA receptor subunit expression and its implications for LTD, LTP, and metaplasticity." Neuropharmacology **55**(7): 1081-1094.

You, H., S. Tsutsui, S. Hameed, T. J. Kannanayakal, L. Chen, P. Xia, J. D. T. Engbers, S. A. Lipton, P. K. Stys and G. W. Zamponi (2012). "Aβ neurotoxicity depends on interactions between copper ions, prion protein, and N-methyl-d-aspartate receptors." Proceedings of the National Academy of Sciences of the United States of America **109**(5): 1737-1742.
Young, J. E. and L. S. B. Goldstein (2012). "Alzheimer's disease in a dish: promises and challenges of human stem cell models." Human Molecular Genetics **21**(R1): R82-R89.
Zador, A., C. Koch and T. H. Brown (1990). "Biophysical model of a Hebbian synapse." Proceedings of the National Academy of Sciences **87**(17): 6718-6722.
Zampese, E., C. Fasolato, M. J. Kipanyula, M. Bortolozzi, T. Pozzan and P. Pizzo (2011). "Presenilin 2 modulates endoplasmic reticulum (ER)–mitochondria interactions and Ca^{2+} cross-talk." Proceedings of the National Academy of Sciences **108**(7): 2777-2782.
Zeiger, W., K. S. Vetrivel, V. Buggia-Prevot, P. D. Nguyen, S. L. Wagner, M. L. Villereal and G. Thinakaran (2013). "Ca2+ influx through store-operated Ca2+ channels reduces Alzheimer disease beta-amyloid peptide secretion." J Biol Chem **288**(37): 26955-26966.
Zhabotinsky, A. M. (2000). "Bistability in the Ca 2+/calmodulin-dependent protein kinase-phosphatase system." Biophysical Journal **79**(5): 2211-2221.
Zhang, H., S. Sun, A. Herreman, B. De Strooper and I. Bezprozvanny (2010). "Role of presenilins in neuronal calcium homeostasis." The Journal of neuroscience : the official journal of the Society for Neuroscience **30**(25): 8566-8580.
Zhang, H., S. Sun, A. Herreman, B. De Strooper and I. Bezprozvanny (2010). "Role of presenilins in neuronal calcium homeostasis." J Neurosci **30**(25): 8566-8580.
Zhao, D., J. B. Watson and C.-W. Xie (2004). "Amyloid β prevents activation of calcium/calmodulin-dependent protein kinase II and AMPA receptor phosphorylation during hippocampal long-term potentiation." Journal of neurophysiology **92**(5): 2853-2858.
Zundorf, G. and G. Reiser (2011). "Calcium dysregulation and homeostasis of neural calcium in the molecular mechanisms of neurodegenerative diseases provide multiple targets for neuroprotection." Antioxid Redox Signal **14**(7): 1275-1288.